UNIVERSITÀ DEL SALENTO
FACOLTÀ DI SCIENZE MATEMATICHE FISICHE NATURALI
XXX CICLO DOTTORATO IN FISICA E NANOSCIENZE

UNIVERSITÉ PARIS 13 – SORBONNE PARIS CITÉ
ECOLE DOCTORALE INSTITUT GALILÉE
DISCIPLINE: PHYSIQUE – SCIENCES DES MATERIAUX

DOCTORATE THESIS IN INTERNATIONAL COTUTELLE AGREEMENT

Diamonds: synthesis and contacting for detector applications

This thesis has been publically presented and defended by

Mary DE FEUDIS

to get the titles of:

Doctor in Physics and Nanoscience from the University of Salento (Italy)
and
Doctor in Physics and Science of Materials from the University of Paris 13 – Sorbonne Paris Cité (France)

Defence date: 30/03/2018 at the University of Paris 13, France

COMMITTEE MEMBERS:

Denis DAUVERGNE	Director of research, CNRS Grenoble	President
Julien PERNOT	Professor, University of Grenoble Alpes	Referee
Samuel SAADA	Researcher engineer – HDR, CEA List, Saclay	Referee
Jocelyn ACHARD	Professor, University of Paris 13	Director of thesis
Maurizio MARTINO	Associate professor, University of Salento	Director of thesis
Khaled HASSOUNI	Professor, University of Paris 13, Director of LSPM	Examiner
Vianney MILLE	Associate professor, University of Paris 13	Examiner
Anna Paola CARICATO	Associate professor, University of Salento	Examiner

Lecce **L**aser **L**aboratory, Italy
Laboratoire des **S**ciences des **P**rocédés et des **M**atériaux **CNRS UPR 3407**, France

Summary

General introduction

Since ancient times, diamonds have aroused curiosity over the world thanks to their fascinating optical properties and incredible hardness. In addition, their rarity increased both mystery and interest about the diamond origin. Among the firsts and fascinating explanations offered for the diamond provenance there is the Greek speculation defining diamonds as “tears of the gods” and the Roman belief calling diamonds as “fragments of fallen stars”. Then, even when the diamond origin was clarified, the popularity of these stones remained so important that diamonds have been traditionally associated to something beautiful, as symbol of wealth and power. However, when the use of diamonds in the goldsmith's art became a custom, scientific interest started. Indeed diamond material, which is composed of carbon atoms arranged in a tetrahedral configuration, owns a wide variety of exceptional properties. For example, its extreme hardness allowed using it for mechanical operations such as cutting and polishing of hard materials, its transparency from deep UV to far infrared allowed the development of diamond window fabrication, and its chemical inertia to various acids, allowed the development of sensors working in aggressive environments [1]. Nowadays great interest by the scientific community has been demonstrated for diamond applications in the field of particles detection and electronic power devices. Indeed, diamond material proves to be extremely radiation hard and perfectly compatible with the human tissue, so as a lot of diamond detectors and dosimeters have been manufactured for the high-energy and medical physics [2, 3]. Moreover, the very high thermal conductivity together with the wide band gap (5.47 eV) have made diamond the ultimate candidate for the fabrication of power components [4, 5].

Nevertheless, diamond naturally grows in special pressure and temperature conditions in the Earth’s mantle, which makes this material rare and expensive. Moreover, in the earth growth conditions, each diamond stone can have very different quality strongly hampering its use for technological applications. That’s the main reason why a strong and permanent effort has been made to develop appropriate techniques allowing growing synthetic diamond. This item has always been a major challenge for scientists for several decades, as evidenced by the work of Moissan dating from the late 19th century. After the first tries of producing synthetic diamond with high pressure and high temperature (HPHT) conditions in the 1950’s, a technique for synthesizing diamond at low-pressure (i.e. under metastable conditions) by chemical vapour deposition (CVD) was developed in the 1970s. After the first attempts carried out by American and Russian research teams [6, 7], it was only in the 1980s that this technique really gained momentum thanks to Japanese works [8-11]. Today, it is a widely used technique which allows growing monocrystalline, polycrystalline and nanocrystalline

diamond films on various substrates. The progresses achieved with the fabrication technology have unleashed a lot of prospects into integrating diamond films in different devices to address a wide variety of applications. Among them electronic devices and detectors have a high potential but are still under development. For these devices, electrical contacting is of prime importance, and this PhD work is mostly focused on this problematic.

This PhD work has been carried out under an international cotutelle agreement between the University of Salento (Italy) and the University of Paris 13 (France). In particular, I worked for the first two years at the Lecce Laser Laboratory (L3) in Italy (where I got the PhD position), before spending the last year at the Laboratoire des Sciences des Procédés et des Matériaux (LSPM) in France. In this manuscript, after a state of the art and instrumentation description in Chapter I and II, respectively, the experimental results are presented in Chapter III for the laser-induced graphitic contact manufacturing (Italy) and Chapter IV for the graphite / metal ohmic contact fabrication on diamond (France). Both experiments deal with diamond contacting, by graphitization and metallization, for detector and electronic device applications. In particular, at L3 I developed (both for hardware and software aspects) an experimental set-up dedicated to the laser-induced diamond graphitization for producing the contacting of all-carbon detector which was the main objective of this laboratory involved in the framework of a new high-energy physics experiment called Positron Annihilation into Dark Matter Experiment (PADME) [12] proposed by the Italian National Institute of Nuclear Physics (INFN). During this first part of my PhD I implemented a protocol to produce ohmic graphitic contacts on diamond surface that meet the specifications of the PADME experiment. This device was the first prototype of the all-carbon detector and was successfully tested in this project.

Afterwards, I worked on the diamond growth and contacting at LSPM with the aim of developing a protocol of diamond graphitization by ion bombardment / metallization to produce ohmic graphite / metallic contacts on lightly boron doped diamond surfaces. Indeed, taking into account the promising results obtained on graphitic ohmic contacts for the all-carbon detector, we have planned to add a graphitic layer underneath the diamond surface in order to improve ohmic contacts for lightly boron doped diamond and compare diamond electrical performance with pure metal contacts and with graphite / metal contacts. This also included extensive processing work in a clean room environment.

As previously mentioned, the Manuscript of this thesis is organised in four chapters.

- Chapter I deals with the state of the art of diamond material starting from the synthesis process until the detector applications. In particular, the main diamond properties, the natural synthesis process and the artificial HPHT and CVD techniques are presented. A focus is given to the

Microwave Plasma Assisted Chemical Vapour Deposition (MPACVD) technique which was used during this thesis work to grow single crystal diamond films at LSPM. Then, diamond doping (n- and p-type) is discussed, with more attention towards the boron dopant, for applications in the field of power electronic devices. The diamond crystalline quality, the electronic properties, the charge mobility and the resistivity values are discussed too before arriving to the diamond contacting section in which the characteristics of the different contact types that can be produced on diamond surface are presented. In particular, starting from the metal-semiconductor junction in terms of energy band diagram, Schottky and ohmic contacts on diamonds are described. Then a wide section dedicated to diamond detectors is presented. The choice of diamond material as sensors, the device design, the process of charge creation when nuclear particles cross diamond and the charge collection distance (CCD) properties are explained. A paragraph dedicated to the different contacting configuration (1D, 2D, 3D) complete this section. Eventually, as an alternative to the traditional metallic electrodes, a new field of graphitic contacts on diamond induced by laser or by ion implantation is presented.

- Chapter II collates the instrumentation data used to manufacture and characterize the samples investigated during this thesis. In particular, the first part of the chapter deals with the description of CVD polycrystalline intrinsic diamond used for detection and of the experimental set-up used to graphitize these samples by laser-writing technique at L3 (Italy). The diamonds were chosen to be contacted and used as all-carbon detectors for the PADME experiment. Afterwards, a second section is dedicated to the instrumentation used at LSPM (France) for diamond growth and contacting. In particular, the protocol of the diamond substrate preparation before the growth process, the description of the MPACVD reactors used for intrinsic and boron doped CVD monocrystalline diamond, in addition to all instrumentation used to graphitize (by ion implantation) and metallize these samples are presented. Then, in the last part of the chapter all the characterization techniques used to analyze the as-grown, graphitized and metallized diamond from structural, morphological, compositional, mechanical and electrical points of view are described.

- Chapter III deals with the fabrication of ohmic graphitic contacts on diamond surfaces by laser-writing technique for all-carbon PADME detector application. A LabVIEW software dedicated to synchronize and control the laser shooting with the sample displacements in order to produce graphitic bi-dimensional pattern on diamond surface has been developed. The graphitic contact manufacturing in addition to an extensive characterization work on them from morphological, structural, compositional, mechanical and electrical points of view are presented. Finally, an introduction to the PADME experiment, the detector assembling step

onto a dedicated PC-board, and the nuclear investigations performed on this all-carbon device are given. The nuclear characterization was done by electron and positron beam at the Beam Test Facility (BTF) at Frascati (Rome, Italy) thanks to which several detector aspects were studied and here reported, such as the time and spatial resolution together with the diamond charge collection distance (CCD).

- Finally, in Chapter IV the CVD homoepitaxial intrinsic and boron doped growth is presented. Spectroscopic and electric characterizations are discussed in order to investigate the boron concentration in the CVD layers and its impact in terms of sheet resistivity. Then, the diamond graphitization process underneath the CVD surface by an innovative ion implantation approach is presented and analyzed by Raman spectroscopy and electrical measurements. Afterwards, a diamond metallization protocol has been developed in this work and it is presented together with electrical characterizations showing the impact and the interest of a graphitic layer particularly for lightly doped samples.

For both experiments, several sample characterization steps were carried out in collaboration with national and international institutes of research which have been mentioned in the text. During the whole time of this PhD I have been an associate member of the INFN for the section of Lecce.

CHAPTER I: STATE OF THE ART

I.1 Introduction

People all over the world generally consider diamond as precious and exceptional material. Historically, the special optical properties of diamond, its extraordinary hardness in addition to its rarity have made it extremely attractive for people on our planet.

Initially, diamond has been used to embellish the jewels becoming symbol of wealth and power. Over the centuries, diamond has fascinated people also for different aspects gaining space for the first technological applications, such as cutting, polishing and drilling instrumentations thanks to its hardness, or more recently as optical windows for high power lasers [1]. Nowadays, diamond has obtained great requests in the scientific applications because of their mix of high thermal, electrical and mechanical properties. For example diamond can be processed as component for power electronic devices [4, 5] or as radiation and particle detectors in the high energy physics and medical physics fields, thanks to its extraordinary radiation hardness and breakdown voltage values in addition to its inertness and its biocompatibility [2, 3].

All these aspects have encouraged and supported several decades of research dedicated at first to the development of different technologies to synthesize and grow high quality diamond, and then to the development of new instrumentations and techniques to adapt the synthetized diamond to the forecast applications (for instance diamond doping for electronic applications).

Last but not the least, diamond contacting has been widely investigated and developed by metallization processes and more recently by graphitization techniques as it represents a fundamental step to obtain a performant diamond electronic device.

In this first chapter, the main diamond properties together with the natural synthesis process and the different techniques to artificially synthesize diamond are presented. A wide space is dedicated to the Microwave Plasma Assisted Chemical Vapour Deposition (MPACVD) technique, which was used during this work.

The growth of polycrystalline and monocrystalline diamond is reported with a particular focus on the homoepitaxy process which allows the high quality CVD monocrystalline diamond growth.

Then, the diamond doping is discussed, reporting the several techniques described in the literature with the different kind of doping (n- and p-type), the advantages and the drawbacks. Here, the “in situ” growth of p-type boron doped diamond is mainly described as it was carried out during this PhD. The diamond quality, the electronic properties, the charge mobility and the resistivity values are discussed too.

Afterward a wide section dealing with the diamond contacting, explaining the metal-semiconductor junction in terms of energy band diagram, Schottky and ohmic electrodes on doped diamonds for power electronic applications and the manufacturing of ohmic contacts on diamonds are reported.
Then, the diamond detectors are introduced. The choice of diamond materials as sensors, the device design, the process of charge formation when nuclear particles cross diamond and the charge collection distance (CCD) properties are explained. The historic diamond detectors used in high energy physics experiments, in addition to the PIN diamond detectors and diamond dosimeters complete the application section.
Here 1D, 2D and 3D diamond contacting configuration are illustrated together with the limits of the metallic electrodes showing the interest of diamond graphitization for detection.
Finally, the diamond graphitization is proposed reporting the techniques of laser-writing and ion implantation. Both processes are illustrated from a physics point of view and in terms of applications until today. A recall of my master thesis results regarding the production of ohmic contacts on diamond surface by laser-writing is given as know-how and starting point of the diamond graphitization experiments.

I.2 Diamond properties

Diamond is a material characterized by extraordinary properties related to the crystallographic structure and atomic bonding. The diamond structure is equivalent to a face-centred cubic (FCC) lattice with a base of two identical carbon atoms, one in the position (0, 0, 0) and the second one at the position (¼ , ¼, ¼) , where the coordinates are assigned as fraction of the cube side. This geometric atom displacement is equivalent to two interpenetrating FCC lattices located along the body diagonal with a distance of one-quarter of the diagonal length. The unitary cell is cubic, with a lateral size a_0 of about 3.56 Å (at room temperature). The distance between two closest carbon atoms correspond to ¼ of the cubical diagonal, namely 1.54 Å. Every atoms can be considered like a sphere having a radius equal to 1/8 of the cubical diagonal. The cube contains the equivalent of eight carbon atoms, the atomic density is 1.77×10^{23} cm^{-3}, which represents the highest atomic density of any material on the earth. Multiplying the atomic density by the average carbon atomic mass, diamond mass density is obtained, which proves to be 3.52 g/cm^3. In Figure I.1, the diamond crystalline structure is presented. The tri-dimensional diamond structure proved to be particularly rigid and dense overcoming each comparison with other materials [1, 5].

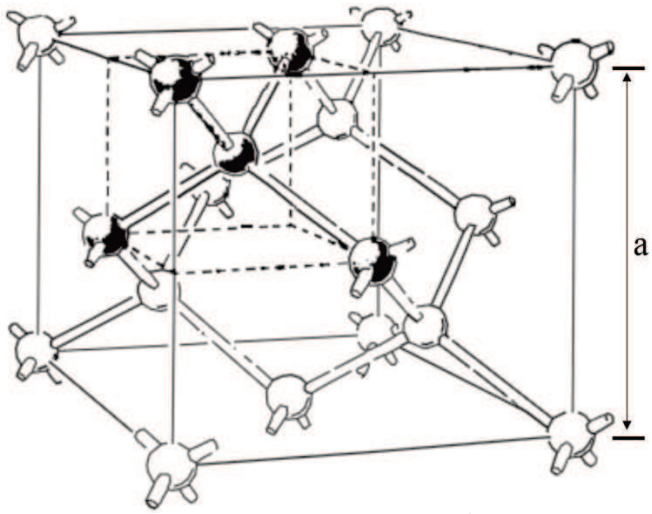

Figure I.1. Sketch of the diamond unit cell, where a = 3.56 Å is the cubic lattice constant [13].

One of the diamond peculiarity is the extraordinary strength bonding of the carbon atoms. In particular, the atoms stick together through strong sp^3 σ-type bonds and the cohesive energy is 3.62 eV/bond or 7.24 eV. This property makes the energy necessary to displace an atom from its site (displacement energy) high, which makes diamonds radiation hard materials for example under particle irradiation. In addition, diamonds register record values in terms of matter hardness, compressibility, carrier mobility, sound propagation speed and last, but not the least, thermal conductivity at room temperature (namely 24 $W.cm^{-1}.K^{-1}$, five times higher than copper).

Table I.1. Properties and application of diamond materials [4, 14, 15].

Property	**Value**	**Application**
Bandgap, eV	5.47	High.-temperature electronics
Carrier mobility, $cm^2/(V\ s)$	1800 h @RT, 0V	Radiation-hard detectors
	2300 e^- @RT, 0V	Optoelectronic switches
Resistivity, Ω cm	$> 10^{11}$	
Thermal conductivity, W/(cm K)	20 − 24	Heat skins
Dielectric constant	5.7	
Optical transmission range	225 nm − RF	Photonics and MW devices
Hardness, GPa	81 ± 18	Tools, surgery blades
Acoustic wave velocity, km/s	18.4 along (111)	Surface acoustic wave devices
Thermal expansion coefficient, $10^{-6}\ K^{-1}$	0.8 @ 293K	Photonic and MW devices
Corrosion resistance	Stable in HF	Electrochemistry
Negative electron affinity		Electron emitters
Biocompatibility		Biomedicine

In addition, diamond material stand out for their high band gap (5.47 eV) which has opened the way to the manufacturing of diamond technologies based on wide band gap semiconductors for power electronic devices.

These and other properties make diamonds precious for several technological applications. The most relevant properties are summarized in the Table I.1.

I.3 The diamond synthesis

During the twentieth century the extraordinary properties of diamond materials, which is of main interest for several scientific disciplines (as shown in the Table I.1), have strongly motivated the research and development of several diamond synthesis technologies. The first primitive man-made diamonds were done by Henri Moissan in 1893 starting from small amounts of carbon subjected to high pressure and high temperature conditions. Systematic studies were carried out in the 1910s in Europe [16]; however it was only in the 1950s that first real technologic progresses was made [6, 17].

The starting point of the diamond synthesis process study has been the carbon phase diagram analyses. Indeed, diamond material constitutes just one of the different allotropic forms in which the carbon structures can evolve depending on the growth conditions, pressure and temperature values, which are extremes for diamonds while they are ordinary for the graphitic allotropic form proving to be the favourite one on the Earth's surface. For completeness, the other carbon allotropic forms present and more recently discovered are the graphene, nanotubes and fullerenes.

In the following, the carbon phase diagram together with the different diamond synthesis techniques are presented.

I.3.1 The carbon phase diagram and the natural diamond classification

The natural diamond synthesis takes place in the Earth's mantle, at 200 km depth, where the pressure and temperature values are very high (temperature of 3000 K and pressure of more than 14 GPa). On the contrary, at atmospheric pressure and temperature values, graphite proves to be the stable thermodynamic carbon phase. Current knowledge of the carbon phase diagram are summarized in Figure I.2.

Historically, the first developed diamond synthesis technique was the High Pressure High Temperature (HPHT), which reproduces the stable thermodynamic conditions to create diamond crystals. Subsequently, the diamond synthesis in metastable conditions, namely with low pressure

values was developed by chemical vapour reactions (Chemical Vapour Deposition, CVD). Both methods make it possible to stabilize the atomic arrangement in the sp^3 hybridization configuration, which characterizes the diamond phase and its properties as the most popular high hardness (see section I.2). On the contrary, at atmospheric pressure and temperature values, the favourite atomic arrangement is the sp^2 structure, which consists of stacked multi-sheets and gives origin to the highly friable graphite phase. Schemes of the two atomic configuration are shown in Figure I.2. Although both diamond and graphite are composed of carbon atoms, it is their different atomic configurations which lead to very different properties in terms of mechanical, optical absorption, thermal and electrical conditions.

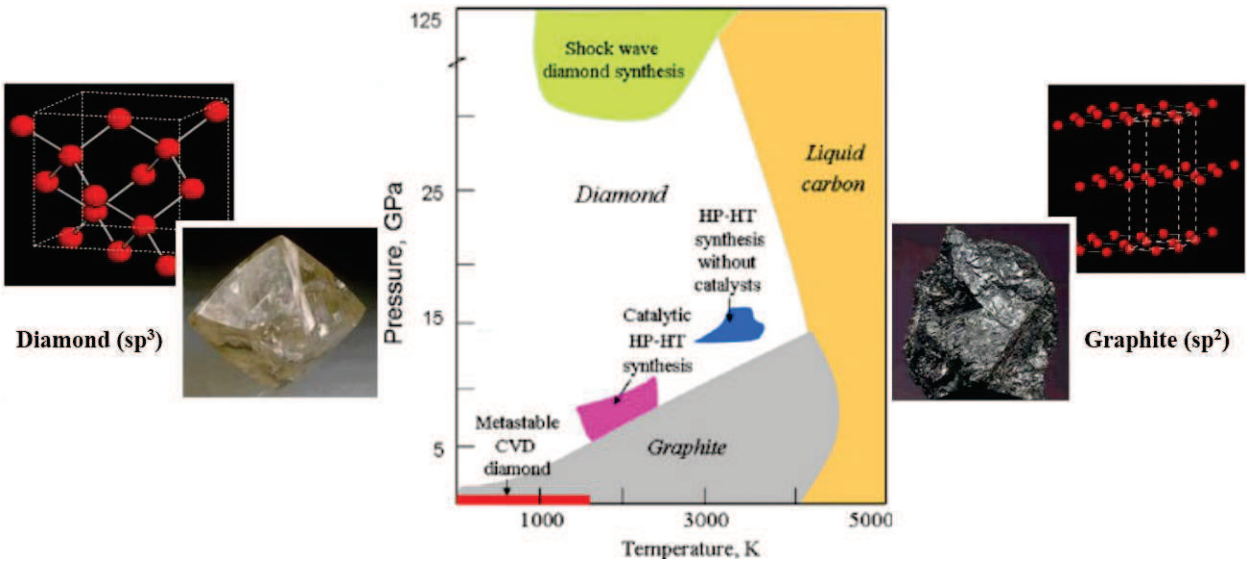

Figure I.2. The central picture shows the carbon phase diagram. The main regions of the temperature-pressure space in which diamond growth occurs by HPTH and CVD synthesis are indicated [18]. On sides, two pictures and the related crystallographic structures for the diamond and graphite materials are reported.

In the phase diagram, it is possible to determine the most suitable conditions to synthesize diamonds. For example, the blue zone marked "HPHT synthesis without catalysts" is an area in which it is possible to transform graphite into diamond by choosing the corresponding pressure and temperature values and without using catalyst materials. In addition, the pink region "Catalytic HPHT synthesis" also represents a range of pressure and temperature conditions within the graphite can be converted into diamond but necessary using a metal solvent (such as Fe, Co, Ni, etc.). Afterwards, changing the synthesis technique from HPHT into CVD it is possible to take advantage of very low pressure (a few tens to a few hundred mbar) and moderate temperature values, as shown in the yellow box in the phase diagram.

Diamond available in nature has been basically classified in two categories depending on the quantity of nitrogen impurities, namely type I and type II which indicate the most contaminated and most pure, respectively. Then, every category type has been split in other two sub-categories Ia and Ib, IIa and IIb [13]. In particular, the type Ia diamonds are the most present in nature and contain aggregated

nitrogen atoms which make them of pale yellow colour, while the type Ib diamonds are more rare. Their colour appear more yellow and they contain nitrogen atoms located at the substitution sites in the diamond lattice. On the contrary, the type II diamonds are classified as type IIa when they are transparent and electrically insulating, therefore they are also called "pure" diamonds; while they are defined as type IIb diamonds if containing some boron impurity tracks, which are typically located into substitutional sites and make the diamonds of blue colour. The colour intensity depends on the boron concentration. The IIb-type diamonds prove to be very rare. In Figure I.3 natural and synthetic diamonds with different colour are shown.

Figure I.3. Diamond single crystals of gemmological quality and different colour cut in jewel form are reported. (a) The synthesis techniques of productions are CVD by Element6 (from 0.21 to 1.04 carats) [19] and (b) HPHT by De Beers [20].

I.3.2 The HPHT diamond synthesis

The first technique developed to synthesise diamond was thought on the idea to reproduce the natural conditions synthesis. The crystal manufacturing began in 1953 by the ASEA electricity company in Sweden which developed the method called High Pressure and High Temperature (HPHT). The physics principle is simple: carbon materials must be submitted to the thermodynamic conditions of diamond formation, which are reported in the phase diagram of Figure I.2. In particular, this process consists in adding a carbon material (as graphite) in a solvent made of transition metals (iron, nickel, cobalt, etc.) and exposing this mixture to a temperature gradient of 1600 – 1800 K and high pressures (few GPa) [21]. The synthesis process is shown in Figure I.4. The diamond crystals synthesized by this method are, in the most cases, contaminated by impurities captured during the growth. For example, residual impurities of the solvent metals (Fe, Ni, Co) are frequently found, but the main impurity is the nitrogen, which is present in significant concentration and limits strongly the electrical properties of the material. Therefore, HPHT crystals are generally not directly usable for electronic applications. Nevertheless, more recently, this process has been strongly improved allowing the

production of high purity material with very low dislocation densities [22-25] but the cost and the availability of such material limit its use up to now.

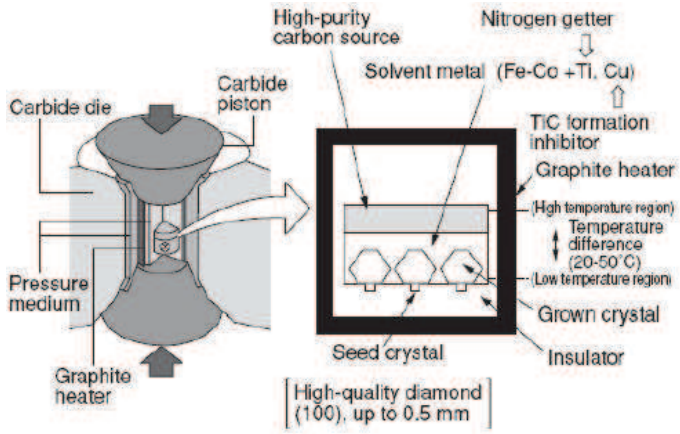

Figure I.4. Instrumentation for the HPHT diamond synthesis [26].

According to the classification offered for the natural diamonds, HPHT synthetic diamonds are produced and classified in the different categories and sub-categories Ia, Ib, IIa and IIb depending on the kind and quantity of impurities.

Although the purity of the HPHT diamond substrates can be not so satisfactory, their crystalline quality and the possibility to obtain large crystals (typically from 3 × 3 to 8 × 8 mm^2) with thicknesses greater than 500 µm represent their major qualities. Nowadays, the HPHT diamonds are widely used as substrates for the deposition of high quality diamond layer by CVD technique, which allows controlling easier the environment in terms of residual impurities.

I.3.3 The Chemical Vapour Deposition (CVD) diamond synthesis

The first studies about the low pressure diamond synthesis date back to the 1950s and have been carried out by American and Russian research teams [6, 7], but it was only in the 1980s that this technique really gained momentum thanks to Japanese works [8-11]. Today, it is one of the most used synthesis techniques.

The basic idea is to synthesize diamond at low pressure (10-100 mbar) and moderate temperature (700 - 900 °C) conditions, in a rich environment of atomic hydrogen. In particular, the fundamental principle of the CVD technique is the chemical species generation in the gaseous phase which participates to the synthesis and growth of the film under metastable conditions. The gas phase activation can be done by different ways, for example by a hot tungsten or tantalum filament, an oxyacetylene flame (which can be performed at atmospheric pressure), an electric discharge or a microwave source. The carbon precursors can be obtained from a hydrocarbon, usually methane (CH_4), as illustrated in Figure I.5. Then, by means of an external energy supply, the gaseous phase is activated and the methyl radical formation occurs which constitute the elementary bricks for the

construction of the crystalline carbon structure. In addition, atomic hydrogen is also formed having the role of selective etching of non-diamond phases deposited under the specific conditions where the graphite phase is the most stable carbon form [27]. Finally, hydrogen is also useful to saturate the dangling carbon bonds of the growing film and to ensure the sp^3 bond formation among the carbon atoms [28]. It was estimated that about 10^4 hydrogen atoms are required to incorporate a single carbon atom into the diamond lattice [28, 29].

Historically, there are two principal ways to activate the gaseous phase, namely by hot filament or by microwave electromagnetic source. If the gaseous phase activation is carried out using a hot filament, the process is called Hot Filament Chemical Vapour Deposition (HFCVD) [30]. A tungsten or tantalum filament is placed very close to the substrate and is heated up to temperatures of 2300 – 2800 K by the electric current circulating. At this temperature, hydrogen and carbon species are dissociated to form radicals essential to diamond growth. Nevertheless, during this process the filament may be partially vaporized and the synthesized layers are consequently contaminated by the filament material. Moreover, the activation temperature is limited by this vaporization and, consequently, the density of atomic hydrogen in the gas phase remains moderate so as to limit greatly the diamond growth rate. Nevertheless, this method presents some interesting advantages, such as allowing covering very large surfaces and/or substrates with complex geometries, which is very useful for applications in the field of mechanics or electrochemistry where the diamond film thickness and purity are not crucial parameters. If the gas phase activation is carried out by a microwave electromagnetic source, the process is called Microwave Plasma Assisted Chemical Vapour Deposition (MPACVD) [31]. In this case, it is possible to reach high gas temperatures by coupling microwaves at high power in the plasma.

A crucial role is played by the methyl radicals CH_3 which are the species responsible of the carbon atom incorporation in the lattice, as explained before. The methyl radical CH_3 production is governed by the following chemical reactions:

$$CH_4 + H_2 \longrightarrow CH_3 + H_2$$

$$CH_3 + H \longrightarrow CH_2 + H_2$$

$$CH_2 + H \longrightarrow CH + H_2$$

$$CH + H \longrightarrow C + H_2$$

In order to obtain a high methyl radical density, the dissociation of a large quantity of hydrogen molecules is necessary, which is reached only for high temperatures. Since the 1990s, the LSPM (Laboratoire des Sciences des Procédés et des Matériaux at the University of Paris 13, France) has carried out research on the CVD diamond synthesis assisted by plasma demonstrating that the

hydrogen molecular dissociation efficiently occurs at temperatures above 3000 K in the core of the discharge [28, 32-34]. However, the methyl radical production requires temperatures below 2200 K [35, 36]. In Figure I.5 it is illustrated the CVD diamond synthesis process assisted by plasma with methane and hydrogen molecules as protagonist gases.

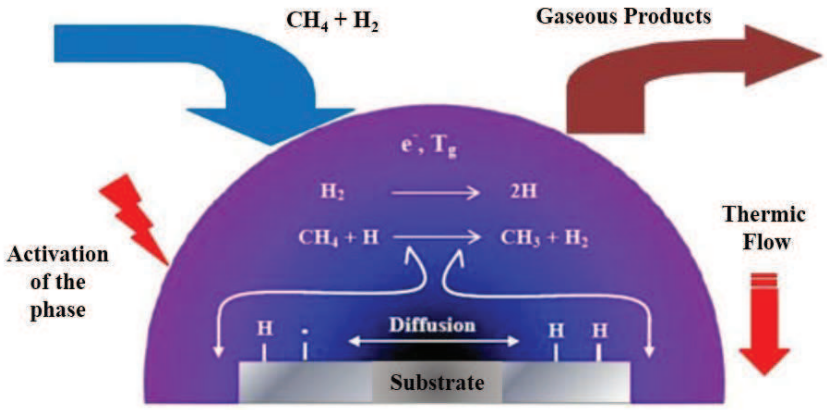

Figure I.5. Scheme of the CVD diamond synthesis.

During the growth process, the substrate temperature is maintained at 850 – 900 °C, which is very low regarding the gaseous environment temperature. Therefore a heat transfer phenomenon occurs from the plasma towards the substrate surface. As a result, the gas temperature sharply decreases, as well as the density of atomic hydrogen as illustrated in Figure I.6 (a) and (b), respectively. Moreover, the diffusion process allows the hydrogen atoms to reach the surface of the substrate and improve the quality of the growing diamond film [61, 62]. In addition, the reduction of the gas temperature at the plasma / surface interface proves to be beneficial since it allows reaching compatible values with the formation of methyl radicals (from 1400 to 2200 K), even though the atomic hydrogen density remains important. This phenomenon results in a high concentration of methyl radicals at few millimetres from the surface (see Figure I.6 (b) close to the substrate).

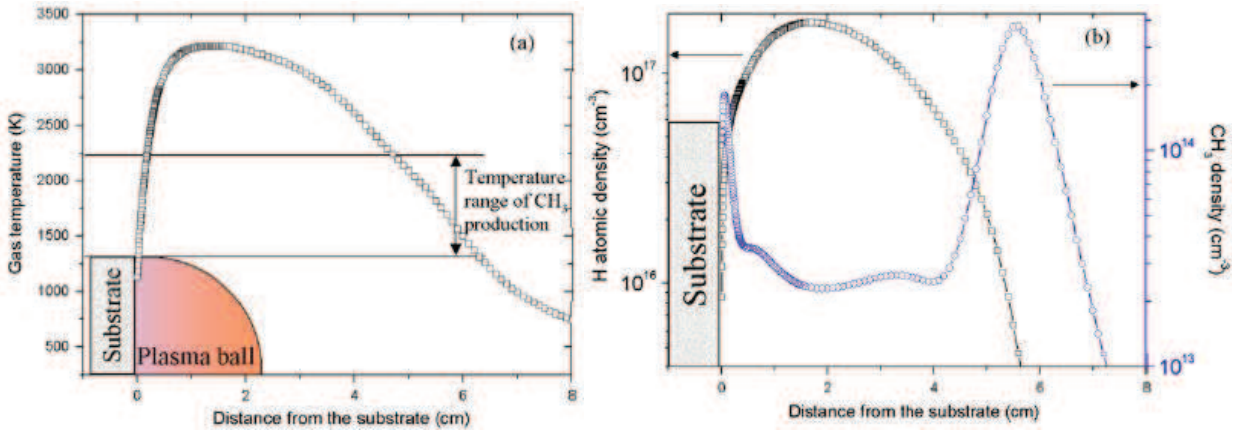

Figure I.6. (a) Gas temperature and (b) atomic hydrogen (blue dots) and methyl radical (black squares) concentrations got by calculation with a 1D axial plasma model for a MWPD of 1000Wcm^{-3}, 4% of CH4 in the H_2/CH_4 gas discharge and a substrate temperature of 1100 K. The substrate is placed at 0 of the X-axes [37].

By this technique, the atomic hydrogen density, as well as the methyl radicals close to the diamond surface, proves to be totally controlled by the temperature gradient of the gas between the plasma core and the plasma / diamond interface. As a result, a larger atomic hydrogen density gradient close to the surface leads to a larger CH_3 density at the plasma / diamond interface. Therefore, the crucial point for MAPCVD is to maximize the gas temperature, namely increasing the microwave power density which is controlled by the couple pressure-microwave power. When this condition is satisfied the production of atomic hydrogen is maximized as well as the CH_3 formation close to the deposition area. By this way, a growth rate close to 70 $\mu m.h^{-1}$ has been reach at LSPM [38] without adding any nitrogen in the gas phase, this impurity being very well known to strongly increase the growth rate [39-41], using pressure as high as 400 mbar. Nevertheless, the control of the growth at such extreme conditions remains difficult and more moderate pressure are basically used leading to growth rate between 10 and 20 μm/h.

Definitely, the MPACVD technique together with the use of pure gaseous sources and a good vacuum control proves to be the most efficient way to efficiently create key species for diamond deposition and allow diamond films synthesis with a very low contamination level. Therefore, this technique proves to be suitable for the diamond film production dedicated to the electronic applications, which require a rigorous control of the impurity level. For this reason and thanks to the LSPM team skills, the CVD diamond samples utilized for the diamond contacting study carried out during the second part of this PhD thesis in international cotutelle were produced by MPACVD depositions.

I.4 Growth of CVD polycrystalline and monocrystalline diamond

The diamond synthesis by CVD technique allows the growth of two kinds of material: polycrystalline material which is obtained starting from a non-diamond substrate and monocrystalline which is obtained starting from a monocrystalline diamond substrate. In the latter case, we talk more particularly of homo-epitaxy. In this section, both materials are presented with a particular focusing on the monocrystalline diamond which was used during this thesis.

I.4.1 CVD polycrystalline diamonds

For the CVD diamond synthesis processing, the choice of the substrate nature is crucial. Indeed, it is necessary to choose substrates composed of chemical elements having a thermal expansion coefficient compatible with a non-delamination of the film and being able to withstand the deposition

conditions. In addition, before the deposition step, a pre-treatment of the substrate is required in order to incorporate diamond seeds onto the substrate surface (see Figure 7 (a)) and permit the nucleation process (which otherwise would be extremely low). This seeding step can be performed by several methods: by immersing the substrate in an alcohol solution with diamond powder and submit it to ultrasonic processing, by deposit nanodiamond solution at the substrate surface by spincoating or by "scratching" the substrate with diamond paste. Once the nucleation sites are created the growth process can start. At the first instants, a lateral and orthogonal grain growth occurs on the substrate surface. The growth proceeds in all the three dimensions as long as the initial crystals are not joined. After the coalescence, only faces having the highest growth rate orthogonal to the surface may continue to move (see Figure 7 (b)). This results in a columnar growth with a so-called textured surface (see Figure 7 (c) Figure 7 (d) and (e)).

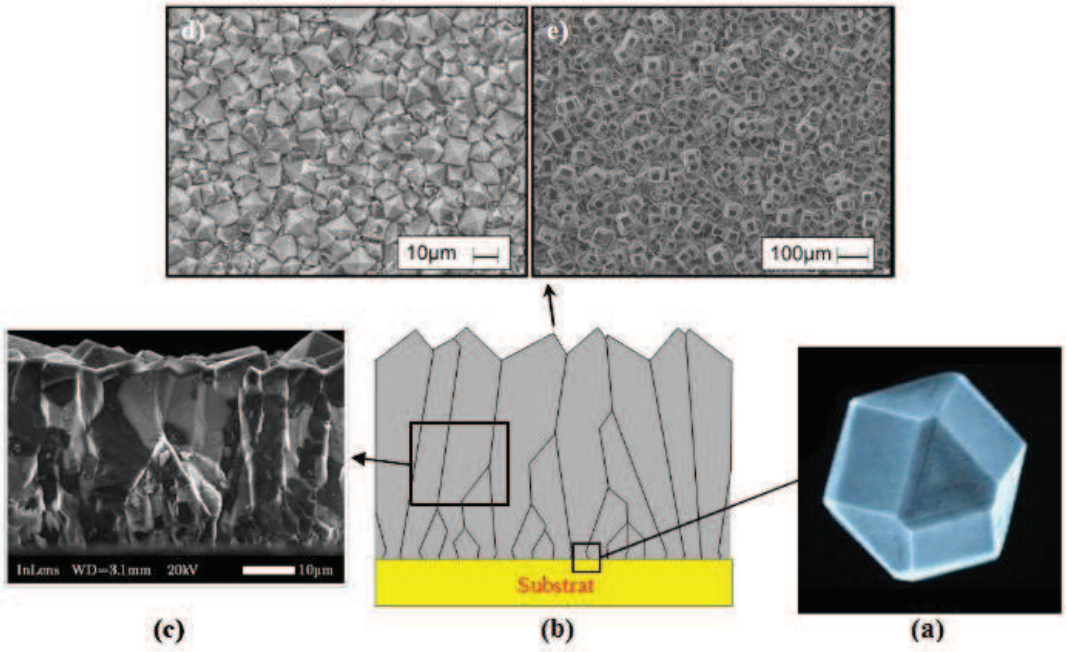

Figure I.7. Pictures of the growth steps of a CVD polycrystalline diamond film: (a) Diamond crystals at the beginning of the growth step, before coarsening; (b) Sketch showing the columnar growth (Van Der Drift model) [42]; (c) SEM cross section image showing a columnar structure [43]; (d) Textured surface with octahedral crystals and (e) Textured surface with cubic crystals [44].

The most important advantage of this technique is the possibility of developing diamond layers with large surfaces. Typically, the polycrystalline layer diameters deposited by microwave processes is two inches. Nevertheless, by decreasing the microwave excitation frequency from 2.45 GHz to 915 MHz, it is possible to increase the plasma size and grow polycrystalline diamond on substrates of four – six inches. This large diameter proves to be suitable for several applications, such as optical windows, radiation detectors, thermal applications and for cutting tools. On the contrary, the presence of grain boundaries related to the singular growth of nano- or micro- diamond seeds (Figure I.7) is a strong limitation for electronic applications.

I.4.2 CVD monocrystalline diamonds

CVD monocrystalline diamonds are obtained by homo-epitaxial growth on monocrystalline diamond substrates. Different types of substrates can be used: natural diamonds, HPHT or CVD substrates. The choice of these substrates, which involves several characteristics such as the crystalline orientation, quality and substrate purity, proves to be crucial as it directly affects the quality, the morphology and the final physical properties of diamond films grown above them. The most common substrates available on the market are the natural IIa diamond substrates, Ib HPHT and CVD IIa synthetic substrates. For completeness, HPHT IIa synthetic substrates are available but less used due to their very high cost.

The substrate impacts on the homo-epitaxial CVD film properties were widely investigated by the LSPM [45]. For example, the CVD films grown on natural IIa substrates presented a very high stress level due to the very high dislocation density, which led to a homo-epitaxial film broken. On the contrary, the best results were obtained using HPHT Ib synthetic substrates, which gave origin to CVD monocrystalline diamonds of high quality [37]. More recently, high quality IIa HPHT substrates, providing by NDT company, have been used leading to the growth of CVD layers with improved properties [46]. Nevertheless, the prohibited cost and low availability of such substrates strongly limit their use for homoepitaxy.

Thus, taking into account the accessible cost of the HPHT Ib substrates and the high quality of CVD films grown above them, for this thesis work, all the CVD monocrystalline diamond depositions were performed on this kind of substrates.

I.4.3 CVD monocrystalline diamond morphology

One of the crucial points for performing CVD diamond deposition is the crystallographic orientation of the substrate. Indeed, the several diamond orientations, namely (100), (110) and (111), present different atomic structures which strongly affect several parameters, such as the growth rate, the impurity incorporations and the final morphology of the grown layer. In this work, all the growth were performed on (100) oriented HPHT diamond substrates with four lateral faces having the same orientation, this kind of substrates leading to best quality of diamond material. Even if the quality is known to be high, some typical defects can be encountered in the grown layers which may have an impact on surface morphology.

The most important are:

- Dislocations;
- Hillocks;
- Not epitaxial crystallites.

The dislocation formation in the CVD diamond films may be of various origins, but is mainly due to the propagation of dislocations initially present in the substrate. They can also be initiated at the growth resuming due to surface defects related to polishing step (see Figure I.8). These defects constitute a main problem for diamond technologies as they strongly affect the crystal quality. For example, for diamond electronic applications, dislocations can limit the mobility of charge carriers and modify the conduction paths causing degradation and limiting device performances, particularly under strong electric field conditions.

It is possible to minimize dislocation density in CVD films both by controlling the growth conditions and performing dedicated pre-treatments on the substrates before the growth [47-49] but nevertheless, nowadays, limitation of such kind of defects remains one of the major challenges [50-53].

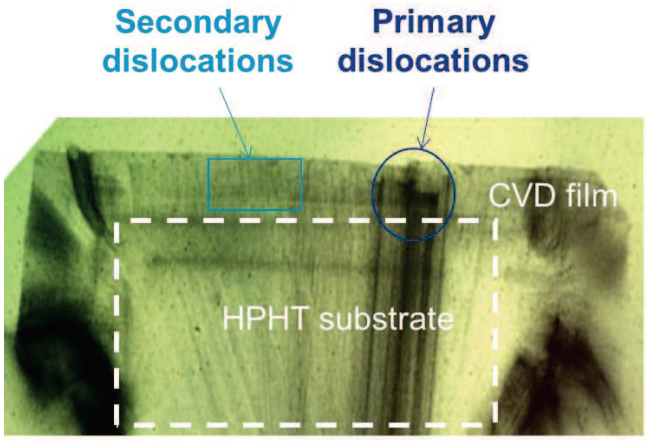

Figure I.8. X-ray section topography picture registered on a CVD diamond film. Primary dislocations correspond to the dislocation initially presents in the substrate and the secondary dislocations correspond to the dislocations initiated at the growth resuming.

Very often, an emergence of dislocation at the surface of diamond, leads to the formation of a hillock defect due to a locally acceleration of the growth rate. The hillocks are small islands with squared base and flat or pyramidal profiles, which are sometimes decorated with a twinned crystal on the top. A set of pictures illustrating two flat hillock defects are reported in Figure I.9.

Finally, the last type of growth defect is a non-epitaxial crystallites (see Figure I.10). These defects have no relation with the imperfection of the substrate. They randomly appear and their formation is controlled by the growth conditions. Their nucleation perhaps appears from a contamination, which

could be related to the diamond substrate holder (and not to the diamond substrate). It is possible to limit the formation of these defects by growing diamond using high microwave power.

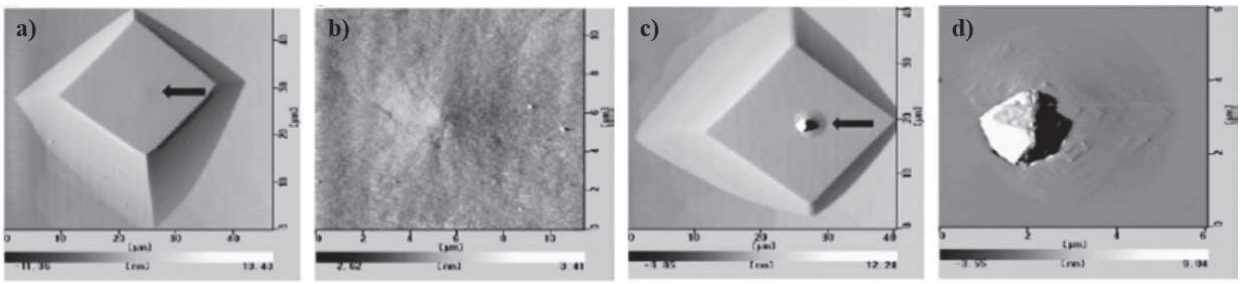

Figure I.9. Set of AFM images taken of a CVD monocrystalline diamond film: (a) a flat hillock defect without twinning and (b) its magnified view of the centre area showing an overgrow feature; (c) a flat hillock defect with twinned crystal in the centre and (d) its enlargement [54].

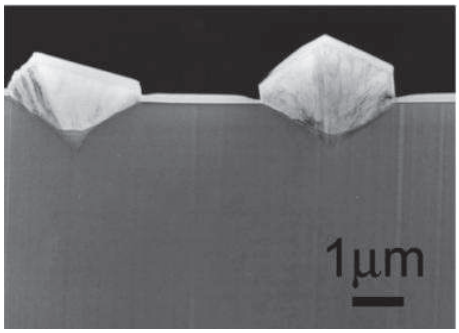

Figure I.10. Cross-section pictures of two non-epitaxial crystallite defects on a CVD monocrystalline diamond film by TEM analyses [54].

I.5 Diamond doping

Diamond materials have a large range of applications in particular in the field of electronic devices. Nevertheless, the development of electronic components based on diamond must be associated to the doping of the device, both n- and p-type, as for the traditional semiconductor materials.

Similarly to other very popular semiconductors composed of elements belonging to the group IV of the Mendeleev's table, such as silicon (Si) and germanium (Ge), the natural dopant elements for diamonds can belong to the group III and V, for p- and n-type doping, respectively. In addition, atom impurities have to be incorporated in the diamond lattice as substitutional atoms in order to be electrically actives. Nevertheless, the diamond lattice characteristics, as the compactness, the rigidity and the low miscibility make the doping element choice very limited, excluding a large number of possible dopants. Last, but not the least, the diamond metastable nature has made the traditional doping techniques by diffusion or implantation (developed for standard semiconductors such as Si and Ga) problematic or even impractical for diamond materials.

In this section, a summary of the different diamond doping techniques, namely diffusion, ion implantation and "in situ" doping, in addition to two sections dedicated to the n- and p-type in situ doping are reported.

I.5.1 The diamond doping by diffusion

The diamond doping by diffusion has not been sufficiently evaluated for this kind of material and only very few works have been published. In particular, the very high atomic density of diamond material strongly limits the diffusion of the impurities (excepted for hydrogen atoms [55]), especially below temperatures of 1400 °C. Several studies demonstrated that this limitation can be overcome by a higher heating, for example in the range 1400-1900 °C [56-58]. Nevertheless, it cannot be neglected that for such high temperatures, the undesired diamond-graphite phase change could occur. Among the successfully published results, Tsai et al. deposited a very thin p-type diamond layer (≈ 50 nm) for electronic applications by rapid thermal diffusion process of boron atoms at 1400 °C obtaining a resistivity of the order of ≈ 800 Ω.cm [56]. Krutko et al. reached a resistivity value close to 0.02 Ω.cm with a hole mobility of about 50 $cm^2.V^{-1}.s^{-1}$ by boron diffusion in a polycrystalline diamond layer (≈ 0.5 μm thick) heated at 1600 °C [58].

I.5.2 The diamond doping by ion implantation

A second developed diamond doping method was ion implantation. This technique has proved to be particularly flexible in terms of control of impurity concentrations and geometric profiles for the most of the semiconductors and then was applied to diamond materials. The first diamond doping attempts by ion implantation were carried out during the 1970s [59] with a great development during the 1990s. In particular, Fontaine et al. in 1996 obtained a hole mobility value of 385 $cm^2.V^{-1}.s^{-1}$ at room temperature for an acceptor impurity (boron) concentration in substitutional sites of 6×10^{16} cm^{-3} [60]. Afterwards, Uzan-Saguy et al. in 1998 improved further the hole mobility value until to reach 600 $cm^2.V^{-1}.s^{-1}$ using an annealing at high temperature (1450 °C, 10 min) and a high energy deep boron implantation (1.5 μm below the surface) [61]. On the other side, Kalish et al. obtained results for donor impurities (nitrogen) [62], where a high fraction of implanted atom impurities (2.8×10^{18} cm^{-3}, namely more than half of the implanted nitrogen) were incorporated into substitutional sites and that defect complexes similar to those found in type Ib diamond were formed as a result of the thermal treatments. In addition, further cathodoluminescence investigations showed

that thanks to a higher annealing treatment (1400 °C) more N atoms were moved on-site and that the radiation damages were further reduced.

Nevertheless, the diamond doping by ion implantation presents some strong disadvantages. In particular, implantation of ions in diamond generates unavoidably a large number of broken carbon bonds and atomic displacements, which can gradually destroy the crystalline periodicity of the material. This phenomenon is even more critical when the implantation dose increases. The dangling bond creation in addition to the presence of interstitial or aggregate defects can lead to the formation of a conductive layer inside the diamond samples [63]. Interesting investigations showed that it exists a threshold of defect concentration above which the broken diamond covalent sp^3 bonds reorganize irreversibly in graphite sp^2 bonds as a result of post-implantation annealing. The defect concentration threshold was estimated for diamond material around 10^{22} cm^{-3} [64]. The post-implantation annealing treatment is required to allow the displacement of implanted atoms located in interstitial sites toward the substitutive sites, in order to contribute to the electrical conduction. This diamond-graphite phase transition aspect can prove very interesting for other diamond applications and it will be presented below in the section I.9.

However, Prawer and Kalish demonstrated also that when ion implantation is performed on a heated diamond (instead of room temperature), namely the so called “hot implantation method”, the implantation damage decreases [63]. By this way, appreciable results for *p*-type diamonds implanted with boron were obtained [65]. Indeed, Tsubouchi et al. produced boron implantation into type IIa diamonds at about 400 °C reaching heavy impurity concentrations of the order of 10^{21} cm^{-3}. These samples showed almost no temperature dependence (in the range 80 - 1000 K) of the carrier concentrations, resistivity and hall mobility, with minimum values of resistivity and sheet resistance at room temperature of 1.4 mΩ.cm and 56Ω/□, respectively. The sample characterizations suggested that very low resistive p-type degenerate semiconducting layers were produced preserving the diamond lattice, namely without diamond-graphite transition, in spite of the high irradiation dose (≈ 10^{17} $ions.cm^{-2}$) used to reach heavily doping concentrations.

Other relevant results have been obtained by Ueda et al. in their studies about the post-implantation annealing treatment for several dopant ions [66-68]. They have established that high pressure and high temperature (HPHT) annealing is much more efficient than the traditional thermal annealing in vacuum conditions. Basically, HPHT conditions (pressure of about 7GPa, and temperature higher than 1200 °C) are located in the thermodynamically stable region of diamond in the carbon diagram phase, this making highly efficient the implantation-induced damage recovery, allowing increasing the implanted dose avoiding the re-crystallization in the graphitic form. The authors studied the

influence of the annealing treatment on the boron concentration by cathodoluminescence measurements. For an annealing at 1350 °C at the pressure of 7 GPa, the boron incorporation rate was registered at 4.6%, higher than the incorporation rates measured for the other methods. In addition, they evaluated the compensation rate of their films after the doping at 3,4 %, and found a high hole mobility of 632 $cm^2.V^{-1}.s^{-1}$ at room temperature. The highest doping efficiency was 7.1% at the annealing temperature of 1400 °C, which is ten times higher than that for vacuum annealing (≈ 0.73%). These results indicate that HPHT annealing is more efficient for activation of ion-implanted dopants in diamond.

Nevertheless, even if improvements have been obtained with this post-treatment annealing, doping efficiency remains very limited and ion implantation cannot be used for developing electronic component.

I.5.3 The diamond "in situ" doping

Finally the last and, to date, the most used diamond doping method is an "in situ" doping. The principle is to introduce a doping gas involving the desired dopant chemical element in the gas mixture during the diamond growth process. This method has been successfully developed both for donors and acceptors atoms, such as nitrogen (N), phosphorus (P) and boron (B).

N-type doping

Basically, the n-type conductivity in diamond is more difficult to obtain than the p-type one. Nitrogen atoms (N) are the natural candidates as donors for diamond and they prove to be easily incorporable into a substitutional site. However, it creates an energetic level in the diamond band gap too deep, namely 1.7 eV below the conduction band (see Figure I.11) which makes the doped material unfit for the production of electronic devices. However, the nitrogen impurities have several applications in the field of quantum diamond devices and magnetometry [69, 70].

To date, the only chemical element useful for the n-type diamond doping in substitutional sites and having a relatively low activation energy (E_a) so as allow electronic application developing is the phosphorus (P) (E_a = 0.6 eV, see Figure I.11) [71, 72]. In particular, for n-type doping, several interesting results have been initially obtained by incorporation of phosphorus atoms on (111) oriented CVD diamond by addition of phosphine (PH_3) or tertiarybutylphosphine (TBP) gases to the

gas mixture [73-75]. Currently, the n-type doping by phosphorus is really effective only on the (111) orientation, even if more recently promising results have been shown on (100) orientation [76-78].

Taking into account the deep donor level of phosphorous, other chemical elements were tested for n-type doping, such as the arsenic (As) which has a theoretical activation energy value of 0.4 eV (see Figure I.11). G. Frangieh et al. studied the incorporation of arsenic atoms by chemical vapour deposition at GEMaC laboratory, but the incorporated arsenic atoms were electrically inactive, which assumes that arsenic atoms were not incorporated into substitution sites but as an interstitial impurities, or that they formed other kinds of defects in the material [79]. More recently, Barjon et al. have been performed As implantation leading to the CL-bound exciton signatures but with no evidence of electrical signatures [80].

P-type doping

Currently, the boron chemical element proves to be the only efficient dopant both for reproducibility and for impurity quantity incorporated by chemical vapour deposition. The typical precursors gas added to the growth mixture are the diborane (B_2H_6) or trimethylboron ($B(CH_3)_3$) [81, 82]. The acceptor level presents an activation energy of 0.37 eV (see Figure I.11).

Nevertheless, the growth quality strongly depends on the crystal orientation. The growth on (111) orientation face is not easy and leads very often to crystalline defects which further complicates the growth of high quality thick films and reduces the electronic properties, besides the low availability of substrates [83].

On the contrary, the growth on (100) orientation is easier to control and boron incorporation proves to be easy in the (100) planes [84]. Nowadays, the process is very well controlled and many research teams can incorporate boron by chemical vapour deposition in a range from 10^{14} to 10^{21} cm^{-3} in thin films [85-87] with mobility that can reach values higher than 1500 $cm^2.V^{-1}.s^{-1}$ [88, 89]. Additional studies with the aim of producing thick films were carried out. Thick and highly boron doped diamond films were produced making the separation of the CVD layer from the substrate possible and thus allowing self-supporting layers production [90-92]. The obtained doped substrates have a very good crystalline quality and it could be considered as the first technological brick for manufacturing vertical components [93-95].

In a recent study carried out by Mortet et al., the growth of (110) orientated monocrystalline boron doped diamond was successfully performed and widely investigated for different doping levels. In particular the electrical, morphological and optical properties were studied proving the location of

boron impurities in substitutional sites, the high incorporation and the good carrier mobility which proved to be comparable to the (111) one, but lower than the (100) one [96].

In Figure I.11 the energy diamond diagram summarizing the nitrogen, phosphorous, arsenic and boron energetic levels introduced into the band gap is shown.

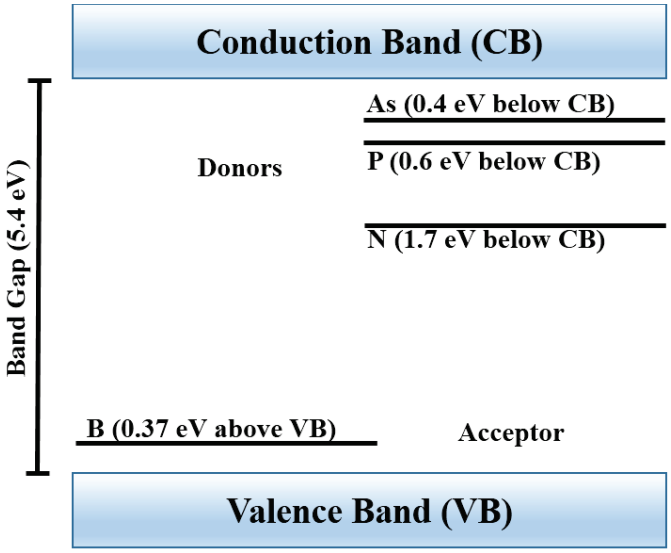

Figure I.11. One dimension representation of the energy diagram of selected states in the diamond band gap.

In this thesis work, all the CVD monocrystalline doped diamond samples were doped by "in situ" technique with boron addition.

I.6 Electronic properties of boron doped diamonds

In this section a summary of the electronic properties of the boron doped diamonds are presented.

I.6.1 The dopant activation energy

The dopant activation energy is affected by the dopant concentration into the material. In particular, for boron doping levels below [B] $\leq 10^{19}$ cm^{-3} into diamond, the boron activation energy E_a proves to be 0.37 eV at room temperature. For boron doping levels above 10^{19} cm^{-3} the E_a decreases with the raising of doping until to be cancelled at the metal-insulator transition (MIT). The metal-insulator transition is usually explained by the overlapping of the impurity band (acceptors) and the valence band [97]. From a theoretical point of view, the metallic transition appears in the diamond for boron concentrations close to 2×10^{20} cm^{-3} [98]. In a most recent study, Klein et al. studied the transport properties of (100) orientated and heavily boron doped diamonds looking for an impurity

concentration threshold allowing the MIT reaching. As a result, the [B] boron concentration threshold into diamond was estimated to be at the order of 4.5×10^{20} cm^{-3} [99].

The activation energy variation as a function of the doping concentration can be described by the Equation I.1 of the Pearson's model [100]:

$$E_a = E_{a0} - \alpha(N_A - N_D)^{\frac{1}{3}} \qquad \text{Equation I.1}$$

where E_{a0} = 0.37 eV, $\alpha = 4.1 \times 10^{-8}$ eV.cm, N_A is the acceptor concentration, N_D is the donor concentration, therefore N_A-N_D corresponds to the effective doping taking into account the compensation.

Figure II.12 shows the evolution of activation energy as a function of boron doping for monocrystalline and polycrystalline diamonds.

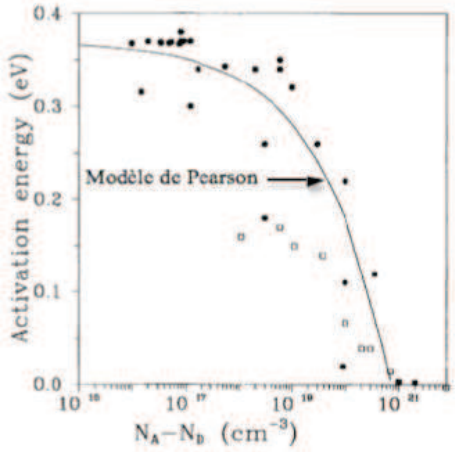

Figure I.12. The energy activation variation as a function of boron doping level for monocrystalline (full dots) and polycrystalline (empty squares) diamonds [97].

I.6.2 The density of the free hole carriers

According to the equation of neutrality, the evolution of the concentration of free holes in a non-degenerated and partially compensated p-doped semiconductor may be expressed by the Equation I.2 [88, 101]:

$$p = \frac{1}{2}(\phi_A + N_D)\left\{\left[1 + \frac{4\phi_A(N_A - N_D)}{(\phi_A + N_D)^2}\right]^{\frac{1}{2}} - 1\right\} \qquad \text{Equation I.2}$$

with

$$\phi_A = 2\left(\frac{g_1}{g_0}\right)\frac{(2\pi m^* kT)^{\frac{3}{2}}}{h^3} exp\left(\frac{-E_a}{kT}\right) \qquad \text{Equation I.3}$$

where $g_1/g_0 = 1/4$ indicating the factor of boron degeneracy; $m^* = 0.908\ m_0$ is the effective mass of the holes where m_0 is the electron mass at rest, h is the Planck's constant, k is the Boltzmann's constant and E_a is the activation energy. Due to the high acceptor activation energy in low doping diamonds, there are very few ionized dopants at room temperature (only about 0.2%) [102], therefore the diamond resistivity remains high.

From Equation I.2 and Equation I.3, the temperature effect on the concentration can be expressed by the Equation I.4:

$$p \approx AT^{3/2} exp\left(\frac{-E_a}{kT}\right) \qquad \text{Equation I.4}$$

where A is a constant. Figure I.13 shows the trend of hole concentration for p-type diamonds as function of the temperature for different doping levels.

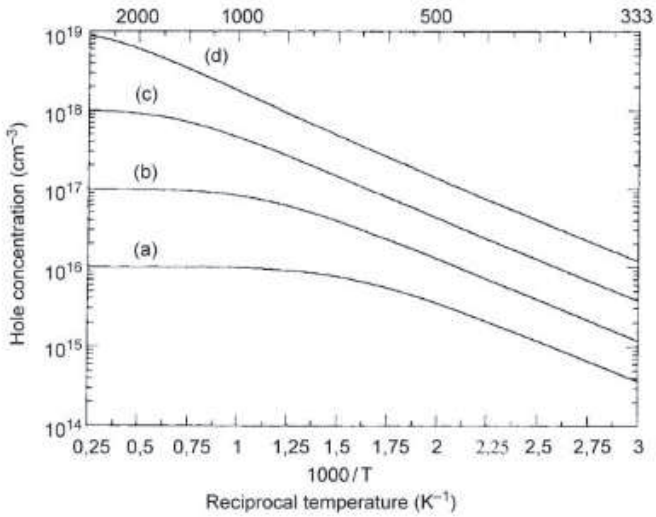

Figure I.13. The hole concentration as function of the temperature for monocrystalline diamonds. Several curves correspond to different boron concentrations: (a) $N_A=10^{16}$ cm^{-3}, (b) $N_A=10^{17}$ cm^{-3}, (c) $N_A=10^{18}$ cm^{-3} and (d) $N_A=10^{19}$ cm^{-3} [103].

I.6.3 The mobility of the hole carriers

The hole mobility in monocrystalline lightly boron doped diamonds reaches about 2000 cm^2.V^{-1}.s^{-1}. at room temperature [104]. However, this limit is very sensitive to the measurement method. In addition, the carrier mobility decreases with the raising of the doping level and the temperature, as in all semiconductors. The evolution of the hole mobility μ for monocrystalline diamonds doped in the wide range (10^{15} - 10^{21} cm^{-3}) and temperature (300 – 500 K) can be computed by the Equation I.5 [88]:

$$\mu(T, N_{imp}) = \mu(300, N_{imp}) \left(\frac{T}{300}\right)^{-\beta(N_{imp})} \quad \text{Equation I.5}$$

where N_{imp} = is the impurity concentration, $\mu(300, N_{imp})$ and $\beta(N_{imp})$ are parameters which have to be evaluated separately according to the doping experimental data.

Figure I.14 collects several data from several studies about the mobility as a function of the impurity concentration for room and high temperatures.

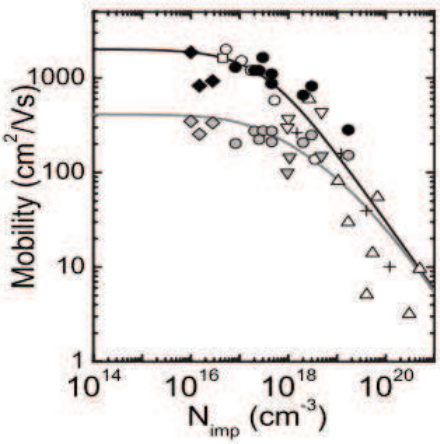

Figure I.14 Hole mobility as a function of N_{imp} at T =300 K and 500 K for monocrystalline boron doped diamonds. The black line fits the experimental data at room temperature; the grey line is a simulation fit at high temperature by the Eq. I.5 [88].

In the previous paragraph concerning the p-type diamond doping, a recent work has been cited about the characterization of the different mobility values depending on the diamond orientation ((111), (110) and (100)) [96]. In Figure I.15 is reported the plot showing the obtained results. The lower mobility values for (111) and (110) layers compared to (100) layer can be ascribed to the higher concentration of defects (compensating donors, passivated acceptors) which limits the hole mobility just by impurity scattering.

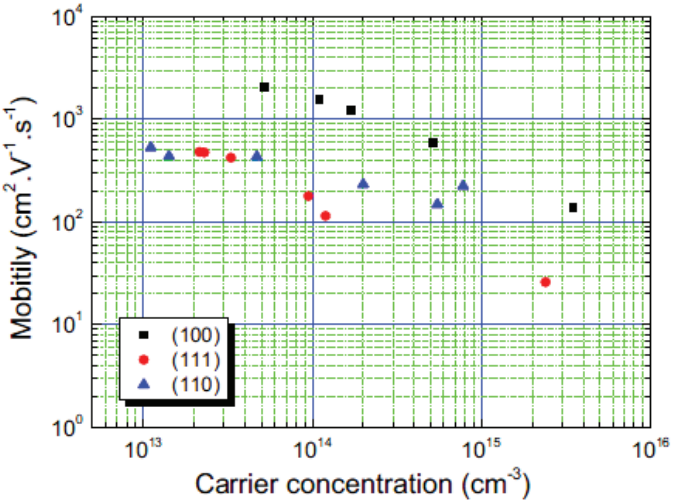

Figure I.15. Evolution of the carrier mobility depending on the carrier density measured at room temperature by Hall effect using Van der Pauw technique for different crystallographic orientation: (100) in black squares, (111) in red circles and (110) in blue triangles [96].

Finally, in Figure I.16 the variation of the resistivity of diamond layers as a function of boron concentration is reported. The resistivity decreases sharply with the increase of the incorporated impurity quantity until to reach an extremely weak value close to the metal transition zone. It is possible to note the progress that have been obtained in the last years: for the same doping level, the resistivity values prove to be almost two orders of magnitude below. This finding is mainly ascribed to the improvement obtained in terms of CVD diamond crystalline quality and to the sharp decrease in the compensation ratio.

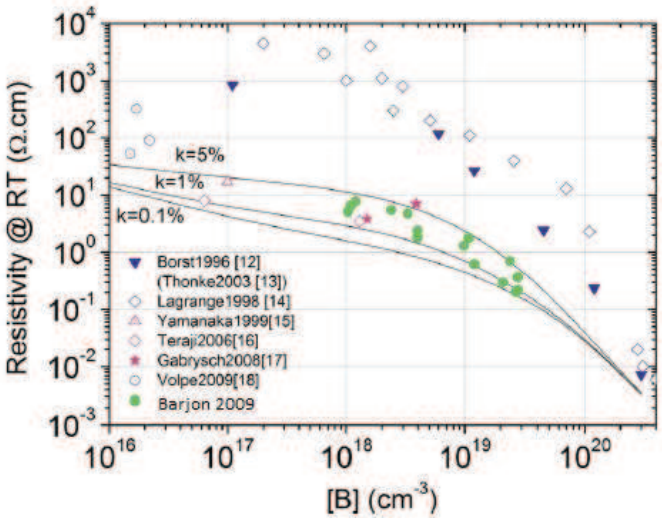

Figure I.16 Variation of the resistivity of boron doped diamonds as function of the boron concentration according to several studies indicated in the legend. The curves represent the evolution of the resistivity by simulations with different compensation rates k (k = 0.1, 1 and 5%). [89].

I.7 Introduction to the diamond contacting

Nowadays, synthetic CVD diamond is widely studied for several applications, in particular doped diamond in the field of power devices and intrinsic diamond for detection. Indeed, diamond properties, such as wide band gap, exceptional thermal conductivity, high breakdown voltage, small dielectric constant and very high carrier mobility, make diamond very attractive to work in these domains.

A crucial point in electronic diamond device fabrication is diamond contacting. Several studies have been carried out in the last decades about diamond electrical contacts which prove to be not an easy task due to the diamond inertness and its wide bang gap. Moreover, depending on the final application, contacts with different electrical behaviour, for example ohmic and Schottky, must be manufactured on diamond surface.

During this thesis, two experiments were carried out and I worked with different diamond samples, namely a set of CVD boron doped diamond samples and a set of intrinsic diamond samples, but in

both cases, the aim was to develop ohmic contacts on diamond surfaces. Different techniques were implemented: diamond graphitization by laser and by ion implantation, and diamond metallization. Therefore, in order to have a better understanding on the key parameters for fabricating ohmic contact on diamond, a paragraph regarding the energetic band diagram for diamond-metal junctions and some examples of power devices based on doped diamond with ohmic and Schottky electrodes are reported in the following section. Subsequently, a deep space dedicated to the key elements for ohmic contact manufacturing together with the state of the art of intrinsic diamond detectors, their electrode configurations and diamond graphitization processes will be presented.

I.7.1 Band diagram for a metal-semiconductor junction

In the solid-state physics literature, the study of energetic band diagram is the base for understanding what occurs when a metal and a semiconductor are placed in contact (MS junction) and how the interface properties change depending on the nature of materials.

Physically, when a MS junction is produced, which means that it can be considered as an only material and an only thermodynamic system, the thermodynamic equilibrium of the full structure has to be reached by exchange of charge carriers. If the Fermi levels of the two materials are already aligned, the equilibrium is satisfied and no carrier exchange is required. This means also that the metal and semiconductor work functions, which define the energy values necessary to extract a charge from the materials to the vacuum level, proves to be equal each other ($\Phi_m = \Phi_s$). In Figure I.17 the band diagram of a metal and a semiconductor satisfying the equation $\Phi_m = \Phi_s$ before (a) and after (b) the contact are shown.

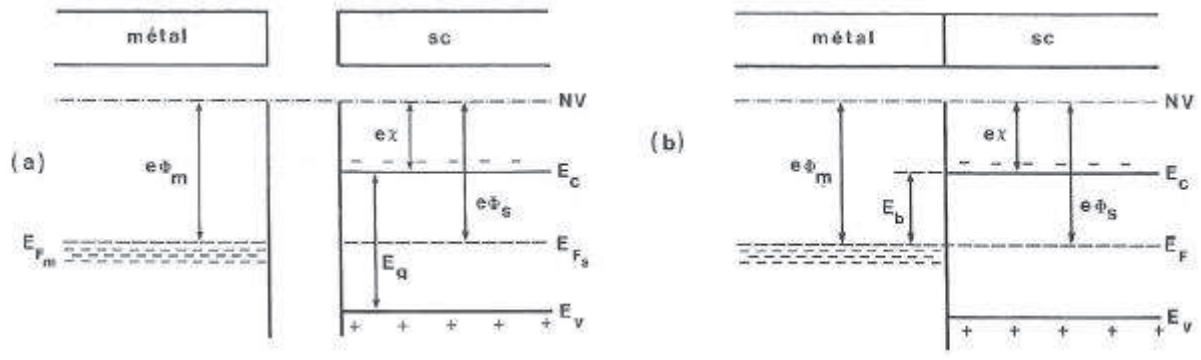

Figure I.17. Metal-semiconductor junction with $\Phi_m = \Phi_s$ (a) before and (b) after the contact [105].

On the contrary, when the Fermi levels are not aligned, a flux of carriers moves crossing the junction interface until reaching the thermodynamic equilibrium. This causes a band bending phenomenon at the interface. The carrier flux and the band bending directions depend on the different values of the

two work functions. The work functions are affected by the metal and semiconductor nature, and by the eventual semiconductor doping in terms of kind (p- or n-type) and quantity. All these factors, collected in the work function values, give rise to different properties at the junction interface and, as a consequence, a different electrical behaviour of the diamond contact.

For example, considering the diamond material used in this thesis work, namely p-type doped diamonds, there are two possible electrical behaviours:

- Ohmic contact if the metal work function is higher than the semiconductor one ($\Phi_m > \Phi_s$);
- Schottky behaviour when the metal work function is smaller than the semiconductor one ($\Phi_m < \Phi_s$).

In particular, considering the band structure of the MS junction at the thermal equilibrium in the case of $\Phi_m > \Phi_s$, the alignment of the Fermi levels gives origin to the upward semiconductor band bending related to the hole accumulation at the MS interface. In Figure I.18 the band diagram of a metal and a p-type semiconductor satisfying the equation $\Phi_m > \Phi_s$ before (a) and after (b) the contact are shown.

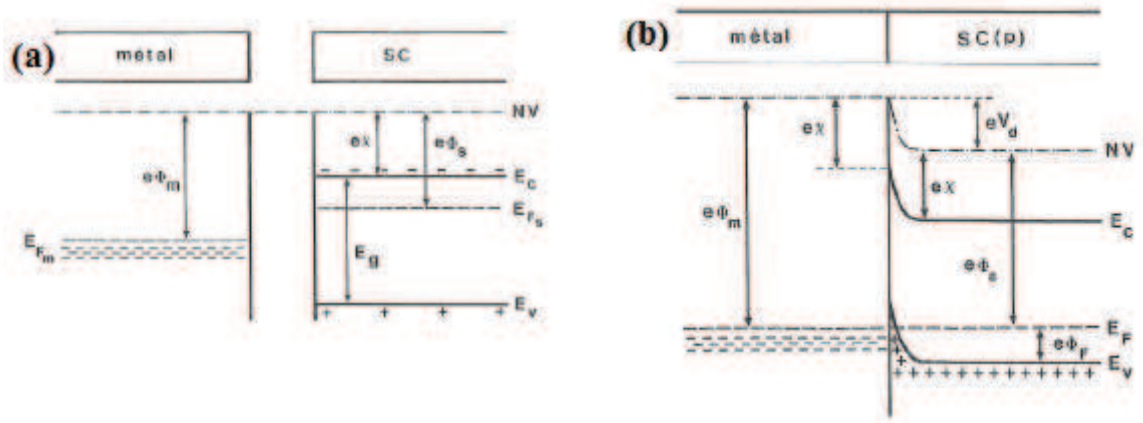

Figure I.18 Metal-semiconductor junction with $\Phi_m > \Phi_s$ (a) before the contact and (b) after the contact at the thermodynamic equilibrium [105].

Then, applying an external voltage bias it is possible to polarize the junction with positive or negative voltage. For example, with a negative difference of potential ($V_s - V_m < 0$), the carrier flux (hole in p-type doping case) is driven into M→S direction and the upward semiconductor band bending operates as a source of holes (anode) (see Figure I.19 (a)). Whereas, the opposite applied bias ($V_s - V_m > 0$) induces a hole flux displacement into S→M direction and no barrier is met by carriers (see Figure I.19 (b)). As a consequence, in both directions, the current can freely circulate and the contact proves to be ohmic.

On the contrary for the case $\Phi_m < \Phi_s$, the alignment of the Fermi energetic levels induces the downward semiconductor band bending and it originates a built-in potential barrier called Schottky barrier at the interface. In Figure I.20 the band diagrams of a metal and a p-type semiconductor satisfying the equation $\Phi_m < \Phi_s$ before (a) and after (b) the contact are illustrated.

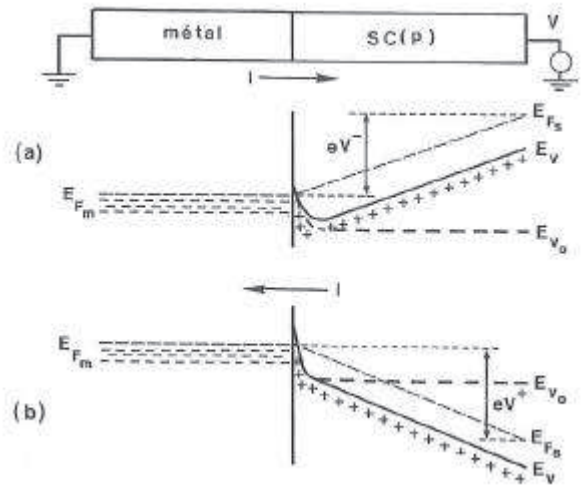

Figure I.19. Metal-semiconductor (p) contact with $\Phi_m > \Phi_s$ under polarization: (a) $V_s - V_m < 0$ and (b) $V_s - V_m > 0$ [105].

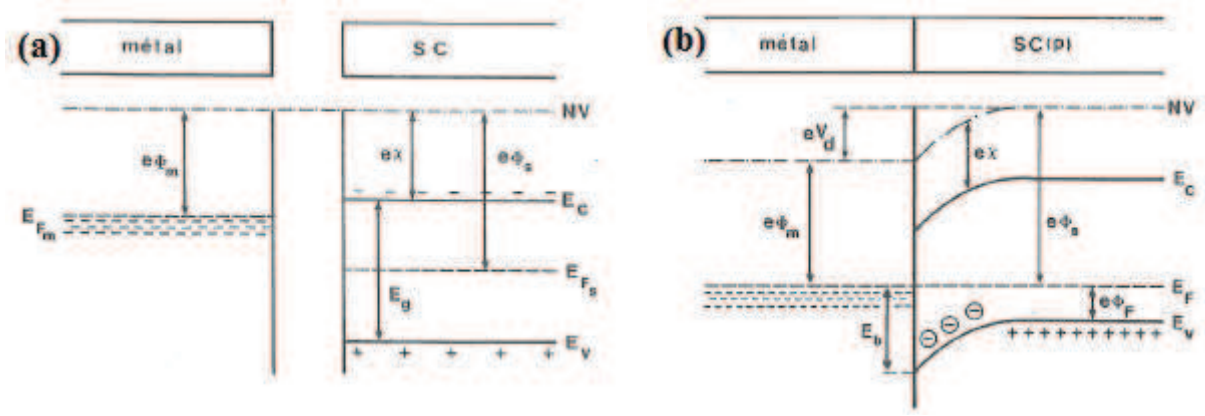

Figure I.20 Metal-semiconductor junction with $\Phi_m < \Phi_s$ (a) before and (b) after the contact at the thermodynamic equilibrium [105].

Then, according to the applied bias, the carriers flux can move into M→S and S→M directions for ($V_s - V_m < 0$) and ($V_s - V_m > 0$), respectively. Nevertheless, the carriers can flow only in the S→M direction encountering a potential barrier which can be overcome and giving rise to the Schottky contact (see Figure I.21 (b)), whilst into M→S direction the high potential barrier forbids any displacement suppressing the carrier flux (see Figure I.21 (a)).

Definitely, it is possible to define a MS junction as an ohmic contact if it owns a linear I-V characteristic in both biasing directions whilst, a rectifying MS junction conducing current in one direction and confining it in the opposite one (forward and reverse polarizations) is called Schottky contact.

Based on this theory, a lot of interesting works have been carried out involving diamond devices development with ohmic and Schottky electrodes. Anyway, the choice of producing ohmic or Schottky contacts is strongly related to the aim of the final diamond device. Once decided, there are several and peculiar aspects, as key elements, which have to be carefully considered to produce the desired contact. Among these, it is worth mentioning the kind of diamond doping, the dopant

concentration, the choice of the metallic layers for contacting, and finally the terminations of diamond surface before the metallization (for example hydrogenated or oxygenated terminations). All these aspects widely affect the nature of the contacts making them ohmic or Schottky in addition to their reliability and performance.

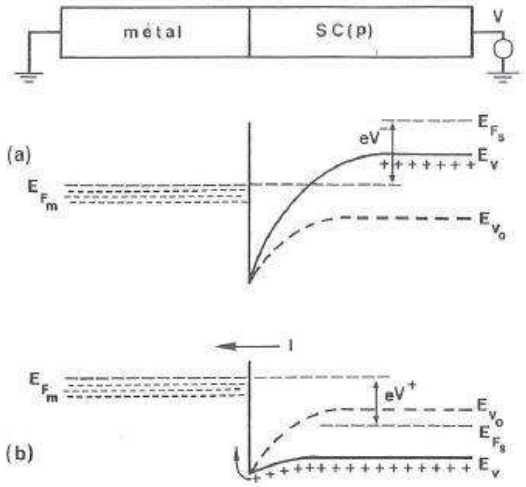

Figure I.21. Metal-semiconductor (p) contact with $\Phi_m < \Phi_s$ under polarization: (a) $V_s - V_m < 0$ and (b) $V_s - V_m > 0$ [105].

I.7.2 Schottky and ohmic contacts on electronic doped diamond devices

The most popular applications of electronic doped diamond devices are the Schottky diodes. A Schottky diode is a unipolar device (one type of charge carriers) based on a metal-semiconductor junction using the non-linear current transport behavior of rectifying under applied bias voltage. In particular, the Schottky diode current transport is related to majority carriers in the active area, which allows the fast switching from forward to reverse bias without minority carrier effects.

To date, a lot of studies has been carried out producing interesting results mainly basic on p-type doped diamond, considering the several difficulties characterizing the n-type CVD synthesis. The Schottky barrier diodes were investigated in particular by Butler et al. and Volpe et al. finding high breakdown voltage [106, 107]; whilst Chen et al. registered high current density [108]. In addition, good compromise between forward and reverse characteristic has been also demonstrated [109, 110].

Nowadays, the Schottky contact manufacturing can be obtained with good results on lightly doped diamonds. Nevertheless it is still under investigation in particular to determine suitable metals which form high Schottky barrier height with good mechanical adhesion, high thermally stable interface to diamond and high breakdown voltage. Koné et al. investigated the performance of several Schottky contacts produced with different metal material on the same monocrystalline p-type lightly boron doped diamond [111]. Tungsten (W), aluminium (Al), nickel (Ni) and chrome (Cr) were evaluated and compared showing different advantages and drawbacks. For example, W and Ni showed the

highest Schottky barrier height value (1.67 and 1.57 eV, respectively), Cr and Ni gave the most interesting values of forward current density range, while W, Al, and Ni the lowest reverse ones, and the best rectifying factor was obtained by Ni (10^{10}). Finally, all the metal presented good thermal stability and adhesion properties except for Cr and W respectively. These findings indicated that nickel material represented the more suitable metallic material for Schottky barrier diode applications. In the same publication, a study of the Schottky barrier heights as function of the metal work functions is reported, and the obtained results are compared to the literature ones for a value range between 0.7 – 2.0 eV.

More recently, Traoré et al. demonstrated an innovative Schottky diode in pseudo-vertical configuration based on an oxygen terminated diamond surface covered by zirconium (metal easily oxidizable) [110, 112-115]. The device presented a high forward current density value of 10^3 A.cm^{-2} at 6 V with very low leakage currents (under 1 pA) at room temperature and without annealing process. Annealing post-treatments at 450°C of the zirconium Schottky diode allowed decreasing the barrier height up to 1 eV. Therefore, the forward power losses was reduced with a reasonable increasing of the reverse leakage current. Contrary to what is generally found in metal-diamond Schottky contacts, the dispersion of the I-V characteristics was extremely weak for 85% of the whole diode population, opening the route for industrial upscaling. A breakdown field of 7.7 MV.cm^{-1}, with a Balligan figure of merit above 244 MW.cm^{-2}, in addition to a high rectification ratio higher than 9 orders of magnitude with a low reverse current (10^{-13} A) were found which is clearly the state of the art up to now.

The more attractive vertical Schottky diode configuration has been also studied. The Schottky contact is formed at the metal / low doped diamond interface, while the ohmic contact is formed on the highly doped back side. Umezawa et al. found high current in a vertically structured diamond Schottky diodes with an Al_2O_3 thick field-plate (1.8 μm) [116]. The maximum forward currents reached were 1 and 5 A at forward voltages of 2.4 and 7.2 V, respectively, and a maximum blocking voltage of 300 V at 250 °C.

In diamond electronic devices, ohmic contacts are typically fabricated on heavily doped (p-type or n-type) layers because of their unique property of decreasing drastically their resistivity, for doping level of the order of 10^{20} cm^{-3} without degrading the crystallinity [117]. The fact that the heavily doping diamond film under the electrodes leads to ohmic electrical behaviour can be ascribed to the tunnelling current through the narrowed depletion region. Indeed, even if the potential barrier height essentially does not change since the material is the same, the barrier thickness proves to be reduced allowing to the charge carriers to reach more easily the metallic contact by tunnelling through the barrier.

In addition, increasing further the doping levels of diamonds it is possible to reach the condition of degenerate semiconductor, when the Fermi level lies within the conduction or valence band (for n-type and p-type doping, respectively), and the MIT occurs. As previously reported, the boron concentration threshold for the MIT into diamonds was estimated to 4.5×10^{20} cm^{-3} [99]. Definitely, in MIT conditions, a MS junction works as an ohmic contact.

On the contrary, the formation of ohmic contacts on lightly doped diamond samples ($< 10^{18}$ cm^{-3}) is more difficult. Indeed, it has been only obtained in particular conditions which will be described in the next paragraph. The high difficult to form ohmic contact on lightly doped diamond was the guideline of this thesis work.

I.7.3 Manufacturing of ohmic contacts on diamonds

Diamond contacts have to satisfy several requests to be considered as good electrodes: good mechanical adhesion, chemical thermal stability over time, potential barrier close to 0 and the possibility of bonding connections. Indeed, the electric contacts directly contribute to the active performance of the device and is of main interest particularly for commercial purpose. For diamonds, the fabrication of good ohmic contacts is still an opened field, especially on lightly doped and intrinsic diamond. Indeed, excluding the heavy doping condition (in situ or by ion implantation) described in the previous paragraph, the other possibilities to create ohmic contacts on diamond are strongly related to the good combinations of the following aspects:

1. Pre-treatments of the diamond surface prior to the metallization;
2. Choice of the metallic layers and carbide formation at the metal / diamond interface;
3. Diamond surface terminations.

Regarding the first point, historically, several kinds of diamond surface treatments prior to the metallization were tested based on the idea to lightly damage the diamond surface. The idea was to modify in someway the nature of a perfect diamond surface so that the voltage drop across the contact was small and negligible compared to the one crossing the active part of the device. For example, reasonable good contacts have been fabricated on diamond surfaces previously mechanically roughened leading to cracks and kinks formation, which cause a high electrical field and high recombination velocities between the metal and the diamond. On these damaged diamond surface metal contacts were created using silver paint [5, 118]. Another solution of diamond surface damaging was experimented by a particle bombardment. For example, Ti, Au and Al ohmic contacts were obtained on lightly boron doped polycrystalline diamond by sputtering the surface before the

metallization causing the formation of graphitic and non-diamond carbon phases on the surface [5, 119-121]. Moreover, it was obtained another kind of damaged diamond using an excimer laser treatment where a carbon phase transformation from diamond to non-diamond phase was observed. Geis et al. induced the diamond-graphite transition and then removed the graphitic structures by chemical and plasma etching, leaving just a thin modified layer (about 60 nm thick) [122]. This layer was composed of a mixture of diamond, graphite and a not well identified non-diamond carbon phase. After, metallic layer was produced using silver paint on this modified areas resulting in ohmic contacts. Nevertheless, about this approach, some problematic points were not solved, as the adhesion between the metal and the modified diamond which proved to be difficult to satisfy once got the graphite transition. In general, these first contacts obtained by this diamond surface damaging proved to be mechanically fragile and electrically very noisy [5].

Among the different diamond surface pre-treatments, Ar sputtering proved to be the most interesting in terms of impact on the electrical properties of the contacts. A set of very interesting experiments were carried out to compare the electrical performance of gold contacts deposited by thermal evaporation on as-grown polycrystalline diamond surface against the same gold contacts deposited on Ar-sputtered polycrystalline diamond surface [119]. I-V curves are reported in Figure I.22. The sputtering treatment was performed in vacuum, with an acceleration voltage of 2 kV and an incident angle of about 65° regarding the normal of the surface.

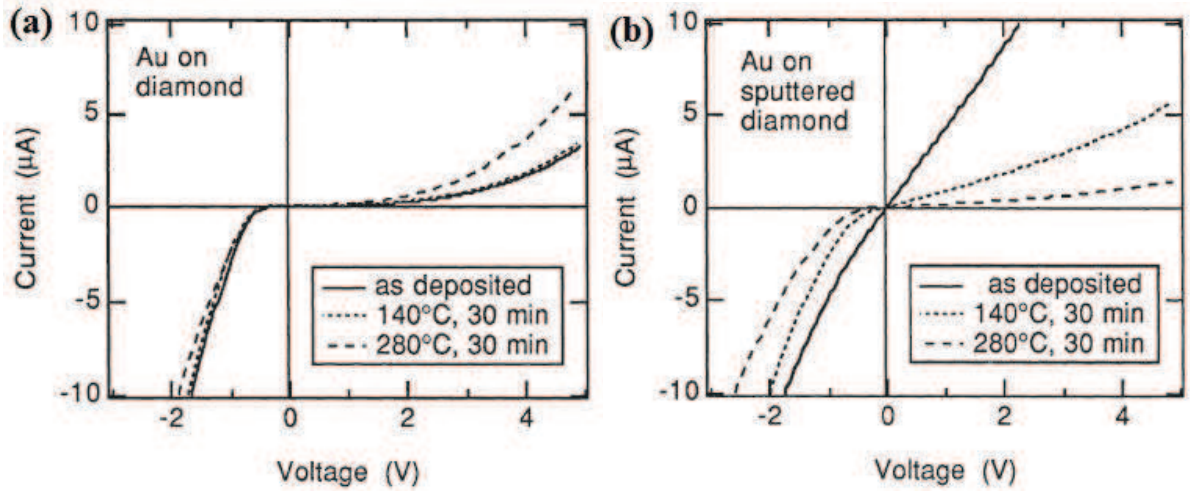

Figure I.22. I-V characteristics of Au contacts on (a) as-grown and (b) sputtered polycrystalline boron doped diamond surface [119].

The as-deposited Au contacts on un-treated diamond surface have not linear behaviour (see Figure I.22 (a)), and even after some annealing treatments (at 140 and 280 °C, for 30 min) they preserved their rectifying behaviour. On the contrary, the I-V characteristic curves of the Au contacts deposited on Ar-sputtered diamond surface have linear behaviour (see Figure I.22 (b)). This finding

was speculatively ascribed to the sputtering treatment creating energy states in the bandgap of the diamond making the valence and conduction band essentially continuous. This would make every metal deposited on diamond ohmic. Nevertheless, these ohmic contacts became rectifying after the same annealing treatments due to the instability of the damaged layer at the diamond surface. Considering that the graphitic carbon phase is thermodynamically more stable than that of diamond in the experimental conditions, it was speculated that the damaged layer was absorbed into the gold layer by the annealing treatment instead of to speculate a diamond self-restoration.

The second key element is the choice of the metallic layers to deposit on the diamond surfaces. Indeed, the chemical reactions at the metal / diamond interfaces can strongly affect its structure and properties [5]. Nowadays, several studies have been carried out about the diamond metallization with the aim of establishing a guide for selecting and processing a suitable contact material on diamond [119-121, 123-125]. Among these, Au and Ti have been widely analysed and chosen in this thesis work. In these previous experiments, the metallization processes were performed in vacuum and by thermal evaporation. The direct gold deposition on as-grown diamond gave rise to rectifying behaviour, as explained before, and no chemical reaction was occurred by annealing treatment. Therefore Au proved to be inactive on diamond. On the contrary, the experiment performed by titanium deposition on as-grown diamond produced different results, as shown by the I-V measurements in Figure I.23 (a) [121]. In particular, Ti contacts proved to be rectifying just after the deposition, but after annealing treatments, for increasing temperature values their characteristic started to become linear (essentially at 430 °C). This findings were obtained from several researchers [126-128]. XPS investigations showed the formation of Ti-C peak confirming the transition of the I- V curves from Schottky to ohmic behaviour because of annealing treatment.

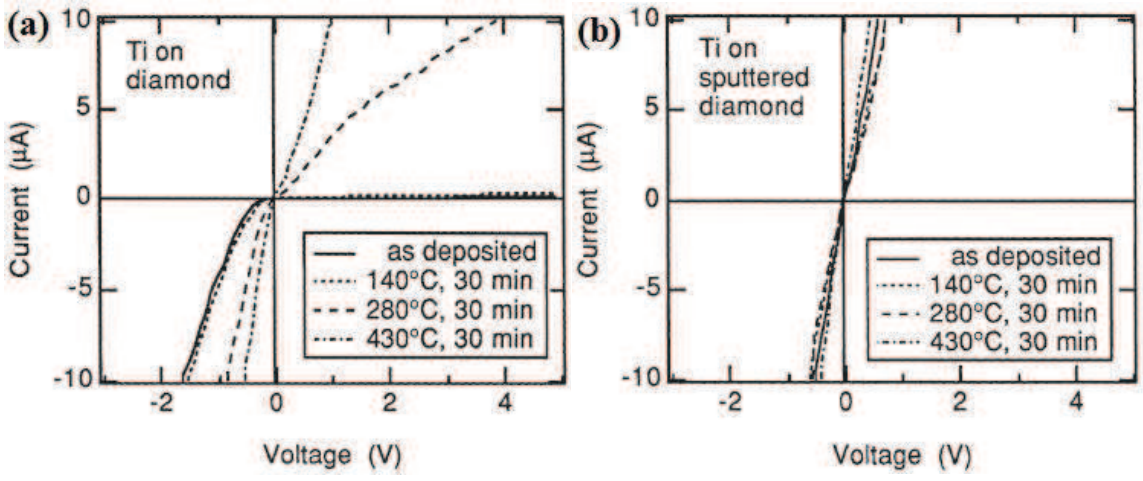

Figure I.23. I-V characteristics of Ti contacts on (a) as-grown and (b) sputtered polycrystalline boron doped diamond surface [121].

For completeness, Ti deposition on Ar-sputtered diamond surface is reported. The I-V characteristics showed an ohmic behaviour for all the experimental conditions, namely as-deposited and after several annealing treatments (see Figure I.23 (b)), in addition to a higher conductivity rather than Au contacts. Finally, XPS analyses indicated that the Ti-C bond formation was more significant for the metallization of sputtered diamond surface than the as-grown one [121].

Unlike Au contacts deposited on sputtered diamond surface which loses ohmic properties by subsequent annealing treatments, Ti contacts proved to be constantly ohmic after annealing treatments thanks to the titanium carbide formation which limited the diffusion of the sputtering-induced defects [5]. In addition, the chemical reactivity at the metal / diamond interface can be explained in terms of carbide formation free energy (ΔG), which proves to be negative for titanium (-42 kcal.mol^{-1} of TiC) and positive for gold indicating that the carbide formation is thermodynamically favourable for titanium material and un-favourable for gold metal [5].

Therefore, the previous interesting results obtained just for Ti contacts after the annealing treatments can be associated to the titanium carbide formation which allows the generation of gap states favouring the tunnelling transport and / or reducing of the barrier height [121].

Considering the good agreement between the thermodynamic data and the experimental measurements it seemed that the thermodynamic data could be used to predict the interfacial reactions and, as a consequence, the nature of the electric contact (ohmic or Schottky). Therefore, a model of band structure interface has been developed [121] in order to explain the effects of the diamond surface treatments and of the carbide formation on the contact electrical behaviour, which is reported here in Figure I.24. Figure I.24 (a) shows a generic metal / diamond interface as-deposited, where the contact has a rectifying behaviour due to the potential barrier Φ_b. The pictures (b) and (c) refer to the ohmic behaviours of annealed Ti contacts deposited on as-grown diamond surface, which can be explained in terms of point defect formation at and near the diamond surface due to the carbide formation and / or Ar sputtering treatments. It is believed that such defects can restrict the depletion width increasing the probability of tunnelling (Figure I.24 (b)) and / or decrease the effective barrier height (Figure I.24 (c)). This model has been supported by several experiments also with different metal material, like aluminium and molybdenum [5, 127].

Several metals have been studied to get the carbide forming metals, such as titanium, Molybdenum (Mo) and Tantalum (Ta) [126-129]. The ohmic behaviour of these metal contacts after annealing has been attributed to the formation of carbide at the interface. Of course, the choice of the metal material has also to take into account the melting point of the metal which can be deduced from the related phase diagram. Carbides are considered as reliable contacts especially for high-temperature devices.

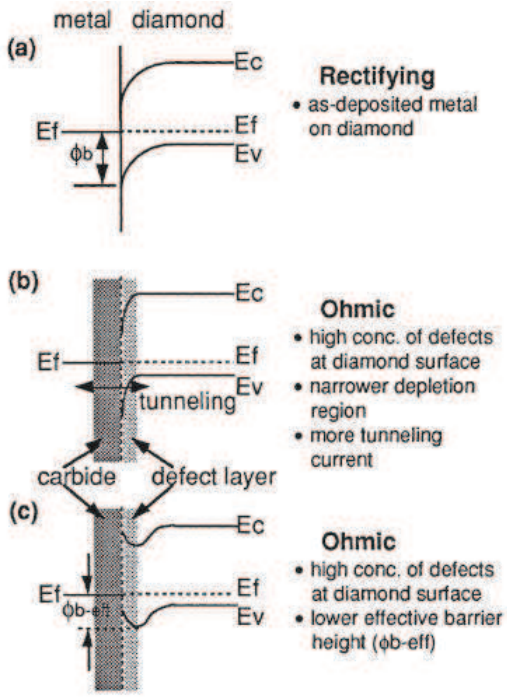

Figure I.24. Model of the interface band diagram of the metal-diamond contact. (a) Interface of the as-deposited metal on diamond; (b) interfaces with high concentration of electrical active defects and consequent reducing of the depletion region width and (c) decreasing of the barrier height due to the carbide formation and/or the ion bombardment [121].

For all of these aspects and the presented interface band structure model, in this thesis work concerning the doped diamond contacting experiment, a titanium layer was deposited on the diamond surface to get the carbide formation, useful for the electrical conduction and adhesion. Afterwards, a gold layer was deposited as top-layer both for avoiding the titanium oxidation and for taking advantage of the good gold electrical properties.

The last key element for ohmic contact deals with the diamond surface termination before the metallization that can be changed. Usually, an as-grown CVD diamond sample surface presents hydrogen termination as the diamond is grown in hydrogen atmosphere (as explained in the Paragraph I.3.3). However, this termination can be changed into oxygen terminations. This modification can strongly affect the electrical behaviour since oxygen terminated diamond surface is electropositive while hydrogenated diamond surface is electronegative [130]. To modify the termination into oxygen terminated surface, it is sufficient to expose the sample to oxygen environment such as acid cleaning solution based on oxygen or to an oxygen plasma.

Among recent studies, several papers have been published regarding the ohmic and rectifying contact behaviour depending on the diamond surface terminations. For example, Teraji et al. demonstrated how the diamond surface termination impacts the electrical performance of gold contact deposited on CVD monocrystalline lightly boron doped diamonds (doping level $\approx 10^{15}$ cm^{-3}) [131]. In particular, the metallization of H-terminated diamond surface produced ohmic contacts, whilst, the metallic deposition on O-terminated diamond surface imparted Schottky properties.

Volpe et al. showed that an oxidizing diamond surface pre-treatment is a necessary step to optimize the Schottky metal / diamond interface on lightly boron doped diamond surfaces [107, 132]. In particular, Ti/Au ohmic contacts and Schottky Au contacts were obtained on the same H-terminated lightly boron doped diamond surface but adding an oxidation treatment (by vacuum ultra-violet (VUV) ozone treatment [133]) for the rectifying electrodes before the metallization [107]. Both Ti/Au and Au contacts proved to be Schottky when deposited after an oxidation treatment of the whole surface [132]. In addition, Kono et al. produced ohmic Au electrodes on H-terminated diamond surface and finding a specific contact resistances in the order of $10^{-3} - 10^{-4}$ $\Omega.cm^2$ [134].
But one of the drawback of hydrogenated surface is its thermal instability and, even if improvement in terms of specific contact resistance can be obtained on such surface, it is highly desirable to develop a deposition process of ohmic contact on lightly boron doped layer starting from an oxygenated diamond surface.

Nowadays, the development of good ohmic contacts is one key element not only for the electronic device fabrication (with heavily and lightly doped diamonds), but also for the manufacturing of performing intrinsic diamond detectors widely used, for example, in the field of high energy physics.

I.8 Diamond detectors

I.8.1 Why diamond detectors?

The large development of the diamond synthesis and growth processes in terms of techniques and technologies in the last decades allowed the manufacturing of several kinds of diamond devices for different applications and among these, there are the diamond detectors. In this thesis work, the experiment performed in Italy has included the fabrication of ohmic contacts on a CVD polycrystalline intrinsic diamond used as particle detectors. Therefore, it is worth understanding why diamond is used for detection applications. It is mainly due to the remarkable properties of the material such as:

- ✓ the high electron and hole mobility which allows a high velocity of signal formation and to operate at high frequencies;
- ✓ the radiation hardness due to its compact and stable structure which determines its great stability and reliability in high radiation environments for several years;
- ✓ the insulator property because of the wide band gap which gives rise to a low leakage current at room temperature;

- ✓ the possibility to get a good spatial resolution during the detection process which is achieved by a high segmentation of the contacts (this point will be presented subsequently).

Historically, the solid state detectors have been based on silicon materials in p-n junction configuration, which have widely satisfied the market requests for scientific applications. Nevertheless, for specific applications, diamond detectors can compete silicon.

In the Table I.2 the most relevant properties from a detection point of view for diamond and silicon are reported.

Table I.2. Comparison between CVD diamond and silicon properties [3, 4, 15, 135].

Property	**Diamond**	**Si**
Bandgap, eV	5.47	1.2
Displacement energy, eV/atom	43	13 − 20
Resistivity, Ω cm	$> 10^{11}$	2.3×10^5
Intrinsic carrier density, cm^{-3}	$< 10^3$	1.5×10^{10}
Mass density, g/cm^3	3.52	2.33
Atomic charge	6	14
Dielectric constant	5.7	11.9
Energy to create e-h pairs, eV	13	3.6
Radiation Length, cm	12.2	9.4
Average created signal/μm, e^-	36	89
Thermal conductivity, W/(cm K)	24	1.5
Breakdown Field, V/cm	$\sim 10^7$	3×10^5
Carrier mobility, $cm^2/(V\ s)$	1800 h @RT, 0V 2300 e^- @RT, 0V	480 h @RT, 0V 1450 e^- @RT, 0V

Comparing the diamond and silicon properties it is possible to understand where the diamond performances overcome the silicon ones. For example, it is clear that the displacement energy, which determines the material radiation hardness, has played a crucial role to the development of diamond detector technologies. Indeed, even if different radiation hard semiconductors are available in the market, such as the oxygen-enriched silicon detectors which reach an irradiation hardening higher than the standard silicon sensors [136], their expensive fabrication cost and their complex engineering have left opened the pave for alternative solutions like devices based on diamonds. Nowadays the diamond radiation hardness represents the main advantage respect to the other semiconductor detectors (one order of magnitude of difference [137]) [3, 4, 138].

However it can be seen that, due to the different band gap energy between the two materials, a higher energy is needed for diamond to create an electron-hole pair than for silicon. As a consequence, the output signal of a diamond detector is largely less than the one from a silicon device. Nevertheless,

the wide diamond bang gap has also a positive impact on the leakage or dark current which is consequently lower than in silicon, also because of the very high resistivity (six orders of magnitude more than that of silicon). Therefore, the diamond signal/noise ratio is considered as acceptable.
In addition, the lower diamond dielectric constant leads a lower capacitance compared to the silicon one having similar dimensions. Finally, the extraordinary thermal conductivity value makes diamond the most attractive material to operate at room temperature and without cooling systems.
Thus, diamond material proves to be excellent candidates to work as an active medium for detection device though cost of fabrication of synthetic diamond is important.

I.8.2 Design of a diamond detector

The diamond detector design is based on the wide band gap property and very low dark current which make not necessary a p-n junction for detection processes. As a result, very simple diamond configuration can give rise to good detectors. Basically, to manufacture a diamond detector it is sufficient to contact the top and the bottom surfaces by metallic electrodes. Through this contacting it is possible to apply a voltage bias so as to create an electric field allowing separating the electron-hole pairs generated in the diamond material when a radiation crosses the device leading to the detection signal. Typical metal electrodes on diamond can be produced by Ti/Au or Cr/Au bilayers as explained previously for diamond diodes. In Figure I.25 a scheme of a simple diamond detector is reported.

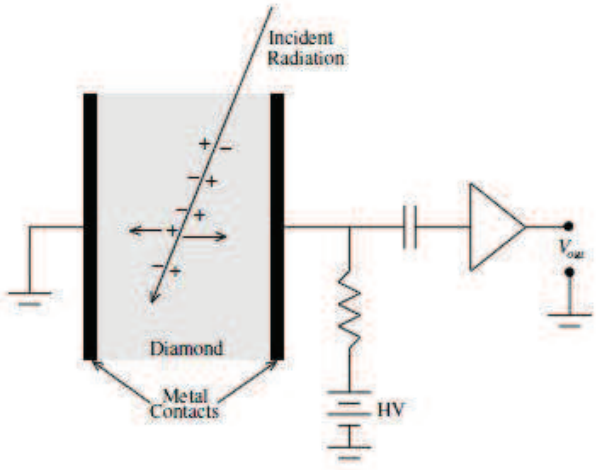

Figure I.25. Scheme of a simple diamond detector contacted on the two surfaces by pad-like metal electrodes. It is worth noting that no depletion region (which is necessary for a p-n semiconductor detector) is needed for diamond materials and all the diamond section is an active area [3].

I.8.3 Charge pairs production and recombination

The charge pairs production mechanism in a diamond device are similar to the one in a semiconductor device. Indeed, when an incident radiation crosses the active region (all the cross section of diamond detectors) electron-hole pairs are produced and, if a voltage bias is applied, the electrons and holes move in opposite directions until reaching the electrodes where an electric signal is generated (see Figure I.25). As shown in Table I.2, a large amount of energy is needed to create one charge pair respect to a silicon detector, which means that with the same energy the charge pairs quantity generated in a diamond device is three times less than in a silicon detector. However, if the diamond signal is compared to a gas detector, the first proves to be three times higher [3]. Therefore, the diamond detector can be considered as a good compromise for the created signal quantity in addition to its advantages to have a very low noise and to be radiation hard.

Once charge pairs are created, recombination phenomena take place. In particular, the charge pair recombination in a diamond device is directly related to the quality of the crystal and the presence of impurities, similarly to the recombination in the standard semiconductors. Indeed, defects and impurities presence contributes to the charge recombination process making it easier by introducing allowed energetic levels in the forbidden band. Therefore, this kind of recombination process have to be added to the standard recombination phenomenon between the conduction and valence bands. As a consequence, the lifetimes of charges recombining is given by both recombination processes, even if it depends mostly on the quality of the diamond. The direct recombination of one electron in the conduction band with one hole in valence band is called “intrinsic recombination” and it can change from a few μs up to about 1 s. Recombination occurring due to intermedium energetic states is defined as “extrinsic recombination” and it can be as low as 0.1 to 10 ns. The average, namely the effective lifetime, can be computed taking into account both processes and it follows the Equation I.6:

$$\frac{1}{\tau_{eff}} = \frac{1}{\tau_{int}} + \frac{1}{\tau_{ext}} \qquad \text{Equation I.6}$$

where the subscripts eff, int and ext indicate the effective, intrinsic and extrinsic lifetime, respectively. The major contribution to the effective lifetime proves to be given by the extrinsic lifetime (namely crystal defects and impurities), therefore the Equation I.6 can be written as the Equation I.7 [3]:

$$\tau_{eff} \approx \tau_{ext} \qquad \text{Equation I.7}$$

I.8.4 CCD and CCE of a detector

One of the required parameter for the manufacturing of a good radiation detector is to own a fast charge collection and in general a fast overall response, which can be satisfied if the free charge mobility is high enough (in the order of 10^3 $cm^2.V^{-1}.s^{-1}$). It is the case of diamond devices, where the electric field profile of charge pair drift velocity is qualitatively similar to the standard semiconductor ones. In particular, the velocity increases with the rising of the electric field intensity until to reach a saturation value. Typically, diamond detectors are used at such high potential that the charge carriers quickly achieve their maximum velocities. A standard electric field applied can be in the order of 1 kV/mm [3].

One of the most important parameter to evaluate the diamond detector performance is the Charge Collection Distance (CCD), which represents the mean distance travelled by electrons and holes before being trapped. The CCD of a diamond takes into account the contribution of electron and hole mobilities together with their deep trapping lifetime under an electric field intensity (E) and is given by the Equation I.8:

$$CCD = (\mu_e \tau_e + \mu_h \tau_h) \cdot E \qquad \text{Equations I.8}$$

where μ_e and μ_h are the electron and hole mobilities, τ_e and τ_h are the electron and hole deep trapping lifetimes, and under the assumption that the detector thickness is larger than the CCD, and the field E is uniform.

The Equation I.8 can be rewritten as in the Equation I.9:

$$CCD = \mu \tau E \qquad \text{Equations I.9}$$

where $\mu = \mu_e + \mu_h$ and $1/\tau = (1/\tau_e + 1/\tau_h)$.

Once the real distance crossed by the carriers (CCD) is assigned, it is possible to define the total charge collected and induced to the readout electrodes (Q_C) by the Equation I.10:

$$Q_C = Q_G \frac{CCD}{L} \qquad \text{Equations I.10}$$

where Q_G is the total charge generated by the incident radiation and L is the physical length (namely the thickness) of the diamond material.

Considering the standard definition of Charge Collection Efficiency (CCE) of a detector as the ratio between the total charge induced to the readout electrodes and the total charge produced by the incident radiation, it is possible to write it as:

$$CCE = \frac{Q_C}{Q_G} = \frac{CCD}{L} \qquad \text{Equation I.11}$$

By the Equation I.11 it is possible to determine the best diamond thickness value so as to make its efficiency close to 1 (namely the 100%), although it is necessary to take into account the not perfect uniformity of the synthetic CVD diamond along its thickness. Depending on the kind of CVD diamond used as detectors, if polycrystalline or monocrystalline, the CCE expected can be around 50% or more than 90% [4].

On the other side, more specifically from an experimental point of view, it is possible to evaluate the goodness of the device during a detection test by computing the CCD value. In particular, by measuring the collected charge Q_C and by knowing the total charge generated Q_G and the diamond thickness L it is possible rewrite the Equation I.10 as:

$$CCD = L\frac{Q_C}{Q_G} \qquad \text{Equation I.12}$$

For example, in high energy physics when a Minimum Ionizing Particle (MIP, namely a charged particle which embody the minimum ionizing losses in materials) crosses a diamond detector generates 3600 electron-hole pairs every 100 μm of material [3, 5], therefore the generated charge can be written as:

$$Q_G = 36 \cdot L \cdot q_e \qquad \text{Equation I.13}$$

where q_e is the elementary charge and the thickness L is measured in micrometers. So, the Equation I.12 becomes:

$$CCD[\mu m] = L\frac{Q_C}{Q_G} = \frac{Q_C}{36q_e}\ [\mu m] \qquad \text{Equation I.14}$$

Nowadays, one of the main efforts in the development of diamond detectors is toward the continuous improvements of the charge collection distance and therefore of the response time. For example, a diamond pre-treatment called “pumping” can be performed with the aim of improving the CVD diamond detector performance in terms of charge collection distance and efficiency. It consists in a

sample pre-irradiation by ionizing radiation, which increases the device efficiency thanks to the deep trap saturation [3, 139].

I.8.5 Intrinsic diamond detectors in physics of high energy

There are a lot of interesting applications for intrinsic diamond detectors, in particular in the field of physics of high energy. Indeed, in the physics of particles, the detectors have to operate in high radiation fields for a long time and in these conditions standard semiconductor devices showed strong deterioration due to the accumulated dose. This limit has been overcome by using diamond. In addition, the high thermal conductivity of diamond makes them the ideal material to work as target where the cooling instrumentations cannot be used.

For example, in the early 1990s, the CVD diamond detectors were investigated and compared to the natural IIa type ones. As a result, the first polycrystalline films were able to sustain field of 1 $V.\mu m^{-1}$ reaching CCD values between 1 and 45 μm [140]. In the subsequent decades, significant improvements were done by the fabrication of particle detector for high flux environment such as the LHC (Large Hadron Collider) experiments, where polycrystalline diamond detectors contacted by pixel- and strip- like electrodes (20 mm by 60 mm) showed a CCD of 300 μm [4, 141].

Other high energy physics experiments such as BaBar at Stanford Linear Accelerator Center (SLAC), Joint European Torus (JET) at CCFE, National Ignition Facility (NIF) at LLNL, and the GSI laboratories, have worked to the diamond detector development [4]. For example, BaBar was the first experiment to apply a diamond detector contacted by pad-like electrodes as a Beam Condition Monitor (BCM) [142]. A BCM device proves to be a very important component in the high energy experiments because of the role to provide a rapid beam abort signal in the event of beam instability, in order to protect other detectors from the radiation damaging. The task can be satisfied just by device with a fast response (< 2 ns pulse FWHM) and radiation hard [143]. Diamonds for BCM applications were installed also in ATLAS and CMS experiments at the LHC [144]. In BaBar experiment the diamond detectors operated for 5 years until to the end of the experiment, demonstrating the reliability in term of radiation hardness and low dark current which did not increase during the irradiation processes. Recently, the RD42 collaboration has started a planning of research and development on diamond detector contacted by strip- or pixel-like electrodes for the next LHC experiments [145].

Neutron detectors were developed by JET experiment [146, 147]. In particular, the fast neutron (MeV energy) measurements can be performed directly in the diamond material by the nuclear reaction $^{12}C(n,\alpha)^{9}Be$ [148]. Indeed, the produced charge particle α induces a charge which can be detected once it has drifted to the electrodes. For completeness, the thermal neutrons (tens of meV energy)

detection can be performed by deposition of thin films of ^{6}Li (typically in the form of ^{6}LiF), or ^{10}B (such as boron free-standing or boron doped diamond) or ^{235}U, as converter layers [149, 150].
In HADES experiment, in Germany, diamond detectors contacted by a strip-like electrodes were used to measure the time of flight under irradiations by heavy ion beams [151].
Finally, also the TOTEM experiment at LHC uses CVD monocrystalline diamond detectors with pad-like electrodes to do temporal measurements with very high precision [152]. For example for a single sensor a time resolution less than 100 ps was measured with a MIP, while combining four detectors this value was reduced of a 2 factor.

I.8.6 Diamond detectors based on the PIN junction

Basically, a simple p-n junction diode (with p- and n-type doping) can also operate as a radiation detector but several disadvantages limit their use [3]. For example, the limited depletion region which proves to be crucial to collect electron-hole charge pairs contributing to the current. When the depletion region is very small the current produced by incident radiation is quantitatively limited. To operate with a larger depletion region, the external electric field on the p-n junction can be increased but with the consequent risk to reach and overcome the breakdown voltage threshold of the crystal structure. A solution to this problem is to introduce an intrinsic layer of a semiconductor material between the p and n layers, namely a thin material wholly operating as depletion region at moderate voltages. This configuration is called PIN (P-type, Intrinsic, N-type) structure. The main advantage of the PIN configuration is to fix the depletion width to the intrinsic layer width in order to get a wide depletion region without applying high reverse bias, solving several problems related to the simple p-n junctions.
PIN diamond devices have been studied and fabricated as detectors in particular for UV radiations. For example, in Figure I.26 a PIN detector scheme and its detection characteristic are reported [153]. The spectrum shows the device photo-response as function of the radiation wavelength, from IR to UV. The maximum responsivity was registered at about 200 nm, while a strong rejection characterized the visible range. The sub-gap response is due to the phonon-assisted indirect absorption. This spectrum became a peculiarity of PIN detectors opening the way to solar blind detection of UV and XUV radiations. For example, this kind of detectors are suitable for space applications considering that they can operate in photovoltaic mode so as no external voltages is needed.

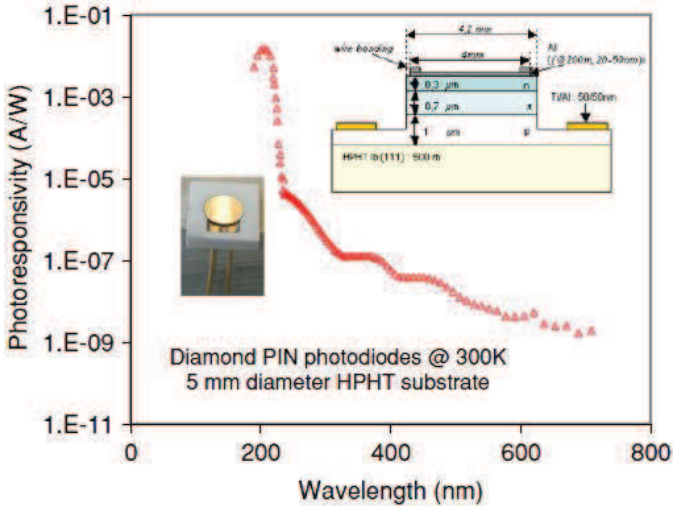

Figure I.26. Scheme of a PIN photodetector and its spectrum after the measurement of the UV solar spectra [153].

I.8.7 Other diamond device applications

As previously discussed, diamond sensors are attractive devices to detect radiations in the UV range and also in the X-ray spectrum thanks to their quick response, radiation hardness, linearity and insensitivity to the visible wavelengths [2, 154]. About the particle detection, in addition to the M.I.P. particles and neutrons, diamond detectors are operated with α-particles, protons and ionization sources [155]. Therefore, additional diamond applications are currently popular and commercialized, such as diamond dosimeters [156] and beam tagging monitor [157] for proton and hadron therapies, respectively. Indeed, a diamond sensor can both track the passage of a single particle and determine its energy and the spatial and temporal distribution of a particle beam. For example, to investigate the radiation damage of living cells, a detector have to be able to detect the passage of every single ion of the incident beam and to resist to the damage of the cumulative dose. Another important property of diamond material characterizing the medical physics applications is called “tissue equivalence” which makes diamond device compatible to the human body feedback under irradiation treatments. Indeed, the human tissue has an average atomic number of around 7.5, which is close to that of diamond (Z = 6), instead of the silicon one (Z = 14).

It is worth mentioning also the positive impact in terms of diamond size on the radiotherapy dose measuring. Indeed, the possibility to produce diamond detector with small sizes (typically 1 mm^3) allows measuring with excellent spatial resolution if compared, for example, to the common utilized ionization chambers.

Finally, diamond detectors can be operated in online mode, which proves to be a fundamental characteristic during a medical treatment.

I.8.8 Diamond contacting configuration and spatial resolution

The possibility to use diamond detectors for all of these applications has emboldened the development of different configurations of diamond contacting, in order to improve the spatial resolution performance so as to better adapt the device to the desired application. The first electrode configuration for diamond detectors was very simple, namely it was composed of two pad-like electrodes (large rectangular metallic contacts) covering the whole areas of both diamond surfaces, as already shown in Figure I.25. In this configuration the detector electrodes were read out with two single electronic channels, one per side, therefore a limit was that the extracted electrical signals did not give any spatial information about the passage of the particles or the radiations [2, 158].

After, the segmentation of the pad-like electrodes was introduced in order to make the detector sensitive to the particle position. In this aspect, the first change was done by building strip-like electrodes, where each electrode was individually read out and thus, one-dimension spatial information could be obtained (1D). In Figure I.27 is shown a typical diamond contacting configuration by strip-like electrodes on the top surface and by a pad on the bottom surface.

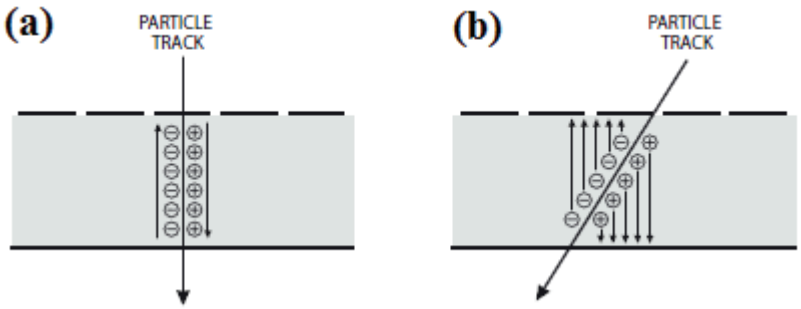

Figure I.27. Detector contacted by strip-like electrodes on the top surface and by a pad-like electrode on the bottom surface. Charges generated by a particle crossing the device (a) orthogonally and (b) with an angle are shown too [159].

In Figure I.27 (a) and (b) a particle crossing the detector orthogonally and with a generic angle are illustrated, respectively. In the case (b), the particle deposits its charge on several electrodes. Here, it is possible to improve the track resolution by means of an evaluation of the charge ratios on the adjacent strips.

In order to reach a bi-dimensional spatial resolution, the electrode segmentation into several strips can be done also by the second pad obtaining two set of parallel strips orthogonally orientated each other. In Figure I.28 a sketch of a detector contacting by strip-like electrodes on both surfaces is shown. In this configuration, every strip has to be individually read out in order to reach a 2D spatial resolution. Indeed, as shown in the picture above, when a particle crosses the device with this electrode configuration, the read out signal can be associated to one strip on the top and to another one on the bottom (black strips) providing the two spatial coordinates. Although the electrodes are segmented, the detector efficiency remains almost the same as a pad detector as only the electric field

close to the surface is changed, while the position resolution is mainly determined by the distance between the centre of two consecutive strips (pitch).

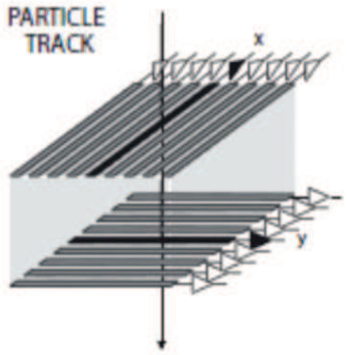

Figure I.28. Detector contacted by strip-like electrodes on both surfaces. The two strip sets are orthogonally orientated each other. When a particle crosses the device two spatial coordinates are obtained (black strips) [159].

Next, a technology based on pixel-like electrodes was developed allowing also a bi-dimensional spatial resolution [155, 160, 161]. In Figure I.29 is reported a diamond detector contacted by pixel-like electrodes used for dosimetry applications.

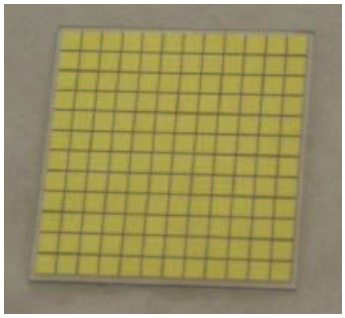

Figure I.29. Top view of a bi-dimensional pixelated diamond dosimeter [161].

The pixel-like geometry for the electrodes consists in dividing a large pad-like electrode into small squares in order to measure accurately the particle position. Indeed, if every pixel is read out individually a granular mapping of the detector surface can be obtained.

Finally, the last option for a 2D spatial resolution is offered by an interdigitated strip-like contact configuration reported in Figure I.30. Here, the electric field is concentrated close to the front surface and proves to be suitable for the detection of photons or particles which do not penetrate in depth, such as UV radiation and α particles [2].

The research and the development in the field of the detector contacting is nowadays still an open field. Subsequently to the development of the first bi-dimensional spatial resolution configurations, Parker et al. were the first to propose the manufacturing of three-dimensional sensor contacting [162]. In particular, the basic idea was to decrease the drift distance of the charged carriers to less than the detector thickness. By this way, the detector materials with a limited mean free path for the carriers due to traps or grain borders, such as a polycrystalline diamond or a heavily irradiated silicon, could

improve their performance. Indeed, while in the traditional planar geometry (pad-like electrodes) the drift distance is given by the thickness of the detector material, in the 3D configuration this distance is assigned by the electrode distance, as shown in the Figure I.31.

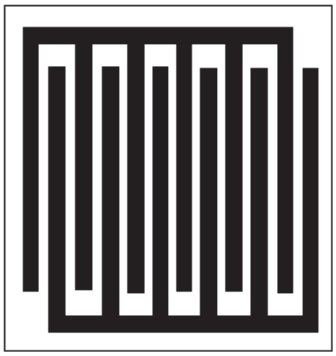

Figure I.30. Top of view of a sketch of the interdigitated strip-like contact configuration [2].

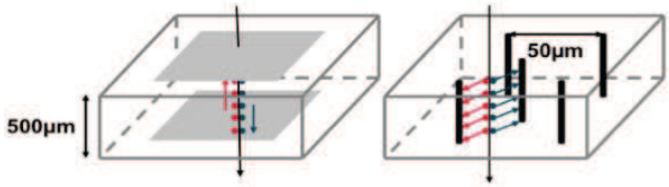

Figure I.31. Sketch of a planar (on the left) and 3D (on the right) electrode configuration for solid-state detectors. The drift distance of the carriers decrease by using a 3D electrode configuration [159].

In addition to a short collection distance, the 3D configuration offers also a fast collection time and low depletion voltage. However, the electric field configuration becomes more complex than for the previous configurations. The 3D technology of contacting has been successfully demonstrated with silicon detectors [163] and the same principle has been applied to diamond, even if a solution to fabricate electrodes inside the diamond bulk should be found. Kononenko et al. micro-structured a diamond bulk by IR pulsed femto-second laser and fabricated a first 3D diamond prototype [164]. Nowadays this technology is successfully applied for diamond detectors and it is under further investigations [165-167]. The diamond irradiation by laser will be presented in the Paragraph I.9.1.
Finally, Liu et al. fabricated and tested last year (2017) a different type of 3D contacting for a UV diamond detector, namely the groove-shaped electrode structure [168]. In particular, the novelty was to create the interdigitated metallic electrodes not on the surface but within 10 µm deep grooves etched in diamond, with the aim of improving the collection efficiency of the carriers induced by UV photons. In Figure I.32 a sketch of both electrode configurations is reported. Preliminary characterizations of the diamond detector contacted by this groove-shaped electrodes structure were carried out and compared with the ones registered on the same diamond detector but contacted by a conventional planar electrode structure. As a result, the responsivity of the new kind of detector was increased up to 50% in the spectral range of 220 − 280 nm compared to that for the planar structure.

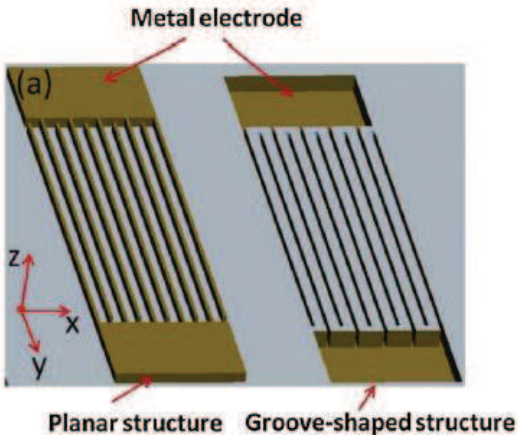

Figure I.32 Sketch of the two electrode configurations fabricated for a UV diamond detector: the conventional planar contact structure (on the left) and the new groove-shaped electrode structure (on the right) are shown [168].

I.8.9 Limitation of ohmic metallic contacting and alternative solutions

The diamond contacting by metallic layer deposition has been already introduced in the sections I.7.2 and I.8.8 about diamond diodes and detectors, and it will be explained step by step in the Chapter IV. Today the scientific community recognises this technique as very efficient, with the peculiar advantage to be reversible (the contacts can be removed and diamonds can be "recycled"), but it is truth that, at the same time, some difficulties have to be overcome during the long and expensive micro-fabrication steps. In particular, as already discussed in the Paragraph I.7.3, even if the manufacturing of ohmic metallic contacts on heavily doped diamonds proves to be well controlled, it becomes a more difficult task on the lightly doped and intrinsic materials. In addition to this aspect, during the diamond metallization process some other crucial points have to be checked, such as:

- The adhesion between metal and diamond;
- The good charge injection of the contacts to avoid polarization phenomena;
- The contact stability, reliability and radiation hardness.

For example, the problem of adhesion is crucial since it strongly influences the good performance of the device. The main difficulty resides in the diamond chemical inertness which makes the metallic adhesion difficult, without excluding the possibility that the metal delaminates, reducing the average life of the device. The polarization phenomenon have also to be checked. This occurs when, during the transition of electrical currents through the diamond, the extraction process proves to be not high enough to compensate the injection one, and therefore the neutrality state is not restored between two consecutive detection events. As a result, a charge accumulation is obtained inside the crystal leading to an electrical filed which works in opposite direction respect to the externally applied one. Finally, contacts should be as stable as possible, durable and radiation hard.

These problematic aspects together with the possible solutions available in literature, such as diamond surface pre-treatments, carbide formation on the diamond surface and surface terminations, have been already discussed in this thesis. Nevertheless, a different approach for the diamond contacting exists in literature, namely the diamond graphitization. In the following last paragraphs the diamond graphitization process will be explained together with the role played in terms of contacting.

I.9 Diamond graphitization

Diamond and graphite are two of the allotropic forms of the carbon, as explained in the diamond material description at the beginning of this chapter (Paragraph I.3.1). The different carbon atomic arrangement of these two materials (sp^3 hybridization for diamond and sp^2 structure for graphite) marks the borderline between the diamond and graphite properties which are very different. For example, diamond material owns an extreme hardness, inertia and transparency, electric insulation and high thermal conduction; on the contrary, graphitic material is soft, reactive and dark, with a good electric conduction and a bad thermal one. Nevertheless, this borderline between the two materials can be crossed allowing the transition from one phase to the other one. In particular, the so called "diamond graphitization" allows obtaining transition from diamond phase to graphitic phase. This kind of transition allows locally inducing graphite on or into diamond material. Nowadays several studies have been carried out about the diamond graphitization in terms of physics of the process, techniques and related applications. The diamond graphitization has been central in my thesis work carried out in Italy and has been the most important key element of my research work developed in France.

In the following, the processes of the diamond graphitization induced by laser and by ion implantation and their applications in terms of diamond contacting will be presented.

I.9.1 Diamond graphitization induced by laser

The diamond-graphite transition can be induced by heating the diamond material so as to reach and overcome the transition threshold temperature. For example, when a portion of diamond material is heated by a laser radiation at temperatures higher than the threshold graphitization temperature $T_g \approx 700$ °C (in air) it is possible to give rise to the breakdown of carbon atom sp^3 bonds which consequently re-arrange themselves into sp^2 configuration, which is more stable at atmospheric conditions. From a diamond lattice point of view, the energy acquired by carbon atoms proves to be enough to undergo a diffusion jump and end up into sp^2 state in a new lattice cell. As a consequence of this phase transition, the atom binding energy decreases while the mean distance between adjacent

atoms increases. Therefore, it is easy to imagine how the diamond graphitization takes place easier close to free volume of material, such as close to the surface or near defects [14].

A lot of studies have been carried out about the diamond graphitization process and in particular about the laser-induced graphitization [14, 169-176] . During the radiation-matter interaction between a laser beam and a diamond material, the laser radiation is absorbed by free electrons in elastic collisions with atoms and ions in the process of "inverse bremsstrahlung". Several processes can contribute to determine the initial concentration of electron, namely the multiphoton absorption, tunnelling of electrons into the conduction band for radiation with high intensity, or direct inter-band transitions for laser radiation with short wavelength. In addition, impurities and defects can absorb laser radiation and produce free electrons. From an irradiation point of view, the laser pulse intensity and duration prove to be crucial parameters to describe what kind of graphitization process could take place [14, 169]. In particular, it has been demonstrated that for low intensity and nanosecond or longer laser pulses, excited electrons transfer kinetic energy to the lattice, the electrons-lattice system is in thermal equilibrium and the electrons heat the lattice gradually up to reach $T \approx T_g$ during the irradiation process as the electron-lattice relaxation time is about 10^{-12} s. When the intensity is high enough, an electron avalanche can be developed, so that the electron temperature can overcome the lattice atom one, and the electron concentration can be much higher than under equilibrium conditions. Fast electrons can reach sufficiently high energy to induce carbon atom ionization by direct impact. Laser pulse energy absorbed by plasma is transferred finally to the lattice and can also heat it up to $T \geq T_g$. On the contrary, for femtosecond laser pulses, the laser energy is transferred to the electrons in a short time interval of only a few hundred femtoseconds, which is shorter than the electron lattice relaxation time. Therefore, the laser pulse energy will be deposited and will stay in the electron system, and the lattice will not be thermally equilibrated with electrons. Anyway, the duration of the laser pulse is longer than the relaxation time of the electronic gas, which is about 10^{-14} s. Thus, the electron system will be in thermal equilibrium at a high temperature while the lattice will be cool under femtosecond laser irradiation. Definitely, depending on radiation beam parameters, the result of laser action can be quite different: from formation of micro- (nano-) regions with sp^2- dominated bonding up to a complete transformation of the diamond into a graphitic phase.

Another very important processing parameter is the laser radiation wavelength. Diamonds present an interesting optical absorption spectrum useful for the choice of the irradiation wavelength. The spectrum is reported in Figure I.33. In correspondence of the wide diamond band gap (5.47 eV) namely for energy less to the correspondent wavelength of 225 nm there is no absorption, such as in the visible range which makes diamond transparent. On the contrary, for wavelength less than 225 nm there is a direct transition from valence band into conduction band. However, looking the

spectrum around the IR range, diamond exhibits bands of absorption related to the contribution of two and three phonon (2.5 – 6.5 μm), while the absorption at one phonon is forbidden due to the cubic symmetry of the crystal [177].

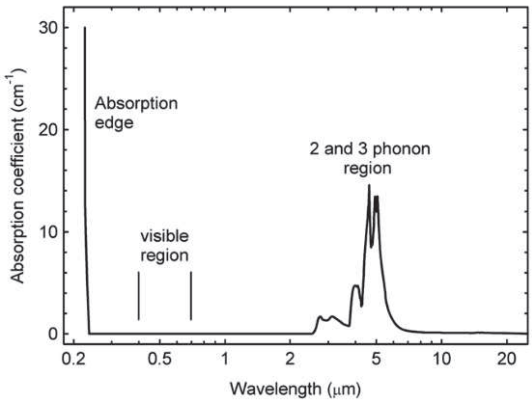

Figure I.33. Absorption spectrum of a pure diamond in the ultraviolet – visible – middle infrared range [177].

In the Lecce Laser Laboratory (L3) at the University of Salento, an excimer laser working with ArF or KrF gas mixtures (λ = 193 and 248 nm, respectively) was available. For this thesis work the ArF mixture was selected to take advantage of the good results and the know-how developed during my master thesis work about the production and characterization of graphitic structures induced by such a laser on diamond surface [178].

Naturally, the results of the radiation-matter interaction depend also on the kind of diamond material, namely on the diamond quality. Indeed, it is possible to see in literature how, for different qualities of diamond crystals, the same laser radiation can be more or less absorbed. For instance, in Figure I.34 (a), the light absorption coefficient (α_0) changes as a function of the laser wavelength are illustrated and for diamonds with different quality, in addition to the graphite feedback for comparison.

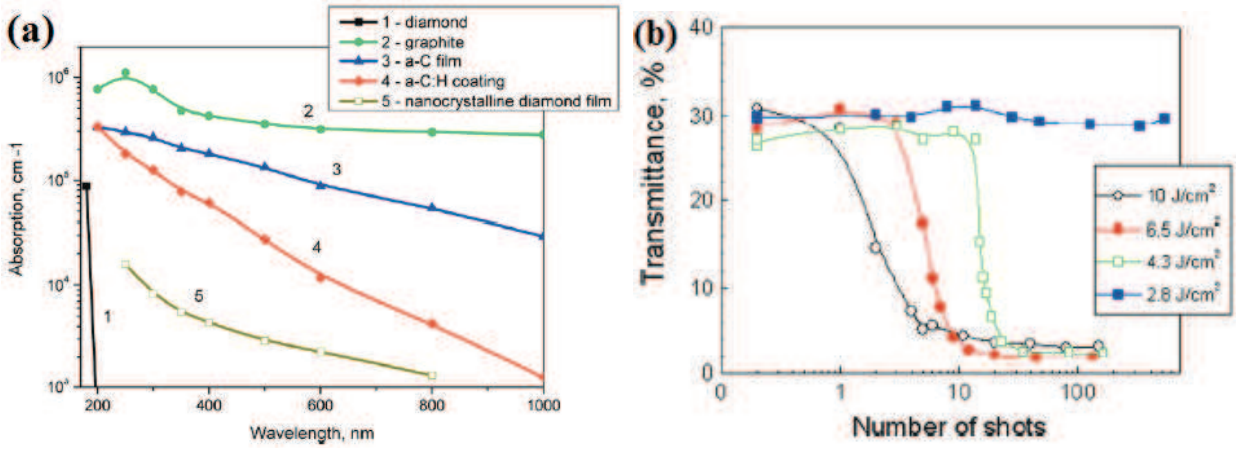

Figure I.34 (a) Trend of the optical absorption coefficient against the radiation wavelength for different materials: 1- diamond, 2- graphite, 3- amorphous carbon film, 4- coating of hydrogenated amorphous carbon, 5- nanocrystalline diamond film. (b) Trend of the transmittance of a CVD polycrystalline diamond as function of the laser pulse number (shot) for different laser fluence [14, 171].

As a result, single-crystal CVD diamonds are transparent to the laser light outside the UV range, while for the other materials the absorption increases with the decrease of the quality. Graphitic materials show the higher values of absorption. Considering the higher value for the graphite absorption coefficient, during the transition diamond – graphite, the optical transmittance is expected to decrease. In Figure I.34 (b) is shown the transmittance change as a function of the laser pulse (or shot) number for different laser fluences registered on a CVD polycrystalline diamond irradiated by a picosecond laser (λ = 539 nm). It is possible to understand how the fluence laser strongly influences the graphite formation: for example at 10 J.cm^{-2}, only one pulse is enough to begin the graphitization process, while at 2.8 J.cm^{-2} the transition seems to not start due to a too low laser fluence. Intermediate values of laser fluence can need several laser shots to start the diamond graphitization process. This finding suggest that, during a diamond irradiation process, the first laser-induced micro-defects becoming radiation absorption centres for the next shots so as to give rise to the graphitization process [14]. Physically it is worth reporting also that, when a laser beam hits a diamond surface with enough fluence to allow the beginning of the local graphitization by only one laser shot, it can also cause a bump on the surface profile due to the density difference between diamond and graphite ($\rho_{diamond}$ = 3.5 g.cm^{-3}, $\rho_{graphite}$ = 1.9 g.cm^{-3}). In addition, if the laser fluence is sufficiently large, a part of the graphite material can even be heated up to the sublimation temperature (T_S = 4000 °C) and to be ablated away giving rise to the formation of a crater in the irradiated zone. In their several studies, Konov et al. demonstrated that irradiating a turbostratic carbon film by a KrF laser, the graphitization process starts at the laser fluence of $F \approx 0.4$ J.cm^{-2}, while the transition from only graphitization to the ablation regime in a single-pulse action takes place at the laser energy density (or fluence) of $F \approx 5$ J.cm^{-2} [173]. For higher laser fluence values, the ablation rate became so high that a large crater can be produced even in only one single pulse.

In my master thesis several studies about this evolution of the diamond irradiation process from the graphitization regime to the ablation one were carried out. In particular in Figure I.35 is reported the average heights of the spot-like graphitic structures induced by ArF laser at a constant fluence value (F = 5 J.cm^{-2}) and variable number of pulses (N = 1, 2, 4 and 8) on a CVD polycrystalline diamond [178]. The plot shows positive average heights of the graphitic structures for the first laser pluses (N = 1 and 2) and negative ones for many pulses (N = 4 and 8). This finding suggests a bump formation in first, then a partial ablation of the graphitic bump with two laser shots, and after the ablation phenomenon proved to be dominant by the increasing of the pulse number. In general, the ablation rate of a graphitic material depends on the laser fluence, but also on the pulse duration. In particular, for long pulse duration and high thermal conductivity of the material the ablation depth depends on the penetration of the heat in the diamond. On the contrary, for short pulses, the laser

energy released in the graphitized layer is used only to vaporize the material and the heat loss in the sample is negligible [14, 172].

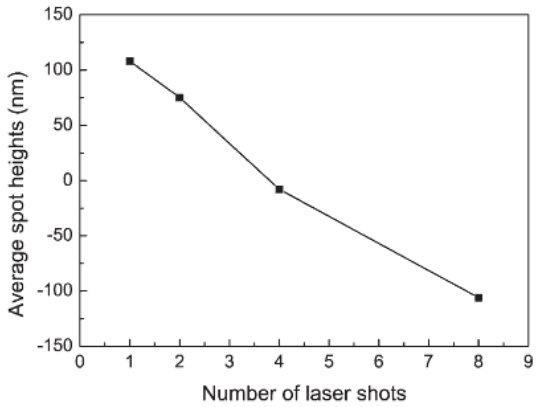

Figure I.35. Average height of the spot-like graphitic structure obtained by a UV laser fluence of 5 J.cm^{-2} and a variable number of laser shot (N=1, 2, 4 and 8) on a CVD polycrystalline diamond measured by AFM. The zero level refers to the flat unirradiated diamond surface [178-180].

I.9.2 Laser-writing technique applied to develop all-carbon detectors

Once the diamond graphitization process has been understood, several works have been carried out trying to apply the technique in several fields, in particular the domain of diamond contacting. Indeed, as previously explained, diamond contacting by the traditional metallization methods require expensive micro-processing instrumentations, time and several surface pre-treatments, especially to obtain the ohmic behaviour formation. On the contrary, diamond graphitization can be performed in a laboratory equipped of an appropriate laser with few other less expensive instrumentations, in a shorter time, with no particular surface pre-treatments. In addition, the diamond-graphite transition ensures a strong mechanical adhesion between the graphite and the last diamond layers under the irradiated zone. As last, but not the least, the graphitized areas on diamond prove to be good ohmic conductors as expected for a graphitic material. Thanks to all of these advantages, several works have been already published about diamond devices contacted by graphitic structures, such as the so called "all-carbon detectors".

During my master thesis, several set of graphitic strips were produced by laser-writing on a diamond surface with different values of fluence and cycles of irradiation, and electrically characterized showing always ohmic behaviour. The strip form of the graphitic structures was adopted to simulate the subsequent step of diamond contacting for detector applications. Among this graphitic structures, the graphitic strip showing lower resistivity value ($\rho = 4 \times 10^{-3}$ Ω.cm, in line with the expected one for graphite [14]) were characterized also by micro-Raman and AFM analyses confirming the graphitic nature of the material and a good homogeneity of the structure along the whole area [178,

179]. Therefore, the corresponding experimental irradiation conditions were used to produce a first strip-like all-carbon detector using a CVD polycrystalline diamond. Then the device was tested by nuclear investigations. At first, a preliminary and rough comparison between the performances of the all-carbon device and those of a metallized diamond was carried out with a 500 MeV electron beam at the Beam Test Facility (BTF) in Italy, demonstrating similar characteristics of the two detectors [181]. Afterwards, a more complex investigation was performed with a 120 GeV pion beam at CERN infrastructures. In Figure I.36 the charge distribution of the all-carbon detector as measured with ultra-relativistic pions and its Landau curve fit are reported. Data analyses show good nuclear detection performances of all-carbon device, with a charge collection efficiency (CCE) of 42% (in agreement with the expected value reported on supplier datasheet) [180].

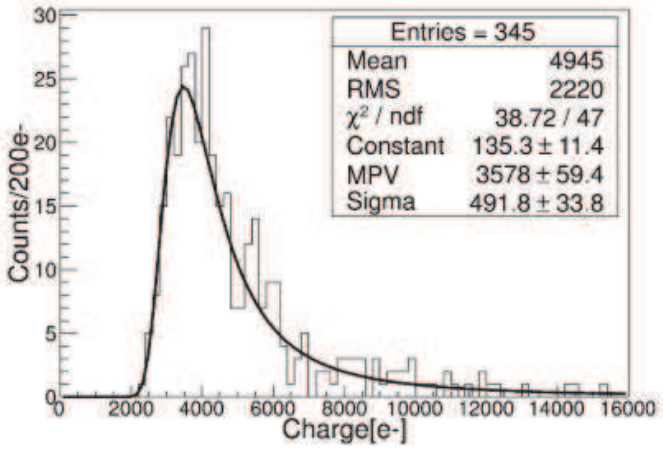

Figure I.36. The charge distribution with a Landau curve fit of an all-carbon detector of dimensions 5 × 5 × 0.325 mm^3 irradiated by a 120 GeV pion beam at CERN infrastructures [180].

I.9.3 Diamond graphitization into the bulk

For completeness, it has been demonstrated in literature that the laser-induced diamond graphitization can be obtained not only on the surface but also in the bulk. In order to graphitize inside the diamond, some conditions must be meet, such as [14, 164, 182]:

- The laser beam must be convergent (focusing plane) in the diamond bulk, in order to get a laser fluence higher in the focal volume rather than in the intermedium one;
- Diamonds must be transparent to the laser radiation with low power;
- A nonlinear mechanism of radiation absorption shall induce a strong increase of the absorption coefficient in the focal volume so as to permit to the beam of overcoming the threshold value in the bulk;
- Structural or phase material changes must take place in the interaction zone;
- To localize the graphitization process it is necessary to minimize the laser pulse energy keeping high intensity level (for example, reducing the pulse duration);

- To produce complex structures in the diamond bulk, a translation system of the focal plane of the beam into the sample must be developed.

Experimentally, it is possible to satisfy these conditions using lasers with a short pulse duration, such as femtoseconds or few picoseconds, and operating with visible and near-infrared wavelengths (with high quality monocrystalline and polycrystalline diamonds).

Similarly to the graphitization process on the diamond surface, in order to graphitize inside the sample, it is necessary to overcome a fluence threshold value. In the Konov's review it is reported also an interesting study about the surface and bulk graphitization thresholds of a single crystal diamond for different laser pulse duration (in the order of femto- and picoseconds) at fixed wavelength (800 nm) [14, 164]. As a result, the bulk graphitization threshold proved to be much higher than the surface one. For example for the femtosecond pulses the laser fluence inducing the diamond graphitization was variable in the range 7 – 30 $J.cm^{-2}$ for the bulk process, while it was about 1 – 2 $J.cm^{-2}$ for the surface one. Basically, when the diamond – graphite phase transition occurs, the difference of material density requires a free volume in the surrounding area to allow the increasing of the mean distance between adjacent atoms, which is higher for the graphitic form. This condition is always satisfied onto the surface. On the contrary, for the diamond bulk, the carbon atoms cannot expand their volume during the transition and the carbon atoms prove to be placed at a distance less than the equilibrium one. Therefore, more energy is required to reach the transition phase.

In addition, in the diamond bulk, as on its surface, the first effect during the laser irradiation is a pronounced "incubation", which is related to the presence and to the accumulation of stable micro- and nano-defects, materials very sensitive to the radiation absorption, and that can produce free electrons useful to heat the sample and to change its phase. Once the graphitization step is started, the next laser pulses give rise to a rapid expansion effect of the graphitic sites, allowing the graphitization propagation along the laser beam direction. Then, if the focal plane is moved inside the sample, the graphitized volume follows the laser focal spot. The scan rate of this operation, in addition to the laser fluence, influences the quality of the graphitic structures in the diamond bulk.

I.9.4 Applications of the 2D and 3D graphitized diamonds

Nowadays several works have been published about graphitic electrodes induced by laser on the diamond surfaces and in the diamond bulks. For example, Pacilli et al. produced an all-carbon detector characterized by graphitic pixel-like electrodes induced by KrF laser on a polycrystalline diamond surface and they tested its good 2D detection performances by beta particles obtained from a radioactive source [183]. Other all-carbon detectors composed by a high quality polycrystalline

diamond and an array of small graphitic pixel produced by ArF laser were investigated by a ^{90}Sr radioactive source. These devices proved to work well as detectors and trackers of particles and moreover, the surface graphitization was demonstrated not to produce bulk or interface defects, which can limit the charge carrier transport and collection property of the devices, confirming that the laser technique is useful for the diamond contacting [184, 185].

Graphitic electrodes in diamond bulk were produced for 3D all-carbon detectors in several studies. Kononenko et al. showed the fabrication of graphitic pillars in diamond by femtosecond laser pulses, characterizing the device performance for signal collection, noise and leakage current [186]. Finally, the diamond graphitization into the bulk has been investigated also for different applications, such as to fabricate microfluidic channels by femtosecond laser into a single crystal diamond [187], and to create graphitic electrodes integrated in a diamond-based cathode prototype for solar cell application [188].

I.9.5 Diamond graphitization induced by ion implantation

Historically, the ion implantation technique has been developed to introduce dopant material into semiconductor crystals as already discussed in the Paragraph I.5.2; however, when the technique is applied to diamond materials, a different and very interesting aim can be reached: the diamond graphitization. Indeed, it is well known in literature that when a material is implanted by ions (such as H^+, He^+, D^+, C^+ and Xe^+ ions), lattice defects in addition to the impurities are induced [189-192]. In particular, if the implanted semiconductor is diamond, it is possible to locally break sp^3 carbon bonds in the crystal and, if the density of the broken bonds reaches a sufficiently high concentration (depending on the implantation experimental conditions), the damaged material may rearrange assuming sp^2 bonds in stable form. Then, when such a diamond amorphization into the material is induced, a subsequent annealing treatment is required in order to transform definitely the amorphized material into graphite. Uzan-Saguy et al. demonstrated that the damage density threshold (critical dose) beyond which the graphitization occurs after the annealing treatment was equal to 10^{22} vacancies/cm^3; on the contrary, for implantation inducing a damage density value below this critical dose, the annealing process restores the origin diamond crystallinity [64]. In the samples implanted beyond the threshold, the annealing treatment not only contributes to the definitive graphitic phase formation but also restores the amorphized material into diamond phase in the area proved not to be enough damaged, which are typically located around the most hit one.

For completeness, in some most recent studies the critical dose of the defect density was found slightly above than that determined by Uzan-Saguy et al. A value equal to 9×10^{22} vac/cm^3 has been

established by Olivero et al. [193]. In the same paper, they attributed this discrepancy to the higher internal pressure for deep implantations which could effectively increase the graphitization threshold, as already suggested in previous studied [189, 194].

I.9.6 The ion implantation process

The experimental parameters characterizing an ion implantation treatment are the nature of ions, their dose and their energy, which together affect the quantity of developed defects and therefore define the achievement of the graphitization threshold or not. Basically, when an ion beam hits a solid state material, its ions penetrate in the crystalline lattice and move through it interacting with both electronic clouds and nuclei of the target [195]. The elastic ion - electronic cloud collisions preserved the ion energy, while the inelastic ion - electronic cloud and ion - nuclear ones transfer energy to the lattice which suffers damages. In particular, if the transferred energy proved to be greater than the displacement energy (E_d) of the target atom, this atom will be displaced from its lattice position. Each displaced atom leaves a vacancy (hole), while the moved atoms can allocate in other vacancies (substitutional atoms) or among the lattice sites (interstitial atoms). Each vacancy and substitutional atom pair recombine at room temperature, while the atoms in the interstitial positions remain in the quantity of the ion implantation dose. The ion energy loss during the inelastic collisions is given by the sum of the both stopping mechanisms (the inelastic electronic and nuclear interactions). In particular, the stopping power (dE/dx) is defined as the energy dE lost by an ion crossing a distance dx by the equation

$$\frac{dE}{dx} = N \int T d\sigma \qquad \text{Equation I.15}$$

where dσ indicates the collision cross section, T is the energy lost by the ion during a collision event and N is the density of scattering centres of the target material. Therefore, the stopping cross section ε is given by

$$\varepsilon = \frac{1}{N} \cdot \frac{dE}{dx} = \int T d\sigma. \qquad \text{Equation I.16}$$

The total stopping power is composed of the nuclear and electronic processes, as described before, and consequently the Equation I.15 can be written as

$$\frac{dE}{dx} = \left(\frac{dE}{dx}\right)_e + \left(\frac{dE}{dx}\right)_n = N[\varepsilon_n + \varepsilon_e] \qquad \text{Equation I.17}$$

where ε_e and ε_n are the electronic and nuclear stopping cross sections, respectively. Theoretical studies predict that incident ions are stopped mainly by nuclear collisions if the implantation energy is low, while the dominant stopping will be given by electronic interactions if the implantation energy is high. In addition, while for the Lindhard's model the ion-electronic interactions do not imply any deviation in the projectile trajectory, the Coulomb interaction between two positive (screened) charges results in both energy loss and significant deviation in the projectile trajectory. This deviation gives rise to the lateral and longitudinal spread respect the depth distribution of the implanted species. At the same time, due to this ion-nuclear collisions, the target atoms are moved from their original positions implying the lattice damaging [195].

From the energy loss, the ion range R can be calculated according to

$$R = \int \frac{dE}{dE/dx} \qquad \text{Equation I.18}$$

where the integration limits are from the initial ion energy to zero. However, the slowing down process of an ion moving in a solid material is a statistical process, therefore the places where the implanted ions stop are also of a statistical nature and should be expressed using statistical variables. The ion range R is related to the mean track length of the ion before coming to rest while the projected range R_P gives the mean penetration depth of the ion relative to the surface. Considering the projected range distribution, the Gaussian approximation gives the implant density n(x) as

$$n(x) = \frac{\Phi}{\sigma_P \cdot \sqrt{2\pi}} \cdot exp\left[-\frac{(x - R_P)^2}{2\sigma_P^2}\right] \qquad \text{Equation I.19}$$

where x is measured along the direction of the beam, Φ is the ion dose (or fluence) and σ_P is the standard deviation in the projected range R_P, also referred as the ion range straggling ΔR_P into the longitudinal and lateral direction respect R_P.

Quantitative information can be obtained by commercial software of simulating for ion implantation processes into crystalline materials. This calculation program are based on Monte Carlo simulations and can give an estimation of the implant damage and the final ion distribution. In this thesis the SRIM software (Stopping and Range of Ions in Matter [196, 197]) has been used to compute the ion penetration depth and to simulate the ion propagation into the diamond targets. The ion beam profile proves to be Gaussian.

For completeness, under particular irradiation conditions, a channelling phenomenon can take place. In particular, the channelling phenomenon occurs when the ion trajectory is in line with the atomic rows causing a slower rate of energy loss. As a result, the ion distribution and the lattice damage

prove to be not Gaussian [195]. The instrumentation available for this thesis experiment exclude this phenomenon. Indeed, the home-made machine is not equipped of a ion focusing system which imply a high ion dispersion once the beam goes out from the accelerator gun to reach the sample.

I.9.7 Applications of the ion implanted-induced diamond graphitization

The idea to use the ion implantation technique into diamond material has found its first applications in the production of defect zones or graphitic layers into diamond device for different aims, and among this the huge problem of the diamond contacting.

Chen et al. in the 2002 studied the graphite / metal contact fabrication on a boron doped diamond studying the electrical performance [198]. In particular, they doped the material by in situ growth technique aiming to obtain a very low boron concentration, which was measured of 6×10^{14} cm^{-3} by Hall effect. After the growth the sample was oxidized in order to replace the hydrogen terminations of the CVD diamond film. Then, the diamond graphitization was induced by Ar^+ implantation at 40 keV with a dose of 1×10^{16} cm^2, and a subsequent Ti/Pt/Au metallic stack in the circular TLM configuration was fabricated as final contact. The authors verified a good ohmic behaviour at the graphite / Ti interface but they registered high values of contact resistance (4.72×10^5 Ω) and specific contact resistance of (1.18 Ω.cm^2).

Most recently (2017), Pinero et al. published a work where they tried to get ohmic contacts on diamond by direct heavy boron implantation [199]. Their idea was to generate defects in a very thin superficial layer in the same time of the diamond doping process, in order to improve the tunnel effect through the bend bending at diamond surface. In addition, they investigated several annealing treatments to reduce the specific contact resistance. As a result, comparing the performance of their implanted, annealed and then metallized sample fabricated on a highly boron doped diamond, a decreasing of the specific contact resistance were registered.

Bolshakov et al. during the last year (2017) fabricated a thin diamond detector for thermal neutrons with a buried graphitic electrode [200]. In particular, they performed the growth of a 3 μm thick CVD diamond material on a HPHT substrate, then they exposed the sample to helium ion implantation at 350 keV. After an annealing treatment to convert the amorphization into graphite, they restarted the diamond growth until reaching about 12 μm. In this configuration, the buried graphitic layer worked as bottom electrode, while the top of diamond surface was contacted by an aluminium pad. The thin detector was successfully tested by radioactive sources emitting γ radiation, α particles and neutrons and the small thickness proved to improve in terms of sensitivity and high energy resolution.

For completeness, Matsumoto et al. (2014) investigated the reduction of n-type diamond specific contact resistance using graphitic electrodes obtained just by heating the sample [201]. In particular, the doped diamond was growth using phosphine (PH_3) gas with a doping concentration of about 10^{20} cm^{-3}. Then, the diamond surface graphitization was performed by direct annealing at 1300 °C for 10 min in vacuum. Afterwards, the diamond metallization was produced by a Ti/Pt/Au stack, and finally the uncovered graphitic material was removed. For comparison a similar diamond sample without graphite layer was fabricated. As a result, the specific contact resistance of the graphite/metallic electrodes proved to be equal to of 0.9 $\Omega.cm^2$, one order of magnitude lower than that of metallic contacts.

Finally, another kind of application related to the ion beams into diamonds is the lift-off technique assisted by ion implantation to slice diamonds [202]. Indeed, the preparation of a slice of diamond basically requires the use of a laser or the use of a saw but these standard cutting techniques lead to the loss of a thickness more than 0.2 mm. An alternative solution to minimize the cutting loss is to use a lift off technique assisted by ion implantation which allows creating a damaged layer along the whole area of the diamond bulk. After an annealing step, the graphitic layer can be etched by an electrochemical process so as to separate the diamond film.

I.10 Conclusions

Among the different diamond synthesis techniques, the MPACVD process proves to be the most adapted to synthetize and grow high quality monocrystalline and polycrystalline diamonds, with high purity and crystallinity levels useful for the production of power electronic devices and detectors.

In terms of doping, nowadays the best results are obtained by in situ technique which allows incorporating impurities in a very well controlled way, producing good samples in particular for the (100) oriented crystallographic face. The boron dopant proves to be well incorporating with doping levels in the range from 10^{15} up to 10^{21} cm^{-3}. The obtained doped layers have a very good crystalline quality with an extremely low compensation rate and it could be considered as the first technological brick for the manufacturing of electronic devices.

Every electronic devices or detectors need performant metallic electrodes and the fabrication of good ohmic contacts on diamond surface proves to be still a difficult work. Indeed, even if for highly boron doping (> 10^{20} cm^{-3}) the ohmic behavior is easily reached the manufacturing of ohmic contacts on lightly boron doped (< 10^{18} cm^{-3}) or intrinsic diamonds is still an open field, as well as for phosphorous doped diamond. Several aspects have to be taken into account for this technology step, such as the choice of the metallic layers, the termination of the diamond surface and the eventually

surface pre-treatments. It has been demonstrated that the use of a metal compatible with the formation of a carbide (for instance titanium to get the TiC), the hydrogen terminations and the Ar sputtering pre-treatments can favour the formation of ohmic contacts.

Nevertheless, sometimes these precautions can prove not to be enough and other solutions have to be found. For example, diamond graphitization by laser-writing has been successfully performed and allowed fabricating ohmic, stable and reliable graphitic electrodes on the diamond surface in short time and by not expensive technological steps. The laser technique offers also the possibility to graphitize the diamond in the bulk for 3D detectors. By this approach, the so called all-carbon device have been obtained.

However, another technique can also be used to graphitize diamond, namely the ion implantation. Nowadays, this technique has been successfully applied to dope heavily and at the same time to graphitize diamonds and to induce conductive layers in the diamond bulk (with ion energy of hundreds keV or few MeV) and could constitute a good approach to improve ohmic contacts on lightly doped or even intrinsic diamond material.

CHAPTER II: INSTRUMENTATIONS FOR THE SAMPLE MANUFACTURING AND CHARACTERIZATION

II.1 Introduction

This chapter collects the instrumentation data used to manufacture and to characterize the samples produced in the two experiments carried out during this thesis.

In particular, the first part of the chapter deals with the description of CVD polycrystalline intrinsic diamonds and of the experimental set-up used to graphitize these samples by laser-writing technique at L3 (Italy). The diamonds were chosen to be contacted and used as all-carbon detectors for a new experiment of high energy physics and were provided by Applied Diamond Inc. (USA). This experiment called PADME (Positron Annihilation into Dark Matter Experiment) [12] and supported by the Italian National Institute of Nuclear Physics (INFN) will be presented in the Chapter III.

Afterwards, a second section concerning the instrumentation used at LSPM (France) for the diamond growth and contacting is reported. In particular, the protocol of the diamond substrate preparation before the growth process, the description of the MPACVD reactors allowing synthetizing intrinsic and boron doped CVD monocrystalline diamond, in addition to all instrumentation used to graphitize (by ion implantation) and metallize these samples are presented.

Then, in the last part of the chapter all the characterization techniques used to analyze the as-grown, graphitized and metallized diamond from the structural, morphological, compositional, mechanical and electrical points of view are described.

For both experiments, several sample manufacturing and characterization steps were carried out in collaboration with national and international institutes of research which have been opportunely mentioned in the text.

II.2 Diamond graphitization by laser-writing technique

II.2.1 Diamond samples

The authors of PADME experiment have planned to use a diamond detector as active target and the main candidate for this role, up today, proves to be a detector grade CVD polycrystalline diamond with segmented ohmic graphitic contacts. The choice to propose graphitic electrodes rather than metallic ones is strongly related to the energy loss during the interaction positron beam – electrode matter during the nuclear investigations, which can be reduced using a material with a low atomic number. Details about this will be offered in the Chapter III.

The target dimensions are fixed, namely $20 \times 20 \times 0.05$ mm^3. Considering the large area of this diamond and the related high cost of productions, for this thesis work a set of the same kind of samples

but less large (5 × 5 × 0.05 mm^3) was also bought in order to optimize and characterize the diamond graphitization process on them preserving the real scale samples for the nuclear investigations. All the samples, two large and the whole set of the smaller ones were detector grade CVD polycrystalline intrinsic diamond films provided by Applied Diamond Inc. (USA) [203]. In Figure II.1 the small sample set together with the large diamond are shown.

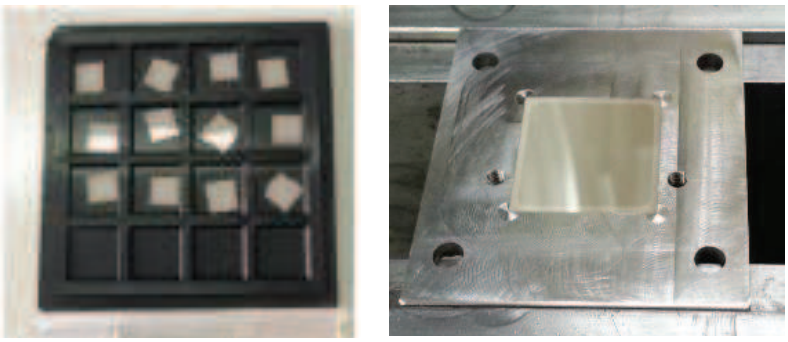

(a) (b)

Figure II.1. (a) Set of small detector grade CVD polycrystalline intrinsic diamonds (5 × 5 × 0.05 mm^3), and (b) one large diamond (20 × 20 × 0.05 mm^3) located in its graphitization holder.

All the diamond samples own the same properties:

- Level of nitrogen impurities < 1 ppb
- Roughness (Ra) < 5 nm for the polished surface (nucleation side)
- Roughness (Ra) < 1.5 μm for the unpolished surface (growth side)
- Electric resistivity > 10^{12} Ω.m
- Thermal conductivity > 1700 $W.m^{-1}.K^{-1}$
- Hardness (Knoop) ≈ 5.700 $Kg.mm^{-2}$

The exceptional sizes of the sample prohibited the use of monocrystalline material. For these reasons, the only samples available on the market were polycrystalline material. In addition, they were only partially treated during the polishing steps, indeed only one surface (the nucleation side) was polished while the other one (the growth side) was left “as-grown”.

II.2.1 Experimental set-up

These diamond samples were graphitized by laser writing technique (which has been already discussed in the Chapter I) in order to produce graphitic contacts on their surfaces. The complete experimental set-up is schematically illustrated in the Figure II.2 (a). The principal components of this set-up are:

- An excimer laser as radiation source;
- An optical system to focus and modulate the laser beam;

- A set of two sub-micrometric motorized translation stages to allow the production of bi-dimensional graphitic patterns;
- LabVIEW software to remotely control at the same time the laser and the X and Y translation stage operations.

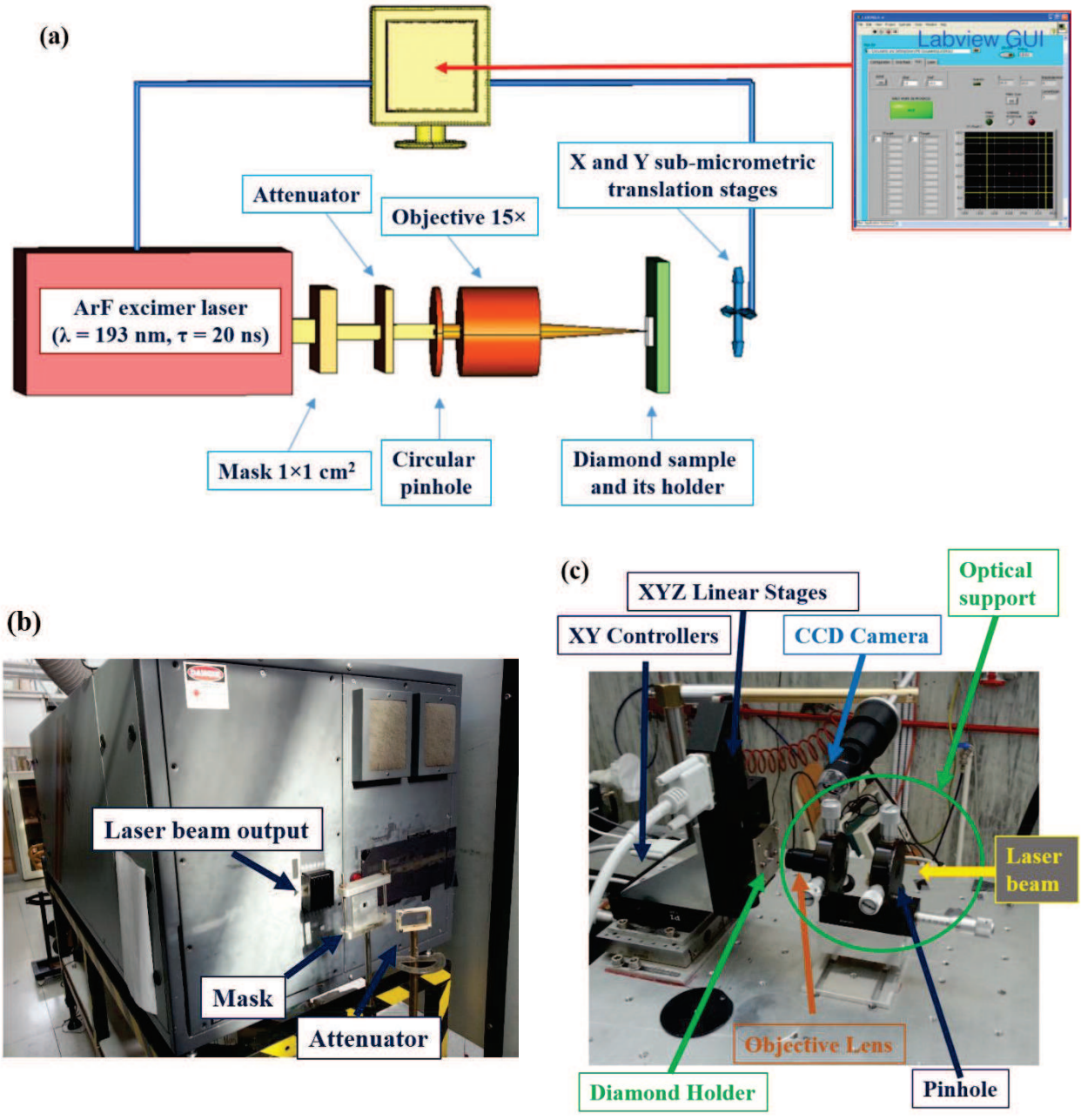

Figure II.2. (a) Scheme of the experimental set-up of laser-induced diamond graphitization process. In the top-right corner a picture of the LabVIEW interface to control remotely the laser and the translation stages is shown. Pictures of (b) the excimer laser and (c) the optical and sample translation system at L3.

The laser source

In this experimental set-up the radiation source was an excimer laser (light amplification by stimulated emission of radiation), as shown in Figure II.2 (b). This device is a molecular laser

involving transitions between two electronic states and allows using opportune gas mixtures as active medium. For example, the mixture can be composed of one rare gas (such as Ar, Kr, Xe) and of atoms of one halogen element (such as F, Cl). In particular, for these kinds of atoms, the molecular state can exist only in the excited one (excimer) as the fundamental state proves to be repulsive. As a consequence, the fundamental state is always empty and leads to population inversion between levels involved by the transition, which is the necessary condition to operate with an excimer laser.

Accordingly, the laser source used to irradiate diamond sample surfaces is a pulsed excimer laser, model LPX305i from the company Lambda Physik, which is interfaced with a computer for the control of the functions. The laser was used with an active mixture of ArF, which is characterized by a wavelength of 193 nm (deep UV) and a pulse duration of 20 ns. The beam maximum energy is about 500 mJ per pulse and the pulse frequency operation was 10 Hz.

The optical system, the translation stages and software

When the laser radiation is emitted, the beam crosses a 1 × 1 cm^2 rectangular aperture named mask and an energy attenuator to modify the beam size and its energy (Figure II.2 (c)). Then, the laser radiation crosses an additional circular pinhole with variable aperture to reduce arbitrarily the beam size. Finally, the beam is focused by a 15× UV objective lens on the diamond surface. The diamond and its holder were fixed on two sub-micrometric motorized translation stages for the movement in the X–Y plane perpendicular to the beam direction with a sub-micrometric resolution (0.1 μm). A third stage in parallel direction of the laser radiation (Z-axes) allowed the manual focusing of the beam on the diamond surface.

Considering the know-how gained in my master thesis during which I worked with the same laser on the diamond graphitization process, at the beginning of my PhD I was entrusted to choose new mechanical components to host the optical lens, which proves to be more efficient in terms of stability, compactness and having more degrees of freedom to modify the pinhole aperture. This components are shown in the “optical support” group in the Figure II.2 (c). Moreover, the diamond holder was home-made taking into account the special sample dimensions (Figure II.1 (b)). In addition, during my PhD I implemented a software in LabVIEW to synchronize the laser shooting with the two controllers of the bi-dimensional diamond-stage displacements, and to control all of them remotely. This software allowed for the first time at L3 fabricating systematic bi-dimensional graphitic structures on diamond surface with great reliability and reproducibility (Figure II.2 (a)). Finally, a CCD camera was used to monitor the graphitization process, take pictures and register short movies (Figure II.2 (c)).

II.3 HPHT substrate preparation before the growth

The CVD monocrystalline diamond growth was performed by homo-epitaxy on commercial (100) orientated Ib HPHT diamond substrates provided by Sumitomo company [204]. The Ib diamonds owns a nitrogen impurity concentration close to 10^{19} atom.cm^{-3} (1 ppm) and have a dimension of $3 \times 3 \times 1.5$ mm^3. The quality of the substrates is crucial for the growing CVD diamond of high quality, and some pre-treatments are required. For example, in order to remove any impurities on the substrate surface and to avoid the generation of defects during growth process, the samples were chemically treated according to a multi-step protocol. Subsequently, the substrates were etched in situ by an H_2/O_2 plasma. These preliminary steps are reported in the following paragraphs.

II.3.1 Diamond substrate cleaning

Before each diamond deposition, the HPHT diamond substrates must be cleaned according to the following procedure:

1. Water cleaning (t = 60 minutes, T = 140 °C): solution composed of 9 ml for the HCl (37%) and 3 ml for the HNO_3 (65%). This step must be carried out in particular safety conditions (gloves, glasses, blouse and under suction hood);
2. Cleaning steps with distilled water (two baths);
3. Ultrasonic bath in acetone (t = 10 min @ RT);
4. Ultrasonic bath in isopropanol (t = 10 min @ RT).

The first cleaning allows dissolving metal particle residues of the catalyst materials during the HPHT growth (Co and/or Ni). The subsequent distilled water baths make it possible to clean the acid remaining on the sample surface. Finally, the acetone bath degreases the sample surface while the isopropanol bath completes the cleaning process removing acetone residue.

II.3.2 Choice of the substrate side for the growth process

The HPHT substrate surface on which the CVD diamond will be deposited have to be carefully selected, so as to minimize defects formation and stresses during the growth. However, during the HPHT growth process it is not possible to avoid the formation of different crystallographic planes and therefore, different growth sectors are presents once the HPHT crystal has been sliced. A large difference in impurity concentrations (mainly nitrogen) characterizes these different growth sectors [205] and it is necessary to select the face having the largest mono-sector. In order to determine what

sample side is the most suitable, all the substrates were analysed by the Diamond View™ set-up supplied by GIA Instruments and available at LSPM. This instrumentation allowed observing the luminescence of the sample which is related to the presence of impurities, and therefore it allowed recognising the appropriate face for the diamond deposition. In particular, the samples were irradiated by UV light (230 nm), namely by photons with energy close to that of the diamond bandgap, so as all luminescent centres having an energy lower than the band gap of diamond can be detected. As a result, a homogeneous luminescence image was obtained in the case of a sample with mono-sector side, while an inhomogeneous luminescence picture was produced for a sample with different growth sectors in the same face. Both cases are shown in the Figure II.3.

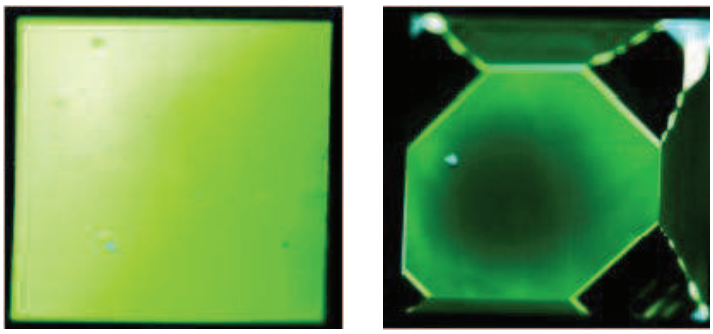

Figure II.3. Luminescence pictures of a HPHT diamond face with a single growth sector (on the left) and with several growth sectors (on the right) taken by Diamond View™.

II.3.3 Surface treatment

The last treatment to perform on the HPHT diamond substrate before starting the homo-epitaxial growth process is a plasma etching with a gas mixture of H_2/O_2 (with 2% of oxygen) during 90 minutes [206]. This step is carried out directly in the growth reactor and makes it possible to remove the hardened layer of the substrate surface. This hardened layer is due to the polishing step and contains a significant amount of impurities and defects, which have to be removed [207, 208].

II.4 Reactors for CVD intrinsic and boron doped diamond growth

All the monocrystalline diamond films used during this work, both intrinsic and boron doped, were grown with a Bell Jar (quartz bell deposition chamber) microwave plasma assisted chemical vapor deposition reactors developed at LSPM in collaboration with the company Plassys. The reactor development at LSPM has started since 1990 with the first prototype and it has been improved in the subsequent decades in terms of electromagnetic simulations associated with the development of plasma models that rely on a phenomenological description of hydrogen / methane microwave plasma

chemistry that has been validated experimentally [32, 33, 209-212]. This reactor was promoted in 2007 and it is now commercially available under the designation BJS150. It has allowed reliably developing thick diamond films of very high crystalline purity or with very high boron doping level [94, 213]. Its design also makes it possible to ensure good sealing with high vacuum conditions (of the order of 10^{-7} mbar), thus limiting the incorporation of impurities, such as nitrogen, during growth process.

Nowadays, at LSPM two BJS150 reactors are available, which are dedicated to the growth of intrinsic and boron doped diamond films. The reactors are shown in Figure II.4.

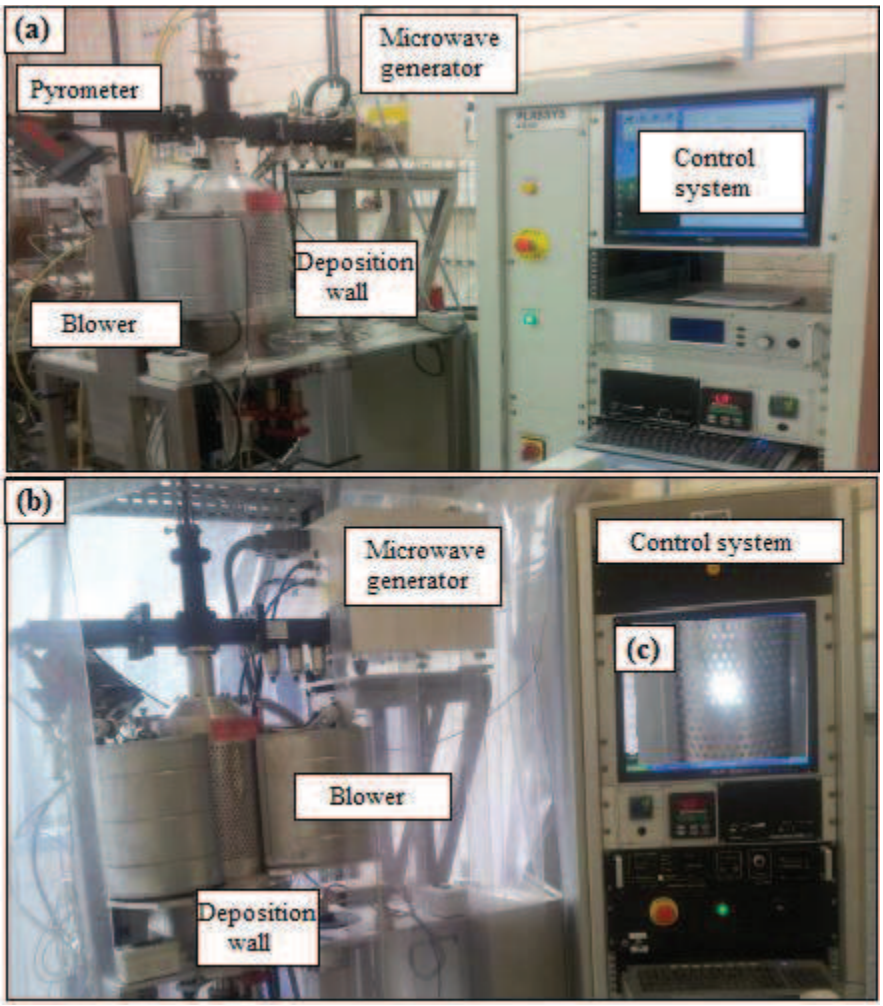

Figure II.4. Pictures of the BJS150 reactors (a) dedicated to the intrinsic diamonds, (b) dedicated to boron-doped diamonds and (c) deposition plasma (LSPM).

Each reactor is equipped with a cooled substrate holder of 2 inches in diameter, which allows decoupling the substrate temperature from the plasma characteristics (pressure, power). The substrate holder can be vertically translated during the process allowing carefully adjusting the position between the substrate and the plasma. It is also very easily accessible thanks to an electric actuator allowing the opening of the reactor by the lower flange, making particularly comfortable the loading

and unloading operations, as well as the steps of preparation and cleaning of the substrate holder. A scheme illustrating the different elements of the reactors is reported in Figure II.5.

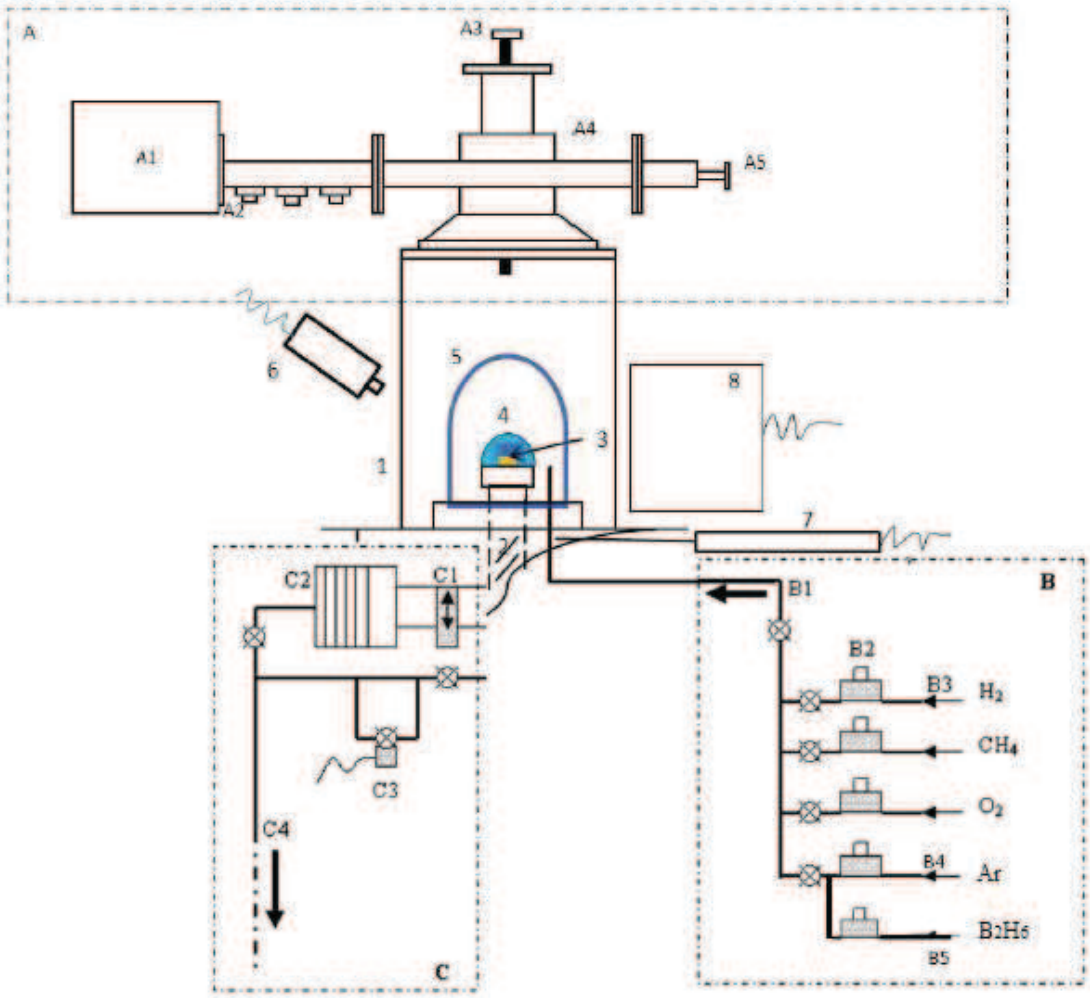

1. Resonant aluminum cavity
2. Water-cooled and height-adjustable sample holder
3. Diamond substrate
4. Plasma
5. Quartz bell
6. Dichromatic pyrometer
7. Pressure gauges (capacitive + Pirani)
8. Blower (cooling of the bell)

A microwave coupling device
A1. 2.45 GHz magnetron head powered by a pulsed generator (Sairem 6kW)
A2. Impedance adapters
A3. Water cooled coupling antenna
A4. Wave Guide
A5. Piston of short circuit

B. Gas panel
B1. Access of gases by pneumatic valves
B2. Mass flow meters
B3. Hydrogen purified by a palladium diffuser
B4. Argon gas
B5. Diborane gas

C. Pumping system
C1. Drawer valve
C2. Turbomolecular pump
C3. Pressure control by solenoid valve
C4. Primary pump by dry spiral pump

Figure II.5. Diagram of the metal cavity deposit reactor and list of the various elements that compose it.

The microwave generator (2.45 GHz) is used to activate the gas phase and it can produce a maximum power of 6 kW. Thanks to a computerized system, the generator can work either in continuous mode (from 10 to 100% of its power) or in pulsed mode (from 10 to 100% of its power) up to 1000 Hz.

During the growth processes the gas mixture is composed of H_2, CH_4 and O_2 for intrinsic diamonds, while in the case of boron doped films, diborane gas (B_2H_6) is added. The gas concentrations with the corresponding growth experimental parameters for intrinsic and doped samples are reported in more details in the Chapter IV.

II.5 Ion implantation machine

The ion implantation instrumentation was also a home-made machine built modifying a standard implantation system. The aim of using this modified instrumentation was to eject light ions towards diamond samples with a low acceleration energy, in order to induce a graphitic layer just underneath the diamond surface. This graphitic layer produced before the metallic contact deposition, was expected to improve the electrode electrical performance.

The main experimental parameters were the ion source, in addition to the applied current and the implantation time which determined the ion dose, and the voltage accelerating the ion beam which affected the penetration depth. During this work it has been developed a useful recipe to induce diamond amorphization just underneath the sample surface: helium source, with a current of 300 μA and a voltage of 10 keV, for an implantation process with a 30 s duration. The implantation treatments were performed at room temperature and under secondary vacuum conditions.

After the ion implantation process, annealing treatments were carried out in order to allow the transition of the amorphous diamond into graphite [214]. The experimental conditions were: T = 1000 °C, t = 60 minutes, vacuum of 10^{-6} mbar.

II.6 Micro-fabrications instrumentations

II.6.1 Evaporator

In order to produce metallic contacts on the boron doped diamond surfaces, a stack of titanium / gold layers was deposited by an electronic-beam evaporator which is schematized in Figure II.6 (a). Several samples can be placed and fixed on the holder on the top of the chamber. The holder is rotated by 180° once the processing starts and can be cooled by a liquid nitrogen system. The top and the bottom of the evaporator chamber are separated by a valve. On the bottom the crucibles are placed with the metals to deposit. An electron beam bombards the metal inducing a local heating. When the metal melting temperature is reached, the evaporation of metallic atoms towards the diamond samples occurs. The e-beam evaporator used for this work was the MEB 550S model provided by company

Plassys and available at the clean room of the University of Paris Diderot (Figure II.6 (b)). For this thesis, the titanium / gold bilayer was chosen [5, 121]. The metallic layer thicknesses were 50 nm and 200 nm for Ti and Au respectively, with a deposition rate of 0.1 and 0.3 nm/s, respectively.

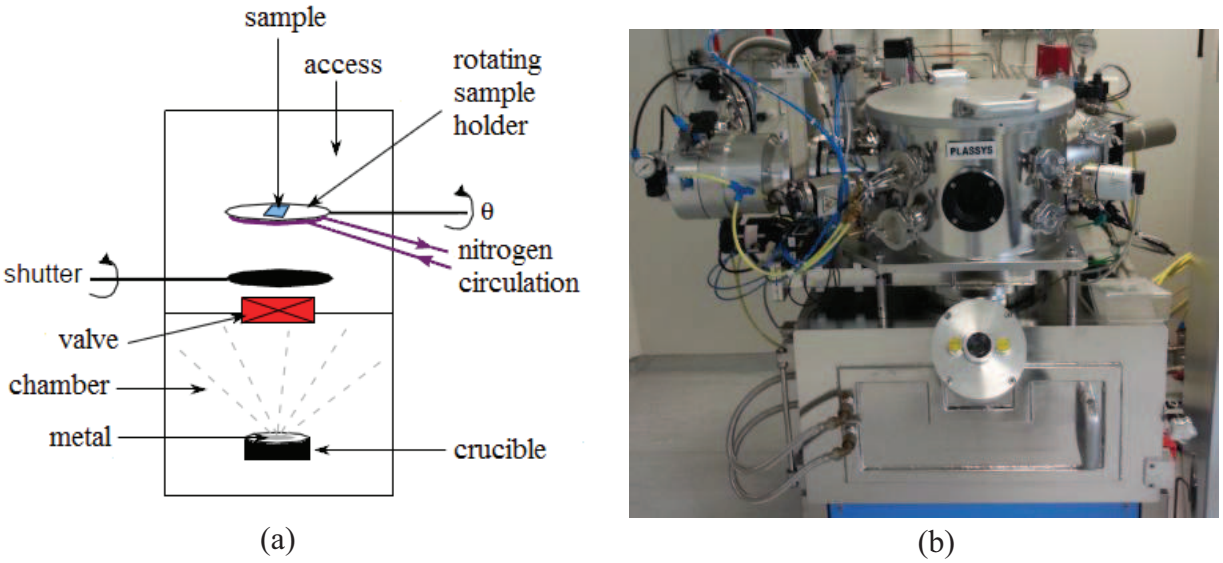

Figure II.6. (a) Scheme of the e-beam evaporator for the metallic depositions. (b) Picture of the evaporator available at the University of Paris Diderot.

Finally, in order to improve the mechanical adhesion between the titanium layer and the diamond surface, a short Ar^+ etching treatment was carried out before all metallic deposition (Ar = 9 sccm, t = 120 s).

Once the metallic pad micro-fabrication was completed, an annealing treatment for the titanium carbide formation was performed in a standard furnace at T = 500 °C [5, 132], for 60 min under secondary vacuum conditions.

II.6.2 PECVD

Plasma enhanced chemical vapor deposition (PECVD) is a chemical vapor deposition process used to deposit thin films from a gas state (vapor) to a solid state on a substrate. Chemical reactions are involved in the process, which occur after creation of a plasma of the reacting gases. The plasma is generally created in the space between two parallel electrodes (a grounded electrode and an RF (radio frequency) energized electrode). A precursor gas mixture is introduced in the reactor and the capacitive coupling between the two electrodes excites the reactant gases into a plasma. This plasma creates reactive and energetic species by collision resulting in the reaction product being deposited on the substrate (Figure II.7 (a)). The other products of the reactions are then pumped away by a pumping system.

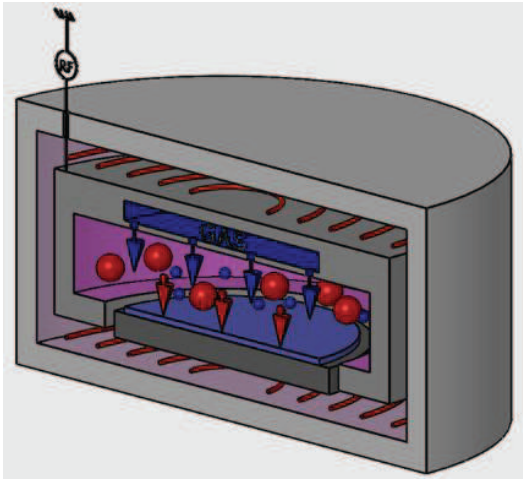

(a)

(b)

Figure II.7. (a) Scheme of a PECVD system used for the dioxide silicon deposition. Picture of the PECVD available at the University of Paris Diderot.

For this work, a commercial Corial D250 PECVD system was used to deposit silicon dioxide (SiO_2) on diamond substrates used as a masking material. This instrumentation was available at the clean room of the University of Paris Diderot (Figure II.7 (b)).

A lot of samples could be processed in the same time and in a very short time. The silica films were 2 µm thick, deposited with a rate of 0.4 µm/min. The deposition parameters were:

- Substrate temperature: 280 °C
- Working pressure: 11000 mTorr
- SiH_4: 40 sccm
- N_2O: 10000 sccm
- Ar: 500 sccm
- RF: 120 W

II.6.3 Reactive Ion Etching (RIE) using Inductively Coupled Plasma (ICP) set-up

The reactive ion etching (RIE) is a chemical etching enhanced by ion bombardment, which takes advantage of both physical and chemical etching mechanisms. The physical mechanism is due to the heavy charged species present in a plasma, which are accelerated by the electric field. These species bombard the sample surface sputtering its atoms. This mechanism is dominant at low pressure due to

the decrease of collisions in the chamber. It produces an anisotropic etching with, overall, low etching rate and selectivity. There is also a chemical etching related to radicals, neutral reactive species which produce volatile species. The chemical nature of the gas mixture is chosen to react spontaneously with the etched target material. This mechanism proves to be dominant at high pressure giving rise to an isotropic etching. Here, the etching rate and the selectivity are higher than physical process. The RIE technique combines each advantages of these two mechanisms and permits to have a best selectivity, a higher etching rate and anisotropic etching. In this thesis, RIE has been performed using an ICP machine which is now an equipment largely used for etching different materials.

In Figure II.8 a scheme and a picture of the instrumentation available at the University of Paris 13 are shown.

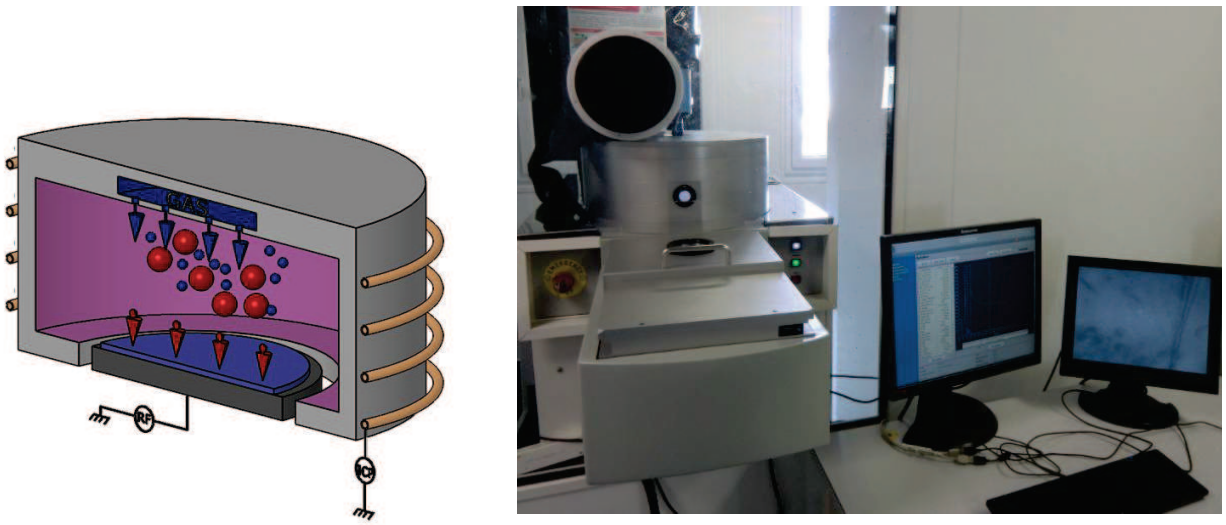

(a) (b)

Figure II.8. (a) Scheme of a ICP-RIE system used for the plasma etching treatments on diamond, silica and titanium materials. (b) Picture of the ICP-RIE instrumentation available at the clean room of the University of Paris 13.

The plasma is generated by an inductive coupling with a radiofrequency (RF) generator. The inductance generates an alternative RF magnetic field and induces RF electric fields. This electric filed increases the electron energy leading to the ionization of the gas molecules and atoms. The generator power increases electronic density and consequently the ions and reactive species density. The auxiliary RF power controls the bias voltage so as the energy and the ion flux.

The use of ICP-RIE leads to several advantages, such as the generation of a higher plasma density at lower working pressure than the classical CCP system (Capacitively Coupled Plasma), and the possibility to control the plasma density and the ion bombardment in an independent way. Moreover, the etching rate and selectivity parameters are, overall, higher than for CCP systems.

The ICP instrumentation was a commercial ICP 200IL provided by the Corial company.

This system is composed of:

- an aluminum chamber where a secondary vacuum is performed by turbomolecular and a dry primary pump. An load lock useful to locate the samples without bringing the chamber at room pressure;
- different available gases: Cl_2, BCl_3, C_2H_4, H_2, CHF_3, O_2 and Ar;
- a helical antenna supplied with a 1000 W maximum power and 2MHz radiofrequency generator;
- a 200 mm diameter polarization cathode supplied by a 300W maximum power and 13.56 MHz radiofrequency generator. The cathode is cooled by water and helium circuits;
- an in-situ etching thickness measurement by 672 nm wavelength laser interferometer.

The etching recipes developed during this thesis were reported in Table II.1 and will be discussed in more details in Chapter IV:

Table. II.1. Working pressure (w.p.), gas concentrations, generator power and etching rates used during the ICP etching treatments for diamond, silica, titanium and residual photoresist.

Material	w.p. (mTorr)	O_2 (sccm)	CHF_3 (sccm)	Cl_2 (sccm)	Ar (sccm)	LF power (W)	RF power (W)	Etching Rate
Diamond	3	97	3	-	-	500	280	0.5 µm/min
Silica	3	3	30	-	-	400	150	0.3 µm/min
Titanium	2	-	-	50	5	200	70	1.8 nm/s
Photoresist	50	20	-	-	-	0	110	-

II.6.4 Other technological steps

Optical lithography

During the micro-fabrication technological steps, photolithography processes were performed in order to transfer the mesa and TLM shapes on the CVD boron doped diamond sample surfaces. The mesa and TLM patterns for the contacts will widely described in the Chapter IV. The instrumentation used for this work was an UV400 band spectra mask aligner (MJB4) provided by the SUSS MicroTec company equipped with HgXE 500 W UV lamp used at a measured optical power of 17 $mW.cm^{-2}$ for an electric power of 355 W.

In order to transfer the desired shape on the samples, photoresist is deposited with spin-coater devices. In particular, negative photoresist was coated and structured for the mesa pattern and positive photoresist was used for the TLM pattern. The experimental parameters are summarized in the Table II.2.

Table. II.2. Experimental parameters of the photoresist coating and photolithographic steps.

Pattern	Photoresist	Coating	Pre-bake exposure	Flood exposure	Development	Post-bake	Thickness (µm)
Mesa	AZ5214	2000 rpm, 30 s	45 mJ	400 mJ	AZ726 MIF, 40 s	80 °C, 10 min	1.8
TLM	AZ1518	5000 rpm, 30 s	150 mJ	-	AZ726, 20 s	80 °C, 30 min	2

The profile of the samples during the micro-fabrication steps were investigated by a stylus profilometer of Alpha step IQ provided by company Kla Tencor type.

Chemical etching of gold

The gold etching was performed using a chemical treatment with potassium iodide solution heated at 50 °C, with an etching rate of about 7.5 nm/s.

Vacuum ultraviolet (VUV)-light irradiation for ozone treatment

In order to change the hydrogen diamond terminations into oxygen ones as it will be discussed in the chapter IV, the samples were exposed to a vacuum ultraviolet (VUV)-light irradiation in oxygen atmosphere [133]. The irradiation source was a monochromatic xenon excimer lamp (wavelength of 172 nm) which leads to the production of ozone in the chamber allowing oxygenated termination at the diamond surface. The oxygen atmosphere pressure was maintained at 2 mbar and the treatment duration was 45 min.

II.7 Characterization techniques

During the work carried out for diamond growth, diamond contacting either by graphitization or metallization, the samples were step by step analyzed and characterized in order to define the diamond contacting protocol. In addition, at the end of the sample manufacturing, final investigations were performed from structural, morphological, compositional, mechanical and electrical points of view. In the following, the experimental set-ups used are presented.

II.7.1 Raman spectroscopy

The Raman spectroscopy constitutes, together with the IR absorption, one of the branches of the vibrational spectroscopy. This technique is based on the radiation-matter interaction between a laser radiation and the sample matter. Indeed, thanks to the incident laser excitation, it is possible to induce

molecular and crystalline lattice vibrations in the material and then to collect the scattered radiations, useful to investigate the composition, the bonding and the crystalline structure of the material. In particular, this technique is very utilized to study carbon materials as it allows obtaining very important information about the samples, like the quality of the crystal, the presence of impurities, the kind of carbon bonding (for example graphite or diamond) and in qualitative way the doping level. In addition, this technique presents the great advantage to be not destructive.

The Raman spectroscopy foresees that a monochromatic electromagnetic radiation with a wavelength typically in the Visible range or in the near IR or UV hitting the sample matter causes a vibrational movement of the molecules, which can lead to the absorption or to the scattering of the photons depending on the radiation frequency ν_0. If the photon has an energy equal to the molecule vibrational energy $h\nu_0 = h\nu_{vibrational}$, it is absorbed inducing a change of dipole moment of the molecule. On the contrary, when the photon energy is much higher than vibrational energy of the molecule $h\nu_0 >> h\nu_{vibrational}$, the photon scattering process becomes dominant and the molecule polarization occurs. In this last case, under the effect of the electromagnetic field, the scattered photons can disturb the electronic cloud (which implies a change in the molecule polarizability), which leads to the transition of the molecular system into a virtual level of excitation. There are three types of scattering process presented in the following and illustrated in the Figure II.9:

- The Rayleigh scattering: the elastic scattering without energy (and frequency) change. During this process, the incident photon induces a vibrational state transition of the molecule in to a virtual state, and the molecule, after the de-excitation of energy $h\nu_{Raylegh} = h\nu_0$, comes back in the original state;
- The Stokes Raman scattering: the first type of inelastic scattering. In this case, the material absorbs a part of the photon energy and after the de-excitation of energy $h\nu_{StokesRaman} = h\nu_0 - h\nu_{vibrational}$, the dis-excited state corresponds to the level $(\nu+\Delta\nu)$;
- The anti-Stokes Raman scattering: the second type of inelastic scattering. In this case, the material gives energy to the photon, and after the de-excitation of energy $h\nu_{Anti\text{-}StokesRaman} = h\nu_0 + h\nu_{vibrational}$, the dis-excited state corresponds to the level $(\nu-\Delta\nu)$.

Accordingly, the detection of the inelastic scattered light allows having access to the absorption or to the emission of photons at a particular wavelength which is characteristic of the studied material. At room temperature, the molecules that populate the first excited vibrational level are less numerous than the ones that populate the fundamental energetic state therefore, the photon absorption process is less likely than the emission one and, as a consequence, the anti-Stokes signals are weaker than the

Stokes one. However, even if the Stokes scattering is 10^7 times lower than Rayleigh one, the Stokes Raman scattering process proves to be particularly suited for diamond characterization [177].

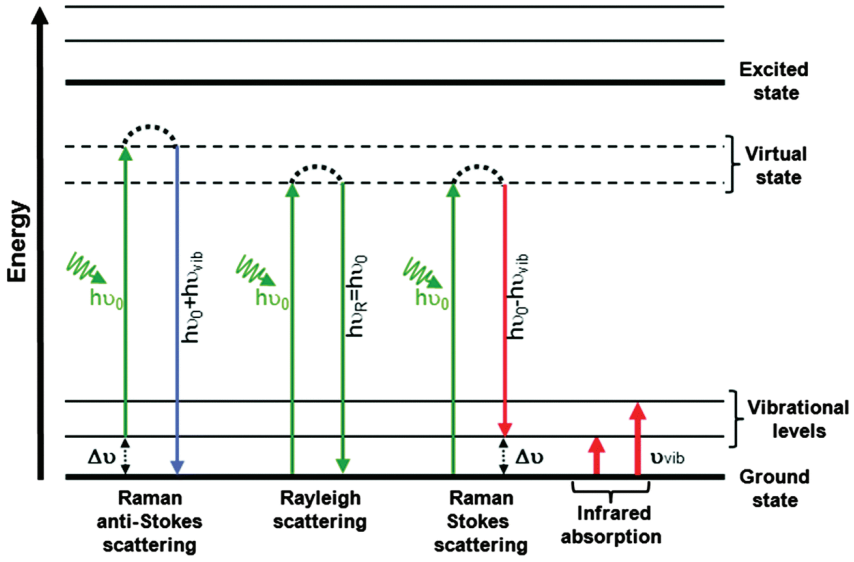

Figure II.9. Scheme of molecular vibrational transitions involved by the interaction radiation-matter.

For completeness, it is reported that often, a Raman spectrum is composed of broad bands overlapping the Raman signals during the data acquisition phase. These bands are related to the fluorescence process in the sample, which is also called photoluminescence (PL). In order to eliminate a good part of this effect, it is possible to use a laser radiation with low energy, for example in the red colour or near IR, which cannot cause the electron transitions responsible of fluorescence in the visible range [215].

During this thesis work, Raman analyses were performed for both experiments. In particular, for diamond graphitized by laser (Italy), the investigations were carried out in collaboration with the Department of Chemistry, Materials and Chemical Engineering of the Polytechnic of Milan (Italy). The machine was a Jobin Yvon Labram HR800 Raman spectrometer equipped with an Olympus BX41 microscope and an X–Y computer controlled moving stage (1 µm of spatial resolution). The spectra were recorded using the 514.5 nm exciting line of an Ar^+ laser (20 mW). The laser beam was focused on the samples by a 50× objective. For the as-grown, ion implanted, and annealed diamond (France), the Raman investigations were also performed with a Jobin-Yvon HR800 spectrometer equipped with two motorized stages for bi-dimensional displacements and available at the LSPM. Several wavelengths were available but for these experiments, all the spectra were recorded using the 623.8 nm exciting line of a He/Ne laser, with a focusing 100× objective lens. For both experimental set-up, the laser spot diameter was approximately few µm, and each spectrum was obtained as the average of four acquisitions.

The experimental set-up used at LSPM is reported in Figure II.10.

Figure II.10. Picture of the Raman spectrometer available at LSPM.

Raman peaks for graphitized and boron doped diamonds

The most important Raman signal for a CVD diamond film or crystal is the well defined and sharp peak centred at 1332.5 cm^{-1}, which is characteristic of an undisturbed carbon structure bound by sp^3 covalent bonds. The Raman peak characteristic of graphitic materials is the G peak, which has a wide band shape centred at 1580 cm^{-1}. For graphitized diamonds, the ratio of the intensities between diamond and G peaks allows getting an estimation of the proportion between these two phases [177, 178]. Typically, in carbonaceous materials the presence of the graphite (G peak) is often accompanied by the presence of other two bands: one around the wave number 1350 cm^{-1}, called disordered graphite D, and the other centred at 2700 cm^{-1} and related to the second order of the previous one, called 2D. All this peaks are related to the carbon structure bound of sp^2 type. It is worth specifying that also not graphitized diamond can present graphitic components, for example in the case of undesired defects get during the diamond growth process. Nowadays, the Raman investigations are widely used to characterize diamond graphitization process [14, 178, 183, 216, 217].

The Raman spectroscopy can also permit a qualitative estimation of the doping level for doped diamonds, in particular boron impurities in the case of this work. When diamond is boron doped, the main effect is that the diamond peak initially present at 1332.5 cm^{-1} shifts towards the shorter wavelengths with, at the same time, a decrease of its intensity [218]. This shift is also accompanied by a deformation on one of the two peak sides depending on the excitation wavelength used. This phenomenon is called Fano effect and it is expected mainly for heavy doping [219, 220]. Other signals can be attributed to the boron presence, in particular bands at 1000 cm^{-1} and 1225 cm^{-1} as well as a

band at 500 cm^{-1} which is generally observed when the doping becomes very strong (> 10^{20} cm^{-3}) [221].

II.7.2 Scanning electron microscopy

The scanning electron microscopy (SEM) is a kind of electronic microscopy developed to observe materials on the micro- and nano-scales, with a magnification much higher than the one obtained by an optical microscope. The working principle of an electronic microscope is based on the usage of a focused electron beam (beam diameter of the order of tens Å) which is sent on the sample surface by electromagnetic lens capable of directing the beam. By bi-dimensional scanning on the sample surface, it is possible to get a bi-dimensional magnified image of the surface with morphological details, holes, bumps, and roughness. A vacuum system is necessary to avoid the losing of electron energy by scattering process between electrons and environment molecules (typically the high vacuum is around 10^{-7} and 10^{-8} mbar).

The products of the electron beam-sample interaction are summarized in the following and illustrated in the Figure II.11:

- Secondary Electrons (SE) characterized by a low level of energy (between 0 and 50 eV);
- Backscattered Electrons (BE) characterized by a high level of energy, which is comparable to the primary electron one (few keV). The probability of the BE emission increase with the atomic number of the investigated material;
- Auger electrons with energy of hundreds of eV. Their emission prove to be very low;
- X-Rays;
- Radiations in UV, Visible and IR ranges.

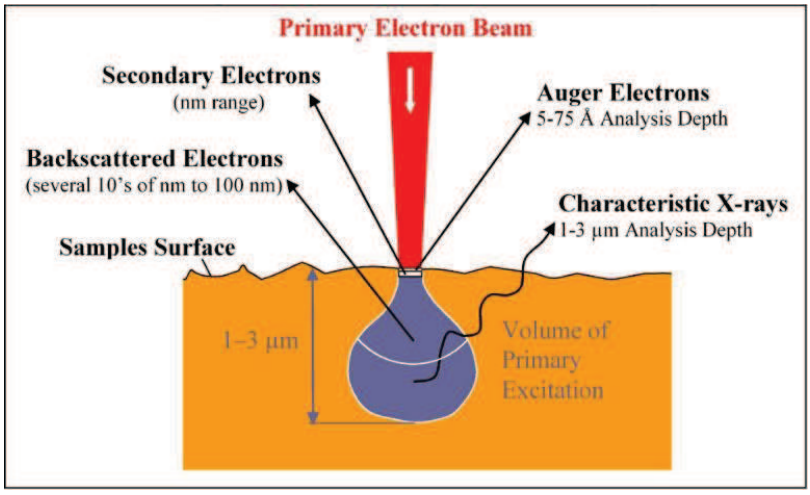

Figure II.11. Scheme of the products of the electron beam-sample surface primary interaction.

The most interesting signals for SEM analysis are given by secondary electrons and backscattered ones. In particular, the SE collected and detected by the microscope detection system are only related to the layers very close to the surface, due to the low level of their energy. The detectable SE are originated within a few nanometres from the sample surface and they are ejected from the bound electronic shells of the specimen atoms by inelastic scattering interactions with beam electrons. Characteristic X-rays may be produced when inner-shell ionization occurs (see Figure II.12). On the contrary, the BE, which have energy higher than 50 eV, are produced during the interaction of the primary beam with the nuclei of sample atoms and give information about average atomic number of the origin area and about the topography.

This technique proves to be particularly useful to appreciate the laser-induced morphological modifications on diamonds [187, 216, 222].

Energy dispersive X-ray spectroscopy (EDS)

Typically, a SEM microscope is equipped with an X-ray detection system able to perform energy dispersive X-ray spectroscopy. As illustrated in Figure II.12, the electron beam-sample interaction can lead to the emission of X radiation due to the passage of an electron from the excited state to the fundamental state by a non-radiative process. In particular, thanks to the excitation of an incident electron, an electronic hole can be created and one electron coming from a more external energetic level can fall in, with an X-ray emission. This emitted radiation represents a peculiar characteristic of the energetic level difference involved in the excitation-emission process. Moreover, the X radiation proves to be also uniquely characteristic of the chemical element which gave origin to the emission.

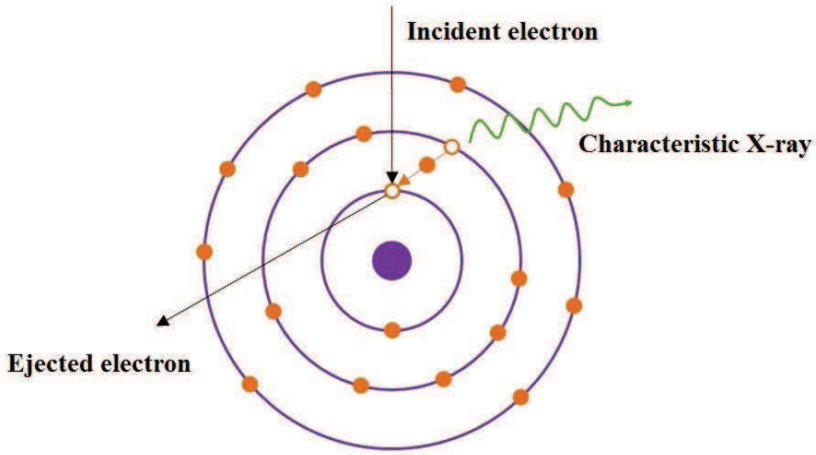

Figure II.12. Schematic representation of the interaction between the beam electron and the sample atom producing an X-rays.

For this thesis work, SEM and EDS analyses were performed in both experiments. In particular, for the experiment carried out in Italy, the investigations were performed in collaboration with the CNR- IMM Institute for Microelectronics and Microsystem of Lecce (Italy) by using a dual beam NVISION40 Focused Ion Beam instrument, equipped with a high-resolution SEM GEMINI column. The instrument was also equipped with an INCA 350 X-Act detector allowing compositional analyses by energy dispersive X-ray spectroscopy (Figure II.13). For the characterization of the diamond samples manufactured in France, a Leica S440 SEM equipped with an XFlash 6 detector for the EDS analyses was available at the LSPM.

Figure II.13. Picture of the SEM microscope at the CNR-IMM Institute for Microelectronics and Microsystem of Lecce (Italy).

II.7.3 Cathodoluminescence spectroscopy

The cathodoluminescence (CL) spectroscopy is considered as a very useful method to characterize monocrystalline diamond films. Indeed, this very sensitive technique makes it possible to estimate the crystalline quality of a diamond film [223, 224] and to quantify the doping level whatever the crystalline orientation [94, 225-227]. CL analyses also make it possible to observe the propagation of dislocations within homoepitaxial films [228]. This technique presents several advantages, such as:

- ✓ It allows generating of a very large number of carriers even in large gap materials due to the high energy of the electron beam compared to photoluminescence;
- ✓ It allows investigating energetic levels present in the forbidden band related to defects or impurities;
- ✓ It makes it possible to quantify impurity atoms actually participating in the doping (namely which are located in substitutional sites), unlike the Secondary Ion Mass Spectrometry which measures all the dopant atoms in the material;

- ✓ It is a non-destructive technique;
- ✓ It allows imaging with good spatial resolution as it is associated with a SEM microscope.

The CL investigations consist in observing the light emissions produced by a sample under the action of an electron beam bombardment of an SEM microscope. In particular, the interaction between an electron beam of several thousands of eV and a semiconductor material can generate electron-hole pairs, giving rise to a locally non-equilibrium state [229]. Then, the equilibrium state is restored by de-excitation phenomena of these excited electronic levels. The de-excitation processes can take place in different ways:

- ➢ Non-radiative transitions (therefore undetectable) for which a large number of phonons with energy kω (lattice vibrations) are produced, resulting in local heating of the sample (Figure II.14 (a));
- ➢ Fundamental radiative de-excitations (band-to-band), (Figure II.14 (b));
- ➢ When intermediate levels (which are related to structural defects or impurities) are present in the band gap, de-excitation can also be radiative via these donor or acceptor levels (Figure II.14 (c));
- ➢ Radiative transitions called excitonic. When the incident electrons collide with the electrons in the valence band (VB), these last are excited in the conduction band (CB). Among the created electron-hole pairs, some of them may undergo Coulomb interacts giving rise to recombination phenomena. These recombinations lead to the formation of a new state or level called "exciton" (Figure II.14 (d)). In this case, the recombination is defined as intrinsic excitonic recombination (“free exciton”, labelled FE). The involved energy is about few meV and everything occurs as if the electron emitted from the VB was in a level of energy Ex very slightly lower than the energy of the conduction band (in the case of diamond Ex = 80 meV). In a doped semiconductor, another recombination can also be carried out via localized states created in the forbidden band by the dopant. In this case, the recombination is defined as extrinsic excitonic recombination (“bound exciton”, indicated BE). Therefore the excitons have, in addition to their binding energy Ex, a localization energy Eb which is the binding energy between the impurity and the free exciton.

Al these possibilities are summarized in the Figure II.14. The theoretical principle explained above is very simplistic because, several semiconductor materials such as silicon, germanium and diamond have a so-called indirect band gap. This means that in the band diagram, with the energy E as a function of the k momentum of the electron, the bottom of the conduction band is shifted with respect to the top of the valence band along the axis of the moments (see Figure II.15).

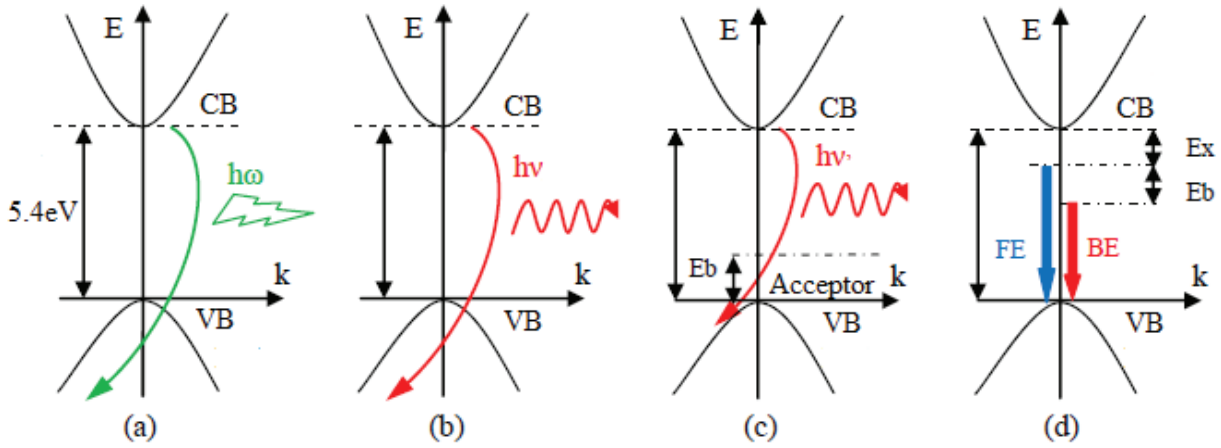

Figure II.14. Scheme of the de-excitation processes after the interaction electron beam – matter (sample) of an electron from the CB to a hole in the VB crossing the bandgap of a semiconductor. (a) Non-radiative transition with phonon production, (b) band to band direct radiative transition, (c) radiative transition via a localized acceptor level, (d) free and bounded excitonic radiative transitions.

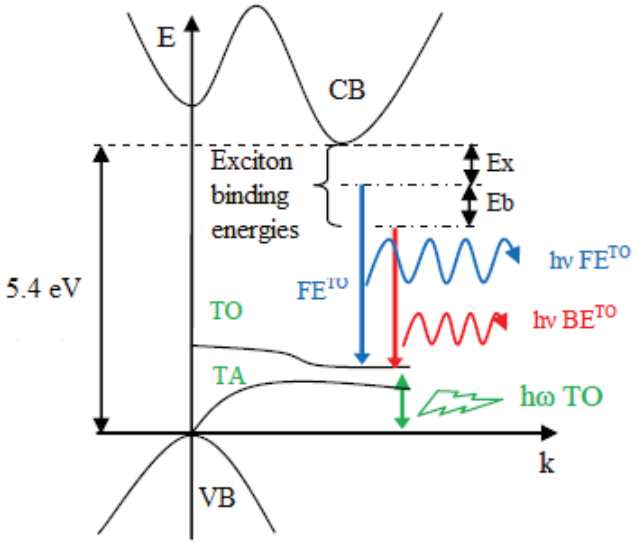

Figure II.15. Scheme of the free exciton (FE) and bound exciton (BE) recombinations through the indirect diamond band gap assisted by a TO phonon. Ex, Eb and hω indicate the exciton binding energy, the impurity – free exciton binding energy and the phonon energy of the momentum conservation, respectively.

Therefore, for diamond materials, there is no probability of obtaining the direct band-to-band transition presented in case (b) of Figure II.14. In order to preserve the momentum of the electron, the transition must be done via two different steps: the emission of a photon which provides almost all the energy, while the required momentum is brought by the production of a phonon (lattice vibration). The energy of this phonon (of few meV) is low as compared to the radiative emission in the case of diamond. The recombination of these free excitons through the forbidden band, thus finally generates a luminous emission of energy (E) close to that of the band gap (BGE) which is given by the following formula: BGE - Ex - hω. Excitons can also be localized in donor and acceptor levels of the material such as those created by phosphorus or boron impurities in diamonds. The energy of the

photon is given by the formula: BGE - Ex - Eb - hω. These bound excitons can be observed in the energy region close to the forbidden band when the material is of high quality [230].

There are also various types of phonons according to the vibration of the considered lattice [229]. Briefly we distinguish the optical and acoustic phonons according to the involved oscillations. In addition, depending on the propagation direction in the crystal lattice, the optical and acoustic phonons may be "transverse" or "longitudinal". Therefore, the CL spectra near the BGE region contain of a lot of data which allow determining the nature and quantity of the impurities (doping), in addition to the quality of a diamond single crystal. Definitely, a high exciton-related light intensity in this area indicates the good crystalline quality of diamond.

In Chapter IV, CL spectra recorded on CVD monocrystalline boron doped diamonds for different doping levels will be reported and will be commented in order to produce reference spectra for the quantitative analyses of the boron concentrations obtained in the CVD doped samples grown in this work.

CL investigations were performed by using the microscopes ZEISS EVO MA-15 (with a LaB6 filament) coupled with a Horiba-Jobin-Yvon cathodoluminescence system available at LSPM. The experimental parameters were: beam current of 20 nA, electron acceleration of 10 keV and measurement temperature of 110 K thanks to a cooling system based on liquid nitrogen. A picture of the CL instrumentation is shown in Figure II.16.

FigureII.16. Picture of the CL spectrometer available at LSPM. In the bottom of this image it is possible to see a bottle of liquid nitrogen which allowed of investigated the sample at the temperature of 110 K.

II.7.4 Nano-indentation analyses

In the diamond contacting experiment by laser-induced graphitization, a study of the mechanical property change of diamond samples before and after the laser treatments was performed by indentation analyses. The basic idea of the indentation investigations is to press opportunely the sample with a load, by a special tip, and to measure the deformation induced on the sample (which can be plastic or elastic). Up today, one of the most important method utilized to perform indentation measurements on nanoscale is the Oliver and Pharr's one. This method is based on the measurement of the penetration depth when a slowly increasing load is applied on a tip [231]. Specifically, for this thesis work, the unirradiated and graphitized sample hardness and their reduced elastic modulus were measured following this method, so as to investigate the laser treatment impact on diamond surfaces in terms of both hardness and carbon atom bonding, respectively. The nano-indentation investigations were performed in collaboration with the Department of Physics, Chemistry and Biology (IFM) at Linköping University in Sweden by using a triboindenter TI950 (provided by company Hysitron) working with a Berkovich diamond probe at room temperature and 40% relative humidity. The penetration depth of the indenter on the graphitized diamond surfaces was limited to 15 nm (< 10% of the possible total thickness [180]) to avoid any effect from the substrates. Hardness and reduced elastic modulus maps were performed with multiple indents in 10 × 120 μm^2 areas to analyze the variations of mechanical properties on the irradiated zones. The triboindenter is shown in the Figure II.17.

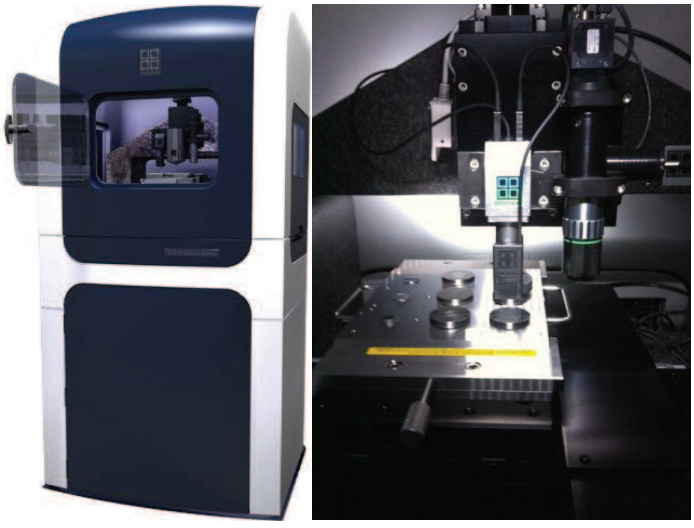

Figure II.17. Picture of the triboindenter used for the nano-indentation analyses carried out in collaboration with the IFM Institute, at Linköping University in Sweden.

II.7.5 Current-voltage measurements

Several electrical characterizations were performed during this work. In particular, for the diamond graphitization experiment (Italy), once graphitic contacts were produced, extensive current-voltage analyses were carried out on a transmission line model (TLM) method (by two probes) [232] to verify the conduction property with focus on the ohmic electrical behavior. In addition to estimate the laser-induced graphite resistivity, the diamond resistivity and the electrical insulation between adjacent contacts have been measured. For the diamond growth and contacting experiments (France), the metallic contact electrical behavior and their specific contact resistance were also investigated by TLM method, for different boron doping level and with or without an intermedium graphitic layer underneath the CVD film surfaces. In addition, the study on the impact of the boron doping on the diamond surface electrical conduction was performed by current-voltage measurements using the "four-point probe method" on the as-grown CVD films [233, 234]. This method was applied also to characterize the sheet resistivity of a CVD intrinsic sample before and after the ion implanted-induced graphitization.

The instrumentations used for the two experiments are described in the following.
For the laser-induced graphitized diamonds the current-voltage measurements were performed in collaboration with the CNR Nanotec Institute at Lecce (Italy). The instrumentation was composed of a probe station with two probes with tungsten tips of 40 μm in diameter moved by two micromanipulators and a LabVIEW software to control a Yokogawa 7651 programmable DC source, a SR570 low noise current preamplifier and a HP34410 digital multimeter.
For the ion implanted / metallized diamonds the I-V investigations were carried out in collaboration with the TELEM team at the University of Paris Diderot. The instrumentation was composed of a probe station with two probes and micromanipulators, a LabVIEW software to control a Yokogawa 7651 programmable DC source and a Femto Amp DLCPA-200 amplifier.

In Figure II.18 a picture taken during I-V measurements by two probes on a metallized CVD boron doped diamond is shown.

Finally, the current-voltage measurements of CVD boron doped film surfaces, in addition to the ion implanted ones, were carried out at the LSPM. The instrumentation used for these measurements was a model 4200-SCS provided by Keithley, equipped with four-point collinear probes with a space in between of 1 mm. The external probes allowed applying the current while the internal ones measuring the produced difference of potential. The imposed current was adjusted according to the resistance of the characterized material.

All the corresponding equations used by the TLM and four-point probe methods are presented and discussed in the corresponding section of the Chapter III and IV.

In Figure II.19 a scheme of the I-V measurement by four-point probes and a picture taken on a diamond sample under the electrical investigations are reported.

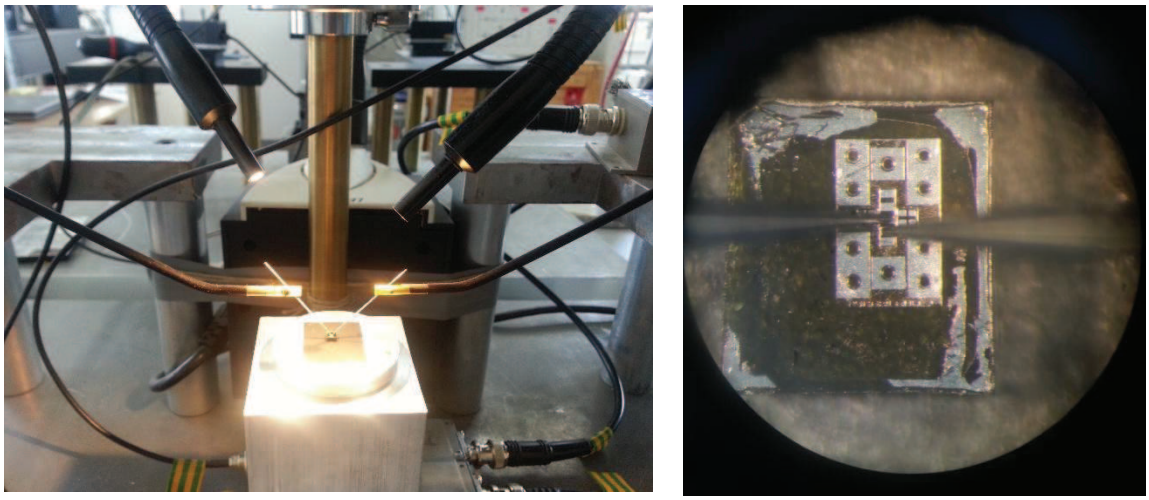

(a) (b)

Figure II.18. (a) Picture taken during the contact probe - metallic pads on a CVD monocrystalline boron doped diamond during the current-voltage measurements by TLM method at the University of Paris Diderot and (b) its enlargement focused on the sample.

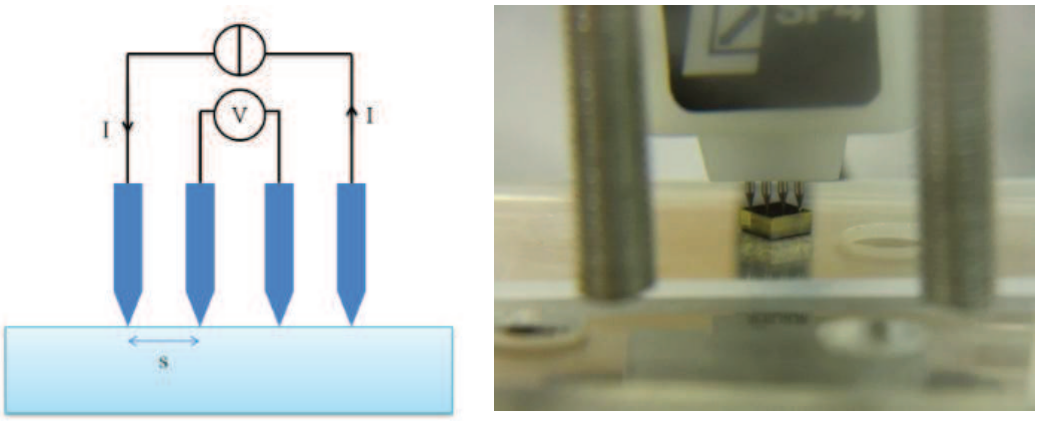

(a) (b)

Figure II.19. (a) Scheme of the I-V four probe instrumentation, where it is possible to apply current I on a sample and measure the difference of potential V by four collinear points (point spacing s = 1 mm). (b) Picture of a diamond sample under I-V investigations by four probe method.

II.8 Conclusion

During this thesis work two experiments were carried out. The first one, developed in Italy, concerned the manufacturing of strip-like graphitic contacts by the laser writing technique on CVD polycrystalline intrinsic diamonds in order to produce all-carbon detectors. The second one, developed in France, was about the growth of CVD monocrystalline intrinsic and boron doped diamonds using Bell Jar type reactors and about the manufacturing and characterization of ohmic contacts on them. In particular, small pad-like metallic electrodes were deposited on the diamond surfaces after having produced mesa structures on the CVD doped films. E-beam evaporator and PECVD were used for the deposition processes, while plasma etching treatments were performed by ICP. In addition, an ion implanted-induced graphitic layer was produced underneath the CVD diamond surfaces in order to improve the contact electrical conduction performance for electronic applications. In this chapter, all the experimental set-up used for the manufacturing of the samples were presented.

Moreover, an extensive characterization work was carried out for both experiments. In particular, the structural, morphological, mechanical and electrical changes induced by laser on the graphitized diamond were investigated. The boron concentration and the sheet resistivity of the CVD doped films, together with the micro-fabrication of the mesa structures and TLM contacts, and the ion implantation process were widely characterized by Raman, SEM, EDS, CL and four probe I-V measurements and all of these experimental set-up have been also presented.

All these characterizations have been possible thanks to the collaboration with several national and international institutes of research mentioned in the chapter.

CHAPTER III: DIAMOND GRAPHITIZATION AND ALL−CARBON DETECTOR PERFORMANCE

III.1 Introduction

In the Chapter I it has been presented the state of the art of the diamond contacting both in terms of the traditional diamond metallization technique and of the most recent diamond graphitization one. In particular, the diamond graphitization can be induced by laser or ion implantation treatments allowing fabricating graphitic contacts onto the sample surface and into its bulk. Both these diamond contacting processes together with their applications has been illustrated [183-186, 200, 235]. An extensive report at today of the main contact configurations together with their related spatial resolutions (1D, 2D, 3D) used on diamond devices has been reported too [2, 3, 158-161].

The first part of this thesis work was dedicated to the fabrication of reliable ohmic graphitic contacts on diamond surfaces by laser-writing technique. In particular, the know-how gained during my master thesis [178-181] because of a wide study about the radiation-matter interaction between the UV laser beam and the diamond surface has been my starting point for the development of a protocol of diamond contacting. In addition, a dedicated LabVIEW software was developed during this PhD in order to produce graphitic bi-dimensional pattern on diamond surface.

Indeed, the main aim of this work has been to contact CVD intrinsic polycrystalline diamonds by graphitic electrodes to produce all-carbon detectors for high-energy physics applications. In particular, the L3 team has been involved in the framework of the PADME project [12] of the INFN institute [236], which has proposed in the role of active target as main candidate an all-carbon detector. Therefore, a diamond graphitization protocol has been defined in this thesis dedicated to satisfy the specific requests of the PADME project about the electrode configuration and their performance.

In this chapter, an introduction to the PADME experiment, the manufacturing of the graphitic electrodes, their characterization from morphological, structural, compositional, mechanical and electrical points of view are presented. Then, the detector assembling step onto a dedicated printed circuit board (PC-board) is discussed. Finally, the nuclear investigations performed on the first PADME all-carbon detector prototype at the BTF facility [237] by electron and positron beam are widely discussed.

III.2 Introduction to the PADME experiment and detector requests

In nuclear physics literature, it is well known that the Standard Model (SM) describes with high precision the strong, weak and electromagnetic interactions of the all known particles, namely the ordinary matter. Nevertheless, several phenomena require unavoidably an extension of the SM. At

nowadays, one the crucial points is the "dark matter". Indeed, while the nature of the dark matter is currently unknown, the experimental evidences got by cosmological and gravitational studies prove that the Universe is composed of dark matter for the most part, and only a small part of the ordinary one. The spiral motion of galaxies, the gravitational lensing, the power spectrum of the anisotropies of the background cosmic radiation, in addition to the abundance of the elements produced by primordial nucleosynthesis are some of several observations indicating the existence of a unknown matter, which does not emit and does not absorb light.

The most studied extension to the SM is the Supersymmetry [238], which presents several theoretical and phenomenological reasons, and which is based on the hypothesis that the dark matter would be composed of massive particle weakly interacting with the ordinary matter [239]. In parallel way, other theoretical and phenomenological studies are carried forward based on a different hypothesis, namely the existence of a "dark sector", where the dark matter lives without sharing no kind of interaction with the SM [240]. One of the simplest models of dark sector just adds an additional gauge symmetry $U_d(1)$ to the SM [241], which describes the mutual interactions of the dark sector particles. In particular, the gauge boson A′ corresponding to the additional gauge symmetry is called "dark photon" [242], which can mutually mix with the SM photon producing a week indirect interaction of the SM matter with the dark sector.

In this field, at the end of 2015 the Italian National Institute of Nuclear Physics (INFN) [236] has approved the Positron Annihilation into Dark Matter Experiment (PADME) [12], searching for dark photons A′. The experiment is designed for detecting dark photons produced by the annihilation phenomena of a 550 MeV positron beam onto a thin diamond target. In particular, knowing the energy and the direction of the incident beam and measuring of final state missing mass by reconstructing only the recoiling photon in $e^-e^+ \rightarrow \gamma A'$ events), it could be possible the determinate the A' existence, regardless of the decays produced by A' (ordinary or dark) [12, 243].

Technically, the most favourable production mechanism for the dark photon in the interaction of a high intensity, mono-energetic electron beam with a target is the analogue of the standard Bremsstrahlung: $e^-(N) \rightarrow e^-(N)A'$. In this case, which is the approach of the majority of the dark matter experiments nowadays, it is very difficult to look for the production of the A′ by looking for the missing energy taken away by the dark photon and its decays products (ordinary or dark). On the contrary, the other possible dark photon production mechanism, i.e. the e^-e^+ annihilation, has a well defined initial state and therefore it would allow searching for the A′ by precise measuring the recoil photon in $e^-e^+ \rightarrow \gamma A'$ events, following a missing mass technique [12, 243]. The latter, has been the approach chosen for the PADME experiment. In Figure III.1 (a) a sketch of the basic interaction is reported.

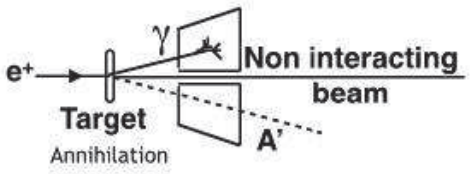

(a)

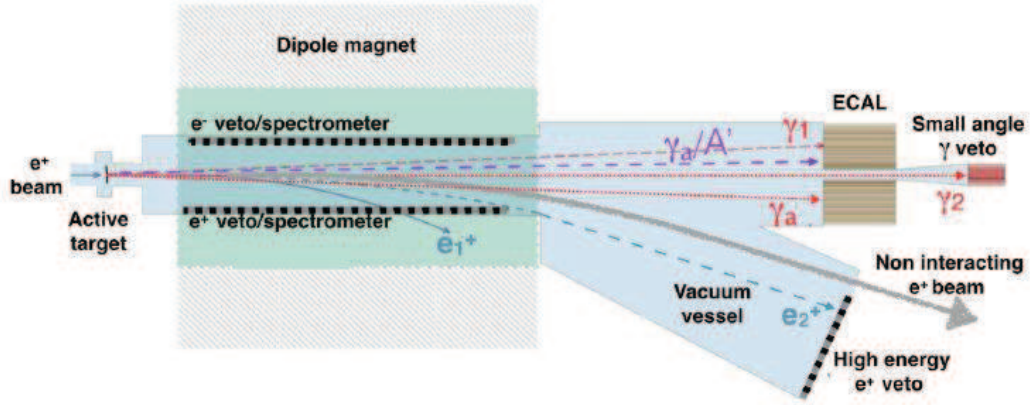

(b)

Figure III.1. (a) Scheme of the positron-electron interaction studied by the PADME experiment. (b) Scheme of the PADME experiment together with the main interactions between a positron beam and a target: (i) bremsstrahlung $e^+N \rightarrow e^+N\gamma$ with large (1) or small (2) energy loss; (ii) annihilation predicted by the SM $e^+e^- \rightarrow \gamma\gamma$ (a related photon is labelled γ_a); (iii) annihilation with production of a dark photon $e^+e^- \rightarrow \gamma A'$ (the ordinary and dark photons are indicated as γ_a and A', respectively) [244].

In Figure III.1. (b) the PADME experiment layout together with the main positron beam-target interactions are presented. The exit of the accelerator, the target and all the detection system are placed under high vacuum conditions. A dipole magnet working with a field of about 0.5 T surrounds the zone behind the target in order to sweep away the interacting (e_1^+, e_2^+) and non-interacting positrons of the beam. These particles can be detected by the veto/spectrometer system and high-energy positron veto. On the contrary, the photons originated by the positron – electron interactions, pass through the magnetic field without suffering any deflection and continue straight their path along the vacuum chamber. Most of these photons are originated from the bremsstrahlung phenomenon due to the positron-electron interactions with large (1) or small (2) energy loss. The corresponding photons γ_1 are collected by the Electromagnetic Calorimeter (ECAL), while the photons γ_2 produced with a small deflection angle, cross the ECAL hole and hit the fast Small Angle Calorimeter (SAC). Finally, all the photons γ_a produced by the positron-electron annihilation interaction ($e^+e^- \rightarrow \gamma\gamma$ and $e^+e^- \rightarrow \gamma A'$), will be detected by the ECAL. In particular, this calorimeter proves to be useful to measure accurately both energy and angle of the ordinary photon emitted with the dark photon.

For this experiment the authors aim to reconstruct the average position of each positron bunch, with a spatial resolution less than 1 mm, without measuring the total flux. No particular requirement was raised about the time resolution.

The choice of the target plays a crucial role in this experiment, indeed in order to favorize the annihilation process with respect to bremsstrahlung one in the interaction between the positron beam and the target, a low atomic number Z for the target has been preferred. This choice enhances the dark photon signal because the annihilation cross-section scales as the atomic number Z of the target, while the bremsstrahlung cross-section scales as the atomic number Z^2 of the target [3, 245]. In this way, the minimization of the degradation of the positron beam in terms of energy and trajectory is obtained by the use of diamonds. In addition, in line with the tentative of preserving the positron beam, a strategic choice has been done also about the thickness of the target. The device should be thin enough to reduce the probability to lose positron energy due to trapping and other interactions with consequential losing of information about the particle paths. Therefore, the proposed target have to be 50 or 100 μm (maximum) thick. Moreover, the target surface dimension must be enough large to intercept the whole area of the positron beam taking into account also the drift in time of its position, so as to maximize the number of positron on target during the data taking. For this reason, a target with surface dimensions of 20×20 mm^2 was assigned [12].

One of the peculiar features and novelty of this experiment is that the target has been thought to play a double role: to act not only as a target but also as detector, namely as "active target". Indeed, in addition "to provide" electrons for the annihilation interactions (namely working as target), the device should also monitor the positron beam and its interactions (namely working as detector). From an experimental point of view, the physical knowledge of the beam spot hitting the target can improve the missing mass resolution and thus increasing the statistical significance of the signal; at the same time, it is well known in literature that diamond materials can work well as detectors [144-147, 151, 152, 246]. Definitely, the tough task of active target can be consigned to a thin diamond device.

In order to potentiate the performance of the diamond detector and to make it a bi-dimensional sensor, a crucial point was given by the projecting of the electrodes. In particular, the electrical contacts should own at the same time several characteristics, for example to be good electrical conductors, robust and stables, capable to eject the signals bi-dimensionally and with a spatial resolution less than 1 mm [12]. In addition, as not negligible condition, the electrodes should have a small atomic number and thin thickness (in analogy to the reasons explained above for the target material). Therefore, as useful compromise it has been proposed of manufacturing graphitic electrodes (namely composed of carbon as the target. Indeed, by this way, the atomic number conditions can be satisfied instead of the traditional metallic contacting which would have implied the deposition of metal layers with high Z values. In this contest, the development of the laser-writing technique on large scale diamonds has become a crucial task. In addition, the different geometric requests for the sensor has made the

PADME diamond target a novelty both in the field of diamond detectors and for the consequent manufacturing of graphitic contacts on so large scale.

In this doctorate work, the manufacturing of thin graphitic contacts, on both whole diamond surfaces ($20 \times 20 mm^2$), with an opportune strip-like shape and orthogonally oriented in the two views, was developed and carried out in order to produce a segmented all-carbon device with bi-dimensional resolution representing the first prototype of PADME active target.

The PADME experiment will be hosted at the DAΦNE Beam Test Facility (BTF) in Frascati (Rome, Italy) where the linear electron and positron accelerator (LINAC) will be dedicated starting from the 2018 [237, 247]. Meantime, a first PADME's beam test took place on November 2015 at the BTF Facility using the first active target diamond graphitized during this doctorate work.

Following, a section about the manufacturing of the graphitic electrodes in the PADME configuration, then the surface characterizations after the laser treatment, and finally the performance of the diamond device irradiated by electron and positron beams are going to be shown and discussed.

III.3 Manufacturing of graphitic contacts on small and large diamonds

The PADME active target has been planned to be large and thin. In particular, the required superficial dimensions are 20×20 mm^2 with a thickness of 50 μm. As explained in the Chapter II, considering the so large diamond area and its related high cost of production, an additional set of smaller diamonds ($5 \times 5 \times 0.05$ mm^3) was also bought in order to optimize and characterize the diamond graphitization process for the contact manufacturing. In this way, the large samples were preserved for the nuclear investigations and the final experiment. All the samples, two large and the whole set of the smaller ones were detector grade CVD polycrystalline intrinsic diamond films provided by Applied Diamond Inc. (USA) [203].

In order to manufacture a segmented all-carbon detector able to detect bi-dimensionally the particle beams with a special resolution less than 1 mm [12], graphitic electrodes with a strip-like shape, a pitch of 1 mm, a small gap between every two consecutive contacts and orthogonally orientated in the two views were manufactured on the diamond surfaces. Therefore, to cover the whole diamond area, 36 graphitic strips (18 for each side) with the dimensions of 18×0.85 mm^2 were produced on the large samples, and 8 contacts (4 for every side) with the dimensions of 4×0.85 mm^2 on the small diamonds. For every sample the strips pitch was 1 mm and the gap between two consecutive strips was equal to 0.15 mm. The experimental laser were: the fixed fluence equal to 5 $J.cm^{-2}$, the energy per pulse of 0.9 mJ and the laser power density of 0.25 $GW.cm^{-2}$, producing a spot diameter size of

150 µm. In Figure III.2 (a), a picture of the small sample after the laser treatment, obtained by an optical microscope, is reported: four strips vertically oriented on the top side are visible. In Figure III.2 (b), a defocused picture of the graphitized diamond is shown in order to visualize both 4 vertical strips (top surface) and 4 horizontal strips (bottom surface), indicated with 1, 2, 3, 4 and 5, 6, 7, 8, respectively. This electrode configuration, which is orthogonally oriented in the two sides, is crucial to obtain bi-dimensional information during the detection process.

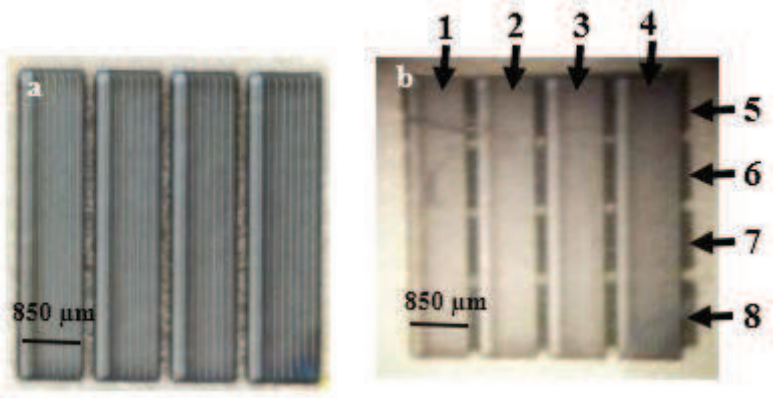

Figure III.2. (a) Focused and (b) unfocused optical microscope images of the segmented all-carbon sensor. Four graphitic contacts with vertical orientation (named 1, 2, 3, 4) and four horizontal contacts (indicated as 5, 6, 7, 8), are visible. Strip dimensions: 4 × 0.85 mm^2, pitch of 1 mm and inter-strip dead gap of 0.15 mm [248].

The diamond graphitization consisted of manufacturing every large strip-like electrode as the sum of several smaller strips (scans) partially overlapped each other. Taking into account that the laser system has a spot size diameter of 150 µm wide, different consecutive small scans were necessary to reach a width slightly lower than 1 mm. In addition, an overlap between two consecutive strips was planned in order to avoid the presence of unirradiated zone (harmful to the proper functioning of the electrical contact). Therefore, during the manufacturing of every single graphitic contact (or electrode), a fixed laser horizontal shift of 100 µm was adopted for the production of two consecutive small strips, providing an overlapping configuration for both sides of every small strip. Eight small vertical strips were necessary to get one large graphitic contact of 850 µm wide.

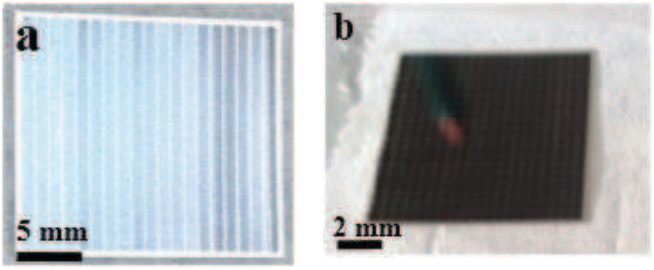

Figure III.3. Optical microscope images of the large segmented all-carbon sensor after the laser treatment on one (a) and both surfaces (b).

In analogy to the Figure III.2 about the small graphitized diamond, in Figure III.3 two pictures about the large diamond after the laser treatment on one side (a) and on both sides (b) are shown. The eighteen contacts per side were produced with the same laser treatment protocol.
In the following section, the contact characterization performed on the small diamonds is presented.

III.4 Contact characterization

III.4.1 Morphological investigations

In order to study how the diamond surface morphology was changed after the laser treatment, SEM investigations were performed. In particular, considering the adopted irradiation protocol a strong periodicity in the laser-induced modifications was expected within every graphitic electrode.
A first SEM image shown in Figure III.4 evidences the changes of the graphitized diamond surface at two different magnification scales. In particular, the inset in the top-right corner shows the sub-structure of one of the large strip in Figure III.2 (a).

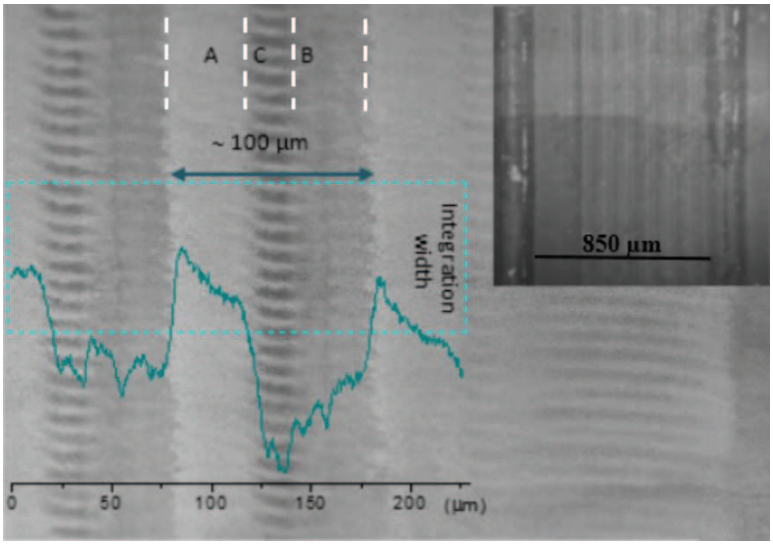

Figure III.4. SEM image of a laser-induced graphitic strip on the diamond surface and integrated contrast profile acquired from the dashed green rectangular area in the image. Three different regions, A, B and C can be identified on the basis of the optical contrast. An overview of the whole strip is shown in the top-right inset [248].

Every single large strip is composed of eight thinner strips each related to a single laser scan. The SEM image reveals a periodic contrast modulation, perpendicular to the strip length, which is clearly highlighted by the integrated contrast profile obtained from the area in the rectangle (the rectangle height corresponds to the integration width, whereas the rectangle base is the length of the contrast line scan, of about 225 µm). It is worth noting that this contrast modulation has a periodicity of about 100 µm, as expected considering the experimental conditions.

By analyzing the SEM image, it is also possible to identify the main contrast variations highlighted in the picture by white dashed lines: i) the presence of brighter (A) and darker (B) regions within each strip and ii) the presence of lens-shape dark details (C), running along every strip and about 10 µm wide. In this section, these contrast variations are analyzed from a morphological point of view and correlated with the laser graphitization process.

Figure III.5. (a) and (b) compare the surface morphology of the regions A and B respectively. The images were acquired with the sample tilted at 45° with respect to the incident electron beam in order to enhance the topographical features of the surface. The surface of region B exhibits a higher density of holes and swellings, suggesting an increase of the laser induced damage. This is confirmed by the high magnification images of the same regions reported in Figure III.5 (c) and (d). The surface modification is here evident at the nanoscale, in particular the presence of small grains, resulting from material ablation/redisposition.

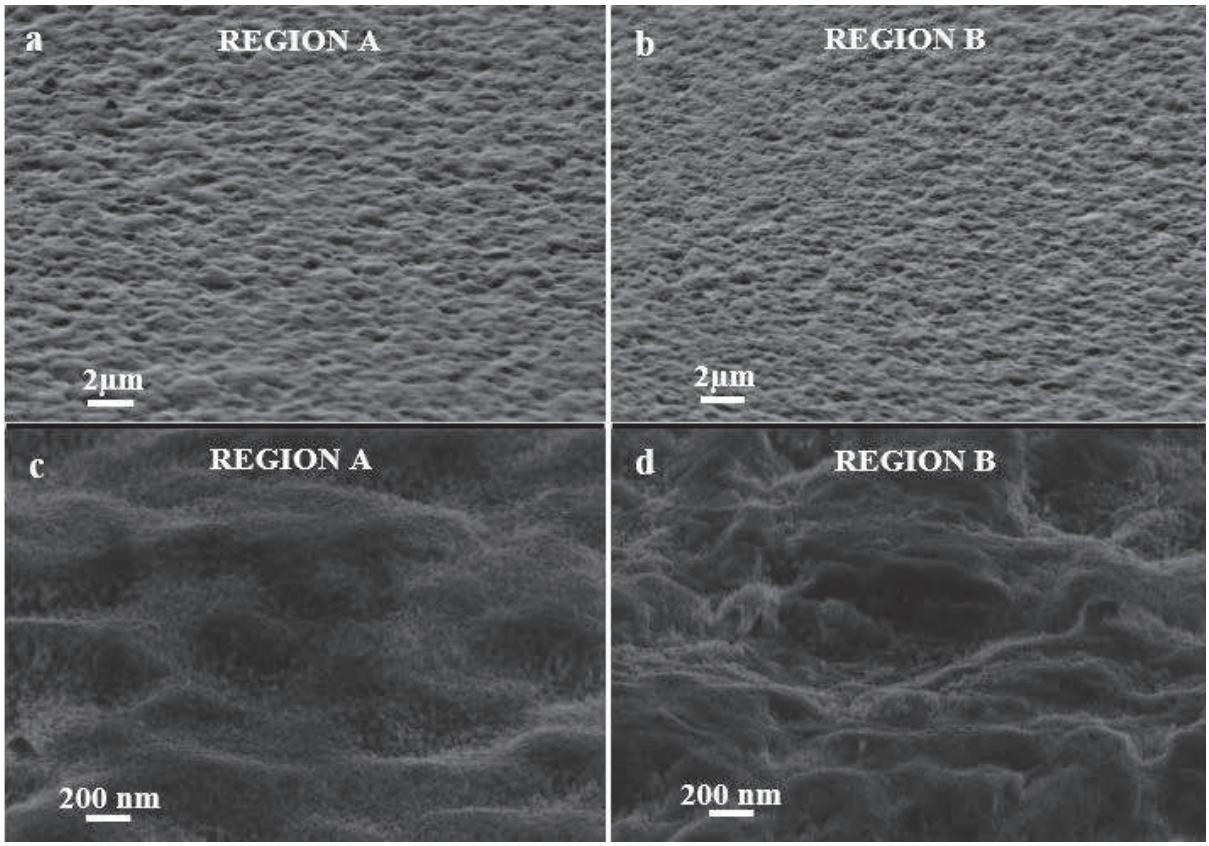

Figure III.5. Comparison of the surface topography of the regions A and B at low (a) and (b), and at high magnification (c) and (d), respectively [248].

Figure III.6. reports the high magnification image of the region C; in particular, the bottom part of the image reveals the enhanced surface damage of the lens-shaped darker region, in comparison with the surrounding smoother areas. These morphological differences inside every laser scan and periodically distributed along every large strip (contact) are related to the laser beam energy

distribution inside the laser spot and to the overlapping phenomena. In particular, the higher damage induced in region C is due to the higher energy density in the center of the laser spots. The peculiar lens-shaped regions are reminiscent of the beam footprints during the vertical displacements of the laser processing. On the contrary, regions A and B are related to the irradiation from the laser beam lateral tails. In particular, their modification is lower than in the zone C, due to less energy absorbed. Small differences detectable in A and B regions, could be ascribed to a small asymmetry of the energy distribution in the beam tails.

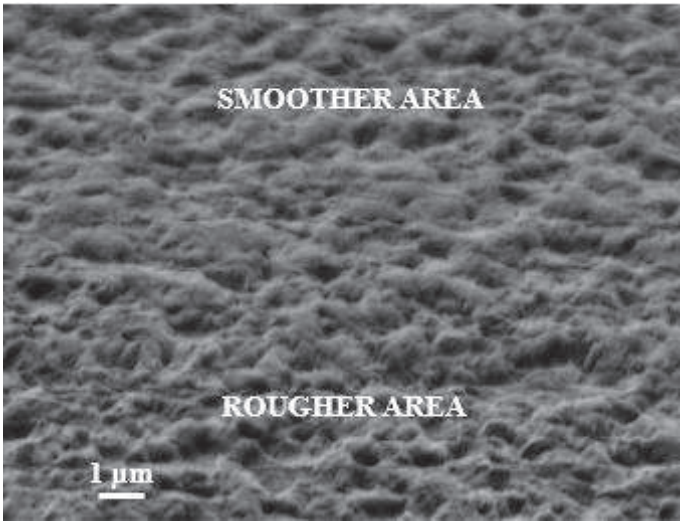

Figure III.6. Surface morphology of region C, showing topographic differences between the bottom part of the image (darker region of the C area shown in Figure III.4) and the top part of the image (brighter region of the C area shown in Figure 2). The image suggests an enhanced roughness in the bottom region [248].

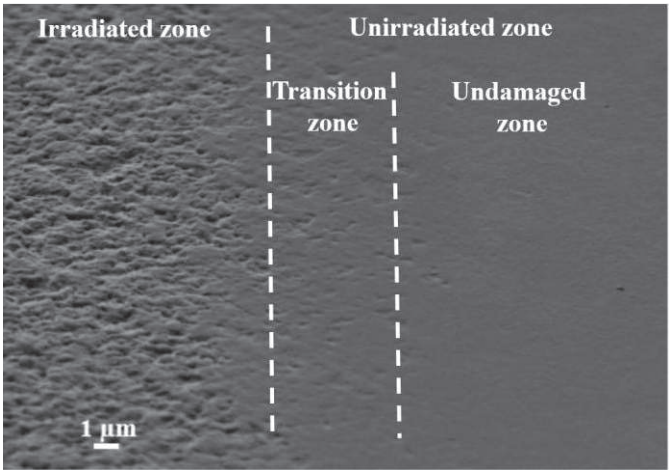

Figure III.7. Surface morphology of the boundary between treated and untreated regions [248].

Finally, the Figure III.7 shows the SEM image of the boundary between treated and untreated sample areas. A transition region, with a width of about 5 µm, is evident between the undamaged and the laser graphitized surface.

III.4.2 Compositional analyses

The laser-induced diamond graphitization was performed in air and therefore the diamond surface hit by the radiation beam was constantly exposed to the chemical species presented in the environment. In order to individualize any modification of the material due to reactions with atmospheric gases, EDS analyses were carried out. In particular, the three regions highlighted by the white boundary lines and showing the contrast features previously discussed, were analyzed. Figure III.8. (a) and (b) show the investigated areas and the acquired spectra, respectively.

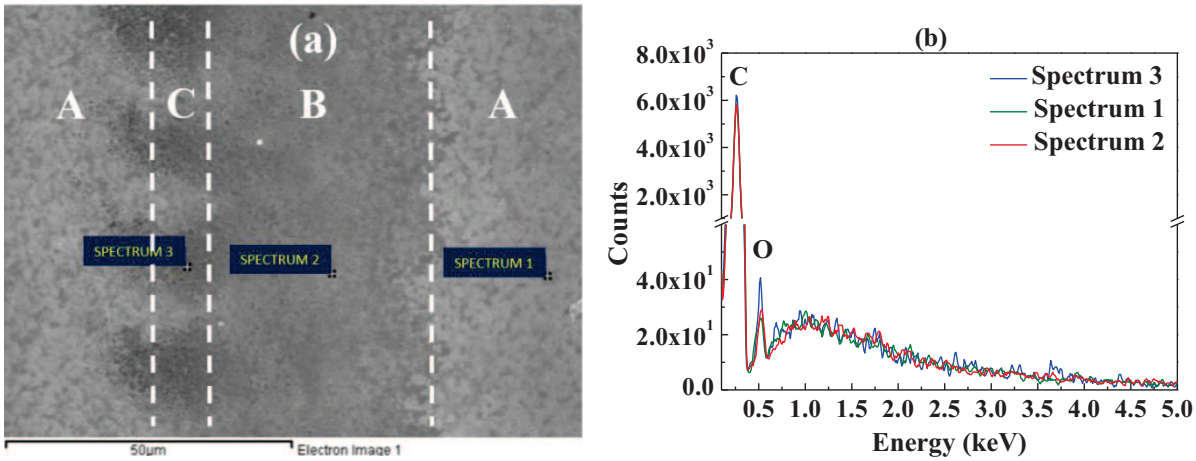

Figure III.8. (a) EDS analyses performed on three different contrast areas (A, B and C regions) and (b) the corresponding spectra [248].

In addition to the obvious presence of the carbon peak due to both diamond and graphite phases, EDS spectra show the presence of an oxygen peak (O) as illustrated in Figure III.8 (b). The oxygen localized in the irradiated areas suggests a widespread absorption process from atmospheric air related to the great reactivity of the carbon atom dangling chemical bonds formed under laser treatment, enhanced by high temperature at the molten target surface; moreover, deep UV laser irradiation can promote dissociation of O_2 molecules. An increase of the oxygen signal was detected moving from regions A and B (spectra 1 and 2, respectively) to the region C (spectrum 3), (Figure III.8 (a)). In particular, zones A and B show an oxygen peak of comparable intensity while a significant higher signal is appreciable in the zone C according to the increase of deposited energy density. The trends described above were confirmed by repeating the EDS analysis in different points of the samples. Based on the above observations it is possible to assume that the enhanced oxidation process could be related to the higher surface damage observed in these regions of the sample.

III.4.3 Structural investigations

To describe the structural changes induced by the laser processing at the molecular level, a study by micro-Raman spectroscopy was carried out. The Raman technique was employed in order to obtain a qualitative estimation of the degree of graphitization/amorphization of the material belonging to the different areas identified by SEM measurements and by visual inspection of the optical microscope images. Taking into account the periodicity of the laser-induced morphological modifications, a Raman mapping recording spectra at different points along a line orthogonal to a strip was performed. In particular, twenty-one measurements with a step of 5 μm were carried out with the aim of investigating the three regions showing the major contrast features. In particular, the mapping starts from the center of a C region, crosses A and B areas and ends in the subsequent C region (see Figure III.9).

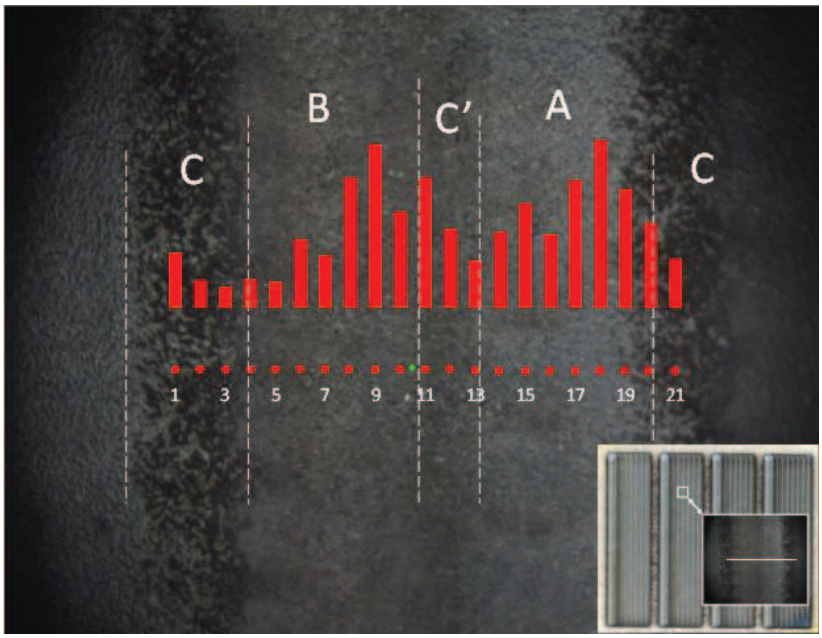

Figure III.9. Optical microscopy image of a selected area of a strip. A, B and C regions can be identified on the basis of the optical contrast. Notice the transition region labelled C' between A and B regions (vertical white dotted lines are shown as guide for the eye). Red dots separated by 5 micrometers along the horizontal pathway indicate the points analysed by Raman spectroscopy. The histogram describes the evolution of the integrated Raman intensity of the diamond Raman line (1332 cm^{-1}). An overview of the investigated zone is shown in the bottom-right corner [248].

The complete set of the Raman spectra in a 3D plot is shown in Figure III.10.

In Figure III.11, several representative Raman spectra are reported, showing characteristic patterns, which can be ascribed to differently modified carbon.

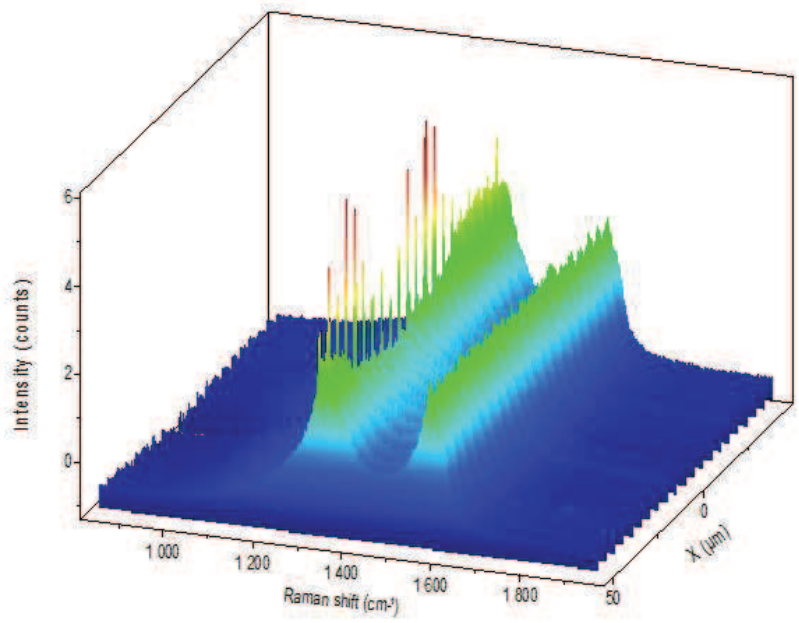

Figure III.10. Complete set of the micro-Raman measurements got mapping the graphitized diamond along a line orthogonal to a strip (red dots Figure III.9).

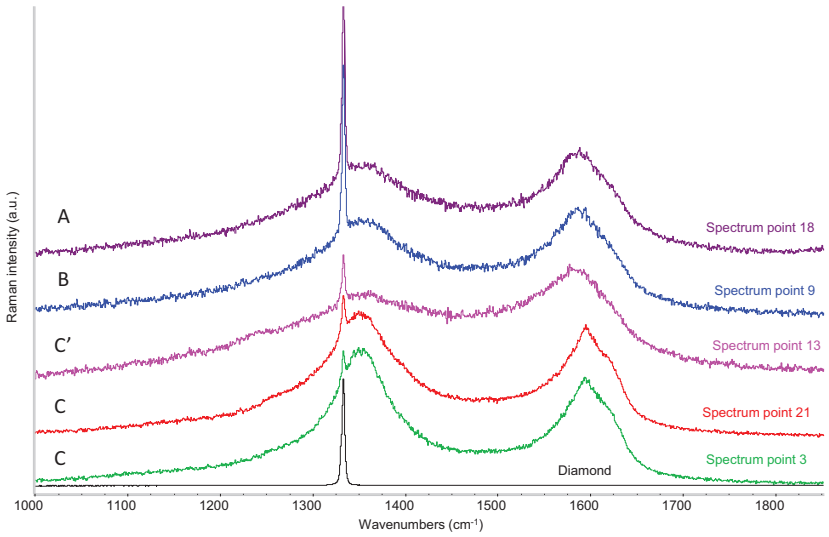

Figure III.11. Plot of Raman spectra representative of the different regions analyzed by Raman mapping (see Figure III.9 to identify the points of measurement). At the bottom, the Raman spectrum of the unirradiated diamond (black line) is reported for comparison [248].

The Raman spectrum of the unirradiated material is also reported in Figure III.11. This spectrum was recorded in a region of the sample distant from strip-like contacts. It shows only the characteristic features of pure diamond, with the sharp Raman line at 1332 cm^{-1} confirming the good quality of the starting CVD polycrystalline diamond sample. Indeed, the spectrum does not show features which can be ascribed to the presence of disordered (e.g. amorphous) carbon, nor to the presence of graphitic domains. Labels A, B, C in Figure III.11 indicate spectra obtained from different regions of a strip-like contact, showing different morphology. All these spectra clearly show features ascribed to graphitic material; moreover, the characteristic Raman line of diamond appears in all spectra, showing

an intensity modulation associated to a change of the measurement point. The presence of two broad features (namely the G and D bands at 1580 cm^{-1} and 1350 cm^{-1}, respectively) can be taken as the signature of the presence of small-sized graphitic domains and/or of the presence of disordered graphitic material [249, 250]. Indeed, the D band is silent in highly crystalline graphite or graphene, because of symmetry selection rules, and it rises in the presence of defects (chemical defects or structural imperfections) as well as when π electrons are confined into small graphene-like islands [251, 252]. The presence of the line at 1332 cm^{-1} suggests that some diamond domains survive in the irradiated regions of the sample, may be because of inhomogeneity in the graphitization of the material (see Figures III.8 and III.9). An alternative explanation could be given considering that the exciting laser beam is also probing the pristine diamond bulk extending below the graphitized/amorphized surface. However, due to the high absorption coefficient of graphite in the visible range, this behaviour is expected only in presence of very thin graphitized domains, extending in depth only for few atomic layers [253].

A careful comparison among the spectra reported in Figure III.11 shows non-negligible differences in band shape and in the intensity pattern, which could be ascribed to the unavoidable inhomogeneity of the modified carbon material. Differently to the spectra recorded in the other regions, the two spectra representative of region C show a sharp G peak. Such a region is characterized by a more effective graphitization, in agreement with the morphological analysis. This finding suggests that in the region C more extended and regular graphitic islands are present.

It is possible to obtain a qualitative estimate and to map the degree of graphitization in the different points analyzed following the evolution of the Raman intensity of the diamond band, moving across the strip. This is illustrated by the histogram reported in Figure III.9, which shows a clear modulation of the diamond content, that is low in region C while increases remarkably in regions A and B. It is possible to notice the presence of a region previously not identified (labelled C' in Figure III.9), located at the edge between A and B areas, and characterized by a relatively low diamond content. A possible explanation of this behaviour is the partial overlapping of the irradiated regions during the laser fabrication of two adjacent thin strips: the enhanced graphitization of region C' could result from the fact that it underwent double laser irradiations, both effective in promoting the carbon transformation from sp^3 to sp^2 carbon structure. Interestingly, according to the geometrical parameters adopted during the "writing" of the strips, also regions A and B have been exposed twice to the photon beam, during two subsequent laser scans. The higher content of diamond observed in these regions can be justified as due to partial ablation of the graphitic material grown during the first scan, and subsequently damaged and/or ablated during the second scan. The balance between processes

responsible of graphitization and laser induced carbon ablation is then crucial in determining the structure of the resulting modified material [14, 180].

III.4.4 Nano-mechanical characterizations

Nano-indentation maps were performed on a portion of a single graphitic strip (10 × 120 μm^2) to study the changes on the mechanical properties of the irradiated surface and to demonstrate the feasibility and the reliability of the laser-writing technique. Figure III.12 (a) and (b) show hardness (H) and reduced elastic modulus (E_r) for three different regions, A, B and C, previously studied (Figure III.4)). Both maps clearly show the modified graphitic surface (vertical band-like) with lower hardness and lower elastic modulus with respect to the substrate. Indeed, for the unirradiated surface the hardness and elastic modulus average values are (2.35 ± 0.17) GPa and (23.2 ± 2.0) GPa, respectively. After the laser processing the H and E_r average values are (0.60 ± 0.05) GPa and (12.5 ± 1.0) GPa, respectively. The change in the mechanical properties can be correlated to the morphological changes. For example, in Figure III.12 (a), it is possible to see a softer central region with two adjacent strip-like harder zones on the two sides (which are however less hard than the unirradiated surface).

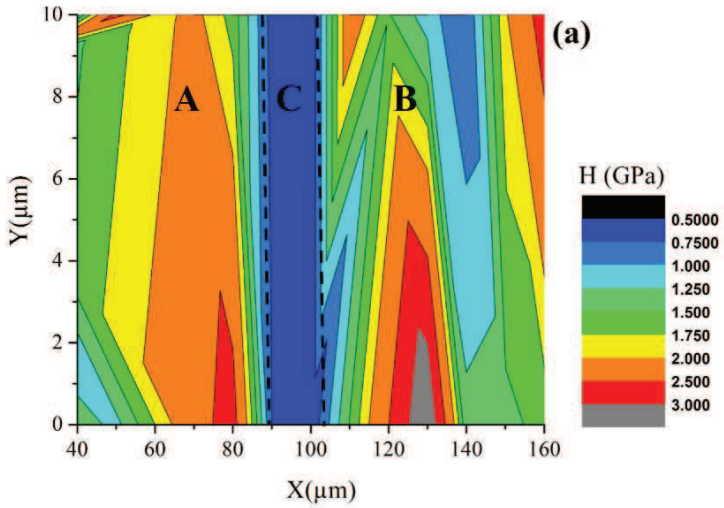

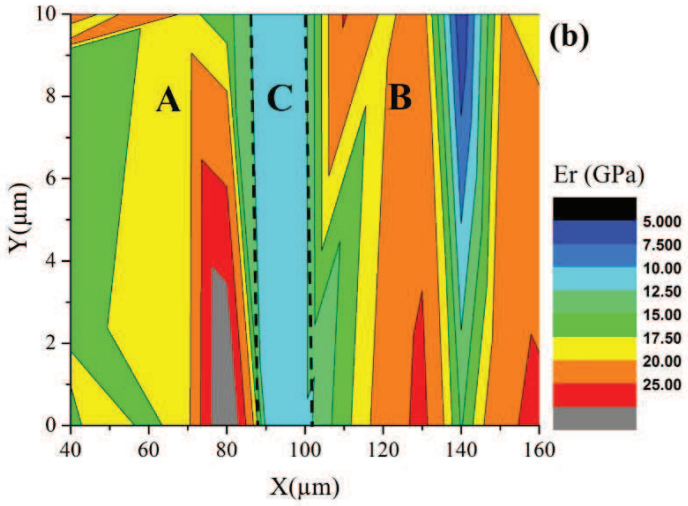

Figure III.12. (a) Hardness and (b) reduced elastic modulus mappings of a portion of a single laser-induced strip. A, B and C regions can be identified on the basis of the mechanical property contrast [248].

These three areas coincide with the three regions A, B, and C identified and characterized by SEM and Raman analyses (Figure III.4 and Figure III.9). A similar behavior is observed for E_r, Figure III.12 (b). In particular, the central (blue band) area is about 10 µm wide in agreement with the width estimated by SEM for the lens-shape dark structures in region C. Furthermore, mechanical results correlate well with the morphological images showing the most damaged zone of the strip (Figure III.7).

The presence of a softer area and with low reduced elastic modulus is compatible with the presence of abundant graphitic domains [254] and the nano-indentation maps suggest that an effective and rather homogenous graphitization occurred throughout the whole region C, in agreement with spectroscopic results (Figure III.9, III.10 and III.11). Here, the energy deposited by the laser beam is larger (center of the spot); moreover, overlapping phenomena between more consecutive laser scans are absent. On the other hand, the two larger areas on both sides of the central strip (corresponding to areas A and B) show a limited change in the mechanical properties, in agreement with the abundance of diamond phase, as proven by Raman experiments (Raman Figure III.9, III.10 and III.11) and confirmed by morphological changes (Figure III.5). As already discussed in Section 4.3, this feature can be justified considering that regions A and B receive a double irradiation dose, such that previously graphitized layers undergo ablation [14]. This process sequence allows interpreting the presence of the diamond peak (thin graphitic layer and inhomogeneous graphitization) and consequently a fluctuation of H and E_r values along the two regions.

Interestingly, at the boundary between A and B regions (left edge of Figure III.12 (a) and III.12(b)) a relatively soft region (colored in green and light blue) occurs. This behavior nicely correlates with

the peculiar characteristic of the C' zone, clearly identified by Raman analysis and described as a region with a relatively low diamond content.

III.4.5 Electrical measurements

TLM method for resistivity measurements

Current-voltage (I–V) measurements were carried out to evaluate the strip resistivity by means of the TLM method [232]. First, a series of I-V tests were performed measuring the current as function of the increasing distance d between the two tungsten probes (diameter in 40 μm). Then, the total resistance R_T from each I-V curve was extracted. Plotting R_T values as a function of the distance d, the contact resistance R_c and the resistivity ρ of the material under investigation are obtained by a linear fit of the experimental data according to:

$$R_T = 2R_C + \frac{\rho}{wt} d \qquad \text{Equation III.1}$$

where w and t are the width and the thickness of the electrical medium to investigate, respectively.

From the Equation III.1 it is possible to obtain the resistivity equation and applying the error propagation law on that, the resistivity error is given by the equation:

$$\sigma_\rho = \rho \left(\frac{\sigma_{R_{slope}}}{R_{slope}} + \frac{\sigma_w}{w} + \frac{\sigma_t}{t} \right) \qquad \text{Equation III.2}$$

where σ_{Rslope} is the standard deviation of the linear fit slope, σ_w and σ_t are the errors on the material width and thickness.

This technique was applied inside every graphitic electrode and among the complainer strips of both surfaces in order to investigate both the electrical conduction of the graphitic electrodes laser-induced and the nature of the contact graphite-diamond.

Measurements inside the graphitic strips

All the graphitic electrodes were manufactured with the same diamond irradiation protocol, therefore two typical I–V characteristics recorded within two graphite strips (on both surfaces) at a distance d varying from 0.5 mm to 3 mm (in steps of 0.5 mm) are shown in Figure III.13. In both plots, each curve exhibits an almost linear trend, which confirms along the whole graphitic area the ohmic nature of the strip and allows extrapolating a resistance value R_T for each separation by a linear fit. Figure III.14 shows the total resistance R_T values against the probe distance for the same strips.

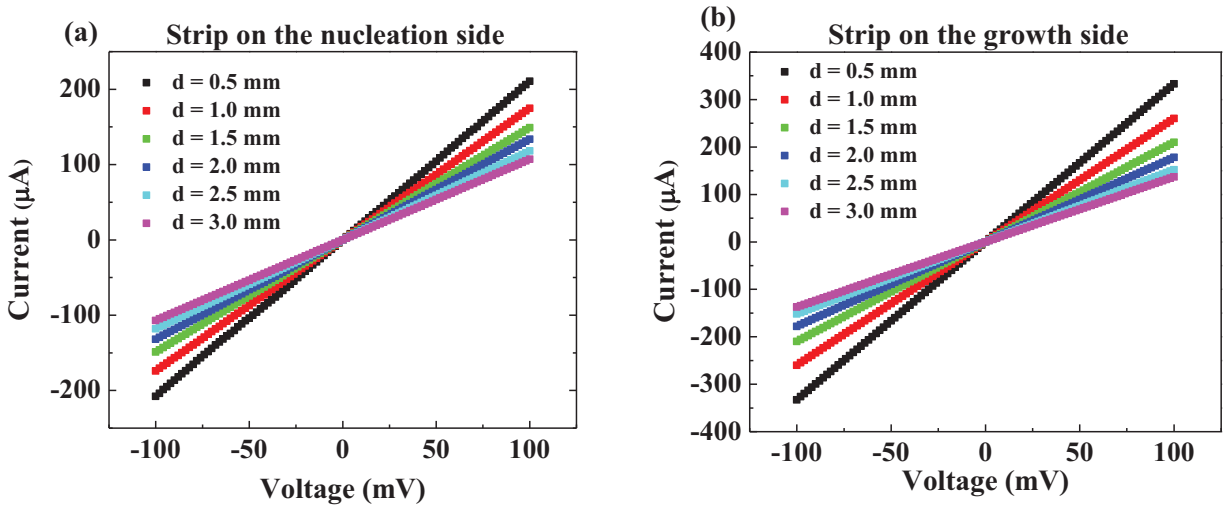

Figure III.13. Typical I-V characteristics recorded inside one graphite strip varying the contact separation distance d on the (a) nucleation and (b) growth side.

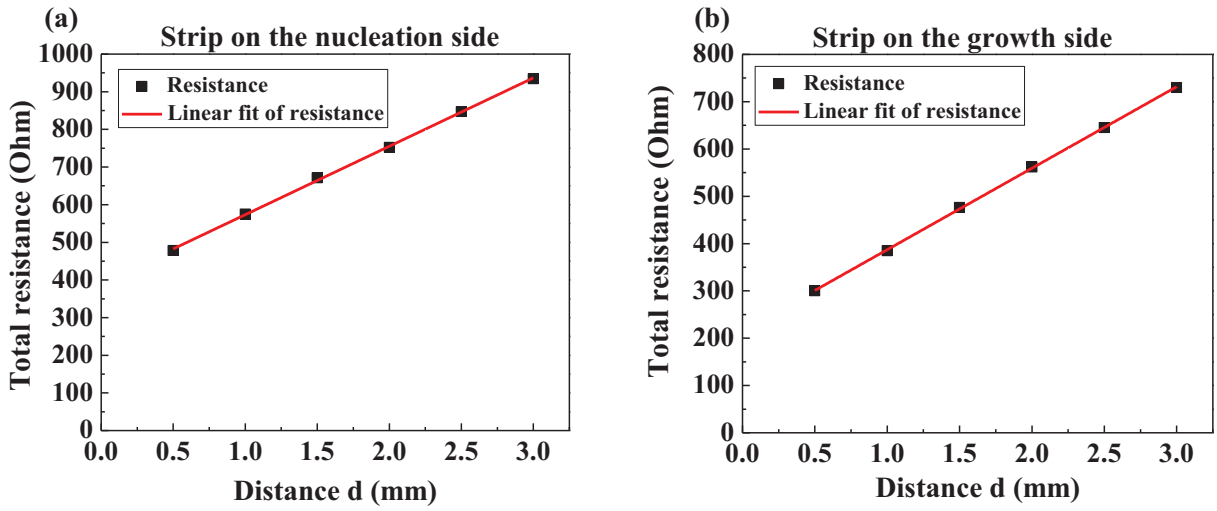

Figure III.14 Plots of the total resistance R_T against the distance d between the probes extrapolated from the I-V curves shown in Figure III.13 for the corresponding strips ((a) on the nucleation side and (b) on the growth one).

To perform an accurate estimate and for statistical analysis, this set of measurements was repeated for all the graphite contacts of each sample side finding always a good linearity both in the I-V curves and in the total resistance as a function of probe separation, which confirmed the reproducibility of the graphitization process.

Then, with the aim of studying if the diamond surface topography affects the result of the graphitization process, a comparison between the total resistance values obtained for the contacts on the polished diamond surface and the ones got from the strips on the unpolished sample surface (nucleation and growth side, respectively) was carried out. Figure III.15 shows the mean values of the total resistance against the probe distance for the strips on both surfaces.

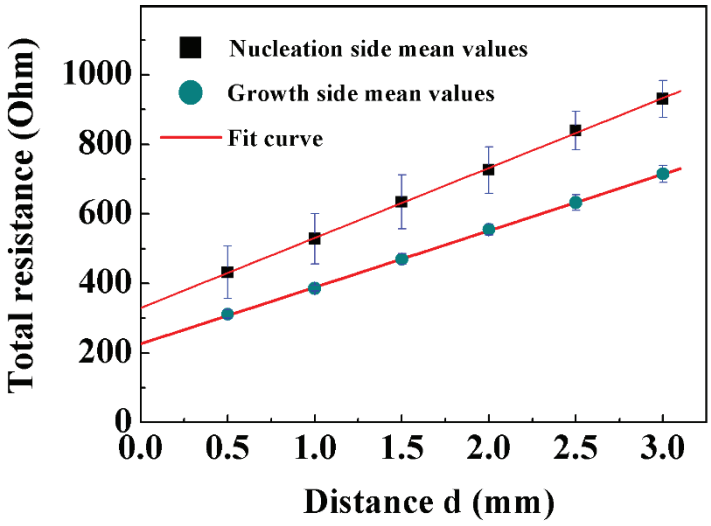

Figure III.15. Mean values of the Resistance R_T plotted against the distance d between the probes for the graphite electrodes produced on both nucleation (a, left) and growth (b, right) diamond surfaces [248].

Fitting linearly the data, an estimate of the slopes was extracted providing mean values among the complainer electrodes of $(2.01 \pm 0.03) \times 10^5\ \Omega.m^{-1}$ and $(1.63 \pm 0.02) \times 10^5\ \Omega.m^{-1}$ for the graphitic strips on the nucleation and growth side, respectively. Since the electrode width is about 850 µm (measured by SEM) and assuming that the strip average thickness is about 180 nm (estimated value for a graphitic strip produced with similar irradiation conditions [180]), the graphite laser-induced resistivity values computed by Equation III.1 proved to be about $(3.08 \pm 0.14) \times 10^{-5}\ \Omega.m$ and $(2.50 \pm 0.10) \times 10^{-5}\ \Omega.m$ for nucleation and growth side, respectively. The errors were computed by Equation III.2 considering that σ_{Rslope} was given by the standard deviation of the linear fit slope, σ_t was the thickness error calculated in a previous study and equal to 5 nm and σ_w was the error on the strip width which was estimated to be about the 12 % of the measure. The resistivity values proves to be in good agreement with the expected ones for graphitic materials $\rho_{graphite} \approx 10^{-5} - 10^{-6}\ \Omega.m$ [14, 180, 255-257].

In addition, it is possible to observe that R_T data evaluated from the I-V curves recorded on the four growth side graphitic strips are characterized by a lower standard deviation than those extracted from the measurements carried out on the nucleation side graphite strips. This result is ascribed to the probes/graphitic electrode contacts, which result to be improved and more reproducible by the higher roughness of the unpolished diamond side, as it is confirmed also by the lower mean contact resistance $R_{c,unpolished}$ evaluated from the fits ($R_{c,polished} = (165 \pm 3)\ \Omega$ and $R_{c,unpolished} = (113 \pm 2)\ \Omega$). In line with this, the total resistance error bar is shorter for the unpolished nucleation side (Figure III.15).

Measurements between couples of graphitic strips

Subsequently, the electric insulation between electrodes was verified by contacting all the coplanar graphitic strips. Exiguous currents of about some hundreds of fA were measured between strips produced on both diamond surfaces besides an almost linear behaviour of the I-V curves over the investigated voltage range, from −10 V to +10 V, which suggests an ohmic nature for the graphite/diamond contact. Typical I-V characteristics recorded by contacting the four coplanar graphitic electrodes for a distance d along the diamond surface are shown in Figure III.16 (a). By using the TLM method (Equation III.1 and III.2) the diamond resistivity was evaluated (Figure III.16 (b)), which results to be of $(8.1 \pm 0.8) \times 10^9\ \Omega$.m in agreement for the expected diamond values.

After these electrical investigations, it is possible to conclude that conductive graphitic contacts, with ohmic behaviour, have been created on diamond surface taking advantage of diamond graphitization process induced by laser.

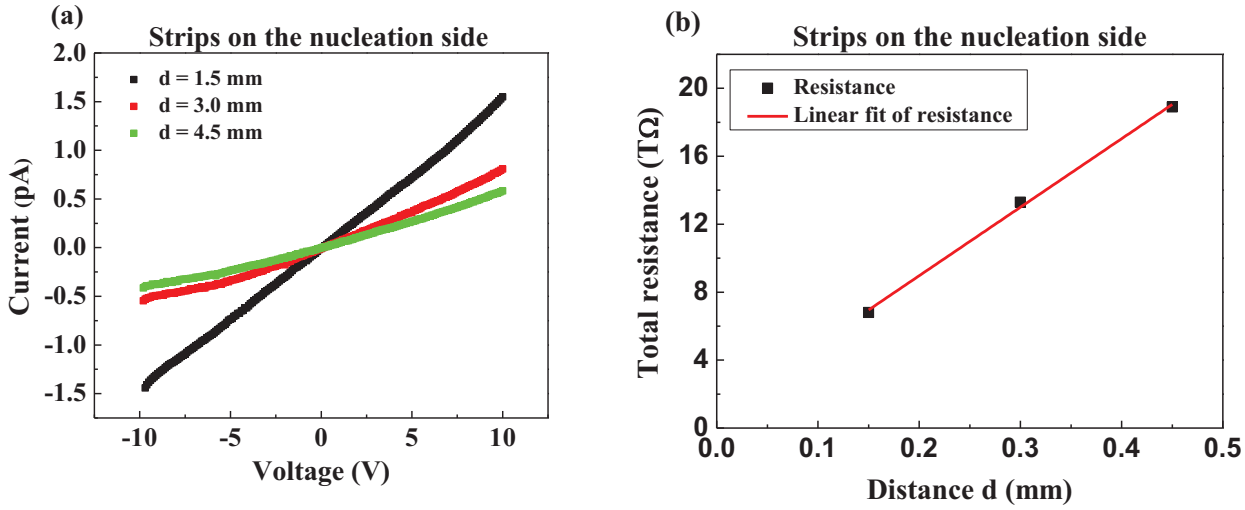

Figure III.16 (a) Typical I-V characteristics recorded on nucleation side by contacting two coplanar graphitic strips for a distance d. (b) Resistance R_T plotted against the distance d along the diamond surface [248].

III.5 PADME beam test set-up

III.5.1 Experimental set-up

A picture of the experiment set-up for the PADME beam test and its schematic representation are shown in Figure III.17 (a) and (b), respectively. The main components are:

- LINAC particle accelerator Figure III.17 (d);
- Diamond detector Figure III.17 (c);

- Calorimeter;
- Medipix detector.

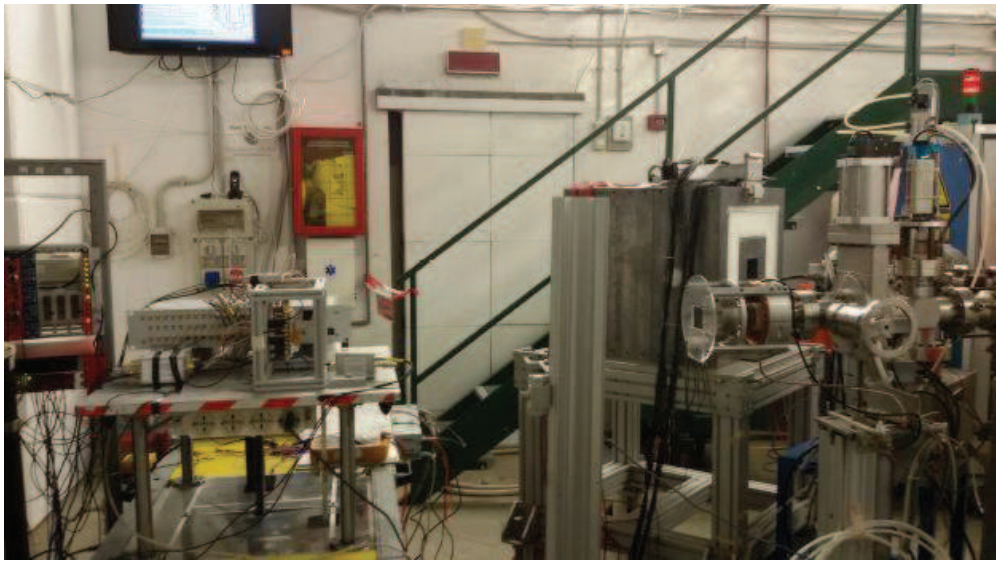

(a)

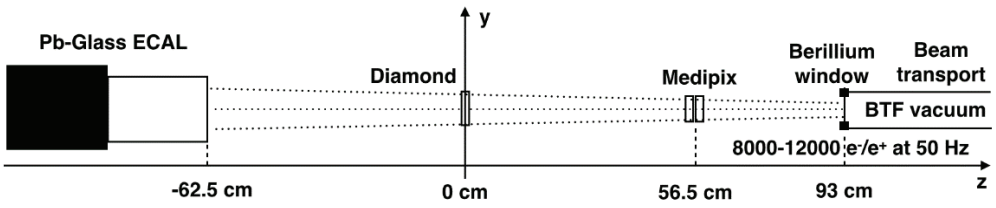

(b)

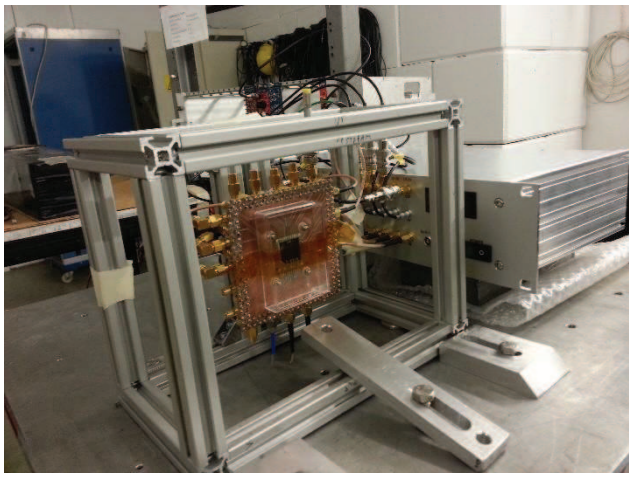

(c)

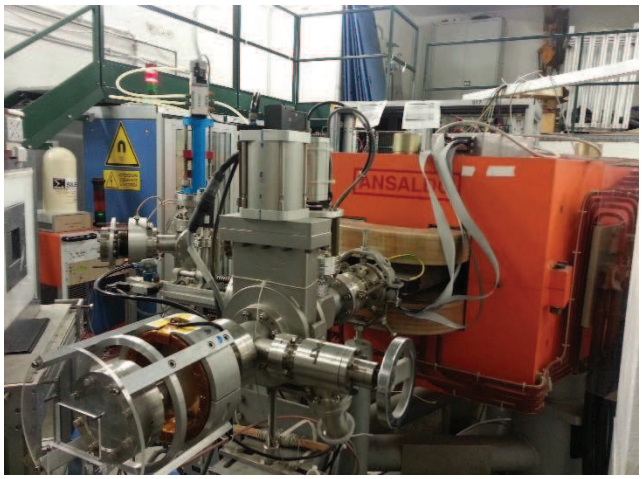

(d)

Figure III.17. (a) Picture and (b) sketch of the experimental set-up of the PADME beam test at the DAΦNE BTF facility [258]. (c) Picture of the diamond target with its PC-board and physical support, (d) picture of the particle output of the LINAC accelerator [237].

The LINAC accelerator works with beams of positrons and electrons, which were arranged in pulsed beams of 450 MeV e^+ or e^-, in 40 ns long bunches at the rate of 50 Hz, with an average multiplicity of 10^4 particles [247]. The electromagnetic calorimeter (ECAL) is made of cylindrical lead glasses for a high resolution measurement of the intensity of the beams [259]. The diamond active target was located at a distance of about 3 m from the calorimeter and 93 cm from the beryllium window of the accelerator with the task to monitor and to collect the particle beam bi-dimensionally (while the estimation of the third spatial component, namely along the diamond thickness, is assigned to the software simulations). Finally, an additional detector called Medipix was placed between the accelerator and the diamond target in order to check the beam profile [260]. Basically, when a particle beam leaves the vacuum pipe through a thin beryllium window (Figure III.17 (d)), in first it hits the silicon pixel detector Medipix (matrix of 256 × 256 pixels of 55 × 55 μm^2), then it arrives on the diamond target and finally it is collected by the calorimeter behind the target.

The diamond device and its dedicated PC-board (home-made) were fixed inside an aluminium support structure (Figure III.17 (c)), which was mounted on a movable table with orthogonal configuration to the beam direction. It was possible to control the detector sub-millimetric translations in the two directions perpendicular to the particle beam remotely.

In Figure III.18, two typical beam profile images taken by Medipix, one for the positron beam (on the left) and one for the electron beam (on the right). It is possible to appreciate some differences between the two particle beams in terms of beam position, shape and intensity.

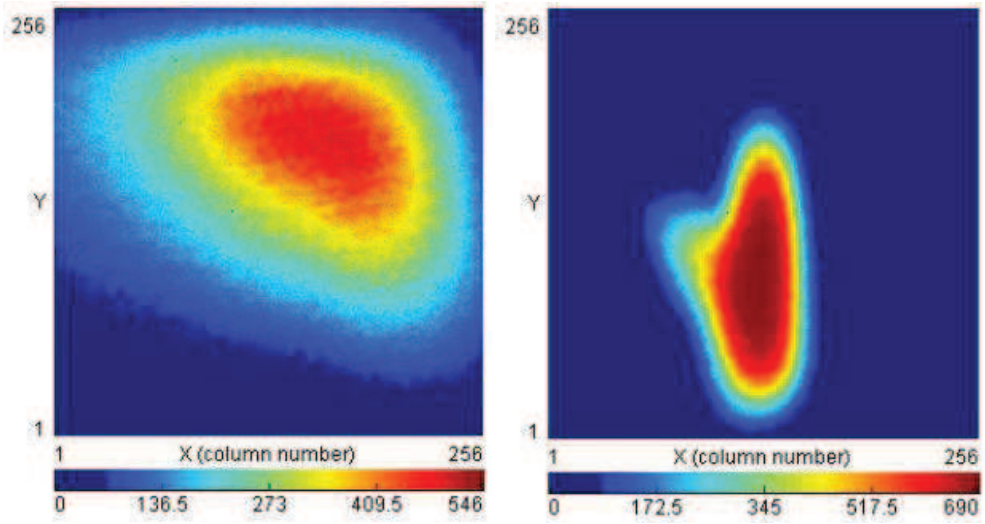

Figure III.18 Images of two typical bi-dimensional profiles of the positron beam (on the left) and of the electron beam (on the right) got by detector Medipix [261].

The diamond detector, as every solid-state detector, needs an electronic system to amplify the signals. During the beam test, the diamond electrodes were opportunely readout by two kinds of commercial amplification systems, a single channel charge amplifier (CSA) or a single channel voltage amplifier (VA) provided by Cividec [262]. Most electrodes were readout by the CSA, while half of the strips

on the second diamond surface were readout by Voltage Amplifiers (VA) terminated by 50 Ω. The CSA had a not negligible size and were connected to the PC-board through a 15-50 cm long input coaxial cable for each channel that can ruin the good signal-to-noise ratio of Charge Sensitive Amplifiers (CSA). On the contrary, the VA have typically a worse signal-to-noise ratio with respect to CSA but are not affected by the length of the input cable. The CSA used in the beam-test had a gain of 5 $mV.fC^{-1}$, with a 100 MHz bandwidth, 2 ns rise-time, 7 ns pulse width and 750 e^- equivalent input noise. The VA had a gain of 100, 2 GHz bandwidth and 25 μV equivalent input noise when terminated with 50 Ω at the input. The analogical signals of the electronic channels were digitized by the multichannel digitizer CAEN V1742 [263] with 12 bit ADC at 1 GHz sampling rate in a time window of 1024 ns. The same readout electronics was reading the signal from the lead-glass calorimeter. The data collecting was done alterning electronic beams with positron at an average energy of 450 MeV. The typical average multiplicity was 10^4 particles in a bunch, with a higher multiplicity (about 20%) for the electron beams. During most of the data taking the active target was operated with a bias voltage of 150 V. The data acquisition system (DAQ) was a prototype version for PADME experiment [264]. It recorded the entire digital waveforms for each channel (36 signals from the diamond strips and one signal from the calorimeter). Figure III.19 shows the typical digitized output signals got by a charge amplifier and by a voltage amplifier from two different electrodes summing 300 consecutive events to suppress the electronic readout chain noise and its fluctuations.

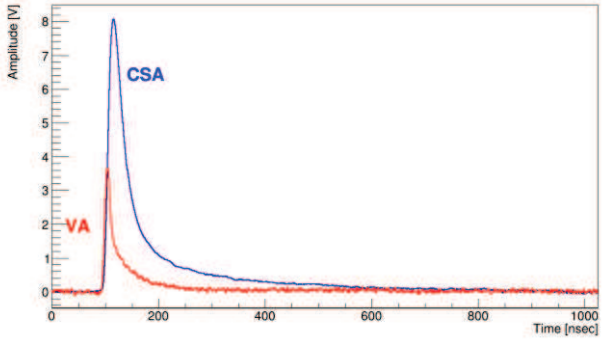

Figure III.19. Typical curves got from the fast charge amplifier (CSA, dotted blue line) and from the fast voltage amplifier (VA, continuous red line) summing the digitized output signals for 300 consecutive events [258].

Finally, to extract the charge collected at the beam passages, all the waveforms were recorded for all the strips of the diamond detector event by event. In particular, the waveforms were processed integrating the signal in the range 80 ns − 500 ns and applying a multiplicative calibration constant previously measured for each amplifier. The calibration procedure was made on bench by injecting a known charge $Q = C.\Delta V$, where ΔV is the amplitude of a low-frequency square wave and C is the AC calibration coupling capacitance of 1 pF. The rectangular pulses were lasting 10 ns, emulating the time structure of a particle bunch of the beam [258].

III.5.2 Diamond target contacting on the PC-board

The graphitized diamond presented 18 graphitic strip-like electrodes for each surface which have to be contacted (Paragraph 3). A made-home PC-board was manufactured for this kind of diamond target, with a hole slightly smaller in size than the diamond area where to site the target. Considering that the electrodes were orthogonally orientated in the two views, in the beam test configuration the contacts vertically placed and upstream were named X strips (X_1, …, X_{18}) with respect to the Y strips (Y_1, …, Y_{18}) which were horizontally orientated and downstream. In this configuration, the X strips proved to be on the diamond top surface, while the Y strips on the bottom side and in contact with the PC-board (Figure III.20 (a)).

Basically, the electrical connections among the Y graphitic strips and the copper paths on the PC-board were created via silver paint spots deposited manually, while the connection among the X strips and the other board traces were established by bonding technique taking advantages of the free surface from any mechanical contact. The bonding connection was performed by aluminium wires (diameter

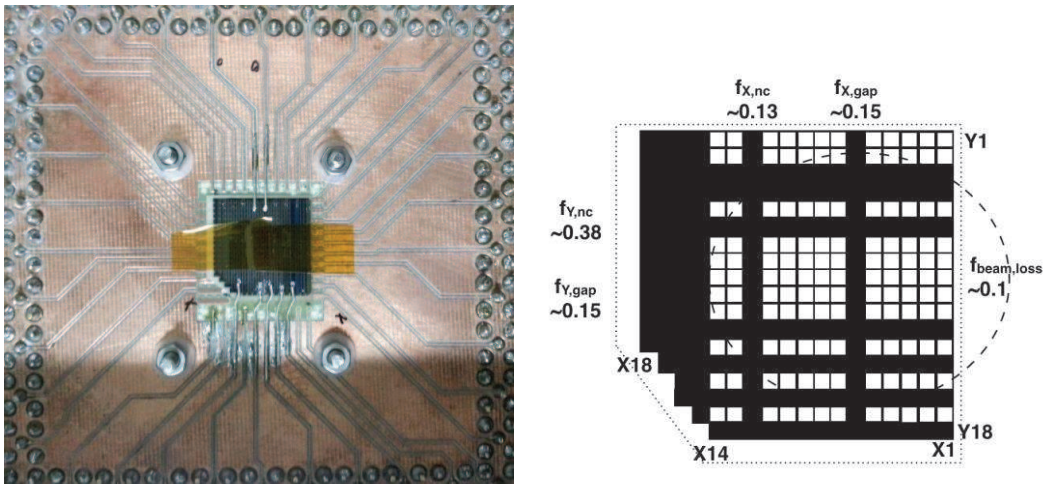

(a) (b)

Figure III.20. (a) Picture of the all-carbon target as assembled on the PC-board and (b) its sketch [258] showing the sensitive area (white colour) to the beam detection after the broking corner and some failed connections (black colour). The physical intersection between the diamond detector (···) and the beam (- - -) during the Charge Collection Distance (CCD) measurements are shown (b). The strip names (X_i, Y_i) and other labels (which are going to be explained later) are placed around the diamond sketch. An orange adhesive tape was placed on the graphitized diamond just to fix better it on the board (a). Both pictures are shown as seen by the particle beams.

of 40 μm), and together with the silver paint glue was already previously tested for an all-carbon device placed on an integrated circuit for nuclear investigations [180], Figure III.21.

During these delicate hand manipulation and assembling phases, which were carried out in laboratory for the first time for this kind of sample (wide area, very small thickness and rigid material, which made it extremely fragile) a small corner of the diamond sensor broke. The poor planarity of the first prototype of home-made PC-board and the many strips to contact on both surfaces made these tasks

huge. Finally, some wire bonding of the X stripes were jumped off during the assembling step, and then they were repaired by additional connection operations done manually via tungsten wires and silver paint glue. As an unavoidable consequence, a reduction of the detector effective sensitive area was obtained. A picture of the graphitized diamond after all the contacting steps on the PC-board is reported in Figure III.20 (a), while a sketch of its final sensitive area useful for the beam detection is shown in the Figure III.20 (b).

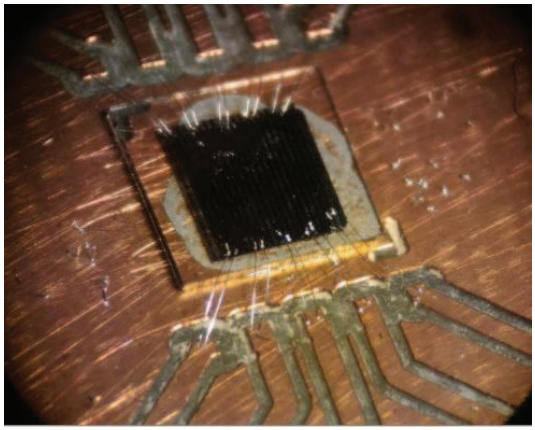

Figure III.21. An all-carbon detector assembled on a PC-board for nuclear investigations. The large graphitic pad on the back side was glued by silver paint, while the stripe-like graphitic electrodes on the front side were contacted by alluminium wire bonding [180].

Definitely, 22 diamond electrodes proved to be correctly connected to the board, as shown a posteriori by reading out the electrical signal from the corresponding channels during the beam test. In particular, 12 X strips of the front side and 10 Y ones of the back side worked well, while 6 X and 8 Y electrodes were unconnected, which can be considered electrically floating and the underneath sensor volume passive. The strip numbering adopted for the data analyses is shown in the sketch of Figure III.20 (b), while the broken corner of the device is not drawn (the bottom-left corner). Anyway, this area did not affect particularly the diamond functionality being located in a peripheral area and the experience gained in the assembling steps of this first target prototype allowed identifying some problematic handling steps which can be fixed for the next samples with the help of additional laboratory tools, such as micro-manipulators, conductive glue dispenser and vacuum pick-up tools.

III.6 Beam test analyses and results

The data collected in the beam test at the Laboratory BTF allowed demonstrating the efficiency of the all-carbon device as monitor detector for intensity and position of the electron and positron beams. In particular, in this section, quantitative measurements of the detector response is terms of timing resolution, charge collection distance (CCD) and spatial resolution are presented.

During this beam test, hundreds of thousands events were collected and processed. One event corresponds to one bunch of particles shot against the diamond target with the same charge (positive

or negative if the particles were positrons or electrons, respectively), duration of 10 ns, frequency of 50 Hz and a multiplicity variable depending on the kind of the particles (on average 10000 positrons or 12000 electrons). The beam characteristics (charge, multiplicity and switching time) depended on the DAFNE's accelerator necessities on those days. During the data collecting, several events were grouped in different runs, where the event number changed depending on the investigation aims. Typically, 300 consecutive events were assigned to every run because they proved to be enough for the collecting data of the different studies.

In addition, it was possible to change run by run the beam shape by the manipulation of magnetic fields near the particle gun and the bias voltage applied (positive or negative).

For every event the charge released by the particles was collected form all the active electrodes and analyzed as following.

III.6.1 Signal characteristic and time resolution

The charge ejected from each strip was digitized into a pulse with a defined timing. The integration of this signal in a fix timing range (t_{min}, t_{max}) provides the charge value injecting into the amplifiers strip by strip. The equation of the charge values is:

$$Q = \frac{\int V dt}{R} \cdot \frac{1}{G} = \frac{\sum_i V_i \Delta t}{R} \cdot \frac{1}{G} \qquad \text{Equation III.3}$$

where Δt is the sampling time (1 ns), R the resistance (50 Ω) and G the charge gain of every amplifier; while the timing range of integration was chosen between 80 ns and 300 ns.

In order to get an estimation of the time resolution different fits were carried out. In first, a Gaussian fit was applied on the every waveform to determine the maximum voltage value and its position; then, using the previous results as initial parameters, a subsequent fit of the waveform was done by a pulse function V(t) composed of the following analytic form:

$$\begin{cases} V_0 & per\ t < t_0 \\ V_0 + V_1 \cdot \dfrac{t - t_0}{t_1} \cdot e^{-\frac{t-t_0}{t_1}} \cdot P_3(t) & per\ t > t_0 \end{cases} \qquad \text{Equation III.4}$$

where t_0 was the arriving time of the signal on one only strip, V_0 was the baseline value, $P_3(t)$ was a third degree polynomial (with the constant term fixed to 1, and two free parameters), while V_1 and t_1 were parameters determined by the previous fit.

After the convergence, the fit is repeated and restricted to the range where the maximum value is the abscissa (t_0) whose ordinate correspond to the 75% of the pulse width.

Then, it was possible to estimate the time resolution from the distribution of the difference in t_0 between two neighbouring strips which collected a similar amount of charge (namely hit from a similar fraction of the beam), in order to limit the beam fluctuation effects. The run was chosen with rather stable conditions and the sampling rate of the digitizer to 5 GS.s^{-1} and with a bias voltage of 150V.

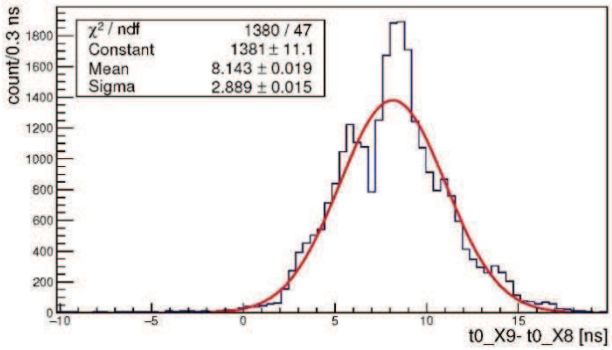

Figure III.22. Distribution of the signal arrival time difference for the strips X8 and X9 (blue line) and Gaussian fit (red line) [265, 266].

In Figure III.22 the distribution of the arrival time difference between the two strips is shown. Fitting the data by a Gaussian curve it was possible to get an estimation of the distribution width σ_{diff}, which is related to the time resolution σ_t by the equation:

$$\sigma_{diff} = \sqrt{\sigma_{t,1}^2 + \sigma_{t,2}^2} = \sigma_t \cdot \sqrt{2} \qquad \text{Equation III.5}$$

where it was assumed that the two strips contributed in equal amount to the time spread. The final time resolution of about 2 ns.

III.6.2 CCD

In diamond detectors, all kinds of defects (impurities, vacancy, and grain edges in the case of polycrystalline ones) can trap the charge carriers preventing their complete collection to the electrodes.

The typical parameter used to characterize the quality of the active medium of a radiation detector is the charge collection distance (CCD), which is defined as:

$$CCD = L\frac{Q_C}{Q_G} \qquad \text{Equation III.6}$$

where L is the sensor thickness, Qc is the charge collected by the electrodes and not trapped in the material bulk and Qg is the charge generated by a relativistic charged particle passing along the detector thickness.

Therefore, in the case of the beam test, it was possible to calculate the CCD of this diamond detector following the equation:

$$CCD[\mu m] = \frac{Q_{TOT}[fC] \cdot 6250[e^-/fC]}{36[e^-/\mu m] \cdot N_{active}} \qquad \text{Equation III.7}$$

where Q_{TOT} is the sum of the collected charge from all the X strips (or Y strips), the generated charge Qg is estimated as the product between the average number of electron-hole pairs generated by a relativistic charged particle crossing one unit of diamond material (36 $e^-.\mu m^{-1}$ [3]), and the number of particle beam hitting the active detector region, N_{active}. Here, the detected particle number (N_{active}) proved to be constantly smaller than the multiplicity measured by the calorimeter behind the detector (which was $N_{positron} \approx 10000$ and $N_{electron}$ 12000) due to different sources of signal losing.

Therefore, in order to evaluate correctly the detector CCD it was necessary to estimate the signal loss introducing some corrector factors [258, 261] (which are also indicated in Figure III.20 (b)). The first factor had to be related to the beam leak due to the beam instability (shape and position), which was called $f_{beam,loss}$. To estimate it, some consecutive events characterized by the only horizontal decentralization, namely the minimum geometric leak of the beam transversal size were chosen as reference and analysed with a bias voltage of 150 V. In particular, the $f_{beam,loss}$ value was estimated assuming that the beam profile was symmetric which means that the portion of the lost charge on one side was identical to the one collected on the other side respect to the maximum point. So, the $f_{beam,loss}$ value representing the part of beam profile outside the area of active target proved to be of the 10%.

The second aspect contributing to the signal lost was related to the inactive detector area due to the gap among the electrodes (f_{gap}), which was deliberately not graphitized to allow segmented and bi-dimensional detecting. Considering that the gap between neighbouring strips was fixed at 150 μm, the fraction of the no active gap was the 15% of the whole area for each surface. Finally, the last and important inefficiency to consider was given by the "dead" electrodes, namely the strips with the not-working connections on the PC-board (f_{nc}). In order to assign an electrical contribute to the unconnected electrodes and to get a complete profile of the collected charge in function of the strip position, the missing charge values were computed by linear interpolation of the collected charge values for the neighbouring strips. Indeed, all the graphitic strips which were correctly connected to the PC-board, resulted to work very well, with a satisfying stability and giving back signals without evidence of degradation with time.

Therefore, if the unconnected strip n had the two nearer strips working, the charge Q_n was assigned follow the equation:

$$Q_n = \frac{Q_{n+1} + Q_{n-1}}{2}$$ Equation III.8

While, if there were two consecutive unconnected strips, n and n+1, the charges Q_n and Q_{n+1} were assigned by:

$$Q_n = \frac{1}{3}(Q_{n+2} - Q_{n-1}) + Q_{n-1}$$ Equation III.9

$$Q_{n+1} = \frac{2}{3}(Q_{n+2} - Q_{n-1}) + Q_{n-1}$$ Equation III.10

In this way it was possible the beam reconstruction on both surfaces, bunch per bunch. An example of beam profiles as seen by PADME active target are shown in Figure III.23 (a) and (b) for the X (horizontal) and the Y (vertical) views, respectively. Here, in order to suppress the beam fluctuations, the profiles obtained in a run of 300 consecutive events recorded under stable beam conditions and at a bias voltage of 150 V, are summed. In the two plots the blue histogram represents the real measurements, while the red bins the interpolated values.

The most damaged surface turn to be the Y side, due to the bad planarity of the PC-board made at home, as explained in the Section 5.2.

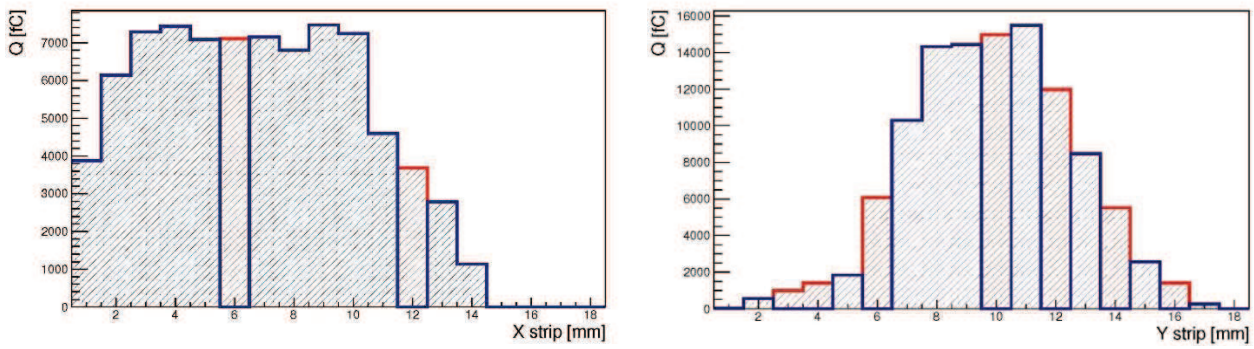

(a) (b)

Figure III.23. Sum of the beam profile for 300 events as measured by the diamond detector in the (a) horizontal and (b) vertical views. The entries for the strips 6 and 12 (a) and 3, 4, 6, 10, 12, 14 and 16 (b), in red lines, were obtained by linear interpolation of the charge measured in the neighbouring strips (blue line) [258].

Then, the no active diamond area underneath the dead electrodes was evaluated by the ratio between the Q_{TOT} and $Q_{interpolated}$, where $Q_{interpolated}$ was the total charge of X and Y strips got summing to real collected charge (Q_{TOT}) the interpolated charge values for the not-connected electrodes. As a result, the fraction of dead strip area intersecting the beam was the 13% for the electrodes measuring the X plane and the 38% for the ones working on the Y plane (Figure III.20 (b)).

Definitely, the detector active region (ε_D), namely the overlapping of all the active regions on both surfaces, can be calculated in first approximation and considering the orthogonality of the electrodes, with the following equation:

$$\varepsilon_D = \varepsilon_X \cdot \varepsilon_Y \qquad \text{Equation III.11}$$

where

$$\varepsilon_{X(Y)} = \left(1 - f_{X(Y),gap}\right) \cdot \left(1 - f_{X(Y),nc}\right). \qquad \text{Equation III.12}$$

Accordingly, the estimation of the particle number crossing the detector active area can be given by the equation:

$$N_{active} = N_{particle} \cdot (1 - f_{lost-beam}) \cdot \epsilon_D \qquad \text{Equation III.13}$$

therefore

$$N_{active} = 10^4 \times 0.9 \times 0.85^2 \times 0.87 \times 0.62 = 3500 \qquad \text{Equation III.14}$$

being 10^4 the beam intensity measured by the calorimeter, and the f factors: $f_{beam,loss} = 0.1$, $f_{X,gap} = f_{Y,gap} = 0.15$, $f_{X,nc} = 0.13$ and $f_{Y,nc} = 0.38$.

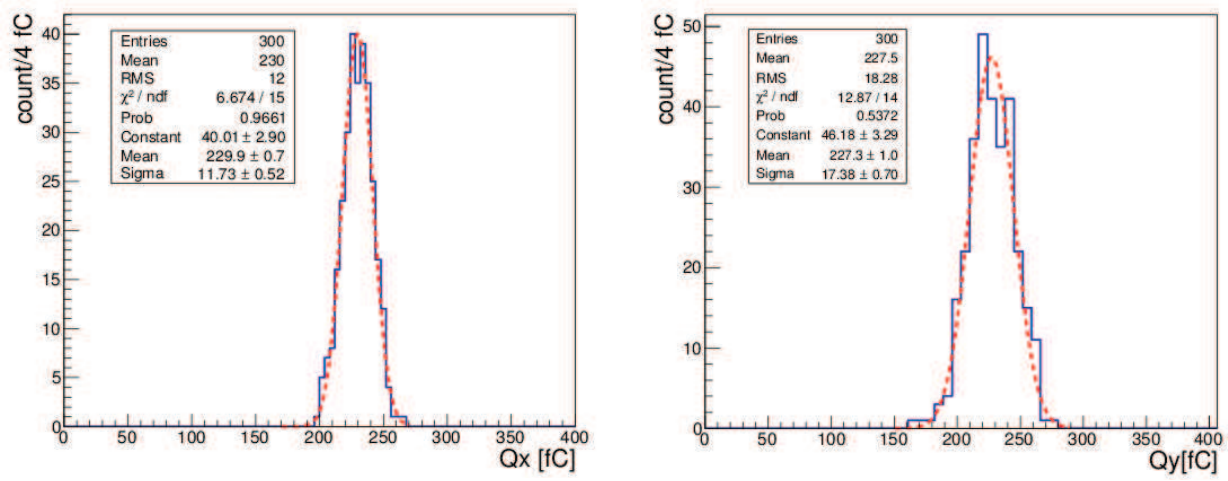

(a) (b)

Figure III.24. Distribution of the total charge collected on diamond the X and Y surfaces ((a) and (b) respectively) in blue colour, and the Gaussian fits in red dashed line [265, 267].

The total collected charge Q_{TOT} to put in the Equation III.7 was calculated as the mean of a Gaussian fit to the distribution of Q in a dedicated run composed of 300 events where the detector operated at a bias voltage of 150 V (see Figure III.24 (a) and (b)), where the values of 230 fC and 227.5 fC were obtained for the X and Y surfaces, respectively.

The final CCD values estimated for both sides were:

$$CCD_X = \frac{Q_X \cdot 6250}{36 \cdot N_{active}} = \frac{230fC \cdot 6250}{36\,fC/\mu m \cdot 3500} = 11.4\mu m$$ Equation III.15

$$CCD_Y = \frac{Q_Y \cdot 6250}{36 \cdot N_{active}} = \frac{227.5fC \cdot 6250}{36\,fC/\mu m \cdot 3500} = 11.3\mu m$$ Equation III.16

The two results turn out to be similar each other as expected with an average value of 11.35 ± 0.05 μm. The error is dominated by a systematic uncertainty related to the calibration (4%); while the difference between the measurements on the X and Y planes (1%) is used as an estimation of other residual systematic effects [258]. This CCD value obtained is in line with the expected performance for this kind of CVD polycrystalline diamond, considering its low quality due the technological processing difficulties (discussed in Chapter II), and no pumping treatments with ionizing radiations was performed by the supplier.
Anyway, the quite low signal originated from this kind of diamonds (CCD < L/2) with respect to much thicker sensors, does not represent a problem for the experiments where several thousands of particles have to be detected.

An other interesting aspect related to the CCD of a detector is to evaluate its dependence on the high voltage applied. Indeed, it is well know that the mean free path of the charge carriers in a detector increases with the carrier velocity, which is related to the electric field within the device.
Therefore, the study of the CCD change in function of the applied voltage was carried out. In particular, the CCD values were computed for different voltages applied between the diamond surfaces in the following ranges (175, 50,) V and (-50, -175) V, and shown in Figure III.25. The obtained CCD values proves to be systematically lower than the estimated ones for a similar diamond after a pumping treatment, as expected. Between the positive and negative bias, a discrepancy is evident for the low voltages, which is presumably indicative of some polarization effect.

In general, it is possible to assert that the all-carbon detector was able to sustain high voltages (with an average 150 V for two weeks continuously) without discharge phenomena, and all the graphitic electrodes well connected to the PC-board worked properly under these voltages. Finally, considering the front-end electronics and the signal transport chain used for this beam test it was possible to estimate the typical equivalent input noises, which proved to be 0.8 fC for the CSA amplifiers and 3.6 fC for the VA amplifiers.
Accordingly, the signal to noise ratio (S/N) estimated for a limited particle number for bunch (1000 m.i.p.) proved to be equal to 80 and 18 for the CSA and VA, respectively. Both values can be considered satisfying even for a rather low intensity of the bunch in the beam.

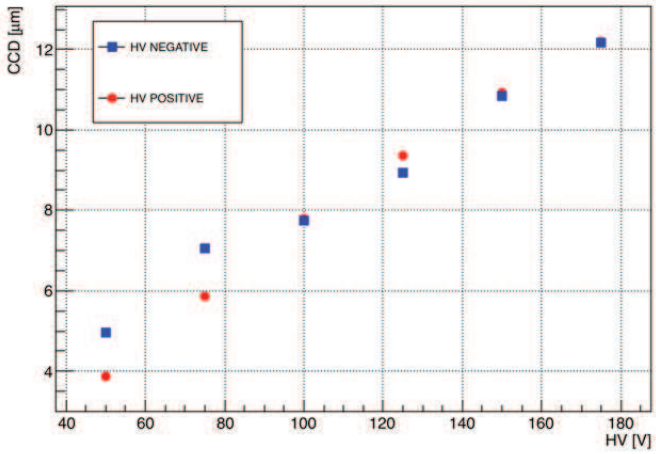

Figure III.25. Evolution of the average charge collection distance values in function of a variable high voltage in the ranges (175, 50,) V in red circles, and (-50, -175) in blue squares. The CCD error bars do not exceed the size of the markers [258].

III.6.3 Spatial resolution

A next very important parameter for a detector is its spatial Resolution. The beam average position in its transversal plane can be estimated for every event measuring the centroid of the charge on both surfaces X and Y, in independent way, following the equation:

$$\langle X \rangle = \frac{\sum_{i=1}^{N_x} Q_i^x \cdot x_i}{\sum_{i=1}^{N_x} Q_i^x} \qquad \text{Equation III.17}$$

$$\langle Y \rangle = \frac{\sum_{i=1}^{N_y} Q_i^y \cdot y_i}{\sum_{i=1}^{N_y} Q_i^y} \qquad \text{Equation III.18}$$

where $N_{x(y)}$ is the number of strips of the X(Y) side, $Q_i^{x(y)}$ and $x(y)_i$ are the collected charge and the coordinate of the i-th x(y) collecting strip. The not connected electrode contribution was computed, and included in the Equations III.17 and III.18 by linear interpolation of the charge collected by adjacent strips (previously explained in the Section 6.2).

Under stable beam conditions, with 10^4 particles for bunch, with a bias voltage of 150 V and a X- Y beam spot of 2×3 mm^2, 300 events were recorded and analyzed. In particular, plotting the distribution of the reconstructed beam centroid in function of the strip position it was possible to estimate the spatial resolution of the beam centroid position by the sigma of the Gaussian fit to the distribution, Figure III.26 (a) and (b). The spatial resolutions obtained for the X and Y sides are (0.20 ± 0.01) mm and (0.32 ± 0.02) mm, respectively. The standard deviation difference between the two diamond surfaces is mainly related to the single particle bunch fluctuation, which is expected to be of about

that size [268], in addition to a small fluctuation of the detector answer. For both results, the PADME experiment request of having a spatial resolution smaller than 1 mm is widely satisfied.

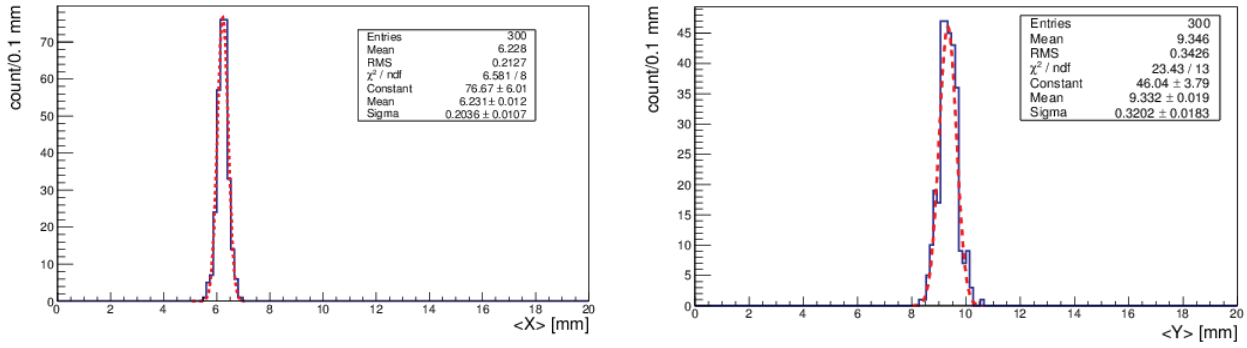

(a) (b)

Figure III.26. Distribution of the average beam position in the (a) horizontal and (b) vertical views computed by the Eq. III.17 and III.18, respectively, (continuous blue line). The corresponding Gaussian fits are shown with red dashed lines [265, 267].

Finally, to study the correspondence between the detector translation by the mobile table and the beam charge centroid shift, 10^4 events were registered and analysed. Technically, the table was moved vertically with steps of 1 mm after about 10 s of data taking, while the horizontal coordinates were left fixed. In Figure III.27 (a) the beam charge centroid evolution as function of the event number is shown.

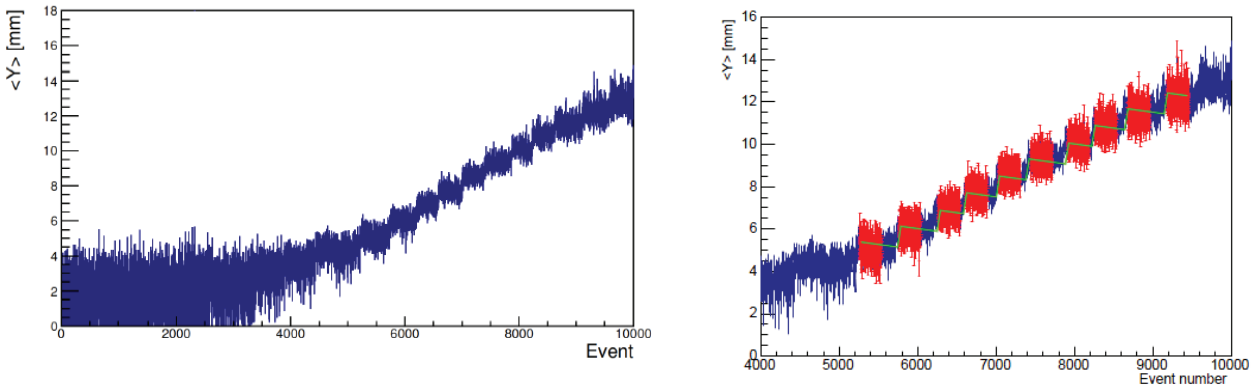

(a) (b)

Figure III.27. (a) Beam charge centroid position against the event number and (b) its enlargement (of the range 4000 − 10000) when the diamond detector is translated along vertical coordinates (Y) with 1 mm steps [258, 265].

When most of the beam is intercepted by the active part of the detector (event number above about 5000 in Figure III.27(a)) the charge-of-gravity method is a good estimator of the beam position Figure III.27 (b). Nevertheless, several important systematic errors contribute to a not perfect linearity, such as the drift of the beam centroid with the time (no null slope of the green fit), the asymmetric and not fully contained beam profile and missing measurements for the unconnected strips.

Additional tests have been planned in order to improve this limit and verify the full linearity, for example a test with a full contacted detector, and a beam profile more narrow and regular in the shape, as expected to be during the experiment.

III.7 Conclusions

In this chapter the laser-induced graphitization of several detector grade CVD intrinsic polycrystalline diamond samples (small and large, $5 \times 5 \times 0.05$ mm^3 and $20 \times 20 \times 0.05$ mm^3, respectively) has been presented. The development of a LabVIEW software allowed fabricating bi-dimensional graphitic pattern satisfying the electrode geometric requests for the segmented all-carbon detector of the PADME experiment. A wide characterization of the graphitic pattern was carried out on the small diamonds by complementary experiments which are sensitive to different properties of the modified material. In particular, SEM and micro-Raman investigations allowed understanding the physical evolution of the graphitization process, and in particular how the morphological and structural changes depend on laser processing. The two techniques indicate a strong periodicity of the surface modifications correlated to the fabrication process. Then, phenomena of absorption from environment were evidenced by EDS analyses, where oxygen impurities were found on all the irradiated areas, with increasing intensity values for the most damaged zones. Afterwards, hardness and elastic modulus mappings were performed showing that hard-soft transformation occurred depending on the locally deposited energy. The finding proves to be in line with the change of hybridization ($sp^3 \rightarrow sp^2$) of carbon atoms recorder by SEM and micro-Raman results. Nevertheless, a difference in the graphitization degree recorded by Raman and nano-indentation investigations, namely the narrow C' region at the border between A and B areas, was not recognized by SEM analyses, so as the morphological study detected small differences between A and B regions, which were not confirmed by spectroscopic and mechanical investigations. These aspects can be further studied by a more in-depth analysis.

Finally, current-voltage measurements allowed investigating the nature of the diamond / graphite contact and evaluating the graphitic strip resistivity values. In particular, good conductive properties and ohmic behavior were observed for all the graphitic strips, with a resistivity average around $2.5 – 3 \times 10^{-5}$ Ω.m along the strips. In addition, exiguous currents of about some hundreds of fA were measured between coplanar strips over the voltage range from −10 V to +10 V suggesting an ohmic nature for the graphite/diamond contact and making the strips suitable as electrodes in all-carbon sensors.

Afterwards, a large CVD polycrystalline intrinsic diamond graphitized with the same strip-like electrode configurations was assembled onto a dedicated PC-board by silver paint and wire bonding, and was tested as first prototype of this all-carbon sensor by 450 MeV electron and positron beams at the BTF of Frascati (Italy) as an preliminary investigation to the PADME experiment. Although great reliability and stability was recorder for the graphitic contacts, some problems of PC-board planarity together with some jumped off wire bonding was met. Taking advantage of the twenty-two graphitic strips correctly contacted a wide nuclear investigation was carried out. The detector CCD was measured of the order of 10 μm for an electric field of 3 $V.\mu m^{-1}$ without pumping, as expected for such an as-grown CVD polycrystalline diamond sensor. By high intensity particle electron and positron beams (of the order of 10^4 per bunch) a time resolution of 2 ns and a space resolution of about 200 μm were obtained. In addition, the detector capability of following the beam position variations with the time was also investigated obtaining first good results and with the possibility to improve them by fixing some systematic errors. Definitely, the all-carbon detector performance prove to satisfy all the requests done for a sensor candidate as active target of the PADME experiment. Finally, these findings show also that this kind of detector can be used to monitor online a particle beam with high intensity.

CHAPTER IV: GROWTH AND CONTACTING OF CVD MONOCRYSTALLINE BORON DOPED DIAMONDS

IV.1 Introduction

In the chapter I it has been discussed what is today the state of art of the diamond contacting with a deep focus on the problem of the ohmic contact manufacturing on lightly doped diamonds. In particular, nowadays it proves to be not particularly difficult to produce ohmic electrodes on heavily p-type doped samples, even if less success has been obtained for lightly doped samples and it is still an open field for n-type doping.

Traditionally, the diamond electrodes can be produced in two ways: diamond metallization or diamond graphitization. In the first case, metallic layers are deposited on the diamond surface with appropriate micro-fabrication technological steps [117, 145, 157, 161]. In the second case, the diamond graphitization process is used to induce the formation of graphitic contacts on the diamond surface or into the bulk. This process has been experimented by laser (for surface and buried contacts) [180, 183-186], or by ion implantation to produce electrodes into the diamond bulk [200] or to generate defects at the surface by direct heavy boron implantation [199].

The main idea of this work has been to combine both techniques in order to improve the electrical conduction at the diamond / metal interface. Indeed, the diamond graphitization just underneath the surface should create some defects and consequently reduce the depletion region width by decreasing the potential barrier height at the diamond / metal interface [121].

In this chapter, the synthesis of CVD monocrystalline diamond films at different boron doping levels, the diamond graphitization process by ion implantation, the manufacturing of mesa structure and TLM metallic patterns on the samples allowing electrical contact characterizations will be presented.

IV.2 Diamond synthesis and characterization

IV.2.1 Synthetized samples

Several CVD monocrystalline diamond films with different boron doping levels were grown. The reactors utilized for the synthesis were two commercial micro-wave chemical vapour deposition reactors (Plassys BJS150) which have been described in Chapter II. One is dedicated to the growth of intrinsic diamond films and the other one to boron doping. The growth conditions were the same for all the samples except for the diborane (B_2H_6) concentration in the gas phase and growth duration. The growths were performed by homo-epitaxy on (100) oriented type-Ib HPHT substrates having dimensions of 3 × 3 × 1.5 mm^3. The substrate temperature was adjusted at 900 °C, the methane

content at 5% of the gas mixture, the gas pressure at 140 mbar, the microwave power at 2.4 kW and the total gas flux at 200 sccm/min.

The $(B/C)_{gas}$ ratio was varied in the range 0 – 15000 ppm for reaching a wide set of boron doping level. Oxygen was added to the gas mixture $H_2/CH_4/B_2H_6$ to limit soot production in the plasma and improve surface morphology as previously demonstrated [269] even if it is well known that the addition of this gas reduces doping level [270]. In addition, in order to overcome the typical boron concentrations reached with a gas mixture involving oxygen atoms, a higher boron level in gas phase ($(B/C)_{gas}$ ratio 15000 ppm) without oxygen gas was performed. The growth duration was varied from 35 minutes to 2 hours and 45 minutes.

For the sample grown without diborane addition ($(B/C)_{gas}$ ratio 0 ppm) the doping was ensured by the boron memory effects in the bell jar reactor. This sample has been labelled "Not Intentionally Doped" (NID) sample [271].

Finally, another sample was grown without dopant gas (B_2H_6) but in a different reactor which has been exclusively dedicated to the synthesis of intrinsic diamond films avoiding any doping.

The sample's growth conditions are described in Table IV.1 and the corresponding sample morphologies are shown in Figure IV.1.

Table IV.1. Diamond samples: growth conditions and geometric parameters before and after the growth processes. The intrinsic and boron reactor are labelled as I and B in the R column, respectively. L, Wi, We, T indicate the sample length, width, weight and thickness, respectively; while the i and f subscript refer to the initial and final states. The growth duration and the CVD thickness are labelled as t and T_{CVD}, respectively.

Sample	Growth Conditions						Geometric Parameters						
	(B/C)gas phase (ppm)	R	Gas H_2 (sccm)	Gas CH_4 (sccm)	Gas O_2 (sccm)	Gas B_2H_6 (sccm)	L_i (mm)	Wi_i (mm)	We_i (g)	We_f (g)	T_i (mm)	t (min)	T_{CVD} (µm)
A	Intrinsic	I	189.5	10	0.5	0	3.16	3.16	0.05091	0.0514	1.477	110	4.9
B	NID	B	189.5	10	0.5	NID	3.18	3.18	0.05179	0.05227	1.496	60	4.7
C	3000	B	184.5	10	0.5	5	3.16	3.16	0.05025	0.05092	1.470	100	6.6
D							3.16	3.14	0.05091	0.05134	1.494	60	4.2
E	6000	B	179.5	10	0.5	10	3.15	2.92	0.04639	0.047	1.475	90	6.4
F							3.17	3.17	0.05115	0.05159	1.484	60	4.3
G	12000	B	169.5	10	0.5	20	3.16	3.16	0.04933	0.05043	1.440	165	11
H							3.17	3.16	0.05036	0.05072	1.474	60	3.5
I	15000	B	165	10	0	25	3.16	3.16	-	-	1.460	35	2
J							3.17	3.16	-	-	1.470	35	2

The thickness of the grown CVD layers were estimated for the samples A, B, C, D, E, F, G and H by measuring the weight before and after the growth associated with the initial dimensions of the substrates. The CVD thickness of the most doped samples, namely I and J, were measured directly using a calliper before and after growth, as a consequence of the very low increase of the weight after growth.

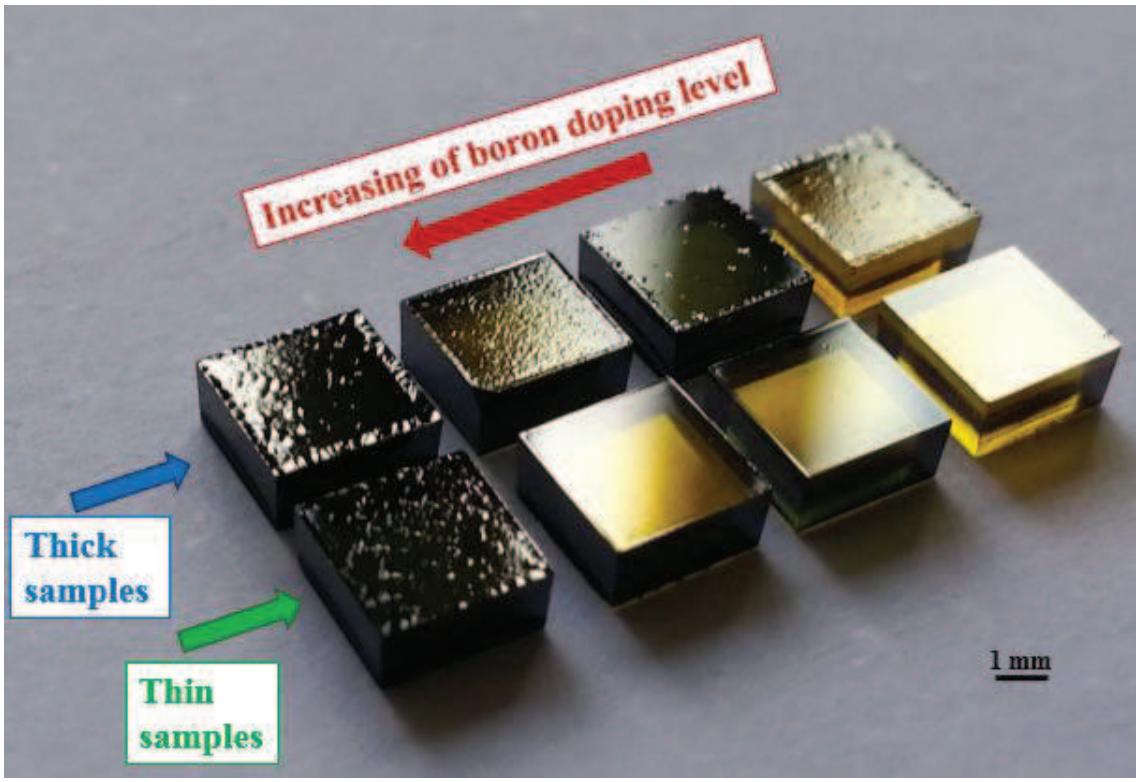

Figure IV.1. Picture of the set of diamond samples as-grown. In the first column on the left two samples with the same boron doping of 12000 ppm $(B/C)_{gas}$ but different thickness (the thicker films on the top and the thinner ones on the bottom) are presented. Similarly, the second and third columns are arranged for the doping levels of 6000, 3000 ppm $(B/C)_{gas\ phase}$. Finally, in the fourth and last column the NID and intrinsic diamonds are placed on the top and bottom row, respectively.

In Figure IV.1, it is possible to appreciate the evolution of the colour and of the surface roughness. Basically, for the intrinsic diamond, a transparent colour is expected but considering that the growth was performed on Ib type HPHT substrates, the typical yellow colour due to nitrogen impurities (which are called H_3 defects) dominates (sample in the bottom-right corner). When the boron concentration is increased, it is evident that the sample's colour becomes darker or even black colour for the most doped samples (diamonds on the left side of the picture). This effect is in line with the presence of boron impurities in the CVD layers [213].

Finally, an evident variability in terms of diamond surface roughness can be observed. In particular, for longer depositions (i.e. thicker CVD layers), the roughness of the sample increases particularly at the edges probably because of a higher local temperature. This is clearly illustrated since the edges appear rougher than the central part of the sample. In addition, at high boron levels, the defect density

and the surface roughness increase. As a consequence, the thinner and less doped sample proved to be the smoother one of all the set (see in the right-bottom corner of the picture).

It is worth reporting that the synthesis of thick CVD boron doped diamond layer was planned to develop the technological micro-fabrication steps. On the contrary, the synthesis of thin samples was dedicated to the full device processing and their characterizations, once the micro-fabrication process is developed.

Then, the investigations of the diamond set from structural, chemical and electrical points of view, are described below.

IV.2.2 Micro-Raman analyses

The micro-Raman investigations can provide information about the boron impurities by the Fano effect which is a distortion of the diamond Raman peak (as explained in the Chapter II). All the samples were analysed using an excitation wavelength of 632 nm. The Raman spectra of the samples labelled B, D, and F proved to be very similar, without evidence of Fano effect, while the spectra of the most doped samples (H and J) presented a small Fano effect. The spectrum of the sample F representing the first group of diamonds, and the spectrum of the sample J showing the Fano effect are reported in the Figure IV.2 (a) and (b), respectively.

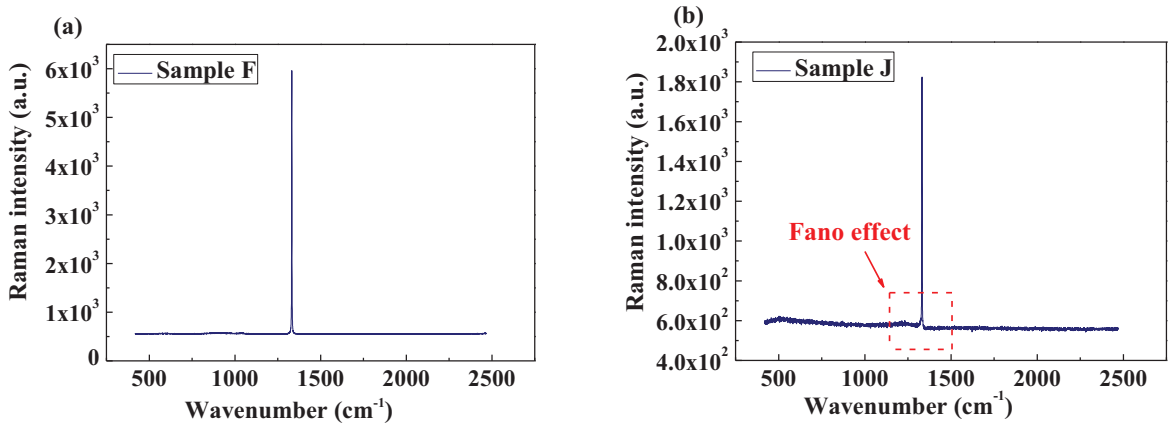

Figure IV.2. Micro-Raman spectra without (a) and with (b) evidence of the Fano effect corresponding to the samples F and J, which were doped with a $(B/C)_{gas}$ equal to 6000 and 15000 ppm, respectively. A red dashed square indicates the zone of the Fano effect (b).

The Fano effect evidences only for the most doped samples is an expected result and can be considered in line with the literature [219, 220]. Therefore, further investigations proved to be necessary in order to obtain a quantitative estimation of the different doping levels.

In the next paragraph, the investigations carried out by cathodoluminescence spectroscopy are presented.

IV.2.3 Cathodoluminescence measurements

Cathodoluminescence (CL) is a non-destructive technique that allows getting a quantitative estimation of the boron concentration in single crystal diamond films [226, 270, 272]. Besides, CL is useful to get qualitative information about the crystalline quality of the films by detecting the presence of extended defects (dislocations, stacking faults…) or other frequently found impurities such as nitrogen or silicon leading to luminescence at different wavelengths.

Barjon et al. studied excitonic emission for a set of CVD monocrystalline boron doped diamond layers with different doping levels (10^{16} – 10^{18} cm^{-3}) by Secondary Ion Mass Spectroscopy (SIMS) and CL, in order to correlate exciton recombination emission with boron concentration in the films [272]. SIMS is a destructive technique that gives a fairly accurate value of the total amount of boron by sputtering a small hole inside the crystal and analysing the resulting ionized atoms with a mass spectrometer. On the other hand CL is only sensitive to substitutional acceptor boron atoms onto which excitons generated through interaction with incident electron beam are bound before recombining. In diamond films with sufficiently good crystalline quality and low doping, almost all boron atoms are actually in substitution to a carbon atom with very low compensation [94].

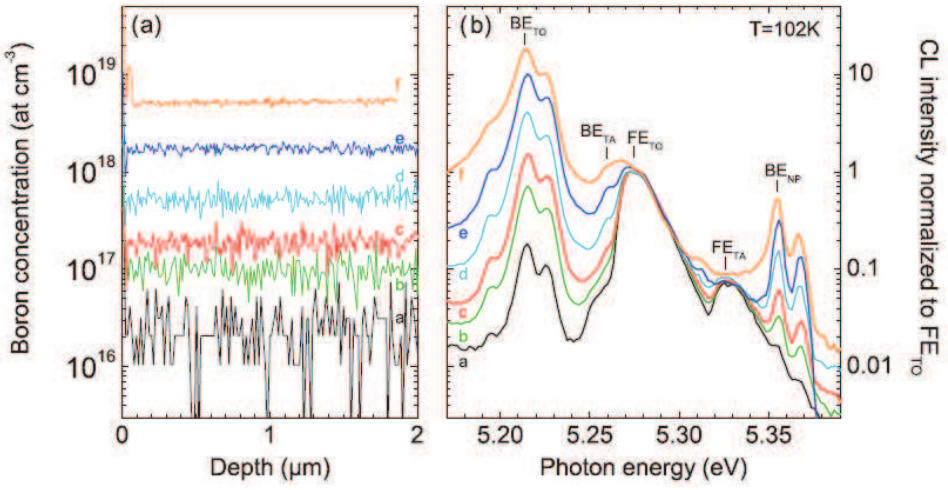

Figure IV.3. SIMS profiles registered on a set of monocrystalline boron doped samples with different doping levels (a); CL spectra for the corresponding samples after normalization to the FE_{TO} peak (b), [272].

In Figure IV.3 (a), SIMS analyses give access to boron concentration for each sample as a function of etching depth [272]. On the corresponding CL curves (b) different emissions from boron bound exciton and free exciton recombinations assisted by transverse optical (TO) or acoustic (TA) phonons,

in addition to the bound boron exciton without phonon participation (NP) are detected. It is possible to appreciate a clear correlation between the evolution of the luminescence intensity ratio of BE_{TO} and FE_{TO} peaks with the corresponding SIMS boron concentrations Figure IV.4.

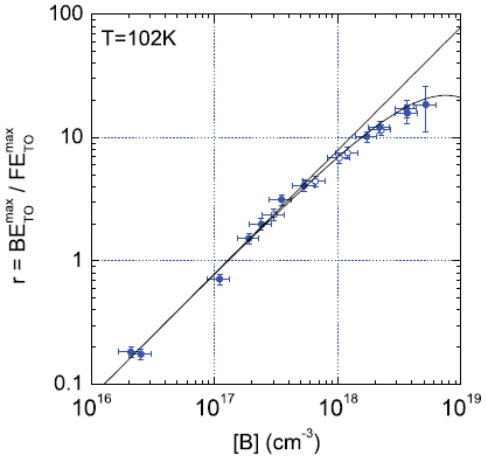

Figure IV.4. Plot of the intensity ratio BE_{TO} / FE_{TO} against the boron concentrations. The data were interpolated by a linear fit, which proved to be in good agreement until the boron concentration [B] ≈ 6 × 10^{17} cm^{-3}, and then by an exponential fit above this value [272].

Fitting the data, this ratio proved to be almost linear up to a B concentration of about 6 × 10^{17} cm^{-3}. Above this value, it substantially deviates from a simple linear relation but can be estimated using an exponential fit up to almost 10^{19} cm^{-3}.

$$\frac{BE_{TO}}{FE_{TO}} = A \cdot [B] \qquad \text{Equation IV.1}$$

$$\frac{BE_{TO}}{FE_{TO}} = A \cdot [B] \cdot e^{(-1.32 \cdot 10^{-19}[B])} \qquad \text{Equation IV.2}$$

where the BE_{TO} / FE_{TO} ratio was measured on the CL spectra, [B] was the boron concentration measured by SIMS, and A an empirical coefficient equal to 7.9 × 10^{-18}.

For heavy doping, free exciton emission becomes quenched and the previous relations can no longer be used. However, since bound exciton recombination emission becomes enlarged and shifted to lower energies it is possible to exploit this relative change to get an estimation of the doping level. This is particularly obvious in the Figure IV.5 below from Baron et al. that presents BE_{TO} linewidth and position as a function of doping measured by SIMS. This observation is consistent with the fact that at sufficiently high doping, B atoms no longer behave as isolated acceptors but form an impurity band with reduced ionization activation energy (illustrated by the dashed line B1 below), or even lead

to a metallic transition typically above 3×10^{20} cm^{-3} (visualized by the dashed line B2 below). The equation describing this was given by:

$$E(eV) = 5.211 - 0.112\log([B]/1.5 \cdot 10^{19}) \qquad \text{Equation IV.3}$$

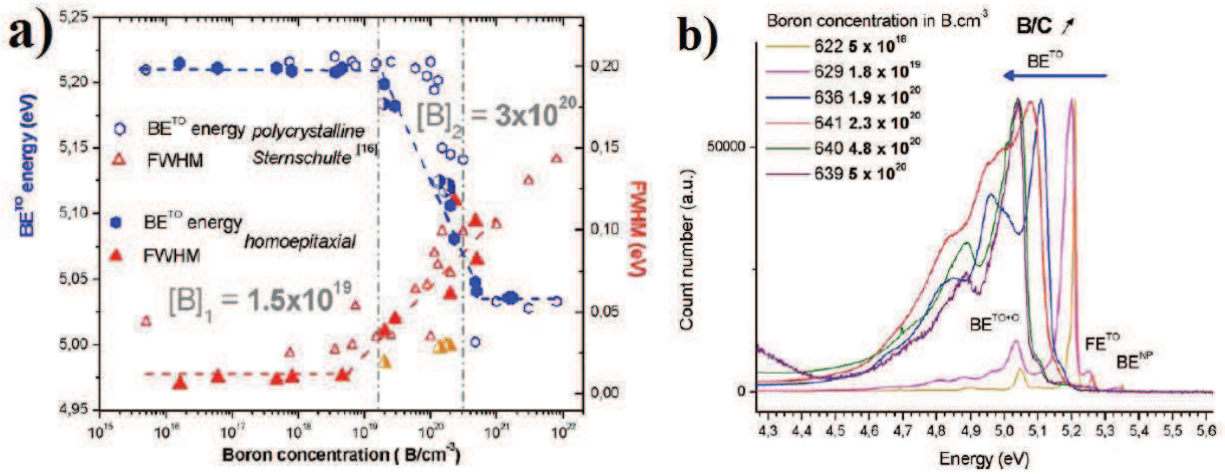

Figure IV.5. (a) Evolution of the BE^{TO} peak energy (left axes) and FWHM (right axes) against the boron concentration for diamond samples with different boron doping level. Full, empty and mixed symbols indicate monocrystalline, polycrystalline or other samples, respectively [226]. (b) Cathodoluminescence spectra registered on CVD monocrystalline boron doped diamonds with different doping levels [226].

In this study, these different empirical formulae were used to evaluate boron doping in lightly (B, D and F) and heavily (H, J) doped diamond films. It should however be emphasized that a more accurate assessment would require that a range of calibration samples having different doping levels measured by SIMS and CL under the conditions of this measurement system is used. Indeed the obtained results strongly depend on the measurement set-up (acceleration voltage, beam current, sample temperature etc.) and cannot be considered as universal.

The Figure IV.6 (a) below presents the CL spectrum of lightly doped diamond film (B) over the full spectral range and acquired at 110 K. One can note that emission from NV centres expected at 575 nm and SiV at 737 nm is absent from the spectra which further underlines the high purity of the layers. On the other hand a large band is detected in the UV range (around 350-400 nm) which is likely related to the presence of extended defects such as dislocations and is known as Band A luminescence [273]. Therefore the films produced by CVD are not free of this kind of defects [274].

A zoom into the excitonic region is also provided from which bound and free exciton recombination emissions assisted by TO and TA phonons can be clearly assigned (Figure IV.6 (b)). This further supports the high crystalline quality and efficient doping of the film. Using Equation IV.1 boron doping level can be estimated to around 1×10^{17} cm^{-3} from a BE_{TO}/FE_{TO} ratio close to unity. Sample B was grown in a reactor dedicated to high p-type doping without any intentional addition of diborane in the gas phase. Therefore boron dopants detected here all come from memory effects inside the

CVD chamber which are known to be very high for this element. In addition, also the samples D and F were investigated showing a BE_{TO}/FE_{TO} ratio of about 4 and 20, respectively, and therefore the obtained boron concentration values are around 4×10^{17} cm^{-3} and 3×10^{18} cm^{-3}, respectively.

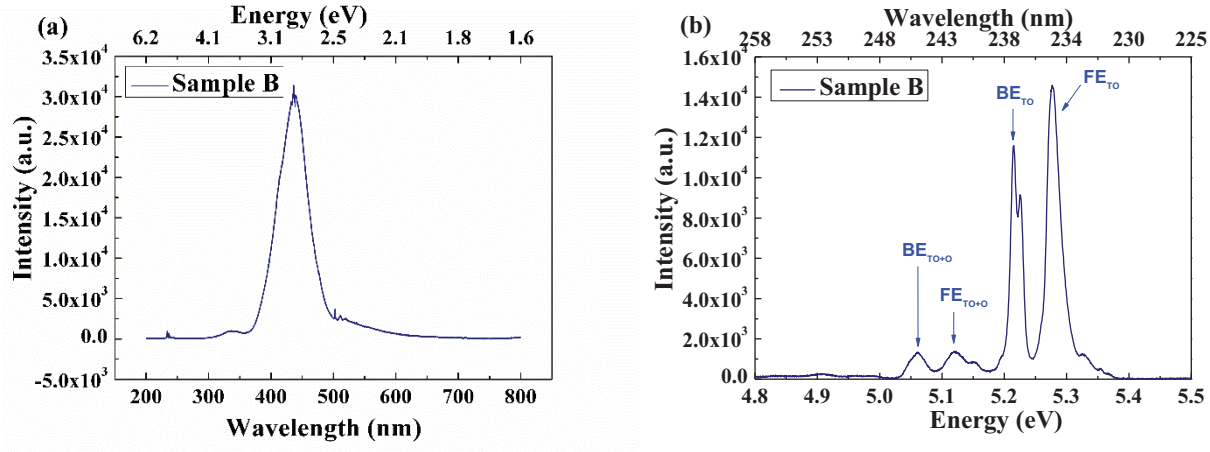

Figure IV.6. Full cathodoluminescence spectrum (a) and zoom into the excitonic region (b) registered for the NID sample at 110 K. The boron concentration is estimated to be about 1×10^{17} cm^{-3} from the BETO to FETO ratio.

CL measurements were also performed for highly doped samples H and J. The spectrum corresponding to sample H is presented in Figure IV.7. One can notice that they are dominated by BE_{TO} recombination that gives a broad and shifted emission line centred around 5.05 eV while FE_{TO} contribution is absent. This indicates a heavy doping level and an efficient incorporation of acceptor atoms inside the film consistent with a $(B/C)_{gas}$ ratio of 12000 ppm in the gas phase. Based on Equation IV.3 doping level is estimated having reached about 3.5×10^{20} cm^{-3} and it is therefore close to the metallic transition.

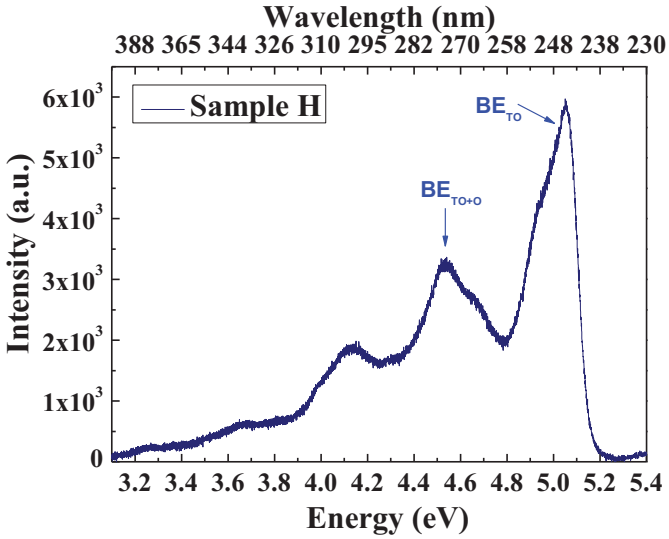

Figure IV.7. Cathodoluminescence spectrum registered on the H heavily boron doped sample at 110 K. The boron concentration is estimated about equal to 3.5×10^{20} cm^{-3}.

Similarly, the sample J was investigated too proving to have a BE_{TO} peak at around 5.04 eV and therefore a boron concentration of 4×10^{20} cm^{-3}.

To summarize this part, an estimation of the boron doping level for the samples measured by CL is presented in Table IV.2.

Table IV.II. Boron concentration levels estimated for the CVD monocrystalline boron doped diamonds.

Sample	(B/C)gas phase	[B] cm^{-3}
B	NID	1×10^{17}
D	3000	4×10^{17}
F	6000	3×10^{18}
H	12000	3.5×10^{20}
J	15000	4×10^{20}

IV.2.4 Electrical characterizations

The presence of boron impurities improves the electrical conduction thanks to the introduction of an acceptor levels in the band gap [89]. In order to assess this in our films, electrical characterization was carried out with a four-point probe instrumentation (as explained in the Chapter II).

Before doing these measurements, all the samples were exposed to a vacuum ultraviolet (VUV)-light irradiation with a monochromatic xenon excimer lamp (wavelength of 172 nm) in oxygen atmosphere, in order to change the hydrogen terminations into oxygen terminations. Indeed, in literature it is known that this kind of treatment can change the electric conduction properties thank to photochemical reactions and excited radicals which act simultaneously on diamond surfaces creating a layer of electrical passive oxygen terminations [133]. The sample exposure to UV lamp was performed for 45 min in oxygen atmosphere with a pressure of about 2 mbar.

During the electrical measurements, different current ranges where applied depending on the sample response. In particular, the applied current modulation was done trying to limit the polarization effects. All the registered current-voltage curves are shown in Figure IV.8.
From Figure IV.8 it is possible to show that all samples have an ohmic behaviour. Moreover, the evolution of the slope indicates that the resistivity decreases when the boron doping level increases.

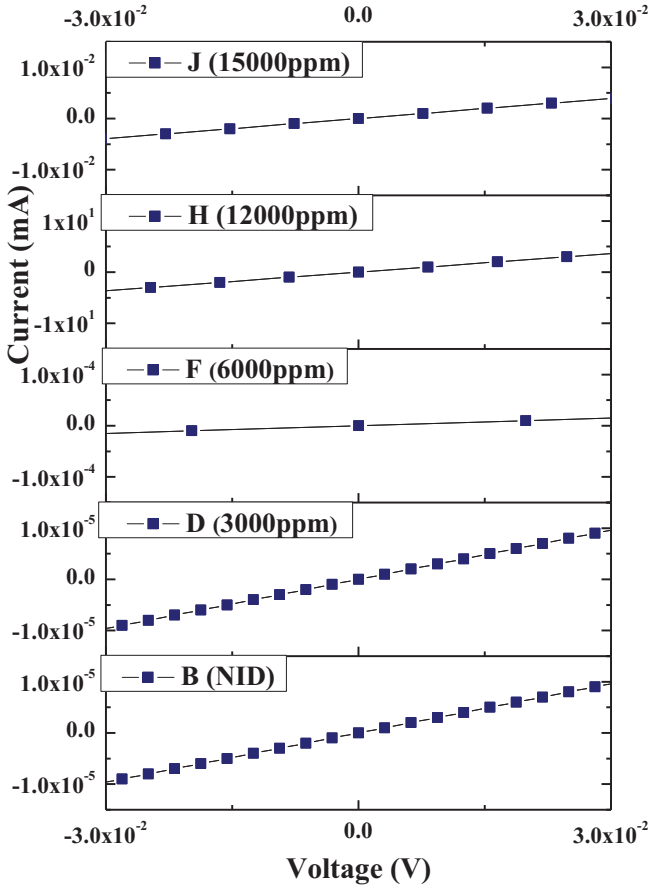

Figure IV.8. Current-voltage measurements on the diamond samples (B, D, F, H and J) with different boron doping levels (NID, 3000, 6000, 12000 and 15000 ppm). For clarity, different Y-axis scales were used.

In order to quantitatively compare the electrical conductivity of the samples, the volume and sheet resistivity values were estimated using the following equations:

$$\rho = \frac{\pi}{ln2} \cdot F \cdot \frac{V}{I} \cdot t \qquad \text{Equation IV.4}$$

$$\rho_{\square} = \frac{\pi}{\ln 2} \cdot F \cdot \frac{V}{I} \qquad \text{Equation IV.5}$$

where F is the correction factor which takes into account the sample limited geometry and proved to be about 0.6, and t is the thickness of the CVD boron doped diamond layer [233, 234].

These results are summarized in Table IV.3.

Table IV.3. Volume and sheet resistivity values computed for the set of samples with different boron doping levels.

Sample	[B] (cm^{-3})	Resistance (Ω)	CVD Thickness (µm)	Volume Resistivity (Ω.cm)	Sheet Resistivity (Ω/□)
B	1×10^{17}	3.1×10^{3}	4.7	4.00	8.49×10^{3}
D	4×10^{17}	3.2×10^{3}	4.2	3.60	8.63×10^{3}
F	3×10^{18}	2.0×10^{3}	4.3	2.32	5.39×10^{3}
H	3.5×10^{20}	8.2	3.5	7.8×10^{-3}	2.20×10^{1}
J	4×10^{20}	7.6	2	4.13×10^{-3}	2.00×10^{1}

These findings confirm that the electrical conduction increases with the boron doping level (samples D, F, H, and J), and they suggest that above a certain threshold, further increasing the doping level (from 12000 to 15000 ppm) has little effect on the resistance value. In addition, for low doping levels, $(B/C)_{gas\ phase}$ of 3000 ppm and NID (samples D and B respectively), the resistivity values prove to be almost the same, which means that it was not possible to reduce the boron concentration in the CVD diamond layer or more properly to decrease the resistance value below a certain value due to the boron memory effect. This behaviour has been confirmed by CL analyses.

Figure IV.9 shows the evolution of the sheet resistivity values as a function of the boron doping levels.

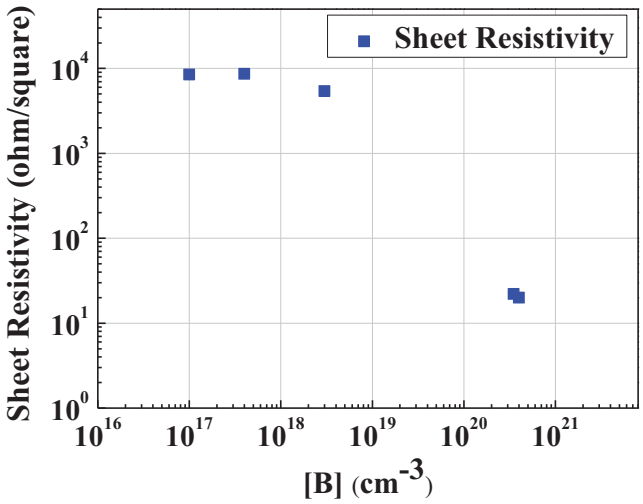

Figure IV.9. Boron doped diamond sheet resistivity as a function of the boron concentration in the CVD layers estimated by CL measurements.

Based on these first electrical measurements, samples D and J with very different electrical behaviour (low and high conductivity respectively) were considered as the most interesting for manufacturing metallic contacts with and without an intermediate graphitic layer.

IV.3 Ion implantation on CVD monocrystalline intrinsic diamond

For heavily boron doped diamond devices, it is possible to manufacture ohmic contact by directly depositing metallic layers [117] on the contrary, for lightly boron doped diamonds it is more difficult to get an ohmic behaviour [131].

To improve the contact electron conduction several tries have been done in literature. For example, in the case of heavily doped samples, Pinero et al. [199] increased the electrical conduction of the contacts by direct boron implantation so as to generate defects in a very thin superficial layer in the same time as the diamond doping process. On the contrary, for lightly doped samples, Chen et al. [198] produced a graphite / metal contact interface which made ohmic the contacts even if the specific contact resistance value remains quite high (≈ a few Ωcm^{-2}). In this case, the graphitization was performed by argon ion implantation at 40 keV. In this thesis work, the idea has been to manufacture graphite / metal contacts by adding the graphitic layer just underneath the diamond surface (and before the metallization) using a modified implantation system allowing the implantation of light ions (helium) at very low energies (only 10 keV). The graphitic layer production for diamond contacting applications was developed for the first time in LSPM during this thesis work.

The key experimental parameters for the ion implantation process are the ionic species, the implantation energy and the implantation dose (as explained in the Chapter I and II).

In order to produce a graphitised layer just underneath the diamond surface, helium was chosen as a suitable ion source. A low energy value of 10 keV was considered adapted to limit the penetration depth to a few tens of nm only. The current value was set to 300 µA and implantation time to 30 s. The implantation dose (Φ) can be computed by the equation:

$$\Phi = \frac{I \cdot t}{Q \cdot A} \qquad \text{Equation IV.6}$$

where I is the current value, t the implantation time, Q the elementary charge equal to 1.6×10^{-19} C and A the cross section of the beam, this latter being estimated from the circular footprint of 5 mm. However, the diamond sample (0.1 cm^2) proved to be smaller than the footprint area (0.2 cm^2), therefore the implantation dose had to be normalized to the sample area. The final implantation dose was estimated to 1.4×10^{17} $ions.cm^{-2}$. The ion implantation treatment was performed at room temperature and in secondary vacuum condition (pressure of 10^{-5} mbar).

During the process development it was necessary to be sure to create a density of vacancies high enough to overcome the diamond graphitization threshold (this point has already been discussed in the Paragraph 1.9.5 of the Chapter I). Thanks to the Monte Carlo simulation performed using SRIM

software it was possible to get an estimation of the vacancy number created by every single helium ion before completely losing its energy through the diamond, and consequently an estimation of the vacancy density created by the whole ion bombardment [196, 275]. In particular, considering the diamond displacement energy of 52 eV [190] and its density equal to 3.52 $g.cm^{-3}$ [5], the carbon atoms number removed from their lattice sites by one ion (h_{ion}) proved to be about 13.8 and the vacancy density ($h_{density}$) generated by the whole ion bombardment computed by the Equation IV.7 was about 3.7×10^{23} $vac.cm^{-3}$.

$$h_{density} = \frac{\Phi \cdot h_{ion}}{d} \qquad \text{Equation IV.7}$$

where (Φ) is the implantation dose and d the penetration depth estimated by the software in terms of projected range. Indeed, by SRIM simulations, it was possible to investigate the penetration depth of the ion beam into the diamond (projected range R_P), its lateral and longitudinal dispersion (ΔR_P) and the distribution of vacancies in the considered material.

For a model of 10^4 helium ions with 10 keV energy reaching a diamond target, the estimated parameters were:

- $R_P = 52$ nm;
- $\Delta R_{P\text{-Longitudinal}} = 18$ nm;
- $\Delta R_{P\text{-Lateral}} = 16$ nm;

The Figures IV.10 shows the SRIM plot of the helium ion beam path into diamond material got for this model.

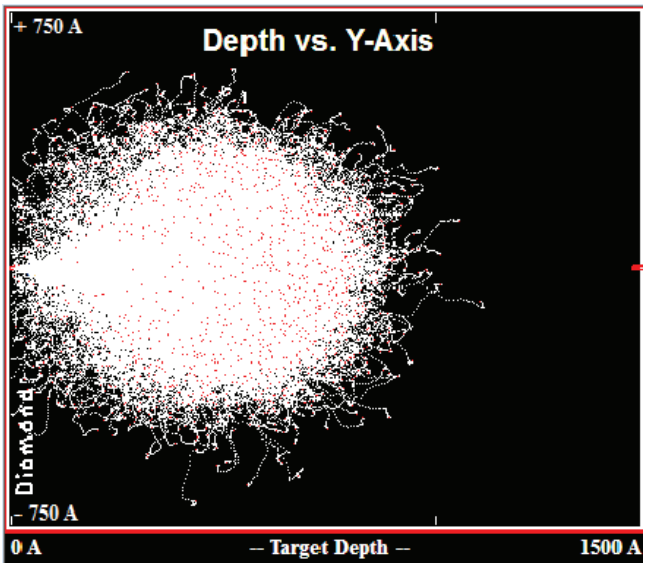

Figure IV.10. SRIM simulations for a model of 10^4 helium ions fired up into a diamond target with energy of 10 keV showing the ion path

This plot shows a white area on a black background which represents the incident ions and the consequent collisions. This zone has a 52 nm deep plume shape, which propagates into the crystal (from the left to the right side), with a longitudinal and lateral dispersion of 18 and 16 nm, respectively. The red and blue points in the plume represent the ion and electron collisions, respectively.

The calculations and the simulations performed for developing the ion implantation recipe predicted successfully the generation of a graphitic layer underneath the CVD diamond surface. Indeed, the obtained vacancies density proves to overcome the different critic graphitization thresholds defined in literature (which are at the order of $\approx 10^{22}$ - 10^{23} cm^{-3}) as reported in the Paragraph I.9.5 of the Chapter I.

Following experimental characterizations of the ion implanted-induced graphitic layer into the CVD intrinsic diamond are reported.

IV.3.1 Optical characterization

The ion implantation recipe was developed on an intrinsic CVD monocrystalline diamond grown on a type-Ib HPHT substrate (sample A). Pictures of the sample before and after the implantation treatment are presented on Figure IV.11. Even if the graphitic layer is estimated to be just underneath the CVD diamond surface (R_P = 52 nm), the impact in terms of colour is very important since the sample appears black.

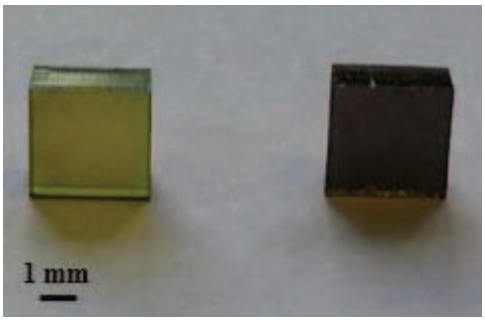

Figure IV.11. CVD monocrystalline intrinsic diamond before (on the left) and after (on the right) the graphitization process on the whole area. The diamond surface turns black.

Using a ring-like shadow mask during the implantation treatment, the contrast yellow / black colour on the same diamond surface can be clearly evidenced as illustrated in the Figure IV.12. This emphasizes that using a simple mask, graphitized layers can be spatially localized, forming a pattern on the crystal surface.

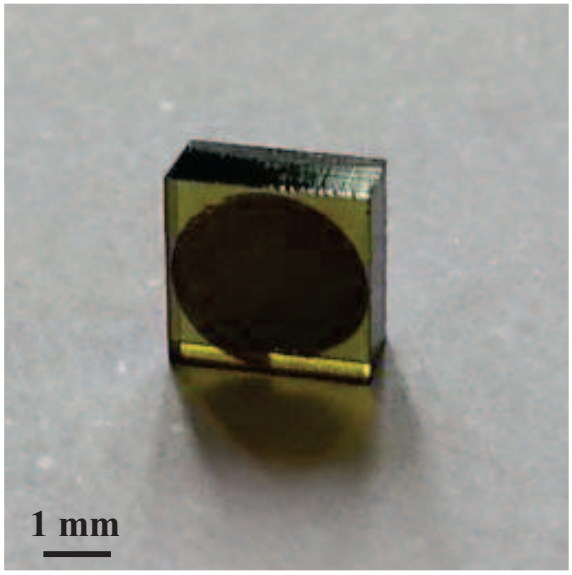

Figure IV.12. CVD monocrystalline intrinsic diamond after the graphitization process using a ring-like shadow mask. The dark circular shape is clearly the graphitic material while the yellow edge around is the CVD monocrystalline diamond on HPHT substrate.

Subsequently, structural and electrical investigations were performed on the ion implanted diamond and are presented below.

IV.3.2 Micro-Raman analyses

In order to study the structural evolution of the diamond sample exposed to the ion bombardment, micro-Raman analyses were carried out before and after the treatment in particular to estimate, step by step, the diamond-graphite phase change into the material.

Micro-Raman spectra registered on the initial intrinsic diamond sample A (on the bottom), after the ion implantation (in the middle) and after a thermal annealing (on the top) are shown in Figure IV.13.

The Figure IV.13 on the bottom shows a typical Raman spectrum of an intrinsic CVD diamond, with the only and well defined diamond peak localized at 1332 cm^{-1}. On the contrary, the spectrum of the picture in the middle presents a broad band in the range 1300 – 1600 cm^{-1}, which is a consequence of the implantation treatment. This result corresponds to the formation of amorphous sp^2-bonded carbon in addition to different types of radiation-induced defects, as expected [190]. Then, the picture on the top shows the structural change of the implanted diamond surface after an annealing treatment at 1000 °C for 60 minutes in secondary vacuum (10^{-6} mbar). The annealing experimental conditions were chosen starting from several studies described in the literature [214, 276]. The annealing role is to transform the amorphous material into graphite for the sufficiently damaged zone, while the surrounding areas are restored into diamond phase (see Chapter I Paragraph 9.5) [64]. As expected, the Raman spectrum of the annealed sample shows a significant decreasing of the previous broad

amorphization band whilst a sharp diamond peak can again be observed. In addition, a broad peak at 1580 cm^{-1} corresponding to the amorphous graphite contribution (G) associated to another broad peak at 1350 cm^{-1} corresponding to the disordered graphite contribution (D) are observed. These peaks confirm the formation of a graphite-like layer.

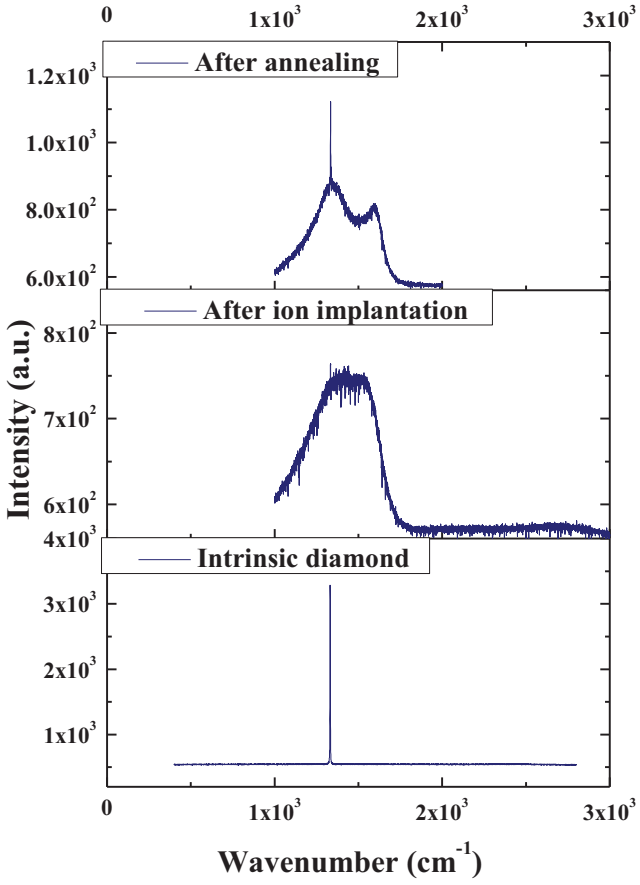

Figure IV.13. Spectroscopic evolution of the diamond and graphite peaks registered on the CVD intrinsic diamond A along three steps: as-grown (on the bottom), after ion implantation (in the middle) and after annealing (on the top).

IV.3.3 Current-voltage measurements

In order to study the electrical conduction changes induced on intrinsic CVD monocrystalline diamond by helium implantation, four-point probe current-voltage measurements were carried out. Before doing these measurements, the sample A was exposed to the VUV-light irradiation treatment for 45 min in oxygen atmosphere with a pressure of about 2 mbar.

The first electrical investigation of the intrinsic sample A was done before the ion implantation treatment in order to define the initial electrical conduction. As expected, the insulator nature of diamond did not allow measuring I-V curves for this sample. Afterwards, the sample was exposed to

the ion implantation and annealing processes while further electrical investigations were performed systematically after every specific treatment. No relevant electrical change was found between the analyses carried out on the ion implanted sample without and with the annealing treatment. This finding can be ascribed to no specific electrical improvement of the sp^2-bonded graphite rather than amorphous sp^2-bonded carbon on the electrical conduction. Therefore, the final current-voltage measurements registered on the sample after both ion implantation and the annealing treatments is directly reported in Figure IV.14. The plot shows an electrical conduction with an ohmic behaviour, which is proper of graphitic materials [14, 178]. A resistance value of 1×10^2 Ω was extrapolated and consequently, the sheet resistivity value was estimated by the Equation IV.5 equal to 282 Ω/□. This shows that we successfully improved contacts on intrinsic diamond through ion bombardment-induced graphitization of the surface.

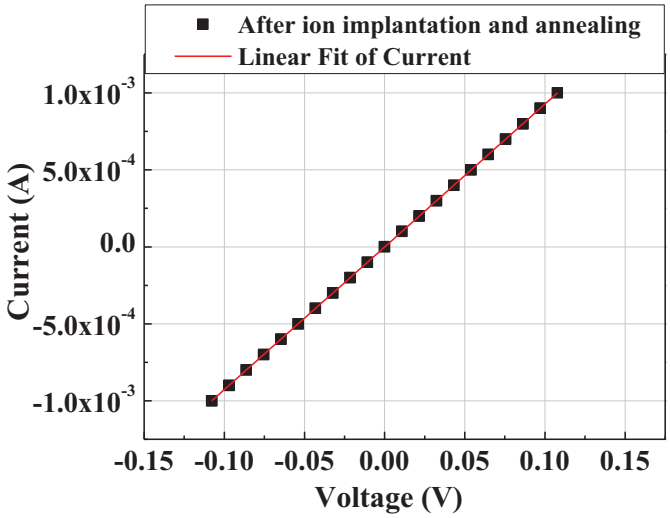

Figure IV.14. Current-voltage measurements on the intrinsic CVD diamond sample A after the ion implantation and annealing treatments.

IV.4 Manufacturing and characterization of TLM metallic contacts on bored doped diamonds with and without graphitic under-layer

In order to study the benefit of a graphitic layer manufactured underneath the CVD boron doped diamond surface, two sets of two samples (samples C and D with a boron doping level of 4×10^{17} cm^{-3} and sample I and J with a boron doping level of 4×10^{20} cm^{-3}) were contacted by metallic patterns with or without an ion implantation treatment. The diamond metallization was performed by the deposition of a typical metallic stacking composed of titanium and gold layers [5, 121, 132] in the common geometric configuration of TLM (Transmission Line Model [232]) pads. To improve the accuracy of the electrical measurements, the metallic pads were manufactured on a mesa structure

with the aim of confining the current lines in the active layer and avoiding electrical conduction on the CVD diamond lateral edges.

During the work carried out at LSPM, a protocol of the technological processing to manufacture the TLM pattern on diamond was developed.

The design and the micro-technological steps to perform TLM patterns on CVD diamond are described in the next paragraph. This work was performed mainly in the clean room of University of Paris 13 "Centrale de Proximité en Nanotechnologies de Paris Nord - C(PN)^2" except for the SiO_2, Ti and Au depositions which were carried out in the clean room of the University of Paris Diderot.

IV.4.1 Microfabrication of the TLM metallic contacts

The processing of mesa structure and metallic contacts started from samples composed of CVD boron doped monocrystalline diamond layers grown on HPHT diamond ($3 \times 3 \times 1.5$ mm^3). As previously explained, only two of the four samples fully processed were exposed to helium ion implantation and annealing treatments before performing the contact micro-fabrication steps (Figure IV.15, point #1). All the samples were preliminary cleaned by chemical washing in an ultrasonic bath with acetone and isopropanol solutions.

The mesa structures on boron doped diamond were performed by ICP deep etching of the CVD layers (Figure IV.15, point #5). The diamond etching plasma was obtained at low pressure and was composed of a mixture of oxygen gas with a small amount of CHF_3 gas to avoid micro-masking phenomena. For this step, a silica (SiO_2) mask was deposited in order to structure the diamond etching (Figure IV.15, point #2). The silica, together with a photoresist mask, was exposed to a mixture of CHF_3 and oxygen plasma to be structured (Figure IV.15, point #3 and #4). The benefits of using ICP technique are to obtain an anisotropy of the deep etching and therefore a relatively good verticality of the etching flank. This will be presented in the result section (Figure IV.18 and IV.19, Paragraph IV.4.3).

For the TLM electrodes fabrication, a titanium/gold bilayer was chosen as metallic materials in line with the typical contact composition used by the diamond community [5, 121, 132, 277]. As explained in Chapter I, the titanium layer was useful to reach a carbide formation with the diamond surface taking advantage of titanium reactivity [121]. Indeed adhesion of the metal on the diamond surface is an important aspect for the mechanical strength both when the electrical measurements and wire bonding are performed.

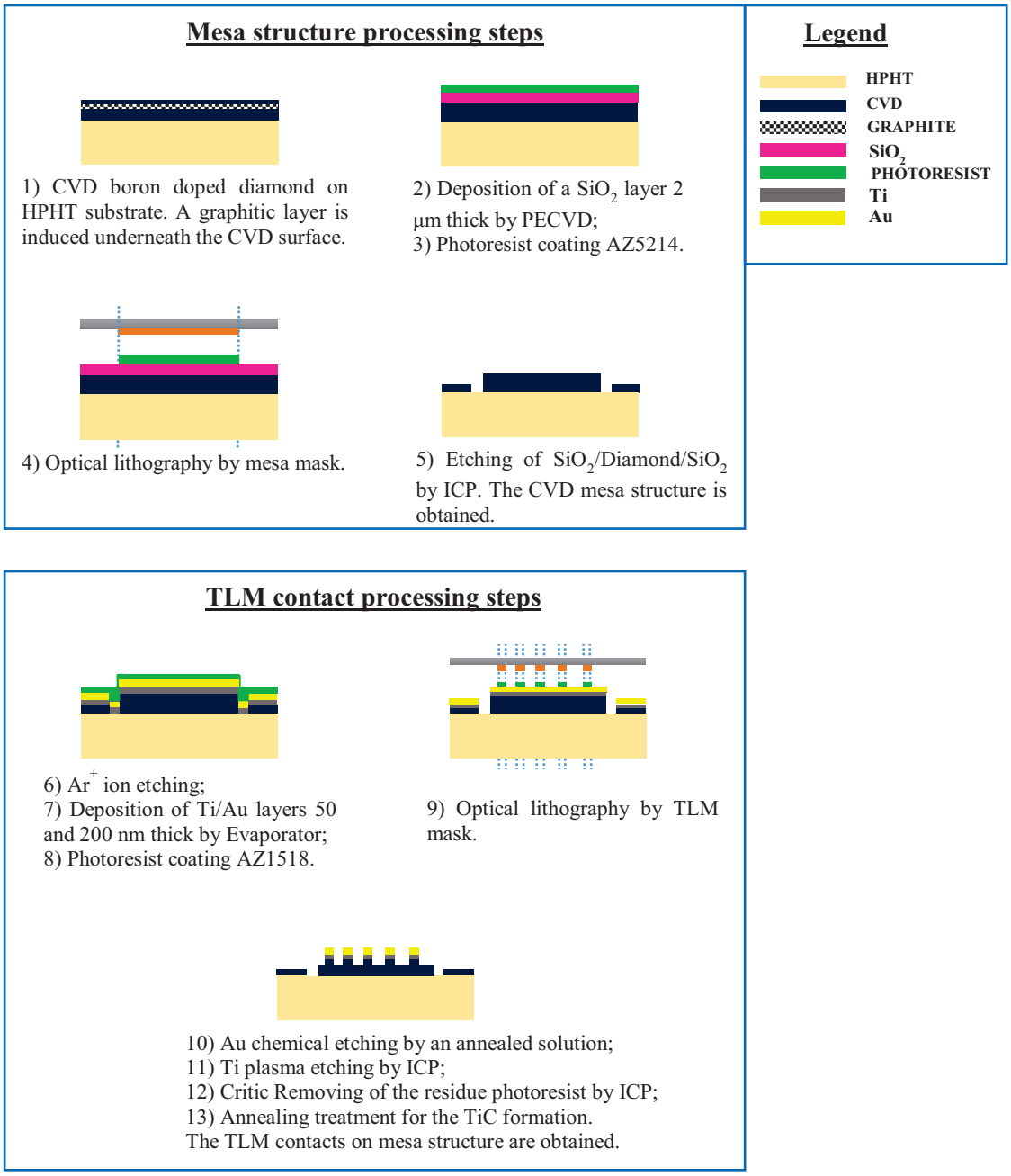

Figure IV.15. Technological steps of processing for the mesa structure and TLM pattern micro-fabrication.

In addition, during the development of the diamond metallization protocol, it has been understood that an etching pre-treatment of the surface was necessary to improve adhesion at the Ti / diamond interface by diamond surface activation (Figure IV.15, point #6). This pre-treatment on diamond samples was performed with an evaporator equipped with an argon plasma etching set-up (at University Paris Diderot). This aspect will constitute one of the critical points of the contact micro-fabrication reported in the next Paragraph IV.4.4. These pre-treatments have already been studied in literature [5] and explained in the state of the art chapter. After this argon etching, Ti/Au stack was deposited with the same evaporator (Figure IV.15, point #7). The gold layer avoids the titanium oxidation and improves the bonding to external circuit. By a subsequent optical lithography process

the TLM pad shape is transferred to the metal layers, while a chemical gold etching and a plasma titanium etching allowed to get the final contacts on CVD mesa diamond (Figure IV.15, point #8, #9, #10 and #11).

After the full development of the first samples it was observed the presence of a residual photoresist layer on the metallic contacts. This aspect constitutes one of the crucial points and it has been widely explained in the next Paragraph IV.4.4. To solve this problem it was necessary to add an oxygen ICP plasma etching step to remove the residual photoresist (Figure IV.15, point #12).

Finally, the last step concluding the contact micro-fabrication protocol was the titanium carbide formation (Figure IV.15, point #13). In particular, the Ti/C bond was promoted by an annealing treatment at 500 °C for 60 minutes in secondary vacuum conditions [132, 277].

The main technological steps are summarized in the previous Figure IV.15.

IV.4.2 TLM pattern design

According to the contact micro-fabrication protocol, to produce the metallic contacts on a CVD diamond mesa structure, two lithography processes were required, with different masks (one layer for each goal). In particular, the most important thing was to align the two complementary lithographic masks for the mesa zone and the metallic pads. In the following picture, both mask are presented.

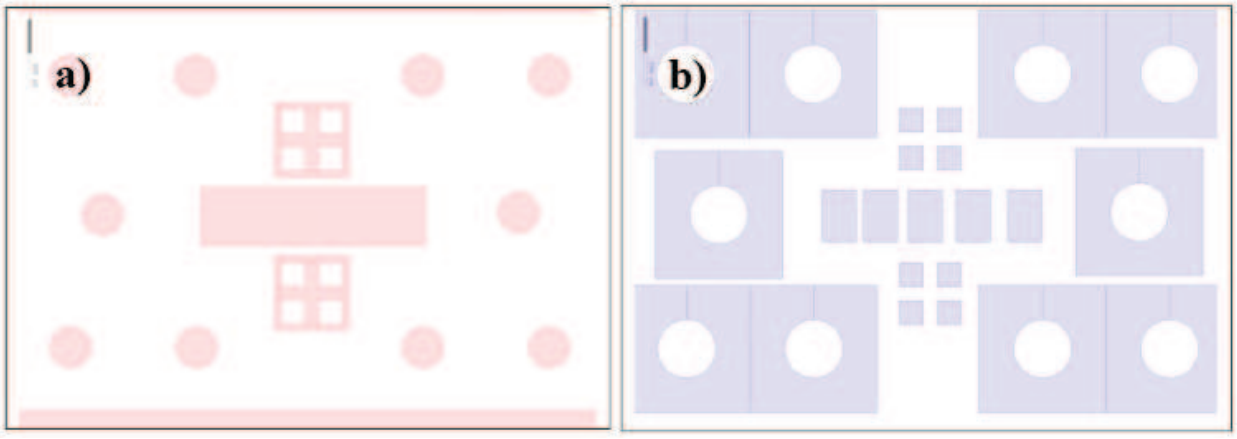

Figure IV.16. Top view of the lithographic mask projects to manufacture the mesa (a) and TLM pattern (b). The pink and blue colours of two pictures represent the sample regions not exposed to the lithographic UV lamp.

The Figure IV.16 (a) shows a central rectangular area representing the mesa zone. Above and below it, two large squares containing four empty squares are present and allow the alignment between the two masks. In addition, several pink spots are distributed on both mask sides and can constitute diode patterns which have not been used in this work. The Figure IV.16 (b) shows the TLM complementary

pattern of the mask (a). Therefore, five blue small rectangle shapes representing the ohmic pads are reported in the central zone. Above and below them are located four small full squares for the alignment, and finally six larger blue areas are also present, which represent ohmic contacts around diodes (empty circles).

The result of the overlapping of the two mask projects is shown in the Figure IV.17.

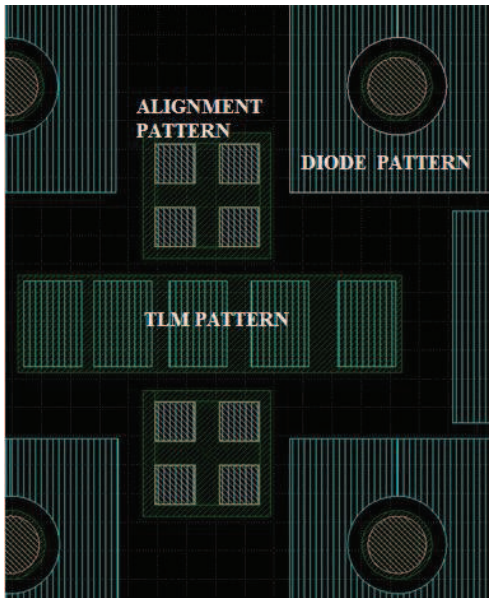

Figure IV.17. Overlapping of the mesa and TLM mask projects.

The ohmic pads are coloured in blue with dimensions of 100 × 150 μm^2, and increasing inter-spaces of 20, 30, 40 and 50 μm. The mesa structure is indicated by the green line around the pads, with a constant distance of 10 μm from them. For completeness, outside the mesa/TLM pattern, are distributed some red areas indicating the diode contacts (diameter of 100 μm), with their corresponding green circular mesa structure (diameter of 120 μm) and blue ohmic zones around them. The large green squares above and below the TLM pattern represent the overlapping of the alignment patterns.

IV.4.3 Characterizations of the micro-fabricated structures

A typical mesa structure obtained on the CVD boron doped diamond layers is presented in the Figure IV.18 with the aim of investigating the diamond plasma etching.

In picture (a) the complete top view of all the structures obtained by the first lithographic process is illustrated and the sample roughness due to the high boron doping is clearly visible (≈ 10^{20} cm^{-3}). In picture (b) is presented the mesa structure zone by optical microscope. Then, in pictures (c) and (d) a corner of the mesa structure is shown at different magnifications. On these 2 pictures, it is evident

that diamond etched surface presents some circular features probably due to a mixture of micro masking phenomena or/and to surface defects. Indeed, it is well known that when an ICP etching treatment is performed, residue clusters of the etched material remains around the sample, and which become "punctual mask" during the subsequent etching step for a different material [49]. In this specific case, the SiO_2 clusters allowed the diamond column formation in spite of the presence of CHF_3 gas in the etching plasma which should limit this phenomenon. In addition, some holes on the diamond surface are visible, probably related to extended defects emerging at the surface of sample [206]. Finally, in the last picture (d) it is possible to see the micro-trenching around and on the bottom of the mesa walls. According to the literature [278], this phenomenon is related to the ion reflection during the etching process from the mesa walls to the surrounding surface.

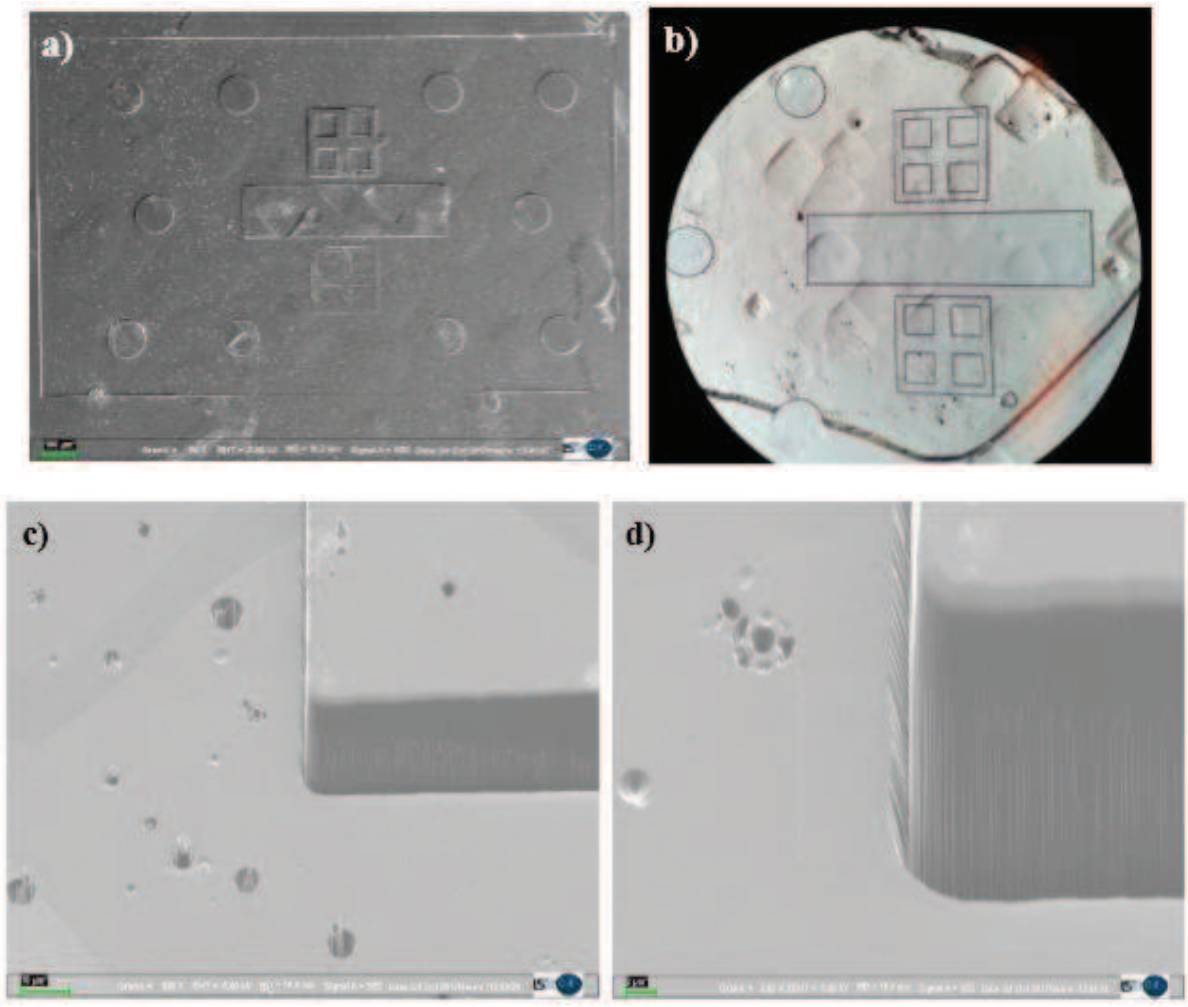

Figure IV.18. Mesa structures produced on the CVD diamond surfaces of two samples. (a) Top view of the whole mesa mask pattern registered on sample G by SEM and (b) top view of the mesa zone taken on sample I by optical microscopy. The different SEM enlargements ((c) lower and (d) higher) of the same mesa structure corner showing the good sharp etching of the mesa wall, with some etch pits distributed around the mesa structure taken on the sample G.

The mesa profile was measured by profilometer and reported in Figure IV.19. The measured mesa height was almost 13 µm.

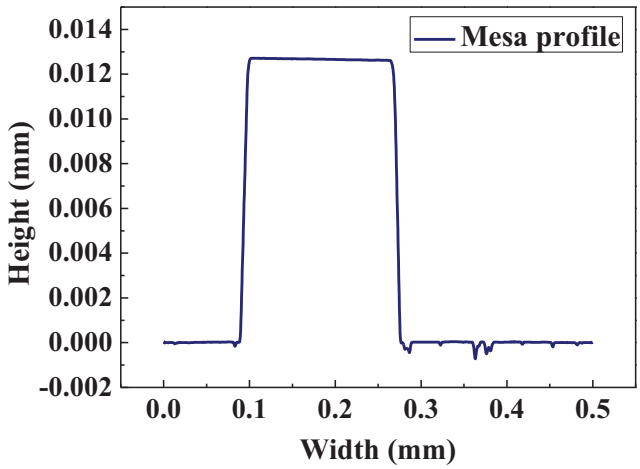

Figure IV.19. CVD diamond mesa structure profile registered by profilometer on the G sample.

Afterwards, additional SEM analyses were carried out on the full processed samples and reported in Figure IV.20. The pictures set have been taken on the metallized E and I samples.

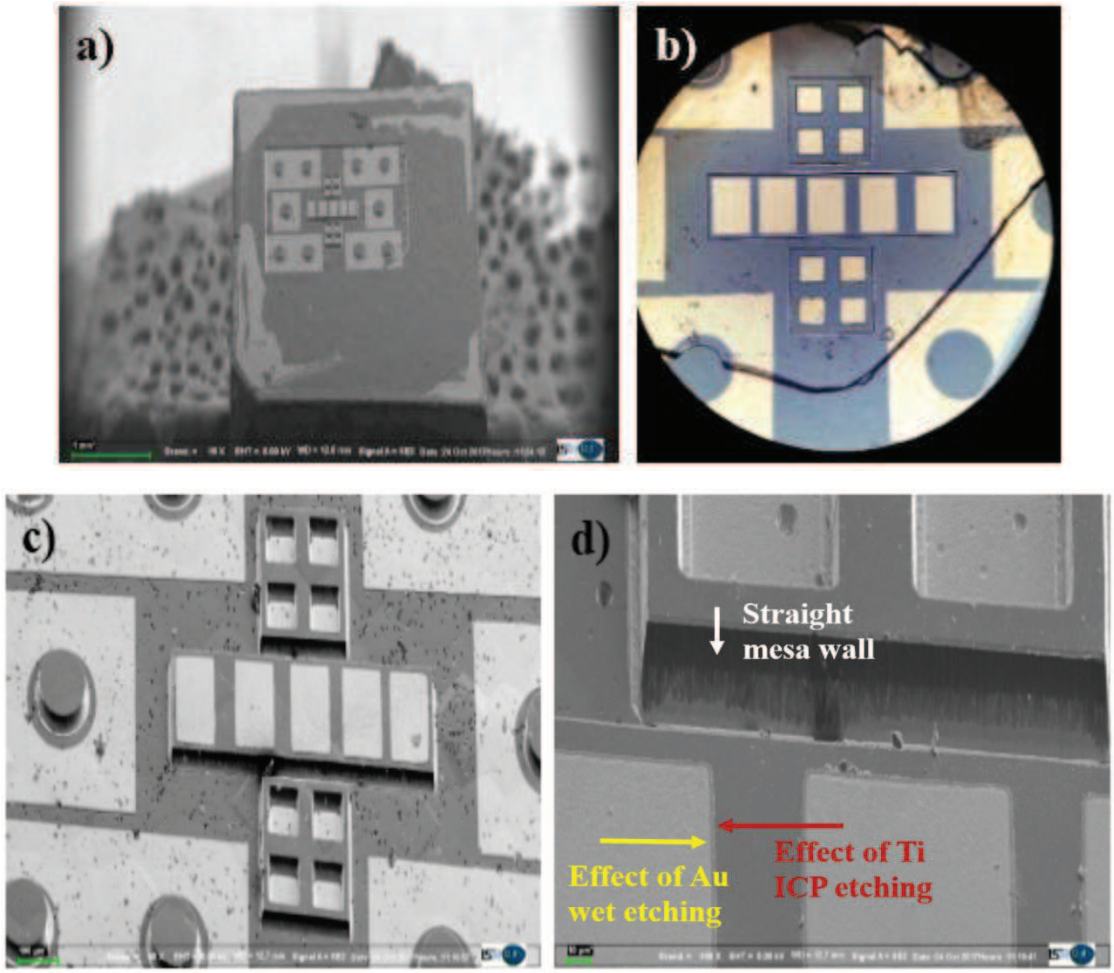

Figure IV.20. Images of two full processed sample surfaces are reported. (a) Top view of the whole mesa/TLM patterns taken on sample E; (b) optical picture of the mesa/TLM zone registered for sample I. (c) Tilted enlargement of the mesa/TLM zone of sample E showing the height of the area with respect to the surrounding surface. (d) enlargement of

the mesa/TLM and alignment pattern zone: the straight mesa wall, the different wet and ICP Au etching effects can be appreciated together with well defined TLM metallic pattern.

Relatively good and well defined patterning of metallic pads onto the doped diamond mesa structure can be seen. The wet etching using to assign the pad shape to the gold layer produced a typical under etching of the metal which reduced the lateral dimensions of the pads which can be seen more easily in Figure IV.20 (d). On the contrary, the under etching of the titanium layer is expected less important because of the anisotropic ICP etching, which proves to be in agreement with the SEM picture (d).

Finally, wire bonding was performed on the metallic pads to test adhesion and quality of the deposited layer for future experiments. In Figure IV.21 the wire bonding performed on the lightly boron doped sample C are shown. The wires were made of gold with a diameter of 30 µm. No problems of peeling off were evidenced during these tests, even when the wires were removed. The stability of the electrical contact proved to be good.

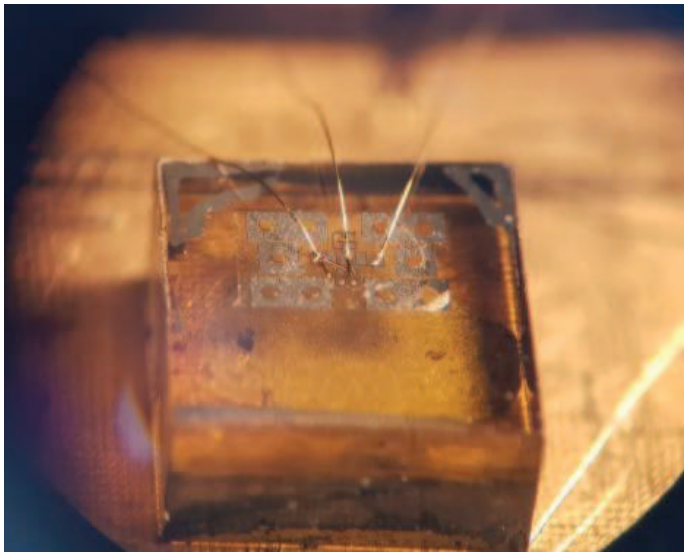

Figure IV.21. Optical picture of the lightly boron doped C sample after a wire bonding test.

IV.4.4 Critical points of the micro-fabrication

During the development of this micro-fabrication protocol several critical points were identified. In the following, the three main problematic steps are described and explained:

1) First of all, the order of the processing steps needed to be chosen. Indeed, the first idea was to process the metallic contacts before and then to fabricate the mesa structures. The choice was based on the consideration that a photoresist coating on a structured and not a flat surface would have implied an inhomogeneous distribution of the polymeric coating so as to make difficult the next lithography step. Following this idea, the mesa structure and TLM contact

processing steps described in the previous Paragraph IV.4.1 were inverted (excepted for the ion implantation step which was in every case performed first). Therefore, after the Ti/Au patterning, the silica deposition was performed directly on the contacts, assuming of not having reaction between Au and SiO_2. Nevertheless, after the mesa structure fabrication, it was more difficult to check the silica etching and remove it uniformly and totally from the metallic pattern. This difficulty was due to the inhomogeneity (i) of the silica layer deposition and/or (ii) of the plasma attack which made the SiO_2 removing without the contact damaging impossible. In addition, it is important to note that the SiO_2 is an insulator material, therefore it was problematic for reading the electrical current. Several try were carried out, but without success. In particular, the etching proved to be always either too strong leading to damaged contacts or too weak leaving insulator material residue on the pads. In the worst case, both possibilities occurred on the same sample as shown in Figure IV.22 where #1, #2 and #3 indicates a silica layer residue covering fully three pads, a portion of pad removed and the peeling off effect of the silica and metallic layers, respectively.

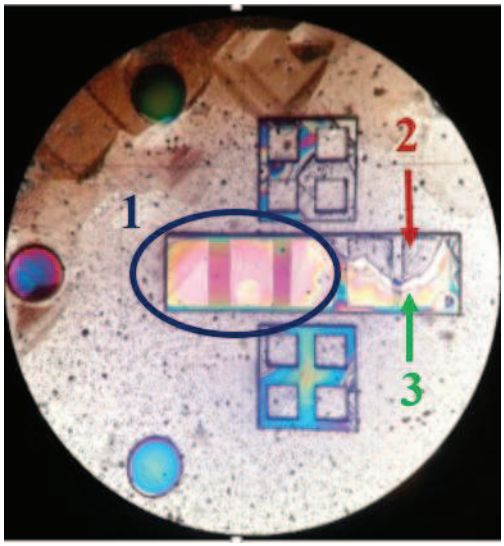

Figure IV.22. Optical picture of the G sample after the silica etching by ICP. (1) Residues of silica covering fully three pads, (2) partial damaged pads and (3) peeling off effects of both Ti/Au and silica are indicated.

Looking at the TLM pattern, it is possible to see the silicon-oxidized diffraction effects (rainbow colour) on the whole three pads on the left side, while on the last two pads on the right side a completely damaged area is visible in addition to a partial exfoliation of the SiO_2 layer.

EDX investigations were also performed in order to verify the chemical elements present on the full processed G sample. In Figure IV.23 the maps corresponding to the Si and O chemical elements in addition to the SEM pictures are reported.

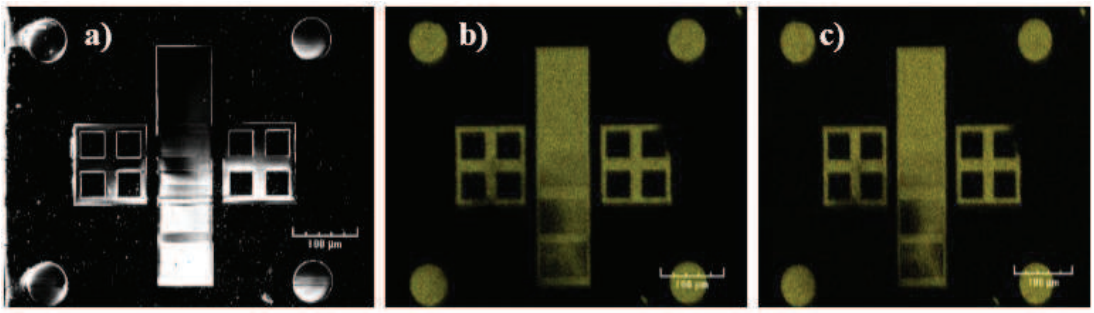

Figure IV.23. Images registered on the G sample after the SiO_2 etching. (a) SEM picture of the sample; (b) and (c) EDX maps based on the silicon and oxygen detection, respectively

From this EDX analyses, the asymmetry of the residue SiO_2 layer presents along TLM zone (silicon and oxygen in (b) and (c) images, respectively) is clearly visible. In particular, in the (a) image only the last two pad shapes (on the bottom) can be seen, while the three others on the top are fully covered by silica as confirmed by pictures (b) and (c).

As a consequence, it was decided to process the mesa structure first and then the TLM contact micro-fabrication. The first tests with this second approach gave good results, therefore it was chosen as the definitive one. Indeed, even if the photoresist coating on the mesa structure was supposed to be critical due to the surface structuring, during the experiment it proved to be manageable and without particular problematic impacts on the subsequent technological steps.

2) Another important difficulty met during this work was related to the mechanical adhesion of the metallic layers on the diamond surface. In particular, the first Ti/Au metallic deposition on CVD diamonds was performed by sputtering in the clean room of University of Paris 13, without Ar^+ etching pre-treatment. In these conditions, the direct Ti/Au deposition on the diamond surface led to metallic layer detachment when exposed to several technological steps. For example, acetone solution washing assisted by ultrasonic waves to remove the polymeric material residue leaded also to the Ti/Au detachment, or peeling off phenomena were registered during mechanical tip tests. In Figure IV.24 an example of Ti/Au peeling off phenomenon is shown.

Considering that one of the required properties for electrical contacts on diamonds is the good mechanical adhesion, this problem had absolutely to be overcome. After several tests, the final solution was to perform a short argon ion etching before the metallic deposition to improve the adhesion at the Ti / diamond interface. Indeed, as already shown in literature, the argon ion bombardment pre-treatment induces local defects and favours the bonding between carbon and titanium atoms [5].

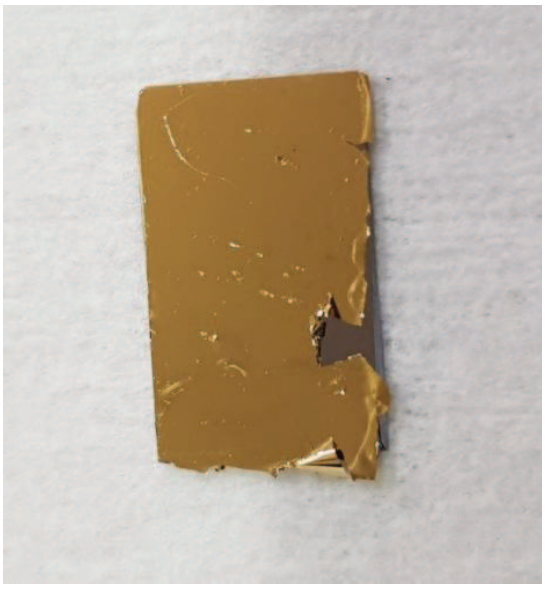

Figure IV.24. Detachment of the titanium / gold layers deposited on silicon wafer by sputtering.

In order to develop such a process, both metallic depositions were performed by an evaporator equipped with an argon plasma etching set-up. After the first tries, large improvements were obtained in terms of adhesion, even under mechanical stress, such as during washing treatment or mechanical proofs of the electrical measuring by tungsten tips. No peeling off was registered and the metallic contacts on diamond samples did not suffer additional mechanical stress due to wire bonding tests (Figure IV.21).

Therefore, the argon ion etching pre-treatment was added to the contact micro-fabrication protocol (Figure IV.15, point #6) and all metallic depositions were performed using the evaporator machine.

A perspective of this work will be to study and improve the adhesion of the metallic layers on diamond surfaces by sputtering depositions.

3) The third critical point was identified at the end of all the technological steps and was related to the photoresist removal after the second lithographic step (Figure IV.15, point #12). In particular, once arrived to this step, a residual layer of photoresist was discovered on all the samples by preliminary accurate optical investigations and then by SEM analyses. Several standard tests were done to try to remove it, for example washings with different chemical solution, assisted by ultrasonic bath at room or hot temperature, but without success. Indeed, the SEM analyses confirmed the polymer surviving, as illustrated for the I sample in Figure IV.25 (a). The definitive solution found for this problem was to perform plasma etching treatments in oxygen atmosphere by ICP. Thanks to this additional step, the polymeric residues were successfully removed from the samples. In Figure IV.25 (b) a picture of sample I surface taken after the oxygen plasma etching treatment is reported.

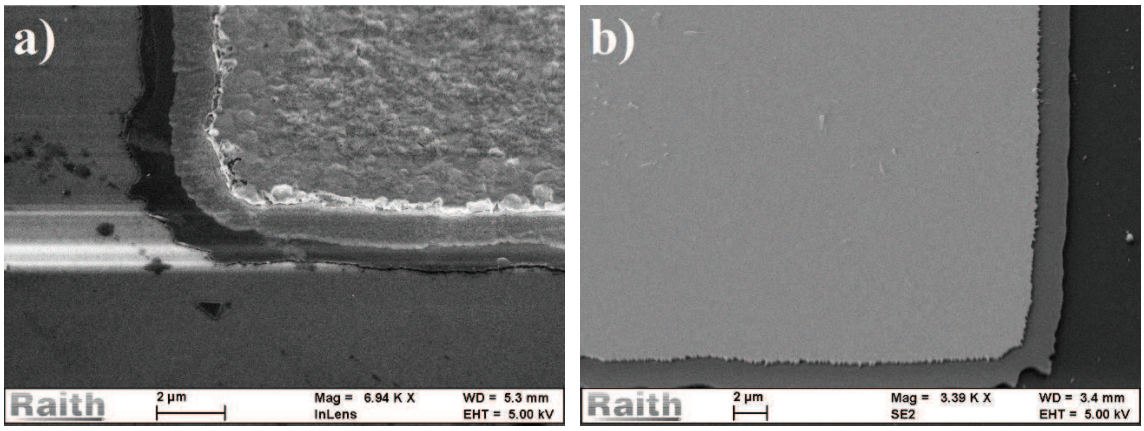

Figure IV.25 SEM pictures taken on sample I before (a) and after (b) an oxygen plasma etching treatment used to remove photoresist residue.

IV.5 Electrical characterization of the TLM structures

For diamond power electronic devices, as largely described before, one of the crucial points is to manufacture good ohmic contacts. In particular, the classical contacting technique is the device metallization, where the metallic contacts have to satisfy several requirements:

- Symmetric and linear current-voltage curves;
- Good mechanical adhesion;
- Stability, reproducibility and reliable properties;
- Low specific contact resistance.

The latter point refers to one of the key parameters characterizing the quality of the metallic contacts, namely the specific contact resistance, which can be evaluated by the Transmission Line Model (TLM) [232]. The following part introduces the contact electrical characteristics, the TLM method for the specific contact resistance evaluation and a section reporting the obtained results on the samples prepared during this thesis.

IV.5.1 Estimation of the specific contact resistance

Basically, there are two geometries to manufacture contacts on electronic devices: vertical and coplanar. In the first case, the electrodes are located on the top and bottom sides of the device, while in the second one the contacts are distributed along the top surface. Depending on the configuration, the current lines crossing the semiconductor from one electrode to another are distributed orthogonally or parallel to the contact interface. Therefore, the specific contact resistance

determination must be calculated differently. In Figure IV.26 two sketches of the current line paths in both configurations are reported.

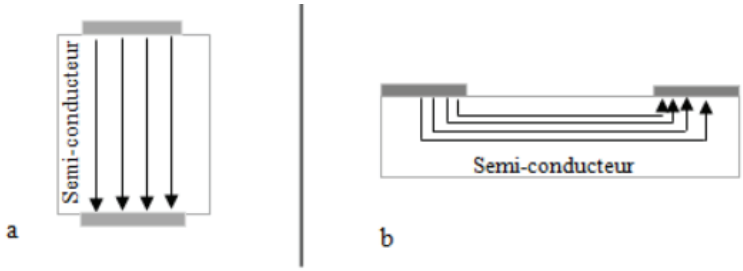

Figure IV.26. Current line paths inside a semiconductor device for the vertical (a) and coplanar (b) electrode configurations.

The Figure IV.26 (a) shows the vertical configuration of the electrodes. In this case, the current lines are orthogonally oriented to the metal / semiconductor interface and they are uniformly distributed along the whole contact area. The Figure IV.26 (b) shows the coplanar configuration of the electrodes and, contrary to the previous case, the current lines move in a parallel direction regarding the metal / semiconductor interface. In particular, they are not homogeneously distributed along the contact area but they cross just a part of it.

Therefore, the specific contact resistances (ρ_c) have to be calculated following two different dedicated equations. For the vertical electrode configuration the equation is:

$$\rho_C = R_C \cdot A_C \qquad \text{Equation IV.8}$$

where R_C is the contact resistance and A_C the contact area. For the coplanar contact configuration it is necessary to estimate the real contact length crossed by the current lines, which is called “transfer length” L_T and it is related to the specific contact resistance by the equation:

$$L_T = \sqrt{\rho_C / R_{SH}} \qquad \text{Equation IV.9}$$

where R_{SH} is the sheet resistance of the semiconductor layer. Both parameters L_T and R_{SH} can be extracted by transmission line model (TLM) method which will be described in the following part. In particular, the specific contact resistance calculation for the coplanar electrode configuration is more difficult to evaluate than for the vertical electrode configuration. Indeed, it is necessary to take into account the potential distribution along the contacts, and the non-uniform distribution of the current lines below the contact areas, which can be thought as a resistance of contact end. Nevertheless, for the specific case in which the contact length $L \geq 1.5\ L_T$, which is the case of these experiments, the final equation is rather simple [233]:

$$\rho_C \approx R_C \cdot L_T \cdot W$$ Equation IV.10

where W is the contact width, while the contact resistance R_C and the length transfer L_T can be extrapolated by TLM analyses.

IV.5.2 TLM method

The TLM method is the most used technique to characterize electrically the device contacts, both to compute the resistivity of the electrode material (for example in the case of laser-induced graphitic electrodes, as shown in the Chapter III) and to estimate the specific contact resistance in the case of electronic devices.

The TLM structure developed for this work presents five metallic pads fabricated on a mesa CVD boron doped diamond. The mesa structure, as previously discussed, is essential to get an electrical insulation around the contacts avoiding current dispersion outside the investigated region. The TLM pattern sketch with the geometric parameter indications are presented in Figure IV.27.

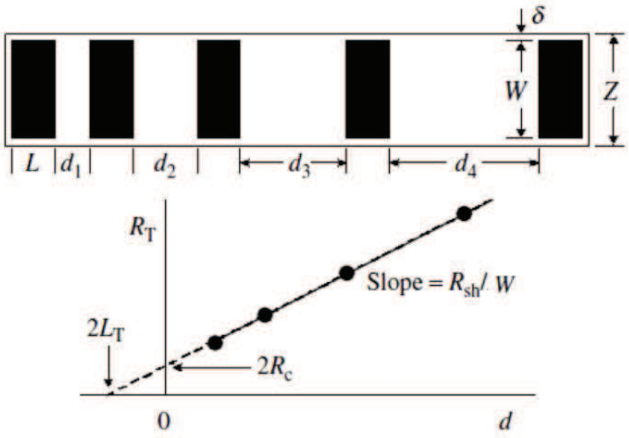

Figure IV.27. TLM method draft. At the top of the picture there is a sketch of the five pads with the geometric parameters: L and W are the length and the width of the contacts, Z is the width of contact added to the mesa edge (δ), and d_1, d_2, d_3 and d_4 are the increasing distances among the pads). On the bottom of the picture the linear fit of the computed IV data is reported [233].

Thanks to the current-voltage measurements by two probes method, it is possible to extract the total resistances (R_T) from each I-V curves and to compute them as a function of the pad distance (d) in analogy to the explanations given in the Paragraph 4.5 of the Chapter III. The linear fit reported on the bottom of the Figure IV.27 follows the Equation:

$$R_T = 2R_C + \frac{R_{SH}}{W} \cdot d$$ Equation IV.11

where the slope is given by the sheet resistivity divided by the contact width, the intercept of Y-axis corresponds to two times the contact resistance R_C and the transfer length L_T can be extrapolated by the intercept to the X-axis ($R_T = 0$ gives $-d = 2\ L_T$).

Last point, the graph slope (R_{SH}/W) corresponds to the slope ($\rho/(wt)$) of the TLM analyses discussed in the third chapter but simply written in a more convenient way for current analyses.

IV.5.3 Sample results

In the chapter I and in the section 2.4 of this chapter, it has been already explained and investigated, respectively, that to reduce the contact specific resistance between a diamond semiconductor and its metallic contacts it is useful to dope diamond. In particular, for heavily boron doped diamond, it is possible to easily fabricate ohmic contacts. On the contrary for lightly boron doped diamond, it is more challenging and in this thesis work it has been proposed to improve this by adding a graphitic layer underneath the diamond surface.

Therefore, four complete diamond devices were manufactured in this work: two devices on heavily boron doped diamond ([B] = 4×10^{20} cm^{-3}, samples I and J) and two on lower doping level ([B] = 4×10^{17} cm^{-3}, samples C and D). In each set of samples, one was graphitized just underneath the CVD diamond surface (J and C) and the other was not (I and D).

It is worth noting that all the samples were affected by a technological problem on the fifth pad (the furthest, 50 μm distant from the previous one) which proved to be systematically in short circuit with the fourth pad probably due to a physical damage of the TLM mask. Therefore, the analysed data involve just four measurement points corresponding to the first four pads.

I-V measurements on heavily boron doped diamonds

In Figure IV.28 (a), the set of I-V curves registered on the heavily boron doped diamond contacted by metallic pad is shown. For sample I, without the graphitic layer underneath the CVD surface, the electrical contacts prove to be almost ohmic since the I-V curves are almost linear whatever the distance between the pads. Then, the electrical resistances increase as a function of the pad distances with values of about 370, 780 and 1200 Ω for distances d equal to 20, 30 and 40 μm, respectively.

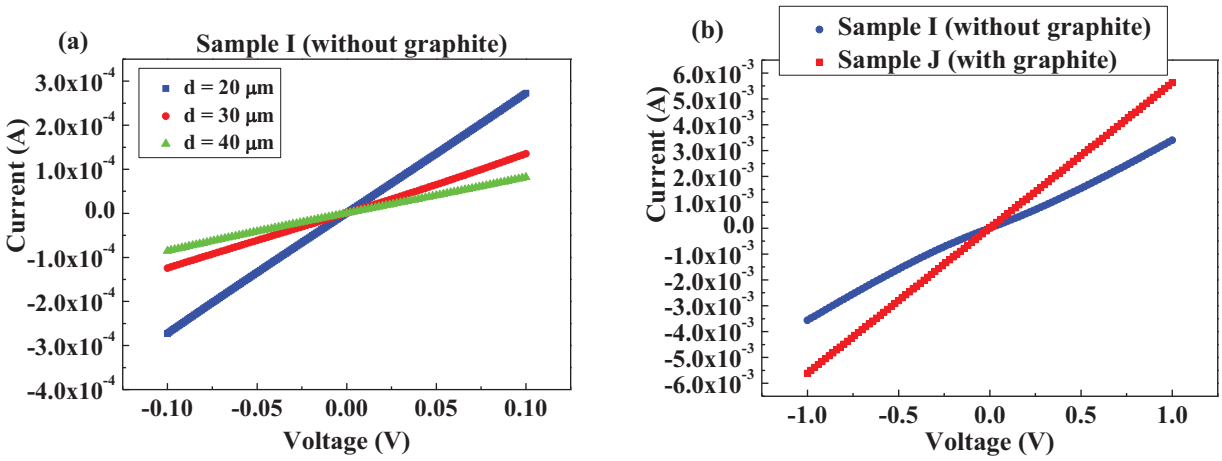

Figure IV.28. (a) Current-voltage curves for the heavily boron doped sample without the graphitic layer at different pad distances. (b) Comparison between two I-V curves registered on the two heavily boron doped samples, without and with graphite, for a distance between pads of 20 µm.

For sample J with the additional graphitic layer an improvement of the electrical conduction is obtained, indeed the I-V curve recorded between the nearest pads (d = 20 µm) proves to be linear and the electrical resistance value has been reduced by a factor of 2 (180 Ω vs 370 Ω), as shown in Figure IV.28 (b). Moreover the ohmic behaviour is demonstrated in a larger voltage range regarding the sample with graphite, namely for (-2,+2) V.

I-V measurements on lightly boron doped diamonds

The lightly boron doped diamond sample D having a boron concentration of 4×10^{17} cm^{-3} was also fully processed and electrically characterized.

The I-V characteristics of this non-graphitized sample are shown in the Figure IV.29. As expected for low-doping level of diamond material, a non-linear behaviour is clearly evidenced.

Quantitatively, the non-linear electrical conduction decreases with an increase of the pad distance, as shown for d = 20 and 30 µm, and then saturates for d = 40 µm.

Taking into account this non-linear behaviour, the specific contact resistance was not extracted from TLM structures.

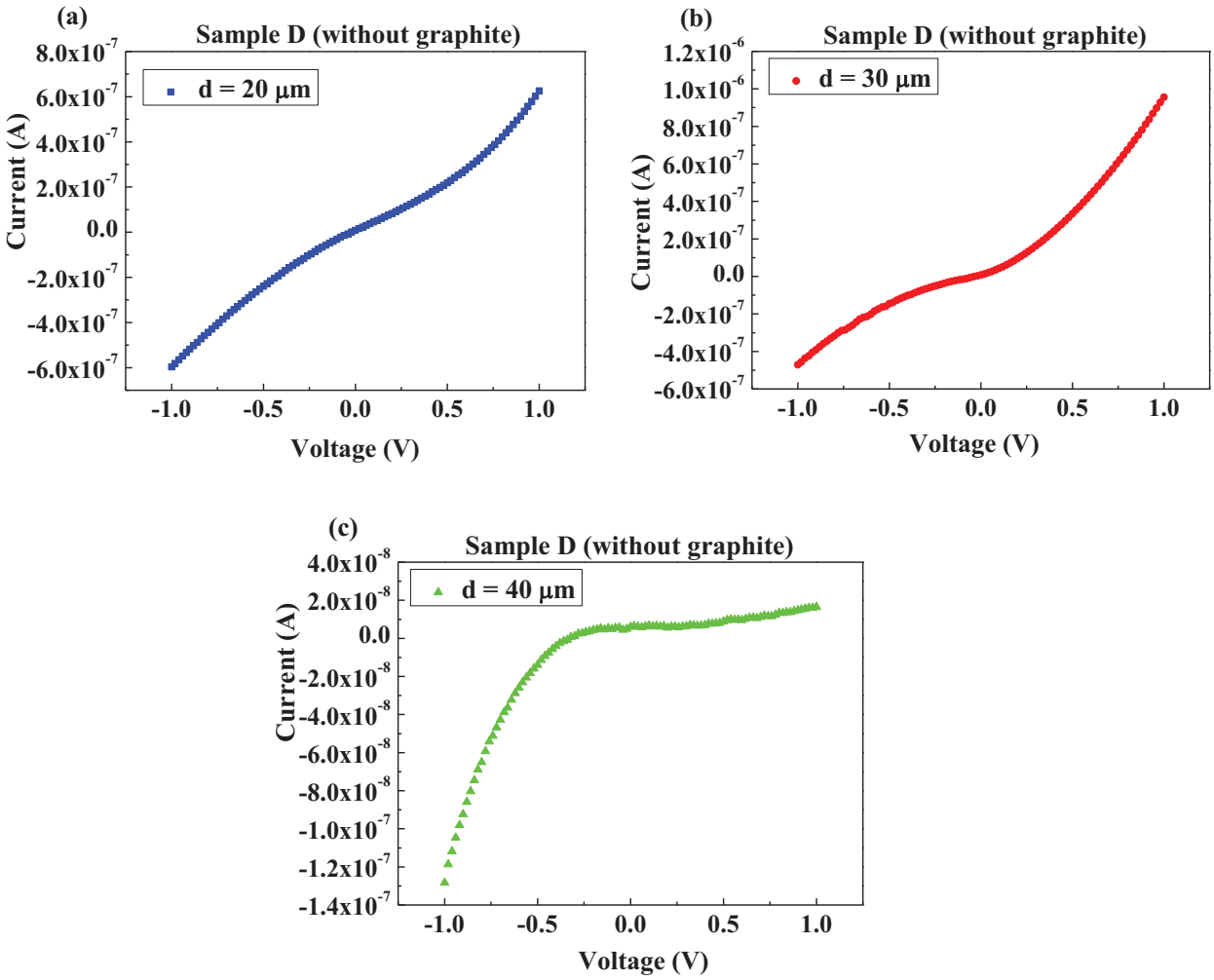

Figure IV.29. Current-voltage curves for the lightly boron doped sample D without the graphitic layer at different pad distance (20, 30 and 40 µm).

On the contrary, after graphitization, the electrical behaviour has been strongly improved as it can be shown in Figure IV.30.

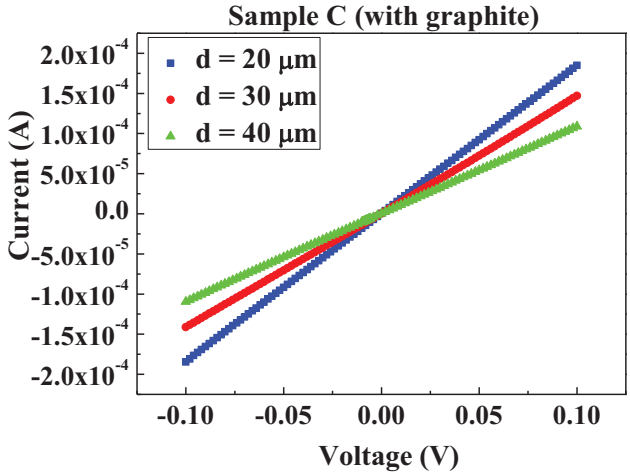

Figure IV.30. Current-voltage curves for the lightly boron doped sample C with the graphitic layer at different pad distances (20, 30 and 40 µm).

All the I-V curves show an ohmic behaviour with a resistance value increasing with the pad distance. In particular, for pad distances d equal to 20, 30 and 40 µm, the electrical resistances were about 540, 700 and 920 Ω, respectively.

Finally, in order to determine the specific contact resistance, the total resistance values were extracted from each I-V curve in the Figure IV.30 and then they were plotted as function of the pad distance d. The corresponding graph is reported in Figure IV.31.

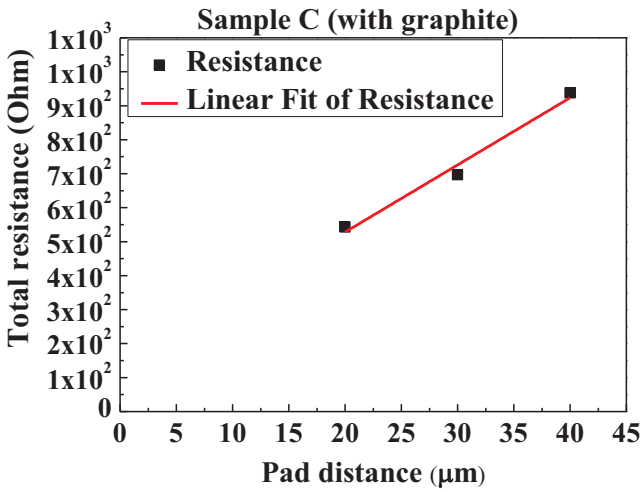

Figure IV.31. Total resistance against the pad distance for the C lightly boron doped sample with the graphitic layer.

As highlighted by the fit shown in the picture, the evolution of the resistance as a function of the pad distance is not fully linear. Nevertheless, it was possible to extrapolate the contact resistance R_C by the intercept of Y-axis, the transfer length L_T by the intercept of the X-axis, and to calculate the specific contact resistance starting from Equation IV.10 but keeping in mind that the specific contact resistance computed here has to be taken as a rough estimation.

The obtained values are:

- $R_C = 66\ \Omega$;
- $L_T = 3.3\ \mu m$;
- $\rho_c = 3.3 \times 10^{-4}\ \Omega.cm^2$.

The measurements were repeated after two months demonstrating the contact stability.

The specific contact resistance is relatively high regarding the values usually obtained for electronic devices but it corresponds to few $10^{-4}\ \Omega.cm^2$ only obtained at such a low doping level for ohmic contact deposited on hydrogenated surface [131] and constitutes a good result demonstrating the interest of adding a graphitic layer just below the metallic contacts.

In addition, in comparison with the Chen's previous experiment [198], who fabricated graphite / metal ohmic contacts on a lightly boron doped sample with oxygen terminations, the specific contact resistance proves to be lower of more than three orders of magnitude.

IV.6 Conclusion

A set of CVD monocrystalline boron doped diamonds was grown by MPACVD technique. The doping range was modulated at different concentrations of boron atoms in the gas phase by changing the $(B/C)_{gas}$ ratio from 3000 up to 15000 ppm. A double sample copy for each doping level was produced in order to manage the micro-fabrication steps by some samples and to preserve others of them for the characterization analyses. Two additional samples, an intrinsic and a Not Intentionally Doped (NID), were also produced. The NID was grown taking advantage of the memory effects of the diamond deposition bell jar used for previous doping. Cathodoluminescence investigations allowed estimating the boron concentration into the CVD layers, which proved to be variable from 1×10^{17} cm^{-3} up to 4×10^{20} cm^{-3}.

Electrical characterizations performed on doped diamond samples with different boron doping levels showed a decrease of the sheet resistance with the increasing of the boron concentration, as expected. The registered sheet resistivity range was $8.49 \times 10^{3} – 2.00 \times 10^{1}$ Ω/□.

Considering the difficulty to manufacture ohmic contacts on lightly doped diamonds, the ion implantation process was first investigated onto the intrinsic diamond sample. A graphitic layer underneath the CVD diamond surface was produced, and afterwards metallic contacts were evaporated. An ion implantation recipe graphitizing successfully the intrinsic diamond was developed. The recipe consists to accelerate helium ions with 10 keV voltage with a dose of 1.4×10^{17} $ions.cm^{-2}$. The vacancies density generated by the ion bombardment was about 3.7×10^{23} cm^{-3}, which overcomes the graphitization threshold. The graphitic layer depth was estimated to 52 nm by SRIM simulations. Optical, micro-Raman and electrical analyses confirmed the ion implanted-induced diamond amorphization and, after an annealing treatment, the transition into graphite. The sheet resistivity of the graphitized intrinsic diamond was equal to 282 Ω/□.

A technological step protocol for the metallic contact micro-fabrication on diamond surfaces was developed and carried out during this work. Ti/Au electrodes were produced in the geometric configuration of TLM pads above a mesa structure made of the CVD boron doped layers having the aim of confining the current lines in the active layer. Optical, morphological and compositional characterizations performed step by step allowed overcoming several critical problems met during

the technological process. In particular, the surface pre-treatment by argon ion etching which was introduced to improve the adhesion at the Ti/C interface.

Finally, four full devices were manufactured: two devices on heavily boron doped diamond ([B] = 4×10^{20} cm^{-3}) and two on lightly doping level ([B] = 4×10^{17} cm^{-3}), where for each couple one was graphitized underneath the CVD diamond surface and the other not. Current-voltage characterizations were carried out on all the samples. For the heavily boron doped diamonds, almost linear I-V curves were registered for the sample without the graphitic layer, while the graphitized diamond showed ohmic contacts, in addition to a reduction of the resistance values by a factor of 2. For the lightly boron doped samples, the I-V measurements exhibited a non-linear electrical conduction, which decreased with the increase of the pad distances. On the contrary, for the lightly doped diamond graphitized underneath the surface, ohmic behaviour was observed. The specific contact resistance was estimated to $\rho_c = 3.3 \times 10^{-4}$ $\Omega.cm^2$ which is rather high. However given the low doping level and the oxygen termination of the diamond surface this is a promising result highlighting the usefulness of this graphitization approach.

General conclusion and outlook

In this PhD thesis two experimental studies about diamond electrical contacting have been carried out under an international cotutelle agreement between the University of Salento and the University of Paris 13. The common aim has been to study and optimize the manufacturing of ohmic contacts on diamond surface for detection and electronic applications by using different techniques: the laser-induced diamond graphitization at L3 in Italy, and the ion implanted-induce diamond graphitization followed by metallization at LSPM in France. In both experiments, a protocol of diamond contacting has been defined and full devices have been successfully produced and characterized.

The Chapter I of this thesis consists of a state of the art to provide the knowledge, tools and scientific references related to my work. First, the growth mechanisms of CVD homoepitaxial diamond films on (100) oriented substrates have been discussed as a function of the experimental deposition conditions. Among the different diamond synthesis techniques, the MPACVD process proves to be the most adapted to synthetize and grow high quality monocrystalline and polycrystalline diamond films, with high purity and crystallinity levels useful for the production of electronic devices and detectors. Different doping techniques are also presented with a specific focus for the in situ boron doping, which allows incorporating impurities in a well controlled way, in particular for the (100) orientation. Boron dopant can be incorporated in a wide range of levels from 10^{15} up to 10^{21} cm^{-3}. The obtained doped layers have a very good crystalline quality with an extremely low compensation rate which makes them particularly useful as the first technological brick for manufacturing electronic devices. Second, a wide space has been dedicated to diamond contacting which represents a fundamental step for obtaining performant electrodes and, therefore, efficient electronic devices or detectors. In particular, the manufacturing of good ohmic contacts on diamond surface proves to be still a difficult work. Indeed, although for heavy boron doping (> 10^{20} cm^{-3}) the ohmic behavior is relatively easily reached, it is much more challenging for lightly boron doped (< 10^{18} cm^{-3}) or intrinsic diamond films. Several aspects have been discussed allowing determining for the fabrication of ohmic contacts, the choice of the metallic layers, the termination of the diamond surface and eventual surface treatments. It has been shown that the use of a metal compatible with the formation of a carbide (for instance titanium to get TiC), hydrogen terminations and Ar sputtering before metal deposition can favor the formation of ohmic contacts. Nevertheless, sometimes these precautions can prove not to be enough and other solutions have to be found. For example, diamond graphitization by laser-writing has been successfully performed and allowed fabricating ohmic, stable and reliable graphitic

electrodes on the diamond surface without involving too many sophisticated technological steps. This technique has been gaining momentum in particular for diamond detection applications as a surface or 3D electrodes. By this approach, the so called all-carbon devices have been obtained. However, another technique can also be used to graphitize diamond, namely the ion implantation. Nowadays, this technique has been successfully applied to heavily dope and at the same time to graphitize diamonds in order to induce conductive layers in the diamond bulk (with ion energy of hundreds keV or few MeV). It could constitute a good approach to improve ohmic contacts on lightly doped or even intrinsic diamond material.

In the Chapter II the experimental set-up and all the instrumentations used in this work have been presented. At first, the laser-writing set up used to graphitize diamond surface for the segmented diamond contacting has been reported. In particular, in this experiment I defined a protocol of bi-dimensional diamond graphitization in addition to developing a LabVIEW software able to synchronize and control the involved instrumentations. Then, CVD deposition reactor assisted by microwave plasma has been described together with the procedure of substrate preparation. A description of all the machines used to deposit metallic contacts and fabricate the mesa structure on CVD boron doped samples (e-beam evaporator, PECVD, ICP), in addition to the home-made ion implantation system, completes this section. Subsequently, the principles of the characterization techniques used in this thesis work (Raman, SEM, EDS, CL and electrical measurements) have been explained. These characterizations were possible thanks to collaborations with several national and international institutes of research mentioned in this chapter.

In the chapter III, diamond contacting by graphitic electrodes has been presented together with the final all-carbon detector performances. The aim has been to produce the first diamond detector prototype for the PADME experiment in collaboration with the INFN institute. In particular, the laser-induced graphitization of several detector grade CVD polycrystalline intrinsic diamond samples (with dimensions of $5 \times 5 \times 0.05$ mm^3 and $20 \times 20 \times 0.05$ mm^3, respectively) has been presented. The development of a LabVIEW software allowed fabricating bi-dimensional graphitic pattern satisfying the electrode geometric requests for the segmented all-carbon PADME detector. A wide characterization of the graphitic pattern was carried out on the small diamonds by complementary experiments. SEM and micro-Raman investigations allowed understanding the physical evolution of the graphitization process, and how the morphological and structural changes depend on the laser processing. These two techniques indicate a strong periodicity of the surface modifications correlated to the fabrication process. In addition, hardness and elastic modulus mappings have been discussed showing that hard-soft transformation occurred depending on the locally deposited energy. The

finding proves to be in line with the change of hybridization ($sp^3 \rightarrow sp^2$) of carbon atoms observed by SEM and micro-Raman. Finally, current-voltage analyses verifying the nature of the diamond-graphite contact and evaluating the resistivity of the strips have been reported. Good conductive properties and ohmic behavior were observed for all the graphitic strips, with a resistivity average around $2.5 – 3 \times 10^{-5}$ Ω.m along the strips. In addition, exiguous currents of about some hundreds of fA were measured between coplanar strips over the voltage range from −10 V to +10 V suggesting an ohmic nature for the graphite/diamond contact and making the strips suitable as electrodes in all-carbon sensors.

Subsequently, the nuclear investigation performed on the large graphitized CVD polycrystalline intrinsic diamond by 450 MeV electron and positron beams at the BTF of Frascati (Italy) have been presented and discussed. Although great reliability and stability were recorded for the graphitic contacts, some problems of PC-board planarity together with some jumped off wire bonding reduced the effective signal read out from the detector. As a result of these investigations, a CCD of the order of 10 μm for an electric field of 3 $V.\mu m^{-1}$ was estimated (as expected for such as-grown CVD polycrystalline diamond sensor without pumping pre-treatment). In addition, good time and space resolutions, namely 2 ns and about 200 μm respectively, were obtained. Therefore, the all-carbon detector performances proved to satisfy the requirements for the detector candidate at the PADME experiment. Last but not the least, these findings show also that this kind of detector can be used to monitor online a particle beam with high intensity.

Finally, in the chapter IV both diamond sample growth and contacting have been presented. Initially, the description of a set of CVD monocrystalline boron doped diamonds grown by MPACVD technique, with different $(B/C)_{gas}$ ratio (3000 − 15000 ppm), and their spectroscopic and electrical characterizations have been reported. The boron concentration in the CVD layers was estimated between 1×10^{17} cm^{-3} and 4×10^{20} cm^{-3}, and the related sheet resistivity decreased with an increase of boron concentration. Then, the manufacturing of graphitic layer by ion implantation treatment has been discussed. The developed ion implantation recipe (accelerated helium ions with 10 keV voltage and a dose of 1.4×10^{17} $ions.cm^{-2}$) allowed obtaining a graphitic layer underneath the CVD diamond surface (around 50 nm deep determined by SRIM simulations). Afterward, a protocol for the Ti/Au metallic contact micro-fabricated above a mesa structure made on CVD boron diamond film to confine the current lines in the active layer has been defined. Optical, morphological and compositional characterizations performed step by step allowed overcoming several critical problems met during the technological process. In particular, a surface pre-treatment by argon ion etching was introduced to improve the adhesion at the Ti/C interface. Finally, four full devices were manufactured: two devices on heavily boron doped diamond ($[B] = 4 \times 10^{20}$ cm^{-3}) and two on lightly

doped diamond ([B] = 4×10^{17} cm^{-3}). For each couple of samples, one was graphitized underneath the CVD diamond surface and the other not. Current-voltage characterizations have been discussed showing that for the heavily boron doped diamond samples without and with the graphitic layer an almost ohmic and ohmic behavior were obtained, respectively. In addition, a halving of the resistance values was recorded for the graphitized diamond. For the lightly boron doped samples, the I-V measurements exhibited a non-linear electrical conduction. On the contrary, after a graphitization step, ohmic behavior was observed and a specific contact resistance estimated to $\rho_c = 3.3 \times 10^{-4}$ $\Omega.cm^2$. Although this value seems to be rather high, taken into account the low doping level of the corresponding sample, this is a promising result highlighting the usefulness of this graphitization approach.

Therefore, in this PhD thesis, an efficient role of the diamond graphitization processes has been demonstrated in the manufacturing of ohmic contacts. In particular, for the all-carbon detector a great reliability of the graphitic electrodes have been recorded in terms of mechanical adhesion, stability and efficiency in the charge ejection on a large scale (cm^2). These results from one side strengthen the promising performances already registered for the first all-carbon sensors on micro- and millimetric scales, and on the other side open the way to the use of such detectors as active targets in high-energy physics experiments. However several aspects would need to be improved through further studies, such as a more homogenous laser-induced graphitization along the whole contact area, a more efficient contacting step between the diamond electrode and the electronic PC-board, in addition to a protocol to manipulate and assemble such a thin sensor without damaging it. Then, additional nuclear investigations performed on a detector fully contacted on its PC-board and under irradiation by a narrow and more stable particle beam can improve the accuracy of the CCD, time and space resolution measurements, in addition to allow verifying the full device performance as online monitor of particle beams with high intensity.

For the graphite / metal contact experiment, interesting margins for further investigations are available. For example, the promising specific contact resistance value obtained for the lightly boron doped diamond with oxygen terminations can be strengthened by further electrical investigations of additional samples to study statistically the reliability and the reproducibility of such technique. Moreover, it could be interesting to characterize the graphite / metal interface to better understand how it morphologically evolves moving from the graphitic layer underneath the diamond surface up to the titanium carbide zone, and to measure the depth of the graphitic layer. In addition, further characterizations on new heavily doped samples, could allow better quantifying the contribution of the graphitic layer to the conduction.

Then, once confirmed the efficiency of this technique, as a perspective, it will be possible to imagine the development of electronic devices that make use of this graphitization step or even apply it to n- doped diamond films on which it is currently particularly difficult to prepare good contacts.

Appendix A: Scientific production

Peer reviewed journals

1. M. De Feudis et al., *Diamond Graphitization by laser-writing for all-carbon detector applications*, Diam. Relat. Mater., 75, (2017) 25-33.

2. A. Taurino, M. Catalano, M. De Feudis et al., *Graphitization of diamond by means of UV laser writing: a transmission electron microscopy study*, Microsc. Microanal. 23 (Suppl.1), 2017.

3. R. Assiro, A.P. Caricato, G. Chiodini, M. Corrado, M. De Feudis et al., *Performance of the diamond active target prototype for the PADME experiment at the DAΦNE BTF*, arXiv:1709.07081 [physics.ins-det], 2017.

4. M. De Feudis et al., *Characterization of surface graphitic electrodes made by excimer laser on CVD diamond*, Diam. Relat. Mater., 65, (2016) 137-143.

Papers as member of the PADME experiment collaboration

1. P. Gianotti on behalf of the PADME Collaboration, *Status and prospects for the PADME experiment at LNF*, EPJ Web of Conferences 166, (2018) 00009.

2. G. Chiodini on behalf of the PADME Collaboration, *The PADME experiment for dark mediator searches at the Frascati BTF*, J. Inst. 12 (2017) C02037.

3. G. Chiodini on behalf of the PADME Collaboration, *A diamond active target for the PADME experiment*, J. Inst. 12 (2017) C02036.

4. P. Valente on behalf of the PADME Collaboration, *The PADME experiment at DAΦNE LINAC*, in Proceeding of the 38th International Conference on High Energy Physics ICHEP, Chicago, USA, Proceeding of Science 204 (2016).

5. S. Fiore for the PADME collaboration, *The PADME experiment at INFN LNF*, Journal of Physics: Conference Series 770 (2016) 012039.

Proceedings

1. F. Oliva, R. Assiro, A.P. Caricato, G. Chiodini, M. Corrado, M. De Feudis et al., *Beam test results of PADME full carbon active diamond target*, in Proceeding of the Conference Incontri di Fisica delle Alte Energie IFAE, Genova, Italy, Il Nuovo Cimento 40 C, (2017) 81.

2. M. De Feudis et al., *Diamond detectors with electrodes graphitized by means of laser*, in Proceeding of the Conference Incontri di Fisica delle Alte Energie IFAE, Rome, Italy, Il Nuovo Cimento 39 C, (2016) 254.

3. M. De Feudis et al., *Realization and characterization of graphitic contacts on diamond by means of laser*, in Proceeding of the IV Workshop on Plasmi Sorgenti Biofisica e Applicazioni PSBA, Italy, Lecce, ISBN 9788883051081 (2015) 63-68.

Communications at International Conferences

1. Award:

- ✓ **1st PLACE** as Best Young Researcher Presentation "Roger Kelly Award"
  M. De Feudis, *Laser-induced graphitization of diamonds for demanding applications in nuclear physics*, 5th International School on Lasers in Materials Science – SLIMS, Venice, Italy, 10th-17th July, 2016.

2. Invited:

- ✓ M. De Feudis et al., *Laser-induced graphitization of diamonds for demanding applications in nuclear physics*, International Symposium "Fundamentals of Laser Assisted Micro- and Nanotechnologies FLAMN 16", St. Petersburg, Russia Federation, 27th June - 1st July 2016.

3. Talk:

- ✓ M. De Feudis et al., *Ohmic metal-graphite contacts on lightly boron-doped diamonds*, International Conference on Diamond and Carbon Materials ICDMC17, Gothenburg, Sweden, 3rd – 7th September 2017.

4. Poster:

- ✓ M. De Feudis et al., *Two-dimensional characterization of laser-induced graphitic strips on CVD diamond*, International Conference on Diamond and Carbon Materials ICDMC16, Montpellier, France, 4th – 8th September 2016.

- ✓ M. De Feudis et al., *Characterization of surface graphitic electrodes made by excimer laser on CVD diamond*, International Conference on Diamond and Carbon Materials ICDMC15, Bad Homburg, Germany, 6th – 10th September 2015.

Communications at National Conferences

1. Talk:

- ✓ M. De Feudis et al., *Realization and characterization of graphitic contacts on diamond by means of laser*, IV workshop nazionale su Plasmi, Sorgenti Biofisica e Applicazioni (PSBA), Lecce, Italy, 17th-18th October 2014.

2. Poster:

- ✓ M. De Feudis et al., *Rivelatori a diamante con elettrodi grafitati mediante laser*, Conferenza nazionale di Incontri di Fisica delle Alte Energie (IFAE), Roma Tor Vergata, Italy, 8th-10th April 2015.

Communications at PhD Schools

1. Talk:

- ✓ M. De Feudis, *Laser-induced graphitization of diamonds for demanding applications in nuclear physics*, 5th International School on Lasers in Materials Science – SLIMS, Venice, Italy, 10th-17th July, 2016.

- ✓ M. De Feudis, *Realizzazione di contatti grafitici per rivelatori a diamante full-carbon*, XXVII Seminario Nazionale di Fisica Nucleare e Subnucleare "Francesco Romano", Otranto, Italy, 4th-11th June 2015.

Communications at International Conferences as co-author

1. Talk:

- ✓ M. De Feudis et al., *Ohmic metal-graphite contacts on single crystal diamond produced by He implantation*, International Workshop "OIST Diamond Workshop 2017", Okinawa, Japan, 29th October – 1st November 2017.

- ✓ A. Taurino, M. Catalano, M. De Feudis et al., *Graphitization of diamond by means of UV laser writing: a transmission electron microscopy study*, International Conference on Microscopy & Microanalyses, St. Louis, Missouri (USA), 6th – 10th August 2017.

2. Poster:

- ✓ A. Valentin, M. De Feudis et al., *Characteristics of He ion implanted layers on single-crystal diamond*, Hasselt Diamond Workshop – SBDD XXIII, Hasselt, Belgium, 7th – 9th March 2018.

- ✓ M. De Feudis et al., Morphological and structural study of the laser-induced diamond to graphite transformation, 10th International Conference of Photoexcited Processes and Applications – ICPEPA, Brasov, Romania, 29th August – 2nd September 2016.

Appendix B: Institutes of collaboration and visited laboratory

Institutes of collaboration

- ✓ INFN National Institute of Nuclear Physics (I have been an associate member during my PhD)
- ✓ University of Paris Diderot, France
- ✓ IFM, Linköping University, Linköping, Sweden
- ✓ CNR-IMM Institute for Microelectronics and Microsystem, Lecce, Italy
- ✓ Department of Energy, Polytechnic of Milan, Italy
- ✓ Department of Chemistry, Materials and Chemical Engineering, Polytechnic of Milan, Italy
- ✓ CNR Nanotec, Lecce, Italy.

Visited laboratory

- ✓ 16^{th} – 27^{th} November 2015
  National Laboratory of Frascati (LNF), Italy
  Topic: Electron and Positron beam test on the segmented graphitized diamond detector for the PADME experiment.

References

[1] Field J.E., *The Properties of Natural and Synthetic Diamond*, Academic Press, Harcourt Brace Jovanovich, 1992.

[2] Mainwood A., *Recent developments of diamond detectors for particles and UV radiation,* Semiconductor Science and Technology 15 (9) 2000, p. R55-R63.

[3] Ahmed S.N., *Physics and Engineering of Radiation Detection*, Academic Press is an imprint of Elsevier ed, Great Britain, 2007.

[4] Balmer R.S., et al., *Chemical vapour deposition synthetic diamond: materials, technology and applications,* Journal of Physics: Condensed Matter 21 (36) 2009, p. 364221.

[5] Pan L.S. and D.R. Kania, *Diamond: electronic properties and applications*, Springer science + business media LLC ed, ed. H.L. Tuller, New York, USA, 1995.

[6] Eversole W.G., *Synthesis of diamond*, in *US patent n° 3 030 187 and 3 030 188*. (1958).

[7] Spitsyn B.V. and B.V. Deryagin, *A technique of diamond growth on diamond's face.* 1956, Inventor's certificate 339, 134: USSR.

[8] Spitsyn B.V., L.L. Bouilov, and B.V. Derjaguin, *Vapor growth of diamond on diamond and other surfaces,* Journal of Crystal Growth 52 (Part 1) 1981, p. 219-226.

[9] Spitsyn B.V. and L.L. Builov, *The growth of diamond and diamond like films from a gaz phase*, Proceeding of the Diamond and diamond-like materials synthesis, Extended abstract, M.R.S. 1988, p. 3-14.

[10] Spitsyn B.V., *Diamond films : Synthesis, properties and some fields of application*, Proceeding of the Science and Technology of New Diamond, Tokyo, KTK Scientific Publishers 1990, p. 1-7.

[11] Spitsyn B., *Chemical cristallisation from the activated vapour phase.,* Journal of Crystal Growth 99 1990, p. 1162-1167.

[12] Raggi M. and V. Kozhuharov, *Proposal to Search for a Dark Photon in Positron on Target Collisions at DANE Linac,* Advances in High Energy Physics 2014 (959802) 2014, p. 14.

[13] Davies G., *Properties and Growth of Diamond*, INSPEC, Institution of Electrical Engineers ed, London, 1994.

[14] Konov V.I., *Laser in micro and nanoprocessing of diamond materials,* Laser & Photonics Reviews 6 (6) 2012, p. 739-766.

[15] Pomorski M., *Electronic properties of signle crystal CVD diamond and its suitability for particle detection in hadron physics experiments,* PhD Thesis, Johann Wolfgang Goethe Universitat - Frankfurt am Main, 2008.

[16] von Bolton W., *The segregation of carbon in diamond form,* Elektrochemie 17 1911, p. 971-972.

[17] Bundy F.P., et al., *Man-made diamond,* Nature 176 1955, p. 51-55.

[18] Bundy F.P., *The P and T phase and reaction diagram for elemental carbon,* Journal of Geophysical Research 85 (B12) 1980, p. 6930.

[19] Martineau P.M., et al., *Identification of Synthetic Diamond Grown Using Chemical Vapor Deposition (CVD)* Gems & Gemology 40 (1) 2004, p. 2.

[20] Shigley J.E., et al., *The gemmological properties of the De Beers gem-quality synthetic diamonds,* Gems and Gemology 23 (4) 1987, p. 187-206.

[21] Liu W.Q., et al., *Effects of additive Al on the HPHT diamond synthesis in an Fe-Mn-C system,* Diamond and Related Materials 16 (8) 2007, p. 1486-1489.

[22] D'Haenens-Johansson U.F.S., et al., *Large Colorless HPHT Synthetic Diamonds from New Diamond Technology,* Contributions to Gemology 15 2015, p. 1-7.

[23] Deljanin B., et al., *NDT breaking the 10ct barrier: World Record faceted and gem-quality diamonds investigated,* Contributions to Gemology 15 (July) 2015.
[24] Sumiya H., K. Harano, and K. Tamasaku, *HPHT synthesis and crystalline quality of large high-quality (001) and (111) diamond crystals,* Diamond and Related Materials 58 2015, p. 221–225.
[25] Hitoshi S. and T. Kenji, *Large Defect-Free Synthetic Type IIa Diamond Crystals Synthesized via High Pressure and High Temperature,* Japanese Journal of Applied Physics 51 (9R) 2012, p. 090102.
[26] http://www.diamondlab.org/80-hpht_synthesis.htm.
[27] Anthony T.R., *Metastable synthesis of diamond*, in *The Physic and Chemistry of Carbides; Nitrides and Borides*, R. Freer, Editor, 1990.
[28] Gicquel A., et al., *CVD diamond films: from growth to applications,* Current Applied Physics 1 (6) 2001, p. 479-496.
[29] Gicquel A., *Le diamant métastable : matériau stratégique ?-partie I-: Les procédés de production, les applications optiques et opto-électroniques.* 1996, ENS.
[30] Clausing R.E., et al., *Electron microscopy of the growth features and crystal structures of filament assisted CVD diamond films,* Surface and Coatings Technology 34/40 1989, p. 199-210.
[31] Kamo M., et al., *Diamond synthesis from gas phase in microwave plasma,* Journal of Crystal Growth 62 1983, p. 642-644.
[32] Gicquel A., et al., *Validation of actinometry for estimating relative hydrogen atom densities and electron energy evolution in plasma assisted diamond deposition reactors,* Journal of Applied Physics 83 (12) 1998, p. 7504-7521.
[33] Hassouni K., T.A. Grotjohn, and A. Gicquel, *Self-consistent microwave field and plasma discharge simulations for a moderate pressure hydrogen discharge reactor,* Journal of Applied Physics 86 (1) 1999, p. 134-151.
[34] Hassouni K., F. Silva, and A. Gicquel, *Modelling of diamond deposition microwave cavity generated plasmas,* Journal of Physics D-Applied Physics 43 (15) 2010, p. 153001.
[35] Gicquel A., et al., *Ground state and excited state H-atom temperatures in a microwave plasma diamond deposition reactor,* Journal de physique III 6 1996, p. 1167-1180.
[36] Hassouni K., et al., *Modeling of H2 and H2/CH4 Moderate-Pressure Microwave Plasma Used for Diamond Deposition,* Plasma Chemistry and Plasma Processing 18 (3) 1998, p. 325-362.
[37] Achard J., et al., *High quality MPACVD diamond single crystal growth: high microwave power density regime,* Journal of Physics D: Applied Physics 40 (20) 2007, p. 6175-6188.
[38] Achard J., et al., *The control of growth parameters in the synthesis of high-quality single crystalline diamond by CVD,* Journal of Crystal Growth 284 (3-4) 2005, p. 396-405.
[39] Cao G.Z., et al., *Growth of {100} textured diamond films by the addition of nitrogen,* Journal of Applied Physics 79 (3) 1996, p. 1357-64.
[40] Jin S. and T.D. Moustakas, *Effect on nitrogen on the growth of diamond films,* Applied Physics Letters 65 (4) 1994, p. 403-405.
[41] Tallaire A., et al., *Characterisation of high-quality thick single-crystal diamond grown by CVD with a low nitrogen addition,* Diamond and Related Materials 15 (10) 2006, p. 1700-1707.
[42] van der Drift A., *Evolutionary selection, a principle governing growth orientation in vapour-deposited layers*. 1967, Philips Research Reports. p. 267-288.
[43] Vaissière N., *Synthèse de films de diamant de haute qualité cristalline pour la réalisation de dosimètres pour la radiothérapie,* École normale supérieure de Cachan-ENS Cachan, 2014.
[44] Mallik A.K., N. Dandapat, and S. Chakraborty, *Characterizations of microwave plasma CVD grown polycrystalline diamond coatings for advanced technological applications,* Processing and Application of Ceramics 8 (2) 2014, p. 69-80.

[45] Brinza O., *Stratégies pour la croissance de cristaux de diamant par CVD assisté par plasma micro-onde,* PhD Thesis, Université Paris Nord - Paris XIII, 2009.
[46] Tallaire A., et al., *Thick CVD diamond films grown on high-quality type IIa HPHT diamond substrates from New Diamond Technology,* Diamond and Related Materials 77 2017, p. 146-152.
[47] Tallaire A., et al., *Reduction of Dislocations in Single Crystal Diamond by Lateral Growth over a Macroscopic Hole,* Advanced Materials 29 2017, p. 1604823.
[48] Naamoun M., et al., *Reduction of dislocation densities in single crystal CVD diamond by using self-assembled metallic masks,* Diamond and Related Materials 58 2015, p. 62-68.
[49] Achard J., et al., *Improvement of dislocation density in thick CVD single crystal diamond films by coupling H2/O2 plasma etching and chemo-mechanical or ICP treatment of HPHT substrates,* Physica Status Solidi (a) 211 2014, p. 2264–2267.
[50] Tallaire A., et al., *Growth strategy for controlling dislocation densities and crystal morphologies of single crystal diamond by using pyramidal-shape substrates,* Diamond and Related Materials 33 (0) 2013, p. 71-77.
[51] Naamoun M., et al., *Influence of surface misorientation of HPHT diamond substrates on crystal morphologies and threading dislocations propagation,* Physica Status Solidi (a) 210 (10) 2013, p. 1985-1990.
[52] Tavares C., S. Koizumi, and H. Kanda, *Effects of RIE treatments for {111} diamond substrates on the growth of P-doped diamond thin films,* physica status solidi (a) 202 (11) 2005, p. 2129-2133.
[53] Volpe P.-N., et al., *Defect analysis and excitons diffusion in undoped homoepitaxial diamond films after polishing and oxygen plasma etching,* Diamond and Related Materials 18 (10) 2009, p. 1205-1210.
[54] Tallaire A., et al., *Origin of growth defects in CVD diamond epitaxial films,* Diamond and Related Materials 17 (1) 2008, p. 60-65.
[55] Saguy C., et al., *Diffusion of hydrogen in undoped, p-type and n-type doped diamonds,* Diamond and Related Materials 12 (3) 2003, p. 623-631.
[56] Tsai W., et al., *Diamond MESFET using ultrashallow RTP boron doping,* IEEE Electron Device Letters 12 (4) 1991, p. 157-159.
[57] Popovici G., et al., *Diffusion of boron, lithium, oxygen, hydrogen, and nitrogen in type IIa natural diamond,* Journal of Applied Physics 77 (10) 1995, p. 5103-5106.
[58] Krutko O.B., et al., *P-type polycrystalline diamond layers by rapid thermal diffusion of boron,* Applied Physics Letters 76 (7) 2000, p. 849-851.
[59] Vavilov V.S., *Ion implantation into diamond,* Radiation Effects 37 (3-4) 1978, p. 229-236.
[60] Fontaine F., et al., *Boron implantation/in situ annealing procedure for optimal p -type properties of diamond,* Applied Physics Letters 68 (16) 1996, p. 2264-2266.
[61] Uzan-Saguy C., et al., *Formation of delta-doped, buried conducting layers in diamond, by high-energy, B-ion implantation,* Diamond and Related Materials 7 (10) 1998, p. 1429-1432.
[62] Kalish R., et al., *Nitrogen doping of diamond by ion implantation,* Diamond and Related Materials 6 1997, p. 516-520.
[63] Prawer S. and R. Kalish, *Ion-beam-induced transformation of diamond,* Physical Review B 51 (22) 1995, p. 15711-15722.
[64] Uzan-Saguy C., et al., *Damage threshold for ion-beam induced graphitization of diamond,* Applied Physics Letters 67 (9) 1995, p. 1194-1196.
[65] Tsubouchi N., et al., *Formation of a heavily B doped diamond layer using an ion implantation technique,* Diamond and Related Materials 17 (4-5) 2008, p. 498-501.
[66] Ueda K., M. Kasu, and T. Makimoto, *High-pressure and high-temperature annealing as an activation method for ion-implanted dopants in diamond,* Applied Physics Letters 90 (12) 2007, p. 122102-3.

[67] Ueda K. and M. Kasu, *High-pressure and high-temperature annealing effects of boron-implanted diamond,* Diamond and Related Materials 17 (4-5) 2008, p. 502-505.
[68] Ueda K. and M. Kasu, *High-pressure and high-temperature annealing of diamond ion-implanted with various elements,* Diamond and Related Materials 17 (7-10) 2008, p. 1269-1272.
[69] Michl J., et al., *Perfect alignment and preferential orientation of nitrogen-vacancy centers during chemical vapor deposition diamond growth on (111) surfaces,* Applied Physics Letters 104 (10) 2014, p. 102407.
[70] Neu E., et al., *Photonic nano-structures on (111)-oriented diamond,* Applied Physics Letters 104 (15) 2014, p. 153108.
[71] Casanova N., et al., *Epitaxial growth of phosphorus doped diamond on {111} substrate,* Diamond and Related Materials 11 (3) 2002, p. 328-331.
[72] Suzuki M., et al., *Electrical characterization of phosphorus-doped n-type homoepitaxial diamond layers,* Diamond and Related Materials 13 (11-12) 2004, p. 2037-2040.
[73] Koizumi S., et al., *Growth and characterization of phosphorous doped {111} homoepitaxial diamond thin films,* Applied Physics Letters 71 (8) 1997, p. 1065-1067.
[74] Kato H., et al., *Growth of phosphorus-doped diamond using tertiarybutylphosphine and trimethylphosphine as dopant gases,* Diamond and Related Materials 14 (3) 2005, p. 340-343.
[75] Kociniewski T., et al., *n-type CVD diamond doped with phosphorus using the MOCVD technology for dopant incorporation,* Physica Status Solidi (a) 203 (12) 2006, p. 3136-3141.
[76] Pinault-Thaury M.-A., et al., *High fraction of substitutional phosphorus in a (100) diamond epilayer with low surface roughness,* Applied Physics Letters 100 (19) 2012, p. 192109.
[77] Kato H., S. Yamasaki, and H. Okushi, *n-type doping of (001)-oriented single-crystalline diamond by phosphorus,* Applied Physics Letters 86 (22) 2005, p. 222111-3.
[78] Pinault-Thaury M.-A., et al., *Electrical activity of (100) n-type diamond with full donor site incorporation of phosphorus,* physica status solidi (a) 2015, p. n/a-n/a.
[79] Frangieh G., et al., *Incorporation of arsenic in diamond grown by chemical vapor deposition,* physica status solidi (a) 205 (9) 2008, p. 2207-2210.
[80] Barjon J., F. Jomard, and S. Morata, *Arsenic-bound excitons in diamond,* Physical Review B 89 (4) 2014, p. 045201.
[81] Locher R., et al., *Optical and electrical characterization of boron-doped diamond films,* Diamond and Related Materials 4 1995, p. 678-683.
[82] Okushi H., *High quality homoepitaxial CVD diamond for electronic devices,* Diamond and Related Materials 10 (3-7) 2001, p. 281-288.
[83] Kasu M., et al., *Formation of stacking faults containing microtwins in (111) chemical-vapor-deposited diamond homoepitaxial layers,* Applied Physics Letters 83 (17) 2003, p. 3465-3467.
[84] Ushizawa K., et al., *Boron concentration dependence of Raman spectra on {100} and {111} facets of B-doped CVD diamond,* Diamond and Related Materials 7 1998, p. 1719-1722.
[85] Deneuville A., et al., *Highly and heavily boron doped diamond films,* Diamond and Related Materials 16 (4-7) 2007, p. 915-920.
[86] Demlow S.N., R. Rechenberg, and T. Grotjohn, *The effect of substrate temperature and growth rate on the doping efficiency of single crystal boron doped diamond,* Diamond and Related Materials 49 (Supplement C) 2014, p. 19-24.
[87] Kadri M., et al., *Effect of oxygen on the cathodoluminescence signal from excitons, impurities and structural defects in homoepitaxial (100) diamond films,* Diamond and Related Materials 14 (3-7) 2005, p. 566-569.
[88] Volpe P.N., et al., *High hole mobility in boron doped diamond for power device applications,* Applied Physics Letters 94 (9) 2009, p. 092102.
[89] Barjon J., et al., *Resistivity of boron doped diamond,* physica status solidi (RRL) – Rapid Research Letters 3 (6) 2009, p. 202-204.

[90] Achard J., et al., *Thick boron doped diamond single crystals for high power electronics,* Diam. Relat. Mater. 20 2011, p. 145-152.
[91] Issaoui R., et al., *Growth of thick heavily boron-doped diamond single crystals: effect of microwave power density.,* Appl. Phys. Lett. 97 2010, p. 182101.
[92] Ohmagari S., et al., *Growth and characterization of freestanding p+diamond (100) substrates prepared by hot-filament chemical vapor deposition,* Diamond and Related Materials 81 2018, p. 33-37.
[93] Achard J., et al., *Freestanding CVD boron doped diamond single crystals: A substrate for vertical power electronic devices?,* physica status solidi (a) 209 2012, p. 1651-1658.
[94] Barjon J., et al., *Homoepitaxial boron-doped diamond with very low compensation,* physica status solidi (a) 209 2012, p. 1750-1753.
[95] Monflier R., et al., *Diodes Schottky diamant fonctionnant à 200° C,* 2015.
[96] Mortet V., et al., *Properties of boron-doped epitaxial diamond layers grown on (110) oriented single crystal substrates,* Diamond and Related Materials 53 (0) 2015, p. 29-34.
[97] Werner M., et al., *The Relationship between Resistivity and Boron Doping Concentration of Single and Polycrystalline Diamond,* Physica Status Solidi (a) 154 (1) 1996, p. 385-393.
[98] Williams W.S., E.C. Lightowlers, and A.T. Collins, *Impurity conduction in synthetic semiconducting diamond,* J. Phys. C: Solid State Phys. 3 1970, p. 1727
[99] Klein T., et al., *Metal-insulator transition and superconductivity in boron-doped diamond,* Physical Review B (Condensed Matter and Materials Physics) 75 (16) 2007, p. 165313-7.
[100] Pearson G.L. and J. Bardeen, *Electrical Properties of Pure Silicon and Silicon Alloys Containing Boron and Phosphorus,* Physical Review 75 (5) 1949, p. 865-883.
[101] Look D.C., *Electrical Characterization of GaAs Materials and Devices*, ed. Wiley, New York, 1989.
[102] Thonke K., *The boron acceptor in diamond,* Semiconductor Science and Technology 18 (3) 2003, p. S20-S26.
[103] Nebel C., *Transport and defect properties of intrinsic and boron-doped diamond in "Semiconductors and semimetals"*, ed. C. Nebel and J. Ristein, 2003.
[104] Mortet V., et al., *Characterization of boron doped diamond epilayers grown in a NIRIM type reactor,* Diamond and Related Materials 17 (7) 2008, p. 1330-1334.
[105] Mathieu H., *Physique des semiconducteurs et des composants électroniques*, Dunod ed, Paris, 2001.
[106] Butler J.E., et al., *Exceptionally high voltage Schottky diamond diodes and low boron doping,* Semiconductor Science and Technology 18 (3) 2003, p. S67-S71.
[107] Volpe P.N., et al., *Extreme dielectric strength in boron doped homoepitaxial diamond,* Applied Physics Letters 97 (22) 2010, p. 223501.
[108] Chen Y., et al., *Diamond Schottky barrier diodes with low specific on-resistance,* Semicond. Sci. Technol. 20 2005, p. 1203–1206.
[109] Umezawa H., Y. Kato, and S. Shikata, *1 Ω On-Resistance Diamond Vertical-Schottky Barrier Diode Operated at 250 °C,* Applied Physics Express 6 2013, p. 011302.
[110] Traoré A., et al., *Zr/oxidized diamond interface for high power Schottky diodes,* Applied Physics Letters 104 (5) 2014, p. -.
[111] Koné S., et al., *An assessment of contact metallization for high power and high temperature diamond Schottky devices,* Diamond and Related Materials 27–28 2012, p. 23-28.
[112] Pinero J.C., et al., *Metal-oxide-diamond interface investigation by TEM: Toward MOS and Schottky power device behavior,* Physica Status Solidi a-Applications and Materials Science 211 (10) 2014, p. 2367-2371.
[113] Eon D., et al., *Recent progress on diamond Schottky diode*, Proceeding of the 28th International Symposium on Power Semiconductor Devices and ICs (ISPSD) 2016, Prague, Czech Republic, IEEE, INSPEC Accession Number: 16177969.
[114] Traoré A., *High power diamond Schottky diode,* PhD Thesis, Université de Grenoble, 2014.

[115] Muret P., et al., *Potential barrier heights at metal on oxygen-terminated diamond interfaces,* Journal of Applied Physics 118 (20) 2015, p. 204505.
[116] Umezawa H., S.-i. Shikata, and T. Funaki, *Diamond Schottky barrier diode for high-temperature, high-power, and fast switching applications,* Japanese Journal of Applied Physics 53 (5S1) 2014, p. 05FP06.
[117] Makino T., et al., *Diamond electronic devices fabricated using heavily doped hopping p + and n + layers,* Japanese Journal of Applied Physics 53 (5S1) 2014, p. 05FA12.
[118] Collins A.T., E.C. Lightowlers, and A.W.S. Williams, *Formation of electrical contacts on insulating and semiconducting diamonds,* Diamond Res. (Suppl. Indust. Diamond Rev.) 1970, p. 19-22.
[119] Tachibana T., B.E. Williams, and J.T. Glass, *Correlation of the electrical properties of metal contacts on diamond films with the chemical nature of the metal-diamond interface. I. Gold contacts: A non-carbide-forming metal,* Physical Review B 45 (20) 1992, p. 11968-11974.
[120] Tachibana T. and T. Glass, *Effects of argon presputtering on the formation of aluminum contacts on polycrystalline diamond* J. Appl. Phys. 72 (12) 1992, p. 5912.
[121] Tachibana T., B.E. Williams, and J.T. Glass, *Correlation of the electrical properties of metal contacts on diamond films with the chemical nature of the metal-diamond interface. II. Titanium contacts: A carbide-forming metal,* Physical Review B 45 (20) 1992, p. 11975-11981.
[122] Geis M.W., et al., *Electrical, crystallographic, and optical properties of ArF laser modified diamond surfaces,* Appl. Phys. Lett. 55 (22) 1989, p. 2295.
[123] Tachibana T., T. Glass, and D.G. Thompson, *Titanium carbide rectifying contacts on boron-doped polycrystalline diamond,* Diam. and Rel. Mater. 2 1993, p. 37.
[124] Tachibana T., I.T. Glass, and R.I. Nemanich, *Effect of surface hydrogen on metaldiamond interface properties,* J. Appl. Phys. 73 (2) 1993, p. 835.
[125] Tachibana T. and J.T. Glass, *Correlation of interface chemistry to electrical properties of metal contacts on diamond,* Diam. and Rel. Mater. 2 1993, p. 963.
[126] Gildenblat G.S., et al., *High temperature Schottky diodes with thin-film diamond base IEEE Electron Device* IEEE Electron Device Lett. 11 (9) 1990, p. 371.
[127] Moazed K.L., J.R. Zeidler, and M.J. Taylor, *A thermally activated solid state reaction process for fabricating ohmic contacts to semiconducting diamond,* Appl. Phys. 68 (5) 1990, p. 2246.
[128] Shiomi H., et al., *Electrical characteristics of metal contacts to boron-doped diamond epitaxial film,* Jpn. J. Appl. Phys. 28 (5) 1989, p. 758.
[129] Moazed K.L., R. Nguyen, and J.R. Zeidler, *Ohmic contacts to semiconducting diamond,* IEEE Electron Device Lett. 9 (7) 1988, p. 350.
[130] Pate B.B., et al., J. Vac. Sci. Technol. 21 1982, p. 364.
[131] Teraji T., S. Koizumi, and Y. Koide, *Ohmic contact for p-type diamond without postannealing,* Journal of Applied Physics 104 (1) 2008, p. 016104.
[132] Volpe P.-N., et al., *High breakdown voltage Schottky diodes synthesized on p-type CVD diamond layer,* physica status solidi (a) 207 (9) 2010, p. 2088-2092.
[133] Teraji T., et al., *Low-leakage p-type diamond Schottky diodes prepared using vacuum ultraviolet light/ozone treatment,* Journal of Applied Physics 105 (12) 2009, p. 126109.
[134] Kono S., et al., *Sheet resistance underneath the Au ohmic-electrode on hydrogen-terminated surface-conductive diamond (001),* Diamond and Related Materials 80 (Supplement C) 2017, p. 93-98.
[135] Koizumi S., C. Nebel, and M. Nesladek, *Physics and Applications of CVD Diamond*, WILEY-VCH Verlag GmbH & Co. KGaA ed, Weinheim, Germany, 2008.
[136] Lindström G., et al., *Radiation hard silicon detectors—developments by the RD48 (ROSE) collaboration,* Nuclear Instruments and Methods in Physics Research Section A: Accelerators, Spectrometers, Detectors and Associated Equipment 466 (2) 2001, p. 308-326.

[137] Adam W., et al., *Pulse height distribution and radiation tolerance of CVD diamond detectors,* Nuclear Instruments and Methods in Physics Research Section A: Accelerators, Spectrometers, Detectors and Associated Equipment 447 (1) 2000, p. 244-250.
[138] Adam W., et al., *Radiation hard diamond sensors for future tracking applications,* Nuclear Instruments and Methods in Physics Research Section A: Accelerators, Spectrometers, Detectors and Associated Equipment 565 (1) 2006, p. 278-283.
[139] Marinelli M., et al., *Trapping and detrapping effects in high-quality chemical-vapor-deposition diamond films: Pulse shape analysis of diamond particle detectors,* Physical Review B 64 (19) 2001, p. 195205.
[140] Plano M.A., et al., *Thickness dependence of the electrical characteristics of chemical vapor deposited diamond films,* Applied Physics Letters 64 (2) 1994, p. 193-195.
[141] Adam W., et al., *Status of the R&D activity on diamond particle detectors,* Nuclear Instruments and Methods in Physics Research Section A: Accelerators, Spectrometers, Detectors and Associated Equipment 511 (1-2) 2003, p. 124-131.
[142] Bruinsma M., et al., *CVD Diamonds in the BaBar Radiation Monitoring System,* Nuclear Physics B - Proceedings Supplements 150 (Supplement C) 2006, p. 164-167.
[143] Pernegger H., et al., *Design and test of a high-speed single-particle beam monitor,* Nuclear Instruments and Methods in Physics Research Section A: Accelerators, Spectrometers, Detectors and Associated Equipment 535 (1) 2004, p. 108-114.
[144] Chong D., et al., *Validation of Synthetic Diamond for a Beam Condition Monitor for the Compact Muon Solenoid Experiment,* IEEE Transactions on Nuclear Science 54 (1) 2007, p. 182-185.
[145] Bachmair F., *Diamond sensors for future high energy experiments,* Nuclear Instruments and Methods in Physics Research Section A: Accelerators, Spectrometers, Detectors and Associated Equipment 831 (Supplement C) 2016, p. 370-377.
[146] Lattanzi D., et al., *Single crystal CVD diamonds as neutron detectors at JET,* Fusion Engineering and Design 84 (7) 2009, p. 1156-1159.
[147] Schmid G.J., et al., *CVD diamond as a high bandwidth neutron detector for inertial confinement fusion diagnostics,* Review of Scientific Instruments 74 (3) 2003, p. 1828-1831.
[148] Angelone M., et al., *Radiation hardness of a polycrystalline chemical-vapor-deposited diamond detector irradiated with 14 MeV neutrons,* Review of Scientific Instruments 77 (2) 2006, p. 023505.
[149] Almaviva S., et al., *Thermal and fast neutron detection in chemical vapor deposition single-crystal diamond detectors,* Journal of Applied Physics 103 (5) 2008, p. 054501.
[150] Lardon P., et al., *Investigations of high quality diamond detectors for neutron fluency monitoring in a nuclear reactor,* Diamond and Related Materials 15 (4-8) 2006, p. 815-821.
[151] Pietraszko J., et al., *Diamonds as timing detectors for minimum-ionizing particles: The HADES proton-beam monitor and START signal detectors for time of flight measurements,* Nuclear Instruments and Methods in Physics Research Section A: Accelerators, Spectrometers, Detectors and Associated Equipment 618 (1) 2010, p. 121-123.
[152] Berretti M., *The diamond time of flight detector of the TOTEM experiment,* Nuclear Instruments and Methods in Physics Research Section A: Accelerators, Spectrometers, Detectors and Associated Equipment 845 (Supplement C) 2017, p. 29-32.
[153] Nesladek M., *Conventional n-type doping in diamond: state of the art and recent progress,* Semiconductor Science and Technology 20 (2) 2005, p. R19.
[154] Girolami M., et al., *Large single-crystal diamond substrates for ionizing radiation detection,* physica status solidi (a) 213 (10) 2016, p. 2634-2640.
[155] Adam W., et al., *Review of the development of diamond radiation sensors,* Nuclear Instruments and Methods in Physics Research Section A: Accelerators, Spectrometers, Detectors and Associated Equipment 434 (1) 1999, p. 131-145.

[156] Cyril M., et al., *Development of a synthetic single crystal diamond dosimeter for dose measurement of clinical proton beams,* Physics in Medicine & Biology 62 (13) 2017, p. 5417.
[157] Gallin-Martel M.L., et al., *Large area polycrystalline diamond detectors for online hadron therapy beam tagging applications*, Proceeding of the 2016 IEEE Nuclear Science Symposium, Medical Imaging Conference and Room-Temperature Semiconductor Detector Workshop (NSS/MIC/RTSD), p. 1-5.
[158] Pomorski M., et al., *Characterization of the charge-carrier transport properties of IIa-Tech SC diamond for radiation detection applications,* physica status solidi (a) 2015, p. n/a-n/a.
[159] Bachmair F., *CVD Diamond Sensors In Detectors For High Energy Physics,* PhD Thesis, Institute for Particle Physics, Department of Physics, ETH Zürich, 2016.
[160] Adam W., et al., *The first bump-bonded pixel detectors on CVD diamond,* Nuclear Instruments and Methods in Physics Research Section A: Accelerators, Spectrometers, Detectors and Associated Equipment 436 (3) 1999, p. 326-335.
[161] Bartoli A., et al., *Dosimetric characterization of a 2D polycrystalline CVD diamond detector,* Journal of Instrumentation 12 (03) 2017, p. C03052.
[162] Parker S.I., C.J. Kenney, and J. Segal, *3D — A proposed new architecture for solid-state radiation detectors,* Nuclear Instruments and Methods in Physics Research Section A: Accelerators, Spectrometers, Detectors and Associated Equipment 395 (3) 1997, p. 328-343.
[163] ViÀ C.D., et al., *3D Active Edge Silicon Detector Tests With 120 GeV Muons,* IEEE Transactions on Nuclear Science 56 (2) 2009, p. 505-518.
[164] Kononenko T.V., et al., *Microstructuring of diamond bulk by IR femtosecond laser pulses,* Appl. Phys. A (90) 2008, p. 645.
[165] Artuso M., et al., *A 3D diamond detector for particle tracking,* Nuclear Instruments and Methods in Physics Research Section A: Accelerators, Spectrometers, Detectors and Associated Equipment 824 2016, p. 402-405.
[166] Venturi N., *Diamond Pixel Detectors and 3D Diamond Devices,* Journal of Instrumentation 11 (12) 2016, p. C12062.
[167] Kagan H., et al., *Diamond detector technology: status and perspectives*, Proceeding of the 25th International Workshop on Vertex Detectors (VERTEX 2016), La Biodola, Isola d'Elba, Italy Vertex2016, p. 027.
[168] Liu K., et al., *Single crystal diamond UV detector with a groove-shaped electrode structure and enhanced sensitivity,* Sensors and Actuators A: Physical 259 2017, p. 121-126.
[169] Wang C.Z., et al., *Laser-Induced Graphitization on a Diamond (111) Surface,* Physical Review Letters 85 (19) 2000, p. 4092-4095.
[170] Nistor L., et al., *Formation of Amorphous Carbon and Graphite in CVD Diamond upon Annealing: A HREM, EELS, Raman and Optical Study,* physica status solidi (a) 186 (2) 2001, p. 207-214.
[171] Kononenko V.V., et al., *Laser-induced structure transformations of diamonds*, Proceeding of the Laser Processing of Advanced Materials and Laser Microtechnologies, SPIE 5121, 2003, p. 259-270.
[172] Kononenko T.V., et al., *Ablation of CVD diamond with nanosecond laser pulses of UV–IR range1Presented at the Diamond '97 Conference, Edinburgh, Scotland, August 3–8, 1997.1,* Diamond and Related Materials 7 (11) 1998, p. 1623-1627.
[173] Komlenok M.S., et al., *Laser microstructuring of the surface of ta-C films,* Nano/Microsystem Technology 3 2008, p. 48-53.
[174] Chan S.S.M., et al., *The effect of excimer laser etching on thin film diamond,* Semicond. Sci. Technol. 18 2003, p. S47–S58.
[175] Kononenko V.V., et al., *Photoinduced laser etching of a diamond surface,* Quantum Electronics 37 (11) 2007, p. 1043-1046.
[176] Taurino A., et al., *Graphitization of Diamond by Means of UV Laser Writing: A Transmission Electron Microscopy Study,* Microscopy and Microanalysis 23 (S1) 2017, p. 2262-2263.

[177] Collins A.T., *The Physics of diamond*, Edited by A. Paoletti and A. Tucciarone, IOS Press ed, Oxford, UK, 1997.
[178] De Feudis M., *Realizzazione e caratterizzazione di contatti grafitici su diamante mediante laser,* Master degree thesis, Università del Salento (Italy), 2014.
[179] De Feudis M., et al., *Realization and characterization of graphitic contacts on diamond by means of laser*, Proceeding of the IV National Workshop on Plasmi Sorgenti Biofisica e Applicazioni (PSBA) 2014, Lecce, Italy, ISBN: 9788883051081 2015.
[180] De Feudis M., et al., *Characterization of surface graphitic electrodes made by excimer laser on CVD diamond,* Diamond and Related Materials 65 (Supplement C) 2016, p. 137-143.
[181] De Feudis M., et al., *Diamond detectors with electrodes graphitized by means of laser*, Proceeding of the Conference Incontri di Fisica delle Alte Energie (IFAE) 2015, Rome, Italy, IL NUOVO CIMENTO 39 (C) 2016, p. 254.
[182] Kononenko T.V., et al., *Femtosecond laser microstructuring in the bulk of diamond,* Diamond and Related Materials 18 (2) 2009, p. 196-199.
[183] Pacilli M., et al., *Beta particles sensitivity of an all-carbon detector,* Nuclear Instruments and Methods in Physics Research Section A: Accelerators, Spectrometers, Detectors and Associated Equipment 738 2014, p. 119-125.
[184] Komlenok M., et al., *Diamond detectors with laser induced surface graphite electrodes,* Nuclear Instruments and Methods in Physics Research Section A: Accelerators, Spectrometers, Detectors and Associated Equipment 837 2016, p. 136-142.
[185] Salvatori S., et al., *Nano-carbon pixels array for ionizing particles monitoring,* Diamond and Related Materials 73 2017, p. 132-136.
[186] Kononenko T., et al., *All-carbon detector with buried graphite pillars in CVD diamond,* Appl. Phys. A 114 2014, p. 297-300.
[187] Su S., et al., *Femtosecond laser-induced microstructures on diamond for microfluidic sensing device applications,* Applied Physics Letters 102 (23) 2013, p. 231913.
[188] Girolami M., et al., *Graphite distributed electrodes for diamond-based photon-enhanced thermionic emission solar cells,* Carbon 111 2017, p. 48-53.
[189] Orwa J.O., et al., *Raman investigation of damage caused by deep ion implantation in diamond,* Physical Review B 62 (9) 2000, p. 5461-5472.
[190] Kalish R., et al., *Ion-Implantation-Induced Defects in Diamond and Their Annealing: Experiment and Simulation,* Physica status solidi (a) 174 (83) 1999, p. 83-99.
[191] Kalish R. and S. Prawer, *Graphitization of diamond by ion impact: Fundamentals and applications,* Nuclear Instruments & Methods in Physics Research B 106 1995, p. 492-499.
[192] Gippius A.A., et al., *Defect-induced graphitisation in diamond implanted with ligth ions,* Physica B 308-310 2001, p. 573-576.
[193] Olivero P., et al., *Characterization of three-dimensional microstructures in single-crystal diamond,* Diamond and Related Materials 15 (10) 2006, p. 1614-1621.
[194] Hunn J.D., et al., *Raman scattering from MeV-ion implanted diamond,* Physical Review B 52 (11) 1995, p. 8106.
[195] Dresselhaus M.S. and R. Kalish, *Ion Implantation in Diamond, Graphite and Related Materials*, ed. U. Gonser, et al., Berlin, Springer-Verlag, 1992.
[196] http://www.srim.org/.
[197] Ziegler J.F., M.D. Ziegler, and J.P. Biersack, *SRIM – The stopping and range of ions in matter (2010),* Nuclear Instruments and Methods in Physics Research Section B: Beam Interactions with Materials and Atoms 268 (11) 2010, p. 1818-1823.
[198] Chen Y.G., et al., *Electrical properties of graphite/homoepitaxial diamond contact,* Diamond and Related Materials 11 (3) 2002, p. 451-457.
[199] Piñero J.C., et al., *Impact of Thermal Treatments in Crystalline Reconstruction and Electrical Properties of Diamond Ohmic Contacts Created by Boron Ion Implantation,* physica status solidi (a) 214 (11) 2017, p. 1700230-n/a.

[200] Bolshakov A.P., et al., *Thin CVD diamond film detector for slow neutrons with buried graphitic electrode,* Nuclear Instruments and Methods in Physics Research Section A: Accelerators, Spectrometers, Detectors and Associated Equipment 871 2017, p. 142-147.
[201] Matsumoto T., et al., *Reduction of n-type diamond contact resistance by graphite electrode,* physica status solidi (RRL) – Rapid Research Letters 8 (2) 2014, p. 137-140.
[202] Mokuno Y., A. Chayahara, and H. Yamada, *Synthesis of large single crystal diamond plates by high rate homoepitaxial growth using microwave plasma CVD and lift-off process,* Diamond and Related Materials 17 (4-5) 2008, p. 415-418.
[203] *http://usappliedddiamond.com/*.
[204] http://www.sumitomotool.com.
[205] Welbourn C.M., M. Cooper, and P.M. Spear, *De Beers Natural versus Synthetic Diamond Verification Instruments,* Gems & Gemology 32 (3) 1996, p. 156-169.
[206] Naamoun M., et al., *Etch-pit formation mechanism induced on HPHT and CVD diamond single crystals by H2/O2 plasma etching treatment,* physica status solidi (a) 209 2012, p. 1715-1720.
[207] Tallaire A., et al., *Oxygen plasma pre-treatments for high quality homoepitaxial CVD diamond deposition,* physica status solidi (a) 201 (11) 2004, p. 2419-2424.
[208] Tallaire A., *Croissance de monocristaux de diamant par dépôt chimique en phase vapeur pour des applications en électronique de puissance,* PhD Thesis, University of Paris 13, 2005.
[209] Hassouni K., et al., *Modeling Species and Energy Transport in Moderate Pressure Diamond Deposition H 2 Plasmas,* J. Phys. III France 6 1996, p. 1229-1243.
[210] Gicquel A., et al., *Diamond deposition in a bell-jar reactor: influence of the plasma and substrate parameters on the microstructure and growth rate,* Diamond and Related Materials 2 (2-4) 1993, p. 417-424.
[211] Silva F., et al., *Microwave engineering of plasma-assisted CVD reactors for diamond deposition,* Journal of Physics: Condensed Matter 21 (36) 2009, p. 364202.
[212] Silva F., et al., *Microwave analysis of PACVD diamond deposition reactor based on electromagnetic modelling,* Diamond and Related Materials 19 (5-6) 2010, p. 397-403.
[213] Issaoui R., et al., *Evaluation of freestanding boron-doped diamond grown by chemical vapour deposition as substrates for vertical power electronic devices,* Applied Physics Letters 100 (12) 2012, p. 122109.
[214] Bosia F., et al., *Modification of the structure of diamond with MeV ion implantation,* Diamond and Related Materials 20 (5) 2011, p. 774-778.
[215] Chase B., *Fourier transform Raman spectroscopy,* Analytical Chemistry 59 1987, p. 881A-890A.
[216] Ohfuji H., et al., *Micro-/nanostructural investigation of laser-cut surfaces of single- and polycrystalline diamonds,* Diamond and Related Materials 19 (7) 2010, p. 1040-1051.
[217] Kononenko T.V., A.A. Khomich, and V.I. Konov, *Peculiarities of laser-induced material transformation inside diamond bulk,* Diamond and Related Materials 37 2013, p. 50-54.
[218] Gheeraert E., et al., *Effect of boron incorporation on the "quality" of MPCVD diamond films,* Diamond and Related Materials 2 1993, p. 742-745.
[219] Ager III W.A., et al., *Fano interference of the Raman phonon in heavily boron-doped diamond films grown by chemical vapor deposition,* Applied Physics Letters 66 (5) 1995, p. 616-618.
[220] Pruvost F., E. Bustarret, and A. Deneuville, *Characteristics of homoepitaxial heavily boron-doped diamond films from their Raman spectra,* Diamond and Related Materials 9 (3) 2000, p. 295-299.
[221] Zaitsev A.M., *Optical Properties of Diamond: A Data Handbook*, Springer, 2001.
[222] Huang M., et al., *Mechanisms of ultrafast laser-induced deep-subwavelength gratings on graphite and diamond,* Physical Review B 79 (12) 2009, p. 125436.
[223] Ghodbane S., F. Omnès, and C. Agnès, *A cathodoluminescence study of boron doped {111}-homoepitaxial diamond films,* Diamond and Related Materials 19 (4) 2010, p. 273-278.

[224] Baron C., et al., *Excitonic recombinations and energy levels of highly boron doped homoepitaxial diamond films before and after hydrogenation,* Diamond and Related Materials 14 (3-7) 2005, p. 350-354.
[225] Barjon J., et al., *Cathodoluminescence as a tool to determine the phosphorus concentration in diamond,* physica status solidi (a) 204 (9) 2007, p. 2965-2970.
[226] Baron C., et al., *Cathodoluminescence of highly and heavily boron doped (100) homoepitaxial diamond films,* Diamond and Related Materials 15 (4-8) 2006, p. 597-601.
[227] Haenen K., et al., *P-doped diamond grown on (110)-textured microcrystalline diamond: growth, characterization and devices* Journal of Physics: Condensed Matter 21 2009, p. 364204.
[228] Tallaire A., et al., *Dislocations and impurities introduced from etch-pits at the epitaxial growth resumption of diamond,* Diamond and Related Materials 20 2011, p. 875-881.
[229] Ali M.O., *Elementary Solid State Physics*, ed. Addison-Wesley, 1975.
[230] Kasu M., et al., *Influence of epitaxy on the surface conduction of diamond film,* Diamond and Related Materials 13 (2) 2004, p. 226-232.
[231] Oliver W.C. and G.M. Pharr, *Measurement of hardness and elastic modulus by instrumented indentation: Advances in understanding and refinements to methodology,* Journal of Materials Research 19 (1) 2004, p. 3-20.
[232] Reeves G.K. and H.B. Harrison, *Obtaining the specific contact resistance from transmission line model measurements,* IEEE Electron Device Letters 3 (5) 1982, p. 111-113.
[233] Schroder D.K., *Semiconductor Material and Device Characterization*, Wiley-IEEE Press ed, Hoboken, New Jersey, 2006.
[234] Valdes L.B., *Resistivity Measurements on Germanium for Transistors,* Proceeding of IRE 42 (2) 1954, p. 420-427.
[235] Kononenko T.V., et al., *Microstructuring of diamond bulk by IR femtosecond laser pulses,* Applied Physics A 90 (4) 2008, p. 645-651.
[236] http://home.infn.it/it/.
[237] http://www.lnf.infn.it/acceleratori/btf/.
[238] Martin S.P., *A SupersymmetryPrimer,* arXiv:hep-ph/9709356 [hep-ph], 2016.
[239] Bertone G., *The moment of truth for WIMP dark matter,* Nature 468 2010, p. 389.
[240] Alexandere J. and e. al., *Dark Sectors 2016 Workshop: Community Report,* arXiv:1608.08632 [hep-ph] 2016.
[241] Fayet P., *U(1)A symmetry in two-doublet models, U bosons or light scalars, and ψ and ϒ decays,* Physics Letters B 675 (2) 2009, p. 267-271.
[242] Raggi M. and V. Kozhuharov, *Results and perspectives in dark photon physics,* Rivista del nuovo cimento 38 (10) 2015.
[243] Kozhuharov V., M. Raggi, and P. Valente, *New Projects on Dark Photon Search,* arXiv:1610.04389 [hep-ex] 2016.
[244] Chiodini G., et al., *The PADME experiment for dark mediator searches at the Frascati BTF,* Journal of Instrumentation 12 (02) 2017, p. C02037.
[245] Patrignani C. and G. Particle Data, *Review of Particle Physics,* Chinese Physics C 40 (10) 2016, p. 100001.
[246] Adam W., et al., *Status of the R&D activity on diamond particle detectors,* Nuclear Instruments and Methods in Physics Research Section A: Accelerators, Spectrometers, Detectors and Associated Equipment 511 (1) 2003, p. 124-131.
[247] Valente P. and e. al., *Linear Accelerator Test Facility at LNF Conceptual Design Report,* arXiv:1603.05651 [physics.acc-ph] 2016.
[248] De Feudis M., et al., *Diamond graphitization by laser-writing for all-carbon detector applications,* Diamond and Related Materials 75 (Supplement C) 2017, p. 25-33.
[249] Ferrari A.C. and D.M. Basko, *Raman spectroscopy as a versatile tool for studying the properties of graphene,* Nature Nanotechnology 8 2013, p. 235.

[250] Pócsik I., et al., J. Non-Cryst. Solids 227-230 1998, p. 1083-1086.
[251] Castiglioni C., et al., *Raman activation in disordered graphites of the A1' symmetry forbidden k≠0 phonon: The origin of the D line,* The Journal of Chemical Physics 115 (8) 2001, p. 3769-3778.
[252] Castiglioni C., M. Tommasini, and G. Zerbi, *Raman spectroscopy of polyconjugated molecules and materials: confinement effect in one and two dimensions,* Philosophical Transactions of the Royal Society of London. Series A: Mathematical, Physical and Engineering Sciences 362 (1824) 2004, p. 2425-2459.
[253] Nair R.R. and e. al., *Fine structure constant defines visual transparency of graphene,* Science 320 2008, p. 1308.
[254] Richter A., et al., *Nanoindentation of diamond, graphite and fullerene films,* Diamond and Related Materials 9 (2) 2000, p. 170-184.
[255] Sun B., P.S. Salter, and M.J. Booth, *High conductivity micro-wires in diamond following arbitrary paths,* Applied Physics Letters 105 (23) 2014, p. -.
[256] Lagomarsino S., et al., *Electrical and Raman-imaging characterization of laser-made electrodes for 3D diamond detectors,* Diamond and Related Materials 43 2014, p. 23-28.
[257] Parrini G., et al., *Laser graphitization for polarization of diamond sensors*, Proceeding of the 10th International Conference on Large Scale Applications and Radiation Hardness of Semiconductor Detectors, Florence, Italy, Proceedings of Science.
[258] Assiro R., et al., *Performance of the diamond active target prototype for the PADME experiment at the DAΦNE BTF,* arXiv:1709.07081 [physics.ins-det], 2017.
[259] Raggi M., et al., *Performance of the PADME Calorimeter prototype at the DAΦNE BTF,* Nuclear Instruments and Methods in Physics Research Section A: Accelerators, Spectrometers, Detectors and Associated Equipment 862 2017, p. 31-35.
[260] http://medipix.web.cern.ch/.
[261] Oliva F., *Sviluppo e caratterizzazione del bersaglio attivo dell'esperimento PADME,* Master Thesis, Università del Salento, 2016.
[262] http://www.cividec.at.
[263] http://www.caentechnologies.com/.
[264] Leonardi E., M. Raggi, and P. Valente, *Development and test of a DRS4-based DAQ system for the PADME experiment at the DAΦNE BTF,* J. Phys.: Conf. Ser. 898 2017, p. 032024.
[265] Chiodini G., et al., *A diamond active target for the PADME experiment,* Journal of Instrumentation 12 (02) 2017, p. C02036.
[266] Oliva F., et al., *Bersaglio attivo in diamante per l'esperimento PADME*, Proceeding of the V National Workshop on Plasmi Sorgenti Biofisica e Applicazioni (PSBA) 2016, Lecce, Italy, ISBN: 978-88-8305-130-2 2015.
[267] Oliva F., et al., *Beam test results of PADME full carbon active diamond target*, Proceeding of the Conference Incontri di Fisica delle Alte Energie (IFAE) 2016, Genova, Italy, IL NUOVO CIMENTO 40 (C) 2017, p. 81.
[268] Foggetta L.G., B. Buonomo, and P. Valente, *Beam Optimization of the DAFNE Beam Test Facility*, Proceeding of the 6th International Particle Accelerator Conference (IPAC) 2015, Richmond, Virginia, U.S.A.
[269] Issaoui R., et al., *Influence of oxygen addition on the crystal shape of CVD boron doped diamond,* physica status solidi (a) 208 (9) 2011, p. 2023-2027.
[270] Omnès F., et al., *Study of boron doping in MPCVD grown homoepitaxial diamond layers based on cathodoluminescence spectroscopy, secondary ion mass spectroscopy and capacitance–voltage measurements,* Diamond and Related Materials 20 (7) 2011, p. 912-916.
[271] Tallaire A., et al., *Growth of thick and heavily boron-doped (113)-oriented CVD diamond films,* Diamond and Related Materials 66 2016, p. 61-66.
[272] Barjon J., et al., *Boron acceptor concentration in diamond from excitonic recombination intensities,* Physical Review B 83 (7) 2011, p. 073201.

[273] Iyer S.B., et al., *Vibronic model for band A emission in diamond,* Physical Review B 55 (7) 1997, p. 4093.
[274] Tallaire A., et al., *Identification of Dislocations in Synthetic Chemically Vapor Deposited Diamond Single Crystals,* Crystal Growth & Design 16 2016, p. 2741–2746.
[275] Kinchin G.H. and R.S. Pease, *The Displacement of Atoms in Solids by Radiation,* Reports on Progress in Physics 18 (1) 1955, p. 1.
[276] Drumm V.S., et al., *Surface damage on diamond membranes fabricated by ion implantation and lift-off,* Applied Physics Letters 98 (23) 2011, p. 231904.
[277] Brandes G.R., et al., *Ion implantation and anneal to produce low resistance metal–diamond contacts,* Diamond and Related Materials 8 (10) 1999, p. 1936-1943.
[278] Enlund J., et al., *Anisotropic dry etching of boron doped single crystal CVD diamond,* Carbon 43 (9) 2005, p. 1839-1842.

Abstract

This PhD work has been carried out in international cotutelle agreement between the University of Salento (L3, Italy) and the University of Paris 13 (LSPM, France). The main aim was the manufacturing of ohmic contacts on diamond surface for detector and electronic device applications. The work at L3 was dedicated to the laser-induced diamond graphitization process in order to produce graphitic electrodes on intrinsic diamonds. An experimental set-up dedicated to the laser writing technique on diamond has been developed in both hardware and software aspects and a protocol for the manufacturing of segmented graphitic contacts on diamond surface of large scale (cm^2) has been implemented. An extensive characterization work has demonstrated the diamond-graphite phase transition and an ohmic electrical behaviour for the contacts with a resistivity of the order of $\approx 10^{-5}$ Ω.m. Eventually, an all-carbon detector has been developed and tested with 450 MeV electron and positron beams proving to be a good candidate in the role of active target for a new high-energy experiment (PADME) in the framework of the dark matter. The work at LSPM has been dedicated to the development of a protocol allowing reaching ohmic contacts on lightly boron doped diamond with oxygenated surface grown by MPACVD. The fabrication of Ti/Au metallic contact above a mesa structure has relied on a He ion implantation treatment to induce a graphitic layer underneath the diamond surface. The electrical measurements on lightly doped diamonds ($[B] = 4 \times 10^{17}$ cm^{-3}) with metal or graphite / metal contacts have shown that the graphitic layer makes ohmic the contacts leading to a specific contact resistance as low as 3.3×10^{-4} Ω.cm^2.

Key words: Diamond graphitization, laser-writing, ion implantation, diamond metallization, ohmic graphitic contacts, all-carbon detector, PADME, MPACVD, boron doping, surface characterizations.

Titolo: Diamanti: sintesi e fabbricazione di contatti per applicazioni di rivelazione.

Riassunto

Questo dottorato di ricerca è stato svolto in convenzione di cotutela internazionale tra l'Università del Salento (L3, Italia) e l'Università di Parigi 13 (LSPM, Francia). Il principale obiettivo è stato la fabbricazione di contatti ohmici su superficie di diamante per applicazioni come rivelatori e dispositivi elettronici. Il lavoro a L3 è stato dedicato allo studio del processo di grafitizzazione del diamante indotto da laser al fine di produrre elettrodi grafitici su diamanti intrinseci. In particolare, è stato sviluppato un apparato sperimentale dedicato alla tecnica di scrittura laser su diamante sia nelle componenti hardware che software, ed è stato realizzato un protocollo per la fabbricazione di contatti grafitici segmentati su superfici di diamante di grande scala (cm^2). Un ampio lavoro di caratterizzazione ha dimostrato la transizione di fase diamante-grafite e il comportamento ohmico per i contatti elettrici con una resistività dell'ordine di 10^{-5} Ω.m. Pertanto, un rivelatore costituito solo di carbonio è stato sviluppato e testato con fasci elettronici e positronici di 450 MeV risultando essere un buon candidato nel ruolo di bersaglio attivo per un nuovo esperimento di fisica delle alte energie (PADME) nel contesto della materia oscura. Il lavoro a LSPM è stato dedicato allo sviluppo di un protocollo che ha consentito di ottenere contatti ohmici su diamanti leggermente drogati con boro e con superficie terminata con ossigeno, cresciuti mediante MPACVD. I processi di fabbricazione di contatti metallici Ti/Au sopra una struttura mesa sono stati sviluppato così come un trattamento di impiantazione a base di ioni di He al fine di indurre uno strato grafitico appena sotto la superficie del diamante. Le misure elettriche su diamanti leggermente drogati ($[B] = 4 \times 10^{17}$ cm^{-3}) con contatti o solo metallici o grafitici / metallici hanno dimostrato che la presenza dello strato grafitico rende i contatti ohmici e comporta una resistenza specifica di contatto pari a 3.3×10^{-4} Ω.cm^2.

Parole chiavi: Grafitizzazione del diamante, scrittura laser, impiantazione ionica, metallizzazione del diamante, contatti grafitici ohmici, rivelatori di solo carbonio, PADME, MPACVD, drogaggio con boro, caratterizzazioni di superficie.

Titre: Diamants: synthèse et fabrication de contacts électriques pour des applications de détection.

Résumé

Ce travail de doctorat a été réalisé dans le cadre d'un accord de cotutelle international entre l'Université de Salento (L3, Italie) et l'Université de Paris 13 (LSPM, France). L'objectif principal était la fabrication de contacts ohmiques sur des surfaces de diamant pour des applications telles que les détecteurs et les dispositifs de l'électronique. Les travaux au L3 ont été consacrés à l'étude du processus de graphitisation du diamant induit par laser afin de produire des électrodes de graphite sur des diamants intrinsèques. L'étude se concentre en particulier sur le développement d'un appareil expérimental pour l'écriture laser sur diamant tant sur les aspects matériel que logiciel, et un protocole a ainsi été développé pour la fabrication de contacts graphitiques segmentés sur de larges surfaces de diamant (cm^2). Des travaux approfondis de caractérisation ont démontré la transition de phase diamant-graphite et le comportement ohmique pour les contacts électriques avec une résistivité de l'ordre de 10^{-5} Ω.m. Des détecteurs tout-carbone ont ainsi été développés et testés avec des faisceaux électroniques et positroniques de 450 MeV. Ils permettent d'ouvrir des perspectives en tant que cible active pour de nouvelles expériences de physique des hautes énergies (PADME) dans le cadre de l'étude de la matière noire. Le travail au LSPM a été consacré au développement d'un protocole permettant d'obtenir des contacts ohmiques sur des films diamant faiblement dopé au bore et terminé oxygène, élaborés par MPACVD. Les procédés de fabrication de contacts métalliques Ti/Au sur une structure mesa ainsi que l'implantation par des ions He, ont été développés afin d'induire une couche de graphite juste en dessous de la surface de diamant. Les mesures électriques sur des diamants légèrement dopés ($[B] = 4 \times 10^{17}$ cm^{-3}) avec seulement des contacts métalliques ou graphitiques / métalliques ont montré que la présence de la couche graphitique rend les contacts ohmiques et conduisent à une résistance spécifique de contact égale à 3.3×10^{-4} Ω.cm^2.

Mots clés: Graphitisation du diamant, écriture laser, implantation ionique, métallisation du diamant, contacts graphitiques ohmiques, détecteur tout-carbone, PADME, MPACVD, dopage au bore, caractérisations de surface.